Development of a digital manufacturing process chain for ceramic composites

Dissertation

zur Erlangung des akademischen Grades

Dr.-Ing.

eingereicht an der
Mathematisch-Naturwissenschaftlich-Technischen Fakultät
der Universität Augsburg

von

Neraj Jain

Augsburg, Februar 2022

Erstgutachter: Prof. Dr. Dietmar Koch

Zweitgutachter: Prof. Dr. Michael Kupke

Drittgutachter: Prof. Dr. Alexander Schiendorfer

Tag der mündlichen Prüfung: 6. April, 2022

Contents

List of abbreviations

ACC	Advanced Ceramic Corp.
CAD	Computer-aided Design
CAE	Computer-aided Engineering
CFD	Computational Fluid Dynamics
CFRP	Carbon Fibre Reinforced Plastic
CMC	Ceramic Matrix Composites
CSI	Ceramic Slurry Infiltration
CT	Computed Tomography
CVD	Chemical Vapour Deposition
CVI	Chemical Vapour Infiltration
DEM	Discrete Element Method
DIC	Digital Image Correlation
DLR	German Aerospace Centre
EBC	Environmental Barrier Coating
FEM	Finite Element Method
GE	General Electric
ICME	Integrated Computational Materials Engineering
LCM	Liquid Composite Moulding
LSI	Liquid Silicon Infiltration
MAE	Mean Average Error
ML	Machine Learning
MMD	Micromechanics of Damage Analysis
NASA	National Aeronautics and Space Administration
NDT	Non-Destructive Testing
NOx	Oxides of Nitrogen
PDF	Probability Distribution Function
PEEK	Polyether-ether-ketone
PIP	Polymer Infiltration and Pyrolysis
PL	Proportional Limit
PSPP	Process-Structure-Property-Performance
RMI	Reactive Melt Infiltration

RTM	Resin Transfer Moulding
RVE	Representative Volume Element
SEM	Scanning Electron Microscope
TBC	Thermal Barrier Coating
TEM	Transmission Electron Microscope
TPS	Thermal Protection System
UD	Unidirectional
UHC	Unburned Hydrocarbons
UHTCMC	Ultra-High Temperature Ceramic Matrix Composite
VARTM	Vacuum Assisted Resin Transfer Moulding
WHIPOX	Wound Highly Porous Oxide
WWFE	World-Wide Failure Exercise
XRD	X-ray Diffraction

Acknowledgement

First, I would like to thank Prof. Dietmar Koch and the German Aerospace Centre (DLR) for giving me this opportunity to perform the research work required for this dissertation. Prof. Koch not just supervised my thesis but was always there to motivate me whenever there was a roadblock, during my PhD. I was lucky to have him as a mentor, who gave me freedom to explore new ideas and supported me to grow in a scientific field.

I would also like to thank Prof. Michael Kupke to support the research topic and his constructive feedback during the review meeting. Thanks to Prof. Alexander Schiendorfer on being a part of the review committee of this doctoral research.

I would like to thank all my colleagues at the Department of Ceramic Composites and Structures who supported me directly or indirectly in my research. This work would certainly have not been possible without the friendly and cheerful environment in the department provided by them. I am thankful that I got the opportunity to supervise Marvin Kosin, Mohan Reddy, Ilda Hysa, Muhammad Noman Khaldi, Nikhil Muthyala and Muhammad Hafiz Noman in their internships and master theses'.

I would like to thank Dr. Severin Hofmann and Dr. Yuan Shi, who mentored me during different phases of my career and were always there to have discussions regarding my research ideas.

I am grateful to have a group of friends who have always supported me with their company and encouragement. This thesis would certainly not have been possible without two people. A big thanks to Dr Swaroop Gaddikere Nagaraja with whom I had hours long discussions regarding research and spent hours in finding bugs in the codes. Special thanks go to Linda Klopsch for supporting me in managing the time between my research work and other professional commitments during my tenure at the DLR.

This work would not have been possible without the endless support of my family. I am lucky to have my brother Shubham and parents Snehlata and Mukesh in my life.

Abstract

The development of ceramic matrix composites, with their increasing use in high temperature and corrosive environment applications, is still restricted to ‘trial and error’ approach in comparison to other conventional materials like metals. The main reason behind that is the lack of experimental data due to high manufacturing costs of CMCs which generally includes a chain of several complex processes. This adds to the complexity of this material class and thus, makes it a difficult task to establish a relationship between a component with desired properties and the manufacturing parameters required to realise it.

In the current work, the digital aspects are investigated from two point of views to use numerical methods to support the material design process: ‘material’ and ‘manufacturing process’. The case ‘material’ is the focus of this work where, ‘process-structure-property-performance’ (PSPP) relationship is established to study the entire life cycle of a CMC component, starting from the intermediate products, such as fibre preforms or green bodies prior to siliconization process, used in the processing to the mechanical performance of the final machined component under operating conditions.

Each aspect of the PSPP relationship is discussed in detail and its implementation is demonstrated with the help of a numerical example. Cohesive zone elements at micro-level and homogenous damage development at macro-level were used to define the non-linear behaviour of the material under mechanical loading. Experimental results obtained for different CMCs such as C/C-SiC, C/SiCN, SiC/SiCN and Al_2O_3/ Al_2O_3 were used to validate the results obtained for the finite element models at different scales ranging from micro to macro. With the help of data analysis techniques like image segmentation and machine learning algorithm, computationally inexpensive data-based surrogate models were generated from accurate but computationally expensive physics-based models.

A detailed review of the available numerical methods to model the manufacturing process and the process monitoring techniques is given. Based on the data and information obtained from the modelling of the material and the manufacturing process, a concept is proposed for optimized development of a CMC part. The concept combines the generated data with quantified expertise in the fields of material science to realise a manufacturing process chain to facilitate the material design process for CMCs. With the implementation of such an approach, the production cost of CMCs can be reduced by knowledge-based selection of the CMC constituents and manufacturing parameters. This will open the door for new applications of CMCs which would enable the material community to extend their use to other cost-efficient high temperature applications.

Kurzfassung

Die Entwicklung von Verbundwerkstoffen mit keramischer Matrix, die zunehmend bei hohen Temperaturen und in korrosiven Umgebungen zum Einsatz kommen, ist im Vergleich zu anderen herkömmlichen Werkstoffen wie Metallen noch immer auf ein "Versuch-und-Irrtum"-Konzept beschränkt. Der Hauptgrund dafür ist der Mangel an experimentellen Daten aufgrund der hohen Herstellungskosten von CMCs, die im Allgemeinen eine Prozesskette aus mehreren komplexen Verfahrensschritten umfassen. Dies trägt zur Komplexität dieser Werkstoffklasse bei und macht es somit schwierig, eine Beziehung zwischen einem Bauteil mit gewünschten Eigenschaften und den Herstellungsparametern herzustellen.

In der vorliegenden Arbeit werden die digitalen Aspekte aus zwei unterschiedlichen Blickwinkeln untersucht, um numerische Methoden zur Unterstützung der Werkstoffauslegung einzusetzen: 'Werkstoff' und 'Herstellungsprozess'. Im Mittelpunkt dieser Arbeit steht der "Werkstoff", bei dem die "Process-Structure-Property-Performance"-Beziehung (PSPP) hergestellt wird, um den gesamten Lebenszyklus eines CMC-Bauteils zu untersuchen. Angefangen bei den Zwischenprodukten, wie z. B. den Faser-Vorkörpern (Preform)vor dem Silizierverfahren, die die Basis der Verarbeitung bilden, bis hin zur mechanischen Belastungsgrenze des fertig bearbeiteten Bauteils unter Betriebsbedingungen.

Jeder Aspekt der PSPP-Beziehung wird im Detail untersucht und ihre Umsetzung anhand eines numerischen Beispiels demonstriert. Kohäsive Zonenelemente auf der Mikroebene und homogene Schädigungsentwicklung auf der Makroebene wurden verwendet, um das nichtlineare Verhalten des Werkstoffs unter mechanischer Belastung zu definieren. Experimentelle Ergebnisse, die für verschiedene CMCs wie C/C-SiC, C/SiCN, SiC/SiCN und Al_2O_3/ Al_2O_3 erzielt wurden, dienten zur Validierung der Ergebnisse der Finite-Elemente-Modelle auf verschiedenen Skalen von Mikro bis Makro. Mit Hilfe von Datenanalysemethoden wie Bildsegmentierung und ‚Machine-Learning-Algorithmen' wurden aus genauen, aber rechenintensiven physikalischen Modellen zeiteffiziente datenbasierte Ersatzmodelle erstellt.

Es wird ein detaillierter Überblick über die verfügbaren numerischen Methoden zur Modellierung des Fertigungsprozesses und der Prozessüberwachungstechniken gegeben. Auf der Grundlage der Daten und Informationen, die aus der Modellierung des Materials und der Herstellungsprozesse gewonnen wurden, wird ein Konzept für die optimierte Entwicklung eines CMC-Bauteils vorgeschlagen. Das Konzept kombiniert die generierten Daten mit quantifiziertem Fachwissen in den Bereichen der Materialwissenschaft, um eine Fertigungsprozesskette zu realisieren, die die Werkstoffauslegung für CMCs erleichtert. Mit der Umsetzung eines solchen Ansatzes können die Produktionskosten von CMCs durch eine wissensbasierte Auswahl der CMC-Bestandteile und Herstellungsparameter gesenkt werden.

Dies wird die Tür für neue Anwendungen von CMCs öffnen, die es der Materialgemeinschaft ermöglichen wird, ihre Verwendung auf andere kosteneffiziente Hochtemperaturanwendungen auszuweiten.

1 Introduction

1.1 Ceramic Matrix Composites

The use of composite materials can be dated back to the times when dried straws with mud were used as building blocks by our civilisation. A composite material is a combination of multiple materials which combines the advantages of the involved individual constituents. Ceramic matrix composites (CMCs) are also combination of materials, where a ceramic matrix is reinforced with the help of fibres or particles. They exhibit superior high temperature and corrosion-resistant properties because of the ceramic matrix and the reinforcement of the fibres provides the quasi-ductile behaviour to this class of materials. CMCs are seen as the replacement of the high temperature nickel-based alloys where the demanding temperature conditions of the new generation aero engines is increasing in order to meet the climate goals set by the nations of the world to fight the challenge of global warming. The NOx, CO and UHC (Unburned Hydro-Carbon) emission are reduced with the integration of CMC combustor liners and first stage shrouds and can reduce the fuel cost up to 830,000 US$ per year per machine (MS7001FA gas turbine GE) [1]. They can not only sustain higher temperature in comparison to their metallic counterparts but are also lighter in weight where their density is about one-third of the metals. Silicon carbide fibre reinforced silicon carbide (SiC/SiC) and aluminium oxide fibre reinforced aluminium oxide (Al_2O_3/Al_2O_3 or Ox/Ox) are the two main CMCs used in the gas turbines and have already been integrated into their products by commercial engine manufacturers like GE Aviation, Pratt & Whitney and Safran [2].

Apart from the aeronautical applications, research areas like space, energy and transportation are also looking towards these materials to cater to the needs of demanding temperature and corrosive environments. SiC/SiC has also found its use in the nuclear applications due to its stability in the environment with nuclear radiations [3]. Materials like carbon fibre reinforced carbon (C/C) were used as thermal protection systems (TPS) during the re-entry into the earth atmosphere in the Space Shuttle Program of NASA [4]. In the application with higher temperature conditions above 2000°C, materials like carbon fibre reinforced zirconium diboride (C/ZrB_2), also known as Ultra High Temperature Ceramic Matrix Composites (UHTCMCs) are used thanks to their stable diboride matrix which has its melting temperature above 3000°C [5]. Due to its high temperature stability and hardness at high temperatures, carbon fibre reinforced with matrix of carbon and silicon carbide (C/C-SiC) is used in rocket nozzles in the aerospace industry [6] and disk brakes in the automobile industry [7].

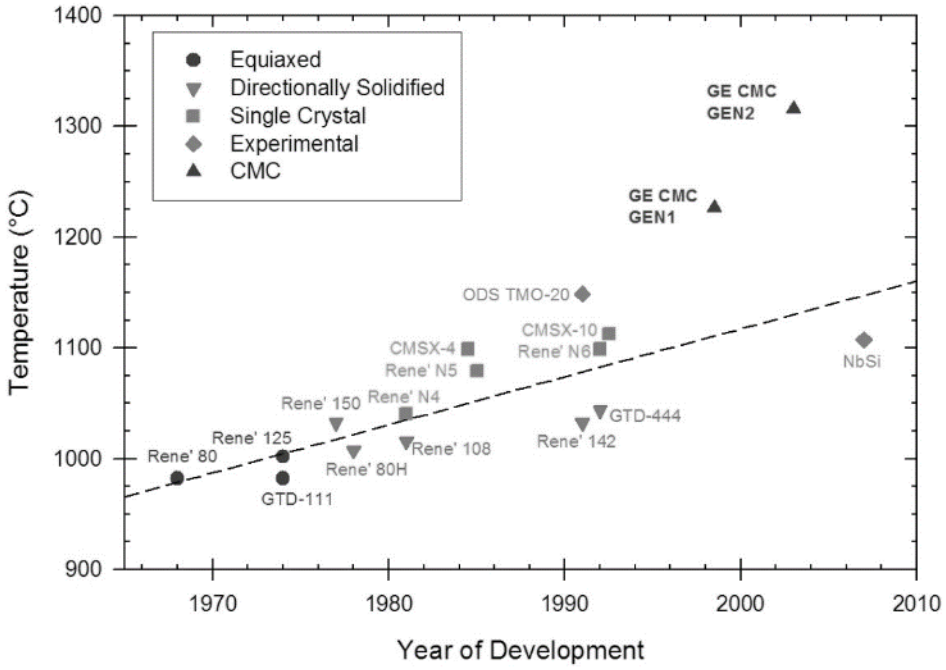

Figure 1.1: Comparison of gas turbine structural materials based on their high temperature capability and their development over time [8]

However, there are certain limiting factors that have restricted the use of CMCs in the above-mentioned applications and the potential of this material class has not been exploited enough. The manufacturing routes include several complex high temperature steps where the formation of processing defects cannot be avoided completely. These defects increase the rejection rate of the structures as the qualification standards of the targeted applications are rather strict. It reduces the confidence in the material as the relationship between the defects and their effects over the component performance is not trivial and requires a rigorous testing campaign with state-of-the-art quality measuring devices to ensure a safe design for any specific application. Moreover, very long (days to several months) high temperature processing steps, high rejection rates and expensive raw materials increase the final cost of any CMC component exponentially which limits their use to niche engineering fields like aerospace and nuclear applications. As a result of this high cost, the number of tests which can be performed, is restricted which in turn, adds to the above-mentioned problem of meeting the quality standards required by certain application. In order to overcome this problem, a deep understanding of the manufacturing process, resulting defects in the material and their effect over the performance of the component is required. This will drastically reduce the 'lab-to-market' time of CMCs and will result in reduced price because of lower rejection rates.

1.2 Process-Structure-Property-Performance Relationship

Process-Structure-Property-Performance (PSPP) relationship is extensively investigated in the literature for all types of conventional materials (as shown in Figure 1.2). The terms in the relationship are self-explanatory except 'Performance' which is often dropped from the relationship. The term 'performance' refers to the performance of the component made of the investigated material under operating conditions. This factor is addressed explicitly because the geometry of the component and the steps to manufacture the component can heavily influence the properties of the same material and in most of the cases, the component exhibits degraded properties in comparison to the laboratory scale samples. Factors like size-effects, where the strength of the material is considered inversely proportional to the volume of the material used, affects the performance of the component, and can result in a flawed design when not considered in the preliminary design development process. In the case of monolithic ceramics and CMCs, where characteristic manufacturing defects are present in the microstructure, this effect is more dominant [9, 10].

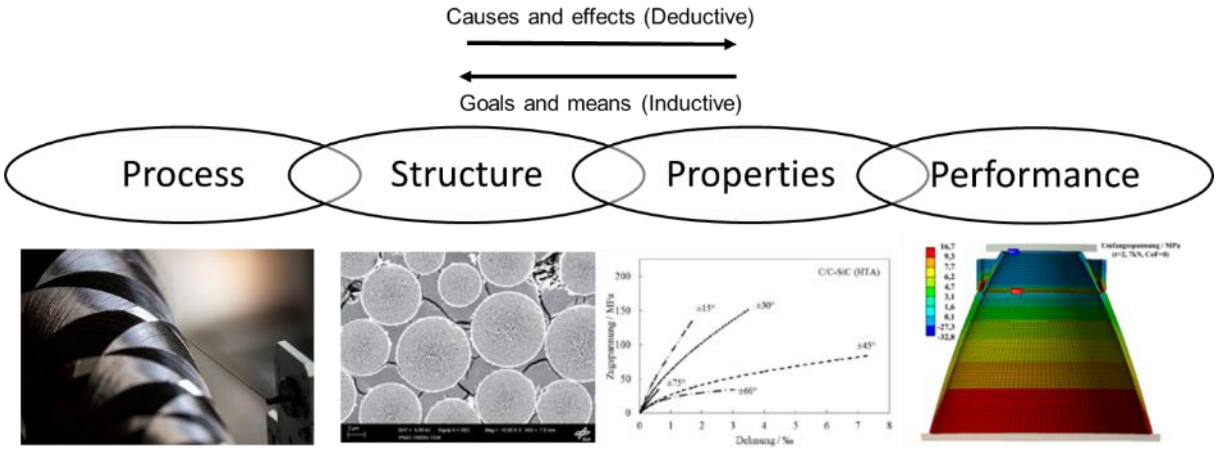

Figure 1.2: A typical process-structure-properties performance relationship where the knowledge about the effects of manufacturing over the performance is utilised to develop a design tailored according to requirements

The computational abilities have grown exponentially in the recent years and the PSPP relationship is majorly investigated by advanced digital methods which fall under the category of Integrated Computational Materials Engineering (ICME). Multiscale modelling and process simulation are integral parts of ICME and are coupled with each other to obtain two types of digital twins:

1. **Material Digital Twin**: These are interlinked multiscale models which have the capability to capture the material behaviour at all the scales (atomic, micro, meso and macro) of the material. These models allow the understanding of the underlying mechanisms behind the behaviour of the material under the real operating conditions. Based on this understanding, the material behaviour can be predicted, and the components can be designed based on the requirements of

a particular application. The impact of manufacturing parameters might be indirectly integrated into the models without modelling them physically by simulating the conditions of a processing step. For example, during tempering of a fibre-reinforced polymer, instead of simulating the physical process of tempering, the residual stresses in the microstructure can be calculated by setting the physical boundary conditions i.e., mechanical, thermal and chemical conditions based on the conditions during tempering. This approach is used in Chapter 2 to model pyrolysis step in manufacturing of CMCs and study the change in the microstructure. In this way, one gets an insight into the process, but the fine tuning of the parameters still poses a challenge because of the assumptions made in choosing the boundary conditions. Nevertheless, this simplified approach helps in understanding the changes that a material undergoes during the processing and is relevant from the viewpoint of a design engineer, where deep understanding of process is not a priority but the modification in the geometries and the properties of a component is of interest.

2. **Process Digital Twin**: It is a digitalized process chain where each individual manufacturing step is modelled using multi-physics simulation and are connected to each other. This digital twin allows the optimisation of manufacturing parameters to save time and resources during the material development: At the same time, the impact of these parameters over the material can be investigated. In the previous example of pyrolysis, an oven will be simulated where the global temperature set by the operator will differ from the local temperature experienced by a component based on its position in the oven. These local temperatures are then used as boundary conditions for the component and a microstructural simulation is carried out to study the effects of the subsequent stages over the thermo-mechanical response of the material. Based on the number of manufacturing steps involved in the processing, the digitalisation of the entire process chain can be challenging because of the complexity of the processes. However, it allows a deep understanding of the process and enables the material scientists to deliver a product with the exact same specifications and properties as per the requirements of an application.

Many such digital twins are reported in the literature for different types of materials. Arnold et. al [11, 12] have proposed the approach to facilitate material selection for aerospace components based on an extensive database containing not only the bulk properties of the materials but also the related information about each material class spread over all the length scales. The software architecture of a ‘Materials information management system’ was developed together with NASA Glenn Research Center which links the data from manufacturing, tests and microstructural analysis with the physics based multi scale simulation models to choose an appropriate material for a particular application with the inclusion of effects from manufacturing. The effect of residual stresses and post-heat treatment over the mechanical response was investigated in [12] to demonstrate these effects in SiC/SiC CMCs.

Ziegler et.al extensively studied the process to manufacture reaction bonded silicon nitride (RBSN) [13]. Thermo-mechanical properties like fracture strength, creep, thermal shock, thermal cycling behaviour and oxidation were investigated where porosity and the pore structure were the deciding factors in deriving these properties. Transmission electron microscopy (TEM) and scanning electron microscopy (SEM) were used to study the grain interfaces and their impact over the measured properties of the material. Polymer derived ceramics are used in manufacturing of CMCs and the PSPP relationship for these ceramics was investigated by Zunjarrao [14]. The effect of processing temperature and hold duration over the mechanical response of the produced amorphous/nanocrystalline SiC was studied and optimum values of these parameters were reported. Clausell and Barba studied the microstructure of CuNiZN ferrite bulk ceramic via SEM and established a relationship between the sintering temperature, average grain size and the electromagnetic properties of the bulk ceramic [15]. Ma et.al investigated the fracturing behaviour of the ceramic proppants prepared from bauxite [16]. It was found that the mechanical properties depend on the sintering temperature. With the help of SEM images, a relationship between the sphericity of the ceramic proppants and their mechanical performance was established. A similar study was performed by Li et.al to understand the effects of sintering temperature for Al_2O_3 manufactured via additive manufacturing [17]. TEM was used to study the microstructural changes with varying sintering temperature and an increase in the crystallite size was observed with increasing temperature.

The manufacturing of composites becomes more challenging in comparison with monolithic ceramics as more steps are involved in the manufacturing process, thus increasing the number of parameters involved in it. Chung reviewed the manufacturing process of carbon fibre polymer-matrix composites and its relation to the thermal, mechanical, electrical and electromagnetic properties of the material [18]. Fibre layups with unidirectional and woven preforms, matrix type, fibre volume content, curing temperature, filler addition, fibre treatments and component coating are some of the parameters which were studied in detail in this work. Carbon fibre reinforced polyether-ether-ketone (PEEK) composites were investigated by Zheng et. al [19]. The focus of this work was to study the effect of the processing temperature and the holding pressure on the thermal and mechanical properties. Qualitative microscopic analysis was performed to understand the underlying mechanisms behind the behaviour of the material under different loading set-ups. Matrix properties, void defects, fibre-matrix interface and interlayer adhesion were found out to be the most important factors for the thermo-mechanical behaviour. Xie et.al published the results of process optimisation for compression moulding of carbon fibre-reinforced thermosetting polymer [20]. Compression temperature, compression pressure, pressure-holding time, cooling rate and mould-opening temperature were ranked as the most important parameters which impacted the mechanical properties of the material. D'Mello et. al discussed virtual manufacturing of composite structures for aeronautical applications with focus on the effect of curing on the mechanical response of composites with the help of finite element simulations [21]. Waas et. al reported few case

studies performed under the framework of ICM2 project together with industrial partners like GE-Aviation, Lockheed Martin Aeronautics Company and Autodesk among others [22]. They reported the effect of the cure cycles over the mechanical response of the fibre reinforced components using an integrated framework. Xu reported the linking of the process simulation with multiscale simulation of carbon fibre composites in order to optimize automotive components from the weight and performance point of view [23]. High dimensionality, high computational costs and heterogeneity of the collected data were identified as challenges in achieving high fidelity digital process chain that will allow optimisation of part design and manufacturing process based on the PSPP relations.

Some more manufacturing steps are added in the case of CMCs which increase the complexity of the manufacturing process of CMCs und subsequent modelling associated with it. An ICME framework for CMCs was first reported by Shi et.al from Rolls Royce and the investigated material was SiC/SiC [24]. Computational tools and the requirements for their integration for CMCs were reviewed and prioritized based on the effort required in the implementation and their importance in the ICME framework. The relevance of the combination of steps involved in the material development with component development via advanced computational models was emphasized.

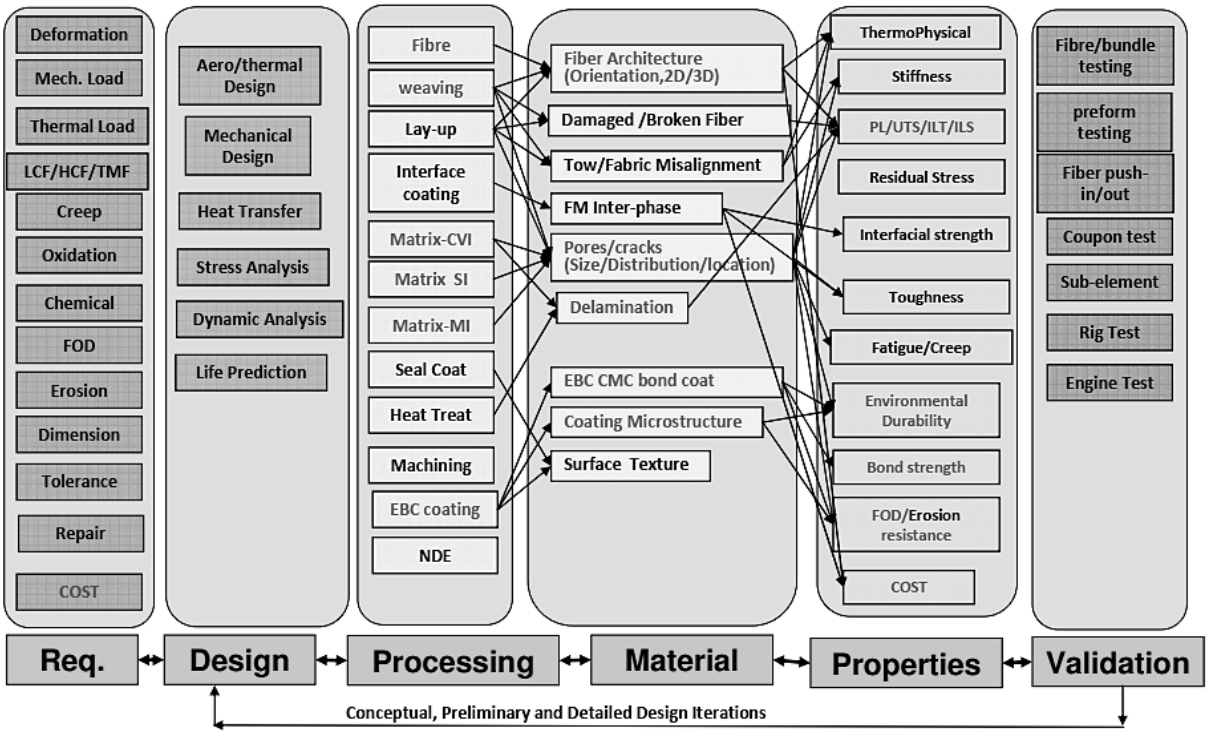

Figure 1.3: Processes involved in the manufacturing of a CMC component and their inter-dependency according to Shi et.al [24].

The topic of ICME is covered extensively by Grujicic in his publications for the development of SiC/SiC [25, 26]. Materials-by-design approach is proposed in this work where the development of new materials is driven by simulation tools and available material databases [27]. All three important constituents of SiC/SiC, namely fibre, fibre coating and matrix, are considered in the multiscale modelling to predict

the performance of the components. Moreover, an optimisation procedure to evaluate optimum manufacturing parameter set was reported keeping the tensile and creep-deformation properties as the target values.

1.3 Scope and objective

The main objective is to establish a conceptual digital process chain for the manufacturing of CMCs with the help of a combination of multiscale modelling and continuous process data extraction. In the literature, multiscale modelling approaches have been proposed for CMCs but a systematic integration of the complex manufacturing steps into the multiscale modelling framework does not exist, to the best of the author's knowledge. Process simulation is not a part of this work but an integration concept with an interface to multiscale modelling is proposed which was developed with the help of the input received from commercial ICME software developers. The integration of data-driven models via machine learning algorithms paves the way of an extensive database with information obtained from processing, experimental analysis and simulation tools. The author is aware of the other processing routes that are available to manufacture the investigated materials but to limit the scope of the current work, the processing routes developed in German Aerospace Centre (DLR) at the Institute of Structures and Design in Stuttgart were focussed on. All the elements of the PSPP relationship are considered in different chapters and is demonstrated with the help of an example followed by a concept development to digitalize the entire manufacturing chain for of CMCs.

Chapter 2 deals with the 'Process-Structure' relationship where the pyrolysis step of the manufacturing process of carbon reinforced matrix made up of amorphous carbon and silicon carbide (C/C-SiC) was investigated. Image segmentation techniques using open-source Python libraries and its application to quantify the microstructural features such as fibre diameter distribution, crack size, etc. is demonstrated in the chapter. These techniques were also used to compare the finite element simulation results with the SEM images. These results were published in the International Journal of Applied Ceramic Technology and the excerpts from the paper have been included with the permission of the journal.

In chapter 3, the 'Structure-Property' relationship is discussed where microstructural features like fibre diameter, fibre volume content and porosity along with constituent properties and their impact on the tensile behaviour of the resulting CMCs are studied. The finite element approach is then validated with the help of tensile tests performed on silicon carbon nitride reinforced with silicon carbide fibre (SiC/SiCN). The models were then used to generate virtual microstructure and a parameter study of varying microstructures and constituent properties was performed to find out the most important features impacting the tensile behaviour of a CMC with the help of machine learning algorithms. A surrogate data-based model is then generated via machine learning algorithms to enable material design based on the data generated by simulation.

Chapter 4 deals with the ‘Property-Performance’ relationship in CMCs. A damage-based failure criterion is proposed for two types of CMCs in order to predict the failure in a component. The proposed failure criterion can also differentiate between failure modes and the results are validated for two CMC variants. The results were published in the special issue- Ceramic-Matrix Composite in Journal of Composites Science and excerpts are included in the monograph after obtaining necessary permissions.

In chapter 5, a concept for digitalisation of the manufacturing process chain is proposed. The techniques involved in data extraction from the equipment used in manufacturing and quality measurement methods of intermediate products are introduced in this chapter. Based on the information obtained from these methods, a strategy is proposed that involves the expertise in different scientific fields required to manufacture a CMC component for a test campaign or for an application.

In chapter 6, the results are summarized and an outlook is provided for the further development of the approach which is introduced as a concept in this work.

2 Process-Structure Relationship

2.1 Introduction

This chapter deals with the relationship between the manufacturing parameters and the resulting microstructure of the material. The manufacturing method depends on the material required by any application. The major processing methods which can be employed to manufacture CMCs are:

- Chemical Vapor Infiltration (CVI)
- Polymer Infiltration and Pyrolysis (PIP)
- Reactive Melt Infiltration (RMI)
- Ceramic Slurry Infiltration (CSI)

There are ample of parameters which can be varied in each process which directly affect the microstructure of the material. For example, if one wants to manufacture SiC fibre reinforced SiC via RMI, there are several steps involved in the process developed at Institute of Structures and Design, German Aerospace Centre in Stuttgart. Firstly, there is a choice of fibre type from the commercially available fibres from different manufactures- Nicalon™, Hi-Nicalon™ and Hi-Nicalon™ TypeS Series from NGS Advanced Fibres; Tyranno SA3 Fibre from UBE Industries, just to mention a few. In order to protect the SiC fibres during the silicon infiltration step and ensure weak interphase between the fibre and the matrix, a fibre coating via Chemical Vapor Deposition is required [28]. A three-layered fibre coating system is employed where each layer has its own functionality and individual layer thickness can be varied to have a material with desired performance. This step is followed by resin transfer moulding (RTM), pyrolysis and liquid silicon infiltration (LSI). Each step comes with an individual set of parameters which can be varied to obtain the required microstructure and are discussed in detail in Chapter 5. This applies for all other CMCs as well and it is crucial to understand this relationship between the manufacturing parameters and the resulting microstructure to choose optimum input parameters. However, to quantify this relationship, the microstructural information needs to be quantified as well. This means that data produced during microstructural analysis via Scanning Electron Microscopy (SEM), Transmission Electron Microscopy (TEM), X-ray Computer Tomography (CT), X-ray Diffraction (XRD), etc. should be quantified as well. Image segmentation techniques are used to extract the microstructural features such as fibre volume content, fibre diameter distribution, cracks size, etc. from 2D microscopic images and discussed in detail in the upcoming section.

In order to demonstrate such a process-structure relationship, the manufacturing step considered in the current work is pyrolysis which is an intermediate step and comes before RMI. The material under investigation is C/C-SiC: a carbon fibre (C) reinforced composite where the matrix consists of carbon (C) and silicon carbide (SiC). Liquid silicon infiltration (LSI) is a subset of RMI, where molten silicon

reacts with the amorphous carbon present in an intermediates phase of C/C to finally form SiC in the matrix. The manufacturing process can briefly be described as follows [29-31]:

1. **CFRP manufacturing**: Current investigated material was manufactured using RTM where two constituents of the composite, namely fibre and resin, are put into two different connected chambers in a mould. The sealed mould is then placed between heat plates and vacuum is generated in the fibre chamber. The fibres are then infiltrated with resin. The heat plates serve as the source for curing to form CFRP which is followed by tempering to reduce the residual stresses developed during curing [32].
2. **Pyrolysis**: The polymeric matrix in CFRP is thermally decomposed into amorphous carbon. This is achieved by placing the green bodies into pyrolysis oven at temperatures around 900°C. The entire process is executed under inert conditions to prevent oxidisation and reaction of the material. The chemical processes which govern this pyrolysis step are explained in detail elsewhere [33-36]. As already pointed out, matrix experiences high shrinkage during pyrolysis, due to which internal stresses are generated within the matrix. These stresses are further enhanced by fibre/matrix interface which hinders the matrix shrinkage and are ultimately released in the form of crack generation. Evolution of these cracks results in exponential increase in open porosity of the material. The crack pattern evolved during this step is crucial for the final microstructure of resulting C/C-SiC composite.
3. **Liquid Silicon Infiltration (LSI)**: Cracks formed in the previous step provide the required space for liquid silicon to enter the matrix and react with carbon to silicon carbide (SiC). It is important to mention here that the cracks within the material should be in optimal range to protect the carbon fibres from siliconisation. If there are cracks between fibres and matrix, then the fibres can be attacked by aggressive liquid silicon and convert them into SiC as well. This degradation of fibres leads to a brittle ceramic composite which do not exhibit the damage tolerance behaviour achieved by crack bridging and fibre pull-out. The desired microstructure is the one (shown in Figure 2.1 b)), where the cracks are primarily formed within the matrix with generation of 'block-like' structures which protect the fibres from being siliconized during LSI process. Only the carbon present on the edges of these block structures is converted into SiC. This is the reason behind the presence of both carbon and silicon carbide as the matrix constituents.

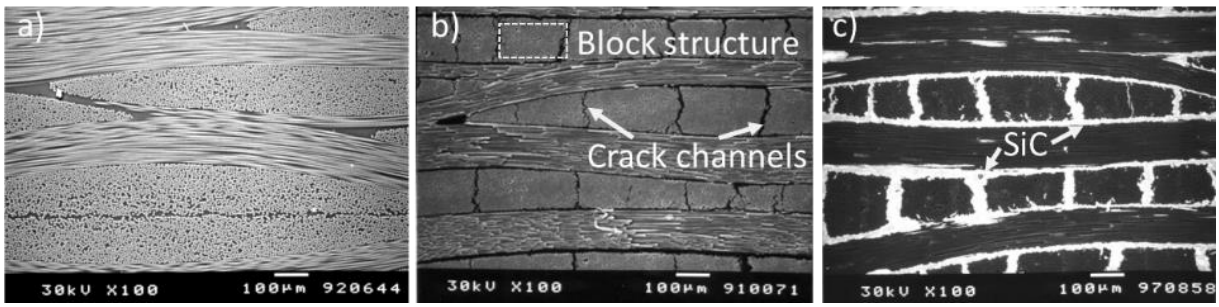

Figure 2.1: SEM images of the microstructure of C/C-SiC after different manufacturing steps: a) CFRP, b) C/C after pyrolysis and c) C/C-SiC after siliconisation [37].

The formation of the block structures, shown in Figure 2.1, due to evolution of crack channels in the C/C state is desirable since these crack channels are later filled up with liquid silicon to form silicon carbide channels and ultimately provide damage tolerance to the material.

At each of the steps mentioned above, many parameters can be changed to achieve the desired 'block' microstructure in C/C state, such as fibre type, resin type, fibre volume content and so on. In the current study, the effect of fibre volume content and fibre diameter over the crack formation is discussed.

2.2 Finite Element Model

Research has been done in understanding the phenomenon of pyrolysis and its effect over crack pattern in a microstructure. Most noteworthy work in this field has been performed by Schulte-Fischedick [38] using an analytic approach based on Micromechanics of Damage Analysis (MMD). The model was able to replicate different crack types, namely fibre-matrix debonding, transversal cracks and partial delamination but did not consider fibre/matrix interface property.

A numerical Discrete Element Method (DEM) approach was used by Wittel et. al. [39]. It gives a realistic visualisation of the microstructure and a good estimate of the increase of the crack-density. However, it fails to give a quantitative estimate of crack area. Moreover, fibre/matrix interactions were not treated explicitly which is a key factor in CMC under consideration. Fibres in this model are regarded as discrete particles with no spatial extent. Finite Element Modelling (FEM), on the contrary, regards all constituents of the composite as a continuum and the influence of fibre properties such as fibre diameter can be studied with help of FEM. The crack is introduced within a finite element mesh, where two nodes separate from each other with a pre-defined displacement entered as input properties of the material interface. The area left behind after the separation of nodes can be considered as a developed crack and can be compared with the physical crack developed in the material allowing a quantitative comparison of crack regions with microscopic images. In this manner, FEM offers more analysis possibilities compared to DEM.

Finite element modelling was employed to model the behaviour of C/C-SiC material during pyrolysis. Volume change in the material during pyrolysis is simulated with the help of 2D models of two different dimensions- 6 x 6 μm^2 and 50 x 50 μm^2. The modelling was restricted to 2D case since crack development in the transverse direction to the fibres is the main focus of the current work. The first model exhibits ideal symmetrical packing of fibres which was used to understand the stress distribution under thermal loading conditions and its influence over the crack initiation and crack growth in the matrix. It also proved useful in fitting the parameters for the cohesive zone model used in the modelling of cracks. The second model with random packing of fibres was implemented to model the realistic behaviour and compare the results with SEM images of microstructure of the material under investigation. Both these models are discussed in detail in the following sections.

2.2.1 RVE with symmetrical packing of fibres

A 2D representative volume element (RVE) was generated with the help of a manually written script to get the desired microstructure of material. The microstructure represents a single fibre with a diameter of 5 μm embedded in matrix, as seen in Figure 2.2. The effective fibre volume content of RVE is 40% and the displacements at the edges are fixed in all directions to generate stresses due to shrinkage in the matrix and initialise formation of cracks to release these stresses. The length of each edge is 6 μm. The objective behind this model is computationally inexpensive evaluation of input parameter for a model with higher number of fibres and then comparison of those results with SEM images of microstructure (discussed in next section).

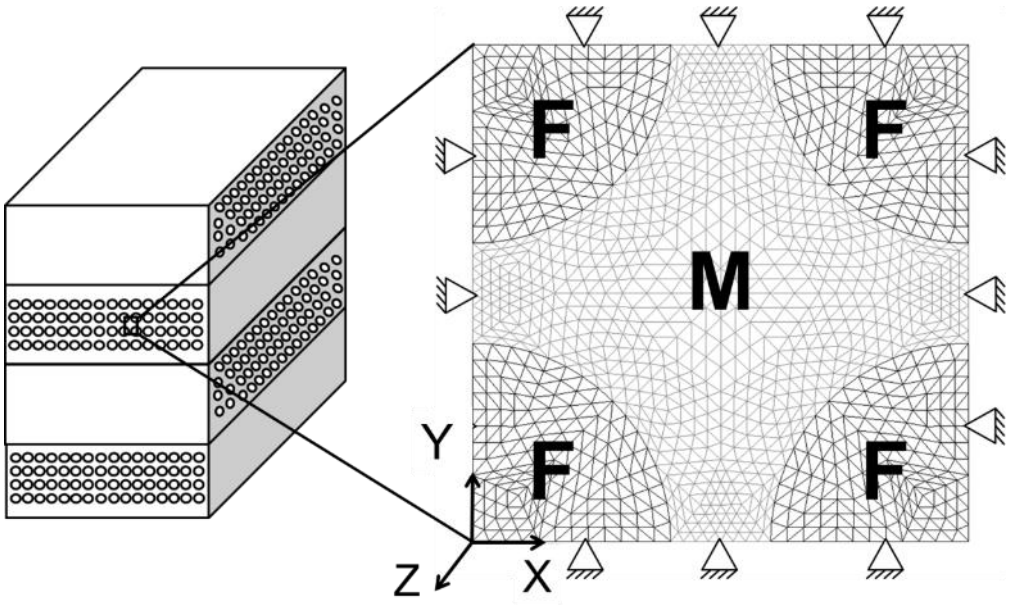

Figure 2.2: 2-D Representative Volume Element (6x6 μm^2) of a composite with square packed fibre arrangement and 0°/90° orientation, where 'F' denotes fibre and 'M' denotes matrix. The displacement on all the edges is fixed in x and y direction.

The boundary conditions on edges are periodic, as the model is assumed to extend infinitely in all the directions. The strains in z-direction are assumed to be zero because of the infinite fibre length which implies that a plane strain analysis has been performed over this microstructure.

2.2.2 RVE with asymmetrical packing of fibres

The second model with realistic random packing of fibres is shown in Figure 2.3. The dimensions of this model are 50 x 50 μm^2. The fibre volume content is 60 % in this model to draw a fair comparison with SEM images which had fibre volume content in the region of 57-63% (obtained from image segmentation). The edges of this model are also fixed in both 'x' and 'y' directions like in the previous model to generate stresses due to shrinkage and to initiate crack generation and eventual growth during the temperature change. The comparison with the SEM images of material microstructure is done with this model since it represents a realistic microstructure with random distribution of the fibres.

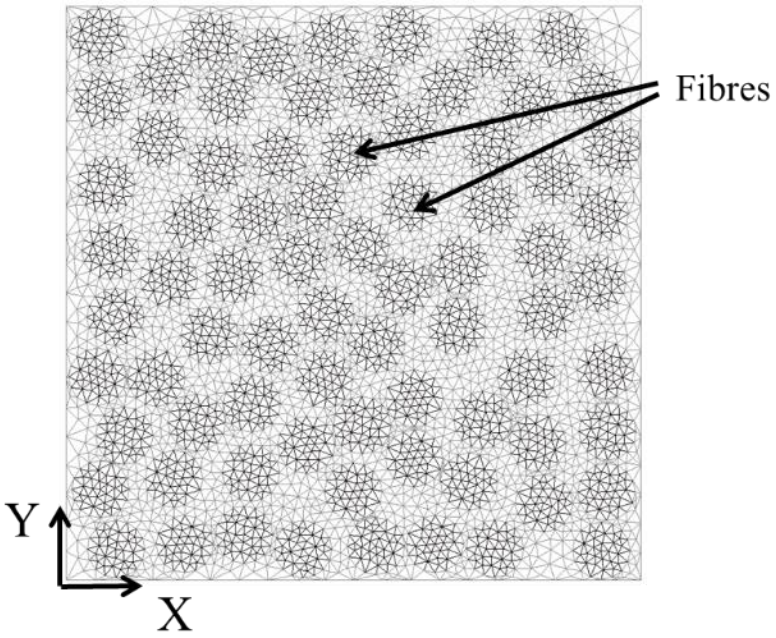

Figure 2.3: A realistic RVE (50x50 μm^2) with randomly arranged fibres and meshed with triangular elements.

2.2.3 Cohesive zone model

The modelling of cracks during pyrolysis has been implemented with the help of cohesive zone models in this work. This approach to model, the initiation and propagation of cracks with cohesive zone elements was first proposed by Dugdale [40] and Barenblatt [41]. As soon as a critical stress value is reached in an element, cohesive zone elements are inserted at the interface between two elements. After reaching this particular value, stress starts dissipating linearly with increasing distance between two crack edges. A crack is assumed to be fully developed after the critical crack opening distance is reached

and there is no more traction between the involved set of elements. The crack opening is irreversible in this case. This is defined in literature as ‘linear decay law’ and is shown in Figure 2.4 [42, 43].

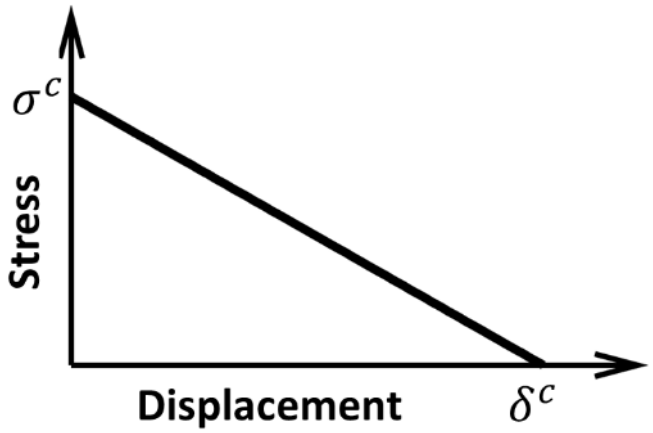

Figure 2.4: Irreversible linear decay law used in the cohesive zone model with critical displacement and critical stress values for crack opening.

The model, implemented in the present work, is available in the commercial software ‘Multimech 18.0’ by Siemens Digital Industries Software (formerly sold by Multimech Inc and taken over by Siemens). Cohesive zone elements are inserted at contact between two different element groups: 1) elements at fibre/matrix interface and 2) elements at matrix/matrix interface. Contrary to implementation of typical cohesive zone elements, which must be defined as a priori before the crack initiates, Multimech 18.0 inserts cohesive zone elements on each and every element interface and activates them as soon as critical stress is reached. More information about the model can be found elsewhere [42].

2.3 Experimental Analysis

Certain measurements were required to get some material parameters for the resin material. Apart from that, microscopic analysis was required to get insight into the microstructure of the material and compare with the simulation results. These test methods are described briefly in this section.

Nano Indenter:

This indentation method was used to obtain the Young’s modulus of the resin sample. Indentation with a tip range of a few micrometres allows to measure material properties in a localised area and can be assumed to represent a homogeneous material without local defects like pores. The measurements were done with an "UNAT" by Advanced Surface Mechanics (ASMEC). A Berkovich indenter with a trigonometrically pyramid-shaped tip was used. The tip is indented into the material until a predefined force is reached before the specimen is unloaded. The indent to obtain the Young’s modulus was repeated five times at different positions and was done with a maximum force of 0.1 N [44].

Dilatometry:

Dilatometry measurements were made to quantify the volume change of the sample under a given temperature range. The equipment used for these measurements was 'DIL 402E' by Netzsch with temperature varying from room temperature to 1300°C at 5° C/min. Measurements were done under Argon to prevent oxidation and contamination of the samples from other elements in the environment. Thermal expansion of coefficient can be evaluated from change in length of sample with the help of the following formula:

$$\alpha_{total} = \frac{\Delta l}{l} \tag{1}$$

$$\alpha_{total} = \alpha_{thermal} + \alpha_{chemical} \tag{2}$$

The measured coefficient of thermal expansion comprises of two parts: thermal and chemical. Since the evaluation of chemical part is out of scope of this work, α_{total} was taken as the value for further calculations to model the shrinkage behaviour with consideration of the volume change due to chemical reactions.

Scanning Electron Microscope (SEM):

Scanning electron microscope is a kind of electron microscope that generates images by scanning the surface of a sample with a focussed beam of electrons. Based on the interaction of the electron beam with the surface topography, different signals with varying intensities are generated and detected to produce an image. The device used is a Gemini Ultra Plus from Carl Zeiss NTS GmbH, Germany. The resolution of a SEM is very high compared to a light microscope and is used to compare the microstructures of CMCs where all the constituents namely fibre, matrix, pores, and fibre coating (when present) can be visualised. The images are then to be processed further to quantify the information such as area fraction of constituents, fibre diameter distribution, pore or crack size, etc. In this chapter, the cracks are segmented out from the images and their size distribution is compared for different variants of C/C-SiC.

Image Processing

Image processing was used in the current work to extract information from the SEM images of the material under investigation. This was required to be able to validate the results obtained from the finite element simulations. Such techniques are also reported in literature for other fibre-reinforced composite. Gelb from Zeiss X-Ray Microscopy investigated structure-property relationship in a carbon-fibre composite [45]. Fibre shape and size distribution were extracted from microscopic images to generate realistic virtual microstructures for multiscale simulation. In a similar way, tools were developed by Bricker et.al [46] to automate the characterisation and quantification of the microstructure of SiC/SiNC. Microstructural models were then generated based on this information to perform finite element

analysis. In extension to this work, an anomaly detection method was developed by Bricker et.al [47] to describe the relative orientation of the fibres. With the help of a probability density function (PDF), the anomalies were classified by their likelihood of belonging to the statistical normal behaviour of a particular feature. In the work of Xu et.al, [48] a 4-step machine learning method was used to determine the most important descriptors or features required to define microstructure of polymer nanocomposites and thus eliminating redundant microstructural descriptors via image analysis. Supervised learning techniques were then used to establish a relationship between the microstructural features and the material properties.

In the current work, Python library Scikit-Image was used to extract and quantify microstructural features obtained from SEM images. Though, only crack density in a SEM image was quantified in this chapter, image segmentation can be extended to extract other features as well based on the information available in the SEM image. For example, the quantification of the distance between the centre of the fibres was performed for a SEM image obtained for a carbon fibre-reinforced ZrB_2-SiC matrix, as shown in Figure 2.5. As a first step, the fibres were detected based on the contrast between the fibres and the matrix. After that, circles were fitted to detect the fibres and the average of the distance to all the nearest fibres was evaluated for each fibre. Based on the distribution of the data, the distribution parameters can be used to generate a virtual microstructure to perform further numerical analysis.

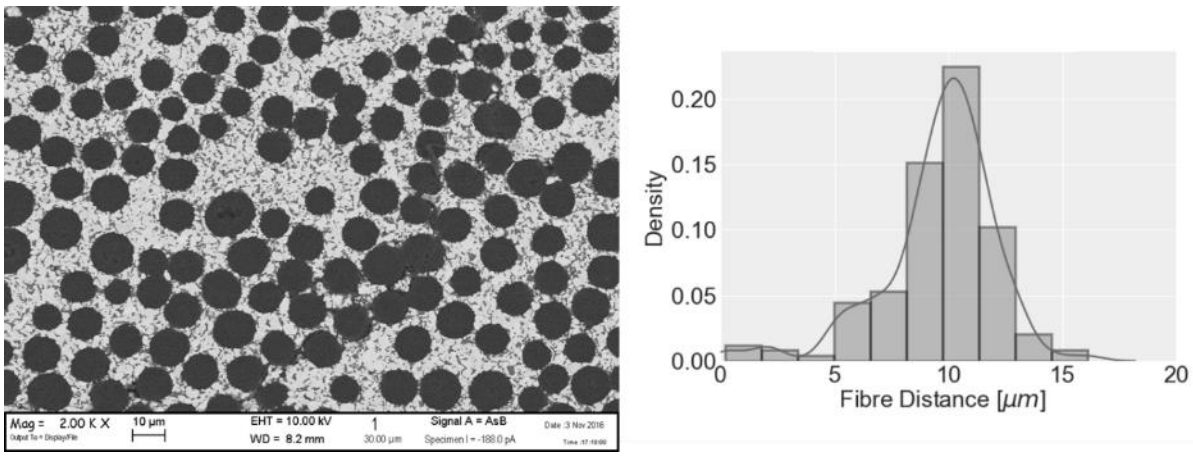

Figure 2.5: Evaluation of probability density function (PDF) of the distance between the centres of the fibres present in the SEM image.

2.4 Results and Discussion

As aforementioned, the characterisation of the resin material was done to gain input parameters for the FEM models. A mesh convergence study was carried out to investigate the effect of mesh size on the FEM solution and to find optimum mesh size without compromising with the accuracy of simulation results. The microstructure of manufactured material was studied with the help of scanning electron microscope (SEM). Image segmentation method has been employed to differentiate and quantify the

two common microstructures observed in C/C-SiC material: 1) presence of carbon fibres in carbon matrix blocks without any debonding as a result of strong fibre/matrix interface and 2) presence of micro-cracks with fibre-matrix debonding as a result of weak fibre/matrix interface. The results from SEM images are then compared with the results obtained from FEM model with random fibre distribution.

2.4.1 Matrix Properties

Dilatometry and thermogravimetric analysis:

Coefficient of thermal expansion as a function of temperature was determined through dilatometry. Due to massive shrinkage of the resin sample of about 10%, the change in length of the sample could only be measured in the range 150°C to 600°C. The sample shrank outside the range of measuring area. This phenomenon is not observed in the fibre-reinforced resin since the shrinkage is blocked by the embedded fibres in the matrix.

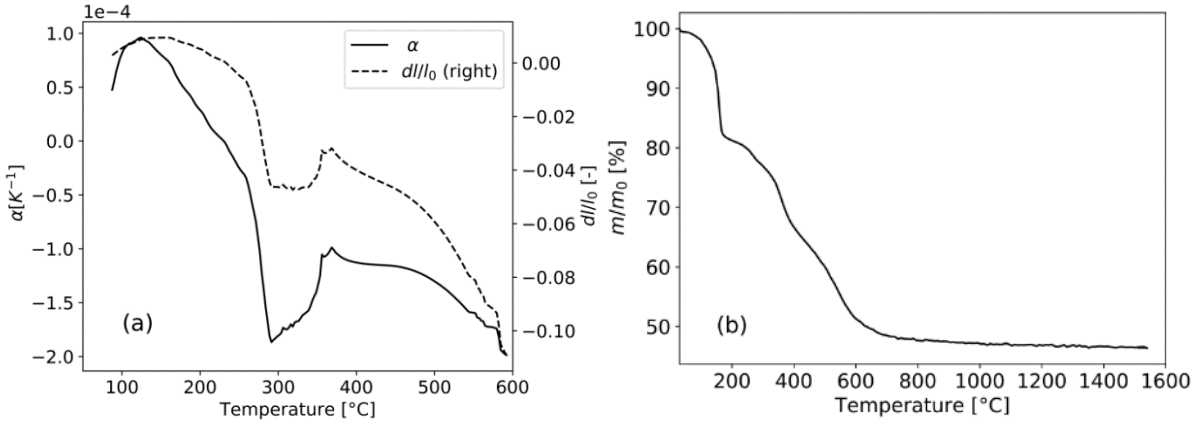

Figure 2.6: a) Thermal expansion coefficient (α, left y axis) and ratio of change in length to original length (right y axis) as a function of temperature; b) mass yield as function of temperature.

It must be kept in mind that the resin sample was cured at 150°C under pressure of 20 bars and might still contain condensed products trapped within it. The sample, after shrinking from 150°C, starts to expand again at around 300°C. A plausible explanation might be shrinkage due to vaporisation of monomers and steam till 300°C, since it is a water-based resin [38]. After this initial shrinkage and cross-linking of molecules, the resin sample starts expanding till 350°C after reaching its glass transition temperature at around 300°C. The sample starts shrinking again till 600°C, which marks the range of major pyrolysis (as shown in Figure 2.6 (a)). Complimentary to dilatometric measurements, mass loss of the matrix sample under high temperature was also studied with the help of thermogravimetric analysis. The results are shown in Figure 2.6 (b), where m is the mass at a given temperature and m_0 is the initial mass of the sample. The mass yield is around 51% at 600°C, which decreases to 46% at 1500°C. Since the major mass loss takes place till 600°C, the assumption during the modelling that the

major pyrolysis takes place below 600°C, is fairly reasonable. The average coefficient of thermal expansion was calculated to be -0.7e-4 K^{-1} over the range between 150°C and 600°C. The negative sign indicates that the material shrunk during the pyrolysis process. The temperatures can go as high as 900°C during pyrolysis but as explained above, the range of 150°C to 600°C has been considered for modelling purposes.

Nano-Indentation:

Nano-indentation measurements were performed in order to obtain the Young's modulus of cured resin material. Term $\frac{\partial P}{\partial h}$ is obtained from the load-unload curves after applying a force (P) to obtain indentation depth (h). The Young's modulus can then be calculated, according to Oliver and Pharr, as follows.[49]

$$E_r = \frac{1}{2}\frac{\partial P}{\partial h}\sqrt{\frac{\pi}{24.5\, h_{max}^2}} \tag{3}$$

The obtained modulus includes the stiffness of both the sample and the diamond indenter which has been used in this test set-up. To evaluate the Young's modulus of the matrix material, a correction of the value is required and is proposed by Oliver and Pharr[49] as:

$$\frac{1}{E_r} = \frac{1-\upsilon^2}{E} + \frac{1-\upsilon_i^2}{E_i} \tag{4}$$

where υ denotes the Poisson's ratio and the index i denotes the indenter properties.

Young's Modulus of matrix at room temperature was measured to be 3.7 GPa. Young's Modulus of amorphous carbon (after pyrolysis) measured by Jenkins and Kawamura [50] turned out to be 40 GPa. Since the temperature dependence of the Young's Modulus of the matrix was not measured, an average value of 3.7 GPa at room temperature and 40 GPa at 600°C was taken and a resulting value of 21.9 GPa was used for the calculations.

Other elastic properties, such as strength and Poisson's ratio are taken from literature and are mentioned in

Table 2.1.

2.4.2 Constituent Properties

The elastic and physical properties of fibre are taken from literature and are listed together with the matrix properties in

Table 2.1.

Table 2.1: Thermo-elastic and physical properties of fibre and matrix used in FE-Modelling.

Properties	**Unit**	**Value**
Fibre		
Fibre Diameter [51]	μm	5
Young's Modulus (transverse direction)[52]	GPa	14.1
Poisson's Ratio[52]	-	0.24
Coefficient of thermal expansion (transverse direction)[51]	K^{-1}	3.8e-6
Matrix		
Young's Modulus (measured)	GPa	21.9
Poisson's Ratio [53]	-	0.35
Coefficient of thermal expansion (measured)	K^{-1}	-0.71e-4
Strength (post-curing) [54]	MPa	200

2.4.3 Effect of weak and strong interface

The model with effectively one fibre embedded in the matrix was used to perform mesh convergence study and fit the parameters to model crack growth with varying fibre-matrix interface properties. The critical crack opening displacement at both matrix-matrix and fibre-matrix interface was a crucial factor in deciding the convergence of the model. The mathematical relation between the nodes provided by Hooke's Law gets destabilized after activation of cohesive zone elements and the number of equations to be solved increases and results in loss of convergence. The value of critical opening displacement was varied between 10 nm and 1 μm. The strength at fibre/matrix interface is a difficult value to evaluate and for study purposes a value 5 times higher than the matrix strength was taken as strength of strong interface (1 GPa) and a value 5 times lower than the matrix strength (200 MPa) was taken as strength of weak interface (40 MPa). Although, the focus of the current work is on the modelling of major crack patterns discussed in the introduction, there might be material variants with interface strengths between the extreme values used in the current work and exhibit a microstructure with presence of both the major crack patterns observed in SEM images.

RVE with symmetrical packing of fibres:

Firstly, a RVE with symmetrical packing of fibres was investigated to fit the parameters which can model the crack development behaviour of the material, as shown in Figure 2.2. Since the number of elements is considerably small, higher number of variations can be tried out to define the final parameters which are then implemented in the realistic model with random packaging of the fibres.

Prior to introduction of cracks into the model, stress distribution within the microstructure was examined in order to detect the critical stresses in the microstructure. It also serves the purpose of validation of the crack growth model in terms of crack initiation sections. One of the basic assumptions in Griffith's theory of brittle fracture is that a material always contains randomly distributed initial flaws within a material. These flaws are the origin for further crack propagation. Flaws in the material are mainly stress-induced cracks and pores due to vaporisation of volatile products and consequent shrinkage of matrix during pyrolysis. With no pre-existing cracks, the elastic energy which is required to initiate a crack in the material becomes equal to cleavage energy of the material [55]. This can be regarded as a constant material property which depends on the material's atomic constituents and their interaction with each other. Thus, the condition to initiate a new crack is reduced to the stress state in the material. The stress which exceeds the material strength in this model leads to the initiation of a microcrack and is referred to as critical stress. In this work, microcracks are defined as cracks which are caused by high stresses and experience no or very little growth. These microcracks are the first step of damage and origin for the formation of larger cracks and the final crack pattern.

The influence of strong and weak fibre/matrix interface strength is shown in Figure 2.7. In Figure 2.7 a), a microstructure with strong fibre/matrix interface strength is illustrated and there is no fibre/matrix debonding at their interface and all the cracks are present within the matrix. The symmetric nature of cracks is due to boundary conditions where displacement is fixed on all the four edges. On the other hand, fibre/matrix debonding takes place in the microstructure with weak fibre/matrix strength. Some cracks are also visible in the matrix with weak fibre/matrix interface which evolve because of stresses within the matrix during fibre matrix debonding and the fixed nodes on the edges of the RVE. The lack of symmetry in the crack pattern despite symmetric mesh is attributed to numerical errors in the solution of finite element problem. The aim of this ideal microstructure is to find the parameters like convergence tolerance, optimum no. of iteration and solver type to achieve convergence within reasonable amount of computation time.

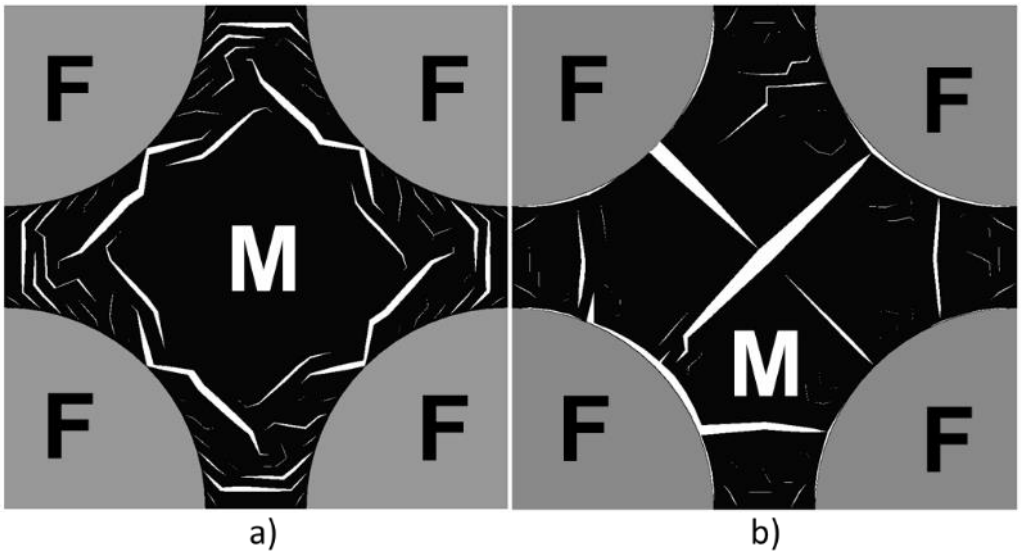

Figure 2.7: Crack formation in an ideal RVE with a) strong fibre/matrix interface and b) weak fibre/matrix interface, where 'F' denotes fibre and 'M' denotes matrix.

RVE with asymmetrical packing of fibres - I

The parameter fitting performed with the help of model discussed in previous section are then implemented in a microstructure with random distribution of fibres and the resulting crack pattern has been compared with SEM images of the C/C sample after pyrolysis.

As aforementioned, crack patterns observed in microstructure of C/C material are crucial for the final microstructure and consequently the damage tolerant behaviour of C/C-SiC. Until now, it has only been optically inspected if a combination of fibre, matrix and manufacturing parameters results in a block structure or micro cracks within the matrix. An attempt has been made in current work to analyse the SEM images with the help of image segmentation technique so that crack patterns can be classified based on the values obtained from image segmentation algorithms. These algorithms help in comparing different SEM images and grade them based on a quantifiable criterion.

The image segmentation script has been written using Python 3.7 with the help of image processing libraries 'OpenCV' and 'Scikit-Image'. In the first step, the image is converted into black and white from grey scale where cracks are marked white, and the rest of the area is coloured black in order to get proper contrast to evaluate the pixel values. Each conglomerate of white pixels is then detected and assigned as one crack. Cracks, which are assigned in the previous step, are now single entities and their properties such as area, perimeter, etc. can be obtained from the script. For the current investigation, the number of pixels in a crack was evaluated for each crack and was converted into crack area.

In Figure 2.8, a comparison between SEM image and simulation results of C/C sample with weak fibre-matrix interface has been shown. Resin material used in this C/C sample was JK60. Fibre-matrix debonding due to weak interface is evident in both the images. The size of the microstructure under

consideration is 33 x 44 μm^2 in the case of SEM image and 50 x 50 μm^2 in the model. Figure 2.9 shows the distribution of cracks in the range of 0.5 to 4 μm^2. The total number of detected cracks, as shown in Figure 2.9, in the case of SEM image is 57 and in simulation 55. The blue digits below the 'x-axes denote the number of cracks present in that particular range. It can be concluded from the plots that most of the cracks are microcracks which form because of dissipation of thermal stresses during pyrolysis.

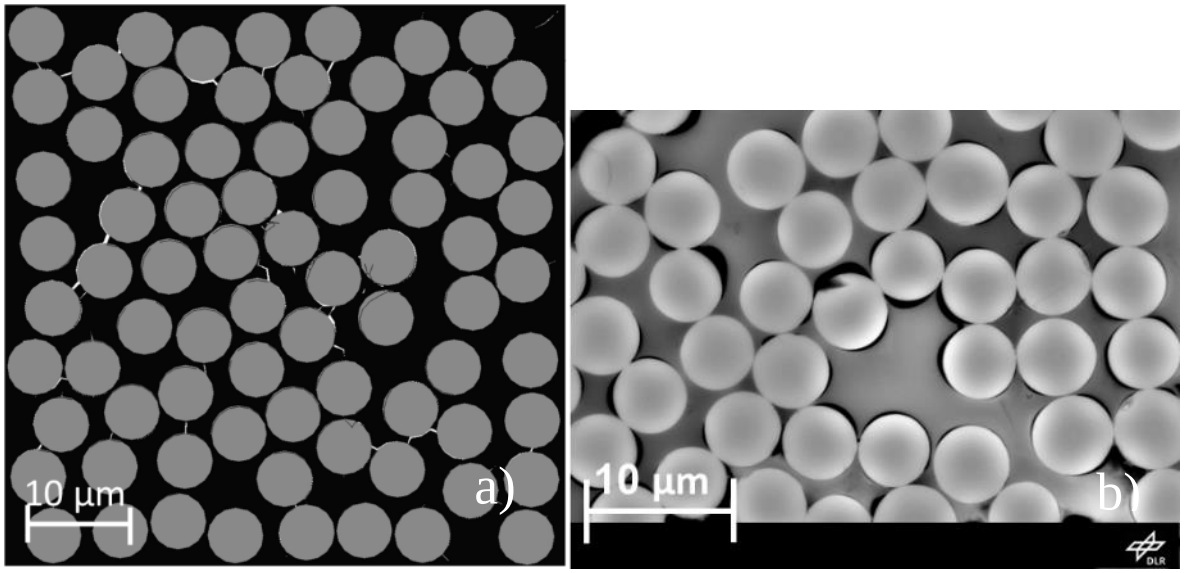

Figure 2.8: Comparison of a) simulation results of C/C material with weak fibre/matrix interface with a b) SEM image.

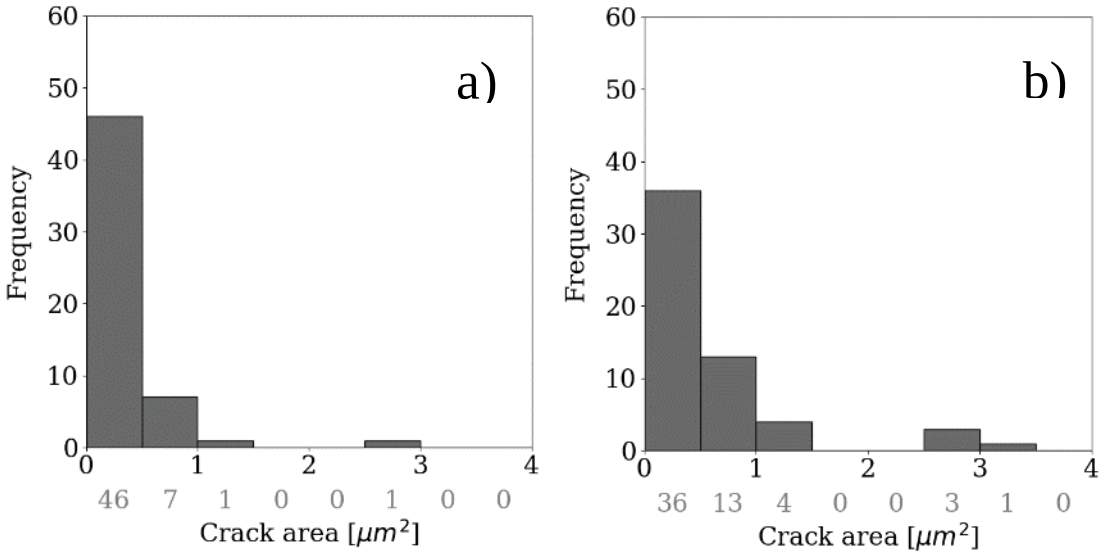

Figure 2.9: Comparison of the crack area distribution between a) simulation results and b) SEM image obtained for material with weak fibre/matrix interface (JK60 resin).

On the other hand, in Figure 2.10, there are very few cracks observed in the SEM image of a material with strong interface where MF43 was used as resin material. Contrary to SEM image with 3 cracks,

there is large number of cracks in the simulation image (177 cracks), as shown in Figure 2.11. The reason is that the SEM image is captured at a magnification of 5000 times (resolution: 3072 x 2304 pixels) and cracks present in the matrix are segmentation cracks which are in the range of hundreds of μm^2, as shown in Figure 2.1. In the case of simulation, only a small microstructure (50 x 50 μm^2) is taken into consideration, which results in large number of small cracks which did not merge to form a segmentation crack. It shows us that because of the strong fibre/matrix interface strength, there is no fibre debonding. Other factors which have been identified to have influence over generation of segmentation cracks are fibre volume content, fibre diameter and presence of defects, like pores within the matrix, before tempering. These factors are already taken into consideration and the results are promising, especially after inclusion of Weibull distribution of matrix strength to represent material inhomogeneity. Nonetheless, the current model can simulate the influence of varying fibre/matrix interface strength over the development of cracks in the composite.

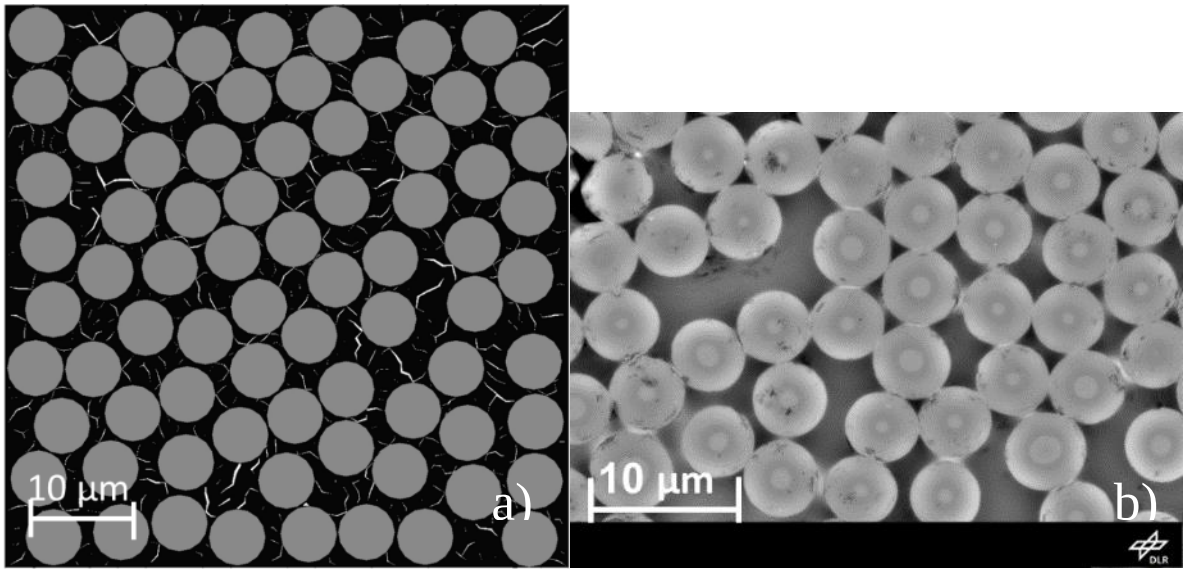

Figure 2.10: Comparison of a) simulation results of C/C material with strong fibre/matrix interface with a b) SEM image (MF43 resin).

It must be mentioned that certain assumptions were made during this study of effect of fibre/matrix strength such as homogeneous matrix, linear elastic behaviour of the constituents and constant material properties at all temperatures. Moreover, the boundary conditions, used in the finite element model, were defined to produce stresses within the matrix which ultimately are released leading to development of cracks. Multiscale approach can be employed to study the influence of fibre architecture of composite over crack pattern where the boundary conditions applied on macro scale and the displacement distribution is then transferred to micro scale. Temperature dependency of material properties, not considered in the current work, also plays a major role in deciding crack pattern in the microstructure. For example, the strength of the matrix should reduce at higher temperature which should lead to a greater number of larger cracks. This effect might be normalized by the decreasing Young's Modulus

of the matrix at high temperatures where thermal expansion will result in relatively lower stresses due to low stiffness.

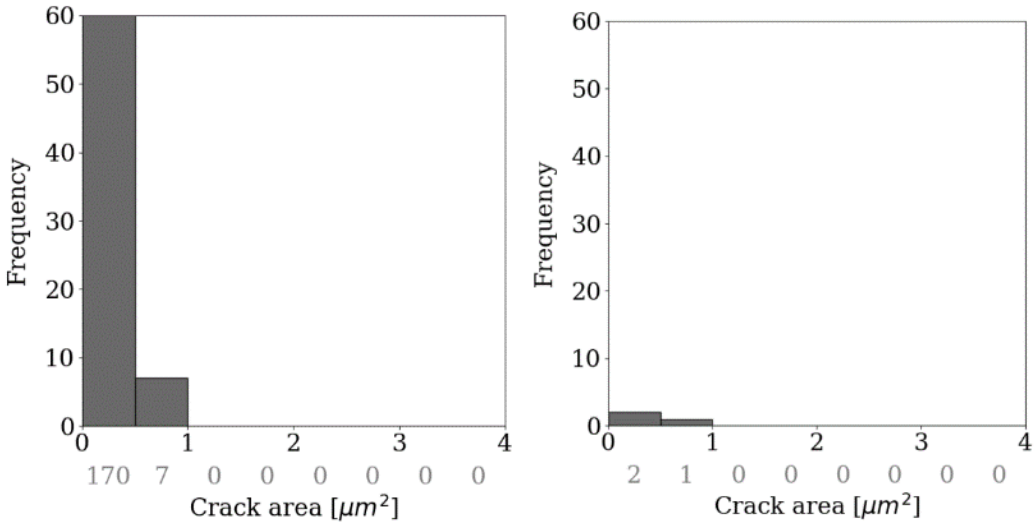

Figure 2.11: Comparison of the crack area distribution between a) simulation results and b) SEM image obtained for material with strong fibre/matrix interface.

RVE with asymmetrical packing of fibres – II:

In order to simulate the material behaviour during pyrolysis and demonstrate the building of block like structures, an RVE with more number of fibres was modelled, as shown in Figure 2.12 [56]. All the edges are fixed in x and y directions and the strains in z-direction are assumed to be zero, which implies that this is a plane strain analysis. In order to capture the cooling-down effect, a temperature gradient of 450°C is applied on the virtual microstructure, just like the smaller RVE.

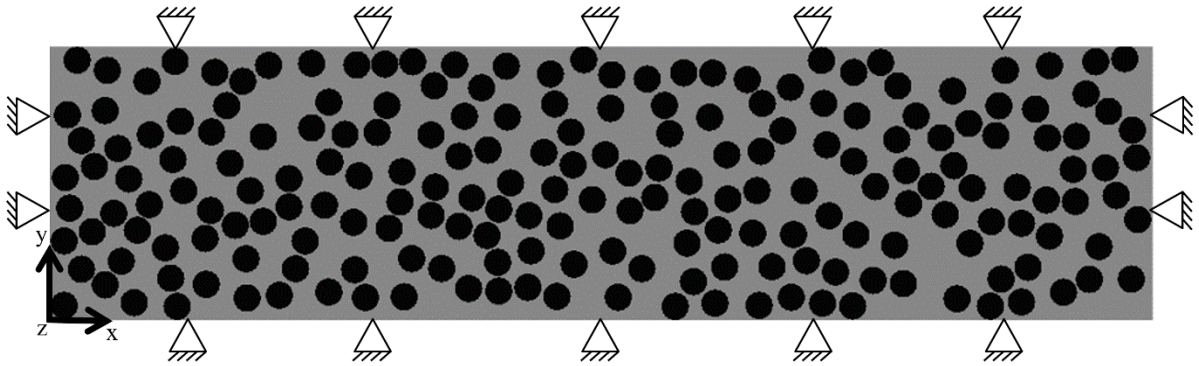

Figure 2.12: The boundary conditions applied on a 2-D representative volume element to model the shrinkage of the microstructure during the cooling down of a sample after pyrolysis.

As expected, the cracks are only within the matrix as the interface strength is very high compared to the matrix strength of the composite. The cracks are present all over the matrix (Figure 2.13) but do not show the formation of the block structure, as shown in the SEM image in Figure 2.1. A plausible explanation is that the strength of the matrix material is same for all the cohesive zone elements which results in formation of cracks in the entire volume of the matrix. In the reality, material is

inhomogeneous and possess different values of strength on different locations because of the defects present in the resin system.

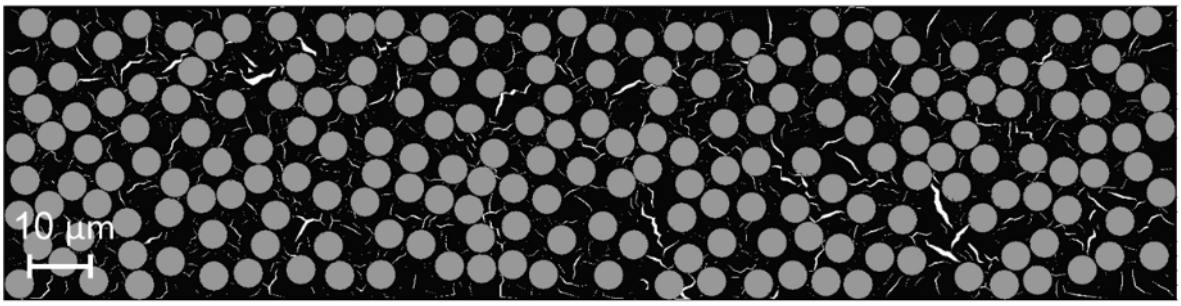

Figure 2.13: Crack formation in the RVE after cooling down from 600°C to 150°C.

In order to capture the inhomogeneity of the material, Weibull distribution [57] of the strength values was used to assign strength to the cohesive zone elements of the matrix material. This statistical distribution is usually used to include the effect of defects in ceramic materials. A shape parameter value of 11 was taken for the Weibull distribution based on the experiments performed on the investigated material and reported by Yuan Shi et.al [58]. After consideration of Weibull distribution of strength values for the matrix material, a tendency towards the formation of segmentation cracks or block structures is observed in the microstructure, as shown in Figure 2.14. These results can be compared with the block structures in the SEM image of the microstructure shown in Figure 2.1.

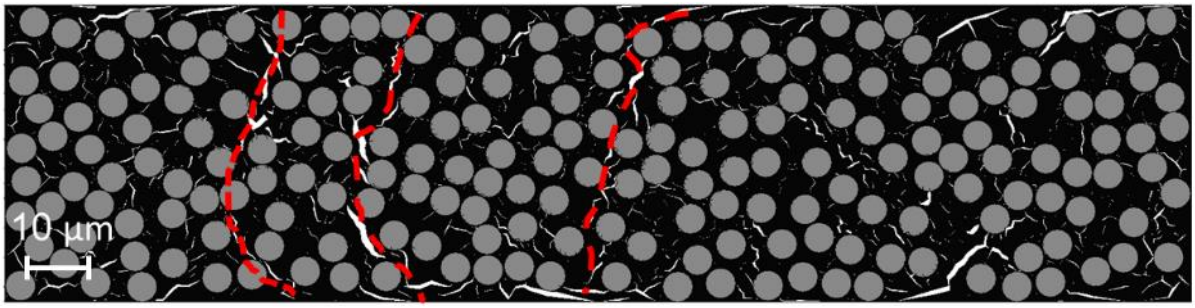

Figure 2.14: Formation of segmentation cracks (red lines) after consideration of Weibull distribution of matrix strength.

After a comparison with the results obtained from the SEM images, the manufacturing parameters such as FVC can be varied and their effect over the crack formation after pyrolysis can be predicted. For example, when the FVC is increased from 40% to 60%, the increased fibres in the sample hinders the merging of cracks to form segmentation cracks and will not result in the desired microstructure for siliconisation in the next step. On the other hand, high FVC is desired for most applications because fibres provide strength and damage tolerance to the material. This implies that an optimum value of FVC needs to be evaluated to meet the requirements of the application.

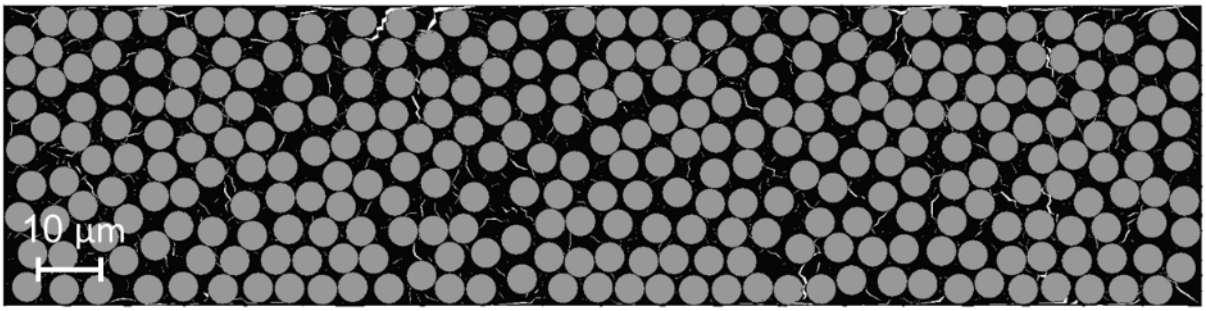

Figure 2.15: Absence of segmentation cracks in the matrix in an RVE with fibre volume content of 60%.

In the study, only one parameter was varied and its impact on the microstructure was shown. However, there are many parameters which can be tuned to tailor the material based on certain application, such as fibre and matrix type, pyrolysis temperature, heating rate, etc. After successful validation of the effect of other manufacturing parameters, the material and parameter selection can be performed virtually which will accelerate the 'lab-to market' time of this novel material class of CMCs.

2.5 Conclusion

In this chapter, an example of the relationship between the manufacturing process parameters and the microstructure of the material is demonstrated. The microstructure development during pyrolysis, which is an intermediate step in the manufacturing process of C/C-SiC, was modelled with the help of finite elements. Fibre/matrix interface strength in the polymeric state plays a major role in deciding the microstructure of material in C/C form after pyrolysis and ultimately the microstructure of final product. This interface strength was taken as a varying parameter and the crack generation due to change in temperature during pyrolysis was modelled with the help of cohesive zone elements. Resulting microstructures are then compared with SEM images to verify the crack pattern generated in the model.

The model was able to reproduce the behaviour accurately in the case of weak fibre/matrix strength but in the case of strong fibre/matrix strength, it showed microcracks in the matrix whereas there were no microcracks observed in the corresponding SEM image. It was found that there are other factors in microstructure which contribute to generation of segmentation crack from microcracks. For example, fibre volume content, and material inhomogeneity were identified to be some of those factors and were included in the model. The initial results are promising and should be investigated in a future work. Temperature dependency of elastic and thermal properties of matrix material will also be taken into consideration in simulation models for pyrolysis. Nonetheless, current work is a first attempt in finite element modelling of pyrolysis and has demonstrated great potential in modelling of crack pattern as observed in real microstructure.

Image segmentation techniques have been employed to measure the size of cracks and compare the crack size distribution of different microstructure. This technique not only helps in comparing the

modelling results with SEM images, but also allows quantification and differentiation between two major microstructures observed in C/C-SiC material. The results shown here are the foundation of an approach where image segmentation techniques are combined with finite element modelling to model transverse cracking during pyrolysis. This helps in quantification of the microstructure of a composite, which in turn, can be used as a target value to optimize the input properties of constituents for simulation such as interface strength.

Apart from the pyrolysis process, other processes which can be modelled are summarized in Section 5.2. The data obtained from the other process models then need to be combined to draw a correlation between the process parameters and the quantified microstructural features evaluated from the 2D SEM images or 3D CT-scans.

3 Structure-Property Relationship

3.1 Introduction

The microstructure of a fibre reinforced composite, like any other material, is responsible for the final properties of the material. As shown in the earlier chapter, the different positions of the cracks present in the microstructure decide the performance of the material. Other features such as the type of fibre, matrix, fibre volume content, fibre diameter, etc. not just influence the formation of matrix cracks, but also the properties of the composite directly. For example, stiffer fibre or higher fibre volume content will lead to a composite with a higher stiffness in the fibre direction. Such predictions can be made with the help of analytical models like 'Rule of Mixtures', which takes the stiffness of the constituents and their volume fraction into account. However, in order to determine properties like strength and failure strain, more advanced numerical methods like finite element analysis have to be employed. With the help of such models, virtual microstructure with different constituent combinations can be generated and the properties of the resulting composite can be predicted.

The physics-based modelling with the help of virtual microstructures is accurate but it can become computationally expensive. There are many parameters at the microstructural level which can be varied to study their effects over the property of the material. Furthermore, the inclusion of multiscale modelling approaches like FE^2 increase the computation time and are not suitable for optimisation purposes where such a study can take days or months based on the number of finite elements. A possible solution to this challenge is the development of data-based models from the physics-based models, so called the surrogate models. With the help of advanced machine learning algorithms, the relationship between the input and output parameters can be established and these relationships can then be used to predict the behaviour of the material. It has to be mentioned at this point that the surrogate models are not supposed to replace the physics-based models but support them in the material designing phase. The initial selection of the constituents and the manufacturing parameters can be done with the help of surrogate models and a more accurate analysis can be performed after this preliminary selection. In this way, the surrogate models will facilitate the material design process and can be used in the initial phases by a material scientist without having profound knowledge of physics-based models. This approach is going to replace the 'trial-and error' approach, which has been the traditional approach in material science. The use of machine learning algorithms is used only for 'Structure-Property' relationship in the current work, but its use is not restricted to it. The aim of this work is to demonstrate its use on a particular problem, but it can be extended to other facets of the 'Process-Structure-Property-Performance' relationship.

The proposed approach of creating surrogate models from physics-based simulations is followed by other researchers as well, where the training data for the machine learning algorithms was obtained from simulations performed at micro-level and meso-level. A general introduction of the use of machine learning in materials science for different applications is given by Mueller et.al [59] and especially for composites by Chen and Gu [60]. Statistical feature extraction based on machine learning was performed by Dabetwar and Dias to evaluate piezoelectric signal and differentiate between the damage levels in a composite [61]. Supervised machine learning techniques like support vector regression and random forest regression were used by Reimann et.al to model crystal plasticity based on different microstructures [62]. Techniques like hyper-reduction of the variables and neural networks were used to model the plastic response of the composites under different stress states by Rocha et.al, where advantages and drawbacks of different algorithms were discussed [63]. Artificial neural networks were also used by Yan et.al in order to determine the progressive damage in fibre-reinforced composites [64]. Mechanical properties of composites with arbitrary shapes and distribution of inclusions were predicted using deep neural networks by Ye et.al [65] and Yang et.al [66]. The thermo-mechanical behaviour of 2D and 3D textile composites was predicted via feed-forward neural network model by Liu [67].

In the field of CMCs, Vinci et.al established the relationship between the process parameters such as the amount of SiC in the matrix and mechanical properties like strength and toughness of UHTCMCs with the help of random forest and regression tree analysis [68]. However, the dataset used for training the models was not large enough for an efficient use of machine learning algorithm. This is mostly the case with CMCs, as the number of samples manufactured is limited due to high-cost factor. Therefore, an attempt is made in the current chapter, where finite element analysis of virtual microstructures is performed and based on this data, machine learning algorithms are trained to understand the relationship between the microstructural parameters and the mechanical properties of CMCs. The material under consideration is SiC/SiCN developed at the Institute of Structures and Design, DLR in Stuttgart. The details about the manufacturing process and a thorough microstructural analysis of the material can be found elsewhere [69]. Keeping the matrix constant, the fibre type was varied and thus changing the mechanical properties of one of the constituents in the finite element simulations. Four fibre types were used in the manufacturing process and the details are given in Section 3.4.

3.2 Finite Element Model

The finite element models used to prepare the training data for machine learning algorithms were generated with the help of commercial software, Multimech 18.0. The models in this chapter are also based on the concept of representative volume element (RVE). The volume of the RVE is defined in such a way that the obtained properties considering the heterogeneities (pores or fibres) present in the material can be compared with the global properties of the material.

Three different finite element models were generated in this study:

- Pores in the matrix (2D): To study the effect of porosity over the matrix properties (Section 3.5.2)
- Fibre-reinforced composite (2D): To study the relationship between the microstructural features and transverse properties of the composite (Section 3.5.3)
- Fibre-reinforced composite (3D): To study the relationship between the microstructural features and in-plane properties of the composite (Section 3.5.4)

3.2.1 Boundary Conditions

Virtual tensile tests are performed in this study which require the definition of the local boundary conditions to be applied on the RVE. Four boundary conditions available in Multimech (Figure 3.1) can be used for virtual testing of the material based on the requirements of the user, as each boundary condition has its own advantages and drawbacks [70]. A brief overview is given in this section.

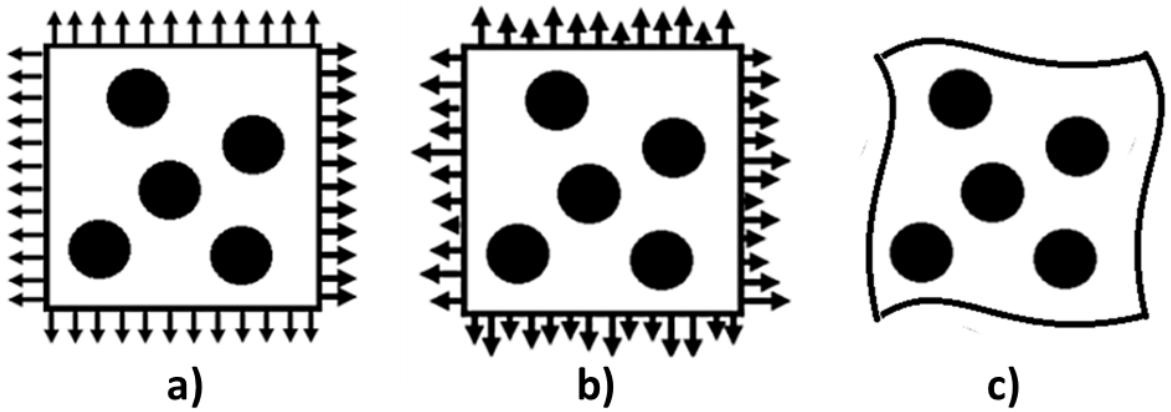

Figure 3.1 The boundary conditions available in Multimech a) linear displacements and planar displacement (no tangential constraints) b) uniform traction and c) periodic displacements.

Linear Displacements

The boundary faces of the RVE are forced to remain planar in the linear displacement boundary condition. There are no restrictions on the nodal loads and their distribution might result in a non-uniform field over an edge or surface. The nodal displacements normal and tangent to the faces are constrained on the other hand. The RVE's under these conditions tend to show stiffer behaviour depending on the size and mesh of the microstructure, due to these constraints. For this reason, this boundary condition was not recommended by the software developers.

Uniform Tractions

There are no constraints applied on the nodal degrees of freedom in the case of uniform traction boundary condition. The nodal loads are assumed to be uniform throughout the RVE boundary which might result in a non-uniform displacement field as well. In this case, the nodes can move freely and

can take any shape during the simulation as the RVE is less stiff than the theoretical stiffness of the material. This behaviour might lead to poorer convergence because of the numerical instability and plausible rigid body movement of the microstructure. Since, the models involved non-linear behaviour of the material due to crack generation, this boundary condition was not used.

Periodic Displacements

The periodic displacement boundary condition is the most used condition for RVEs in the literature. The nodal displacements are enforced but freedom of shape is allowed on the boundary surfaces. There is reduced stiff behaviour due to constraints on the displacements and they are robust as far as convergence is concerned. One setback of this boundary condition is that the nodes on the boundaries must follow a periodic shape on the opposite faces. This makes the generation of microstructures with inclusions or pores computationally expensive as advanced algorithms are required to ensure the periodic shape of the RVE. In the current work, where parameter study with hundreds of microstructures was performed, it was impractical to use this boundary condition.

Planar Displacements

The planar displacement boundary condition, similar to the linear displacement boundary condition, also enforces the external faces to remain planar under load application. There are no further constraints on the loads. The difference in this case is that only normal displacements are enforced, and tangential displacements are unconstrained. In this way, the overly stiff behaviour of the linear boundary condition can be reduced to certain extent while remaining computationally inexpensive. Due to this reason, this boundary condition was chosen for all the RVEs in this study.

3.2.2 Cohesive Zone Elements

Cohesive zone elements are already explained in section 2.2.3, as they were used to model the pyrolysis cracks as well. In this chapter, they were used to model the cracks within the matrix, fibre and at the fibre/matrix interface. However, the material model used to define the behaviour of cohesive zone elements is different in this chapter. The linear decay law from chapter 2 requires the knowledge of critical stress and displacement for all the three interfaces in the microstructure: fibre-fibre, matrix-matrix and fibre-matrix. This would have increased the number of variables required for the parameter study by manifolds. Moreover, it is challenging to determine the critical displacement values for all the involved interfaces. Considering these issues, the ‘elastic contact’ material law was used to describe the behaviour of the cohesive zone elements. The tensile and shear strengths of the individual interfaces are the only values required for this material law. The compressive strength is not considered as the compressive load will not lead to detachment of elements but if the crack appears under compression, it would be due to sliding and shear interaction between the elements [70].

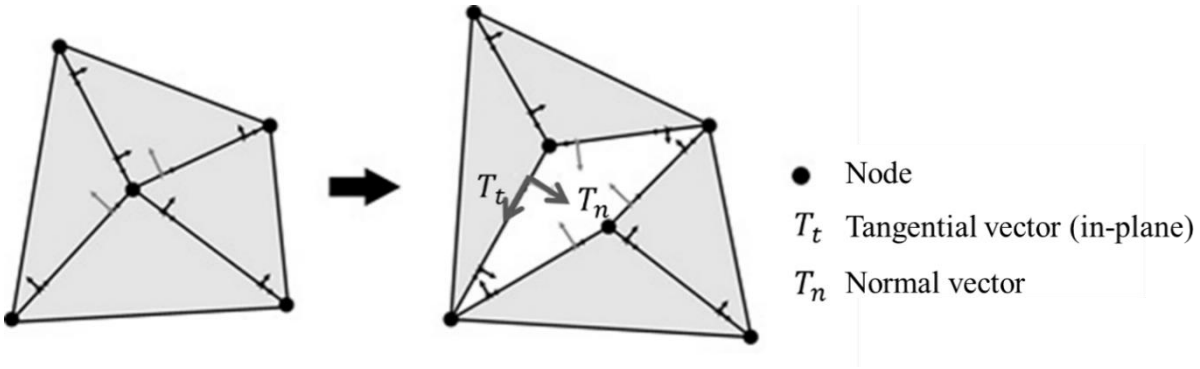

Figure 3.2: The tangential and normal component of traction vectors which need to be defined as material parameter to initiate crack opening at the nodes.

In Multimech, cohesive zone elements are automatically inserted into the finite element mesh as soon as the criterion for the cohesive zone initiation is satisfied. These limits are defined as material parameters for each interface where three components of the critical stress values in the local coordinate system are expected by the model:

σ_t^c: Tangential stress component in t-direction

σ_n^c: Normal stress component in n-direction

σ_s^c: Tangential stress component in s-direction (out of plane direction)

3.3 Machine Learning Algorithms

Machine learning (ML) algorithms have found their applications in all research domains in the last decade. With the rise of the research areas like material informatics, their use has increased manifolds in material science. Machine learning is a branch of artificial intelligence, which enables systems to learn and establish relationships based on existing data to predict the outcomes. The learning process involves no or minimal human intervention after the models are set up and the algorithms become efficient in their predictive abilities with the increasing amount of data. As data serves as the basis of the learning process, it is very important to provide clean and structured data in order to use these algorithms. Based on the problem at hand, the tasks can be broadly classified into two groups:

1. Classification: A classification problem is where the target variable is a class or a group. For example, detecting if an animal in a picture is a cat or a dog is a classification problem where the relationship between the characteristics of images is used to decide if it is a cat or a dog image.
2. Regression: A regression problem is where the target value is a continuous value. For example, in the current study, the microstructural features like fibre type, fibre volume content, etc. are used to predict the failure strength or strain of the CMCs.

The models which are used for prediction can also be classified into different groups based on the input data available for the learning process [71]:

1. Supervised learning: In supervised learning, relationships are established based on the known input variables and the target variable. An inferred function is obtained from these algorithms to evaluate the target variable for a new set of input parameters based on the knowledge gained after learning from existing input and target variables.
2. Unsupervised learning: In the case of unsupervised learning, the variables are not known, and the models need to detect the relevant variables or parameters first or in other words, they assign the definition of variables for unlabelled data. These algorithms are generally used for categorisation problems where the classes or group of variables need to be identified from a big pool of data.
3. Reinforcement learning: This technique is used for the problems where rather than the target variable, a strategy or a chain of decisions required to fulfil a given task is the outcome. The system learns from its experience and based on a reward criterion, decides the most optimum set of steps to achieve the assigned goal. The robots employed in industrial automation are one of the best examples to incorporate reinforcement learning techniques.

In the current study, supervised learning is employed as the input variables and the target variables are well defined. The main aim of the machine learning algorithms is to establish a function based on the training data set and evaluate the mechanical properties based on this function. As mentioned earlier, clean dataset is the key for the application of machine learning algorithms and is the first step in the process. Strategies are required to deal with the missing or unexpected data in the dataset. After cleaning the data, methods such as 'Pearson correlation coefficient' are employed as preliminary analysis of the dataset. This is required to understand if the application of machine learning algorithms is feasible or not.

Pearson Correlation Coefficient

Pearson correlation coefficient is a measure of linear correlation between two sets of data. It is a normalized measurement of the covariance of two variables and the result is always between -1 and 1 [72]. As seen in Figure 3.3, only linear correlation is detected between the variables, the coefficient is zero for the last row of the variables even if there is an evident relationship between them. The value of '1' denotes the perfect relationship and '-1' denotes the perfect inverse relationship between the variables. Even though, the non-linear relationships cannot be described by this coefficient, it is still useful as the first indicator of plausible interdependence among the variables.

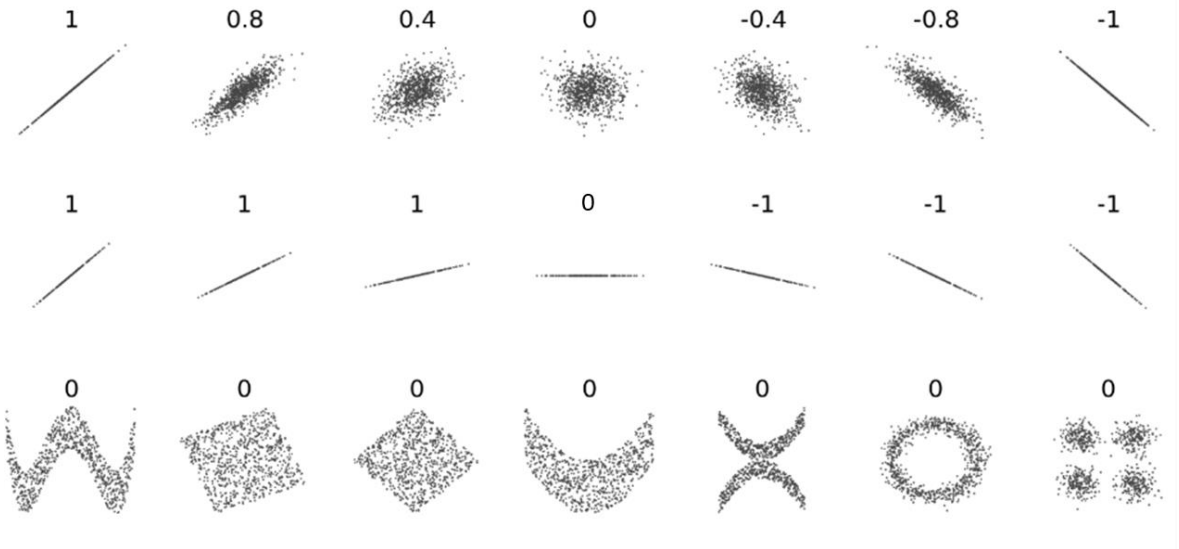

Figure 3.3: Pictorial representation of Pearson correlation coefficient values [72].

Machine Learning Algorithms

After performing a preliminary analysis, the dataset consisting of both the input and the target variables is usually divided in two groups: training data and test data. The percentage of the training and the testing data for this study is 80% and 20% respectively. This implies that 80% of the data is used to establish a relationship between input/output and generate a mathematical function based on it. The accuracy of the evaluated function is then verified with the help of the test data. A brief description of the algorithms employed in the current work is given below:

Linear Regression

It is a linear model that assumes a linear relationship between the input variables and a single target variable [73]. Depending on the number of input variables, the method used may be referred to as 'simple linear regression' or 'multivariate linear regression'. 'Ordinary least squares' method is used to estimate the values of the coefficients, where the algorithm seeks to minimize the sum of the squared residuals. Analogous to Pearson correlation, linear regression is not accurate in predicting non-linear relationships between the variables. Nonetheless, it is very efficient and easier to interpret, as the coefficients can be directly correlated to the weight of the corresponding variables in predicting the target variable.

k Nearest Neighbours

k Nearest Neighbours along with linear regression is one of the most used algorithms in data-driven prediction. As the name suggests, neighbouring points with the minimum distance (k) between the input data point and already trained data points are searched for [74]. Based on the type of problem (classification or regression), the class of most of the k nearest neighbours or the mean of the nearest k neighbours is assigned to the target variable to be predicted.

Lasso Regression

Lasso stands for 'Least Absolute Shrinkage and Selection Operator' [75]. It is a regularisation technique which is used to avoid overfitting of the data. The magnitude of the coefficients is kept in check with the help of penalty terms and the variables with larger penalties might eliminate variables with high bias resulting in a simpler linear regression model.

Support Vector Machines

The objective of the support vector machine algorithm is to find a hyperplane in a space of features dividing them into different classes [76]. The algorithm tries to find a plane that has the maximum distance between the data points of both classes and slices the data into different groups. Since, there are multiple planes based on the variables, non-linear relationships can be described by the support vector machine algorithm.

Decision Tree

A tree-like model with branches is used to make decisions and is commonly used for both classification and regression purposes. It is a collection of 'if' conditions which keeps on growing in depth based on the number of features or input variables involved in the dataset [77]. The end of any branch is the final decision where the target variable has gone through enough 'if' conditions for different features and a class or value is assigned to that leaf (decision). The results obtained from the decision trees can differ based on the 'if' conditions used which might produce different trees for the same training dataset. This can be avoided by decreasing the variance while generating trees by using methods like boosting. In the current work, gradient boosting is implemented to compare the results with and without use of boosting.

Random Forest

Random forest is an ensemble of individual decision trees where the results obtained from the decision trees is averaged [78]. The sensitivity of the decision trees to the dataset can be overcome by implementation of random forest, as different trees with different split conditions are taken into consideration. Not just the conditions differ from each other, but the features used to generate conditions differ as well. These effects are neutralized in the random forest regression or classification algorithm.

3.4 Investigated Composites

The experimental results used in this chapter were conducted in the framework of studies performed at Institute of Structures and Design, German Aerospace Centre (DLR), Stuttgart. The material under investigation was SiC/SiCN manufactured via Polymer Infiltration and Pyrolysis (PIP). Samples with two types of carbon (T800H and XN-90-60s, from now on mentioned as T800 and XN90 respectively) and silicon carbide fibres (Tyranno SA3 and Tyranno ZMI) were manufactured using a commercial polysilazane matrix precursor Ceraset™ PSZ10 (Clariant GmbH, Germany). The information of the

fibres provided by the manufacturer is summarized in Table 3.1. More details about the raw materials and the process parameters can be found in [69, 79].

Table 3.1 Technical data sheet of carbon and silicon carbide fibres as provided by the manufacturers.

Property	**Unit**	**T800 [80]**	**XN90 [81]**	**SA3 [82]**	**ZMI [82]**
Manufacturer	-	Toray	Nippon	Ube Industries	Ube Industries
Diameter	µm	5	10	7.5	11
Filaments	fil./yarn	6000	6000	1600	800
Young's Modulus	GPa	294	860	380	195
Tensile Strength	MPa	5490	3430	2400	3400
Elongation	%	1.9	0.4	0.7	1.7
Density	g/cm^3	1.8	2.2	3.1	2.5
Coefficient of thermal expansion	$10^{-6}\ K^{-1}$	-0.6	-1.5	4.5	4.0
Thermal Conductivity	W/mK	35	500	65	2.5

Unidirectional composites were manufactured for the above-mentioned fibres to obtain four variations of fibre-reinforced SiCN matrix. The measured porosity, density and fibre volume content of the composites is mentioned in Table 3.2.

Table 3.2 Measured porosity, density and fibre volume content of unidirectional-reinforced SiCN [69].

		C/SiCN	**SiC/SiCN**		
Property	**Unit**	**T800H**	**XN-90-60s**	**SA3**	**ZMI**
Porosity	vol %	6.1	8.1	6.0	5.6
Density	g/cm^3	1.9	2.1	2.5	2.3
Fibre Volume Content	%	46	42	45	48

Uni-axial tensile tests were performed at the DLR facilities by Mainzer [69] and Lin [79]. The stress-strain curves and the properties obtained from these tests were used to analyse the accuracy of the simulation results.

3.5 Results and Discussion

In this section, the results from the finite element models and machine learning algorithms are presented. The matrix properties with consideration of pores are discussed first, followed by the representation of pores through Weibull distribution. The homogenised properties of the matrix are then used for the evaluation of the mechanical properties of the transverse direction of the composite with the help of a

2D finite element model. Using the data from the simulations, a data-based model is generated, and the results are compared with each other. In order to evaluate the mechanical properties of the composite in the fibre direction, a 3D model is used, and the simulation results are compared with the experimental results. After this validation, data-based models are generated for the fibre direction of the composite as well using the parameter study based on finite element analysis.

3.5.1 Weibull Distribution

In the current study, it was not possible to physically model both the pores and the fibres simultaneously in the RVE because of the restrictions of the software (Multimech) used for the finite element analysis. Attempts were made to use other commercial microstructure generators like GeoDict from Math2Market GmbH, Germany and export the mesh for further computations in Multimech. However, to be able to perform a parameter study, an interface is required between the microstructure generator and Multimech, which would have required an unlikely collaboration between the two commercial software developers. Instead of this approach, it was decided to use a statistical distribution of strength to simulate the effect of pores/defects over the strength of the composites. Different distributions such as normal, log-normal, gamma and Weibull are reported in the literature to fit the test data considering the variation in the values due to the defects in the materials among pores [9]. Weibull distribution is the most widely used distribution function in the field of advanced ceramics and was found to deliver an optimum fit even for CMCs [58].

The two-parameter Weibull distribution is commonly adopted for the statistical analysis of the fracture data of ceramic materials. The cumulative distribution function can be given by [70, 83]:

$$P(\sigma_i) = 1 - exp\left[-V\left(\frac{\sigma_i}{\sigma_\theta}\right)^m\right] \text{ with } V = \frac{V_e}{V_s} \tag{5}$$

where P is the cumulative failure probability,

m is the Weibull modulus,

σ_i is strength of i^{th} sample

σ_θ is Weibull characteristic strength

V_s is volume of the sample under consideration and

V_e is reference volume of the sample corresponding to Weibull characteristic strength

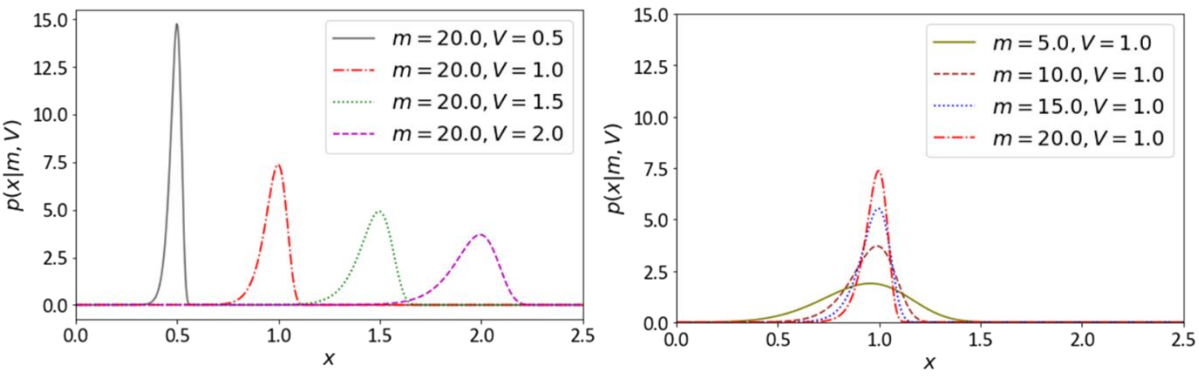

Figure 3.4. Variation of the Weibull parameters and their influence over the distribution of the values with characteristic value on the x axis and probability density function on the y axis.

As observed in Figure 3.4 a), the parameter '*V*' is responsible for the characteristic value of the distribution. This parameter is referred to as scale parameter and can be used to establish a relationship between the characteristic strength and the volume of the material. The size effects observed in CMCs, where the strength might vary with the volume of the material, can be described by this parameter. For example, the bending strength and the tensile strength of the material is usually different in the CMCs because of two reasons. Firstly, the behaviour under tension and compression is different and secondly, the volume under tension is lower in a bending sample than in a tensile sample. The higher volume increases the probability of the presence of a critical defect and thus affecting the strength of the material. Since only tensile samples are considered in the current work, this parameter was not evaluated for the matrix material.

The parameter '*m*', on the other hand, describes the scattering of the values in a sample data. In Figure 3.4 b), the values exhibit higher scattering in the case of *m*=5 and the scattering reduces with the increasing value of *m*. The effect of pore size and the pore volume fraction on this parameter for matrix is studied in this section. In Figure 3.5, the same relation is shown with the absolute probability of failure where the scattering of the values decreases with the increasing Weibull parameter.

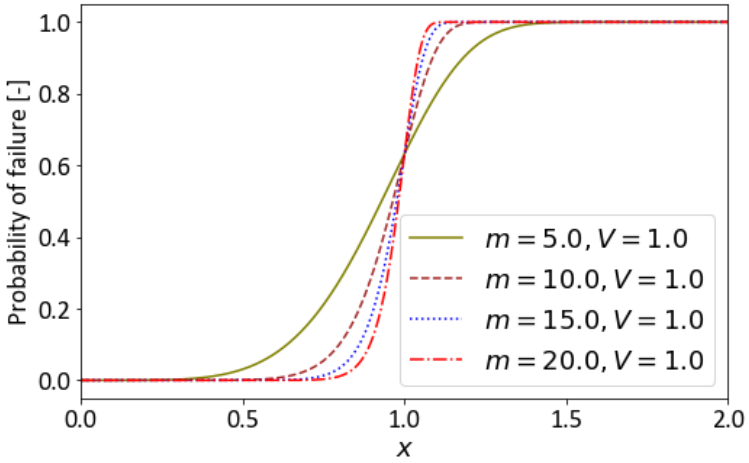

Figure 3.5: Probability of failure with varying value of Weibull parameter '*m*'.

As mentioned earlier that the Weibull distribution is used to represent the pores or defects in the matrix, a study was performed in order to evaluate the minimum number of samples required for employing Weibull distribution. With the help of Python library Scipy, random numbers were generated with a given Weibull modulus ranging from 5 to 50 and a characteristic value of 100. As shown in Figure 3.6, different sample sizes were generated, and the Weibull modulus is plotted against the standard deviation within the samples for each value of Weibull modulus. It can be observed that the standard deviation is higher for smaller values of Weibull modulus and decreases steadily with higher values of Weibull modulus. When the different sample sizes are considered, the variance in the standard deviation reduces till a sample size of 20 and remains unchanged for the larger sample sizes.

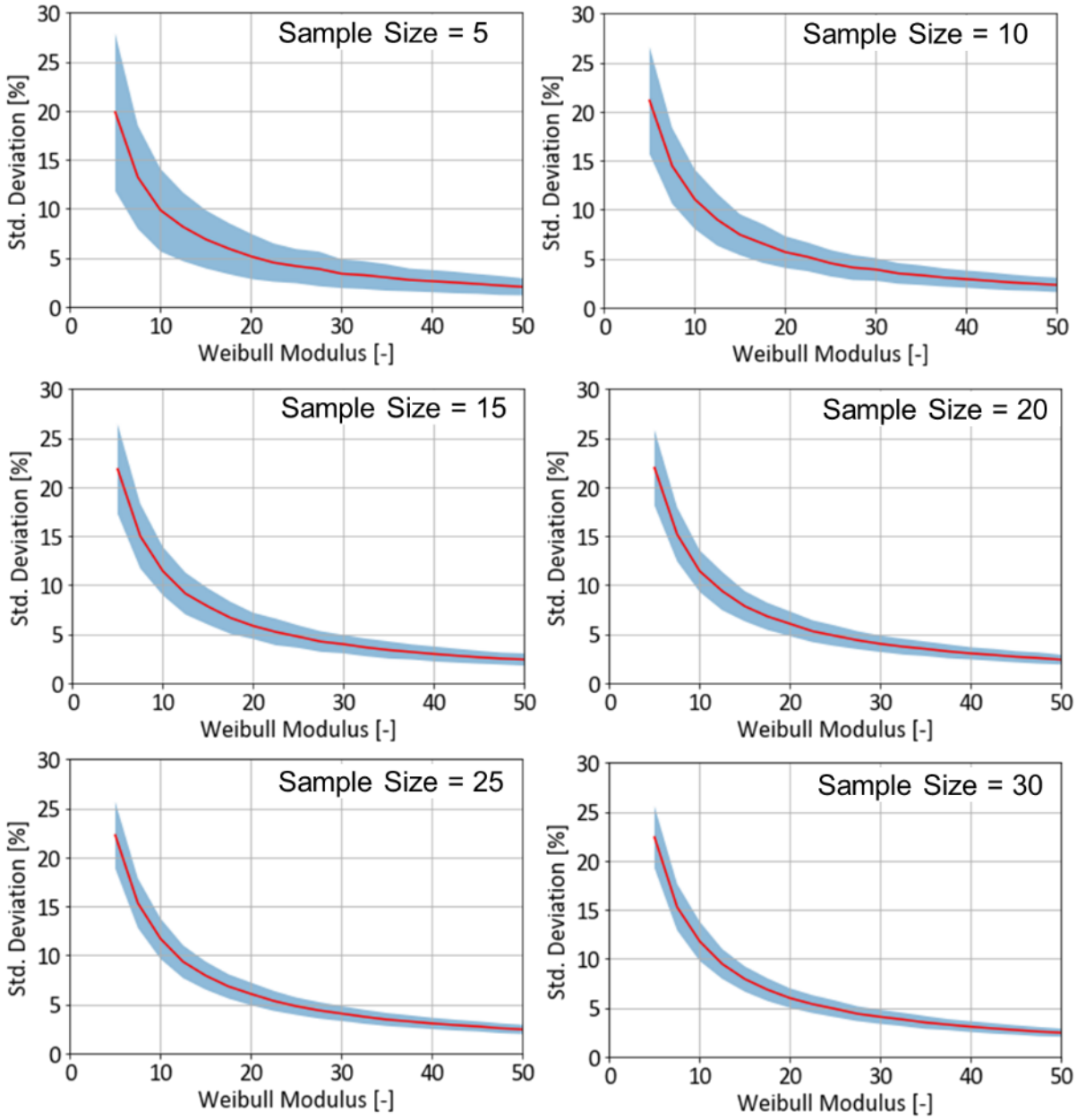

Figure 3.6: Relationship between the standard deviation of the strength of the matrix material with Weibull modulus for different samples sizes where the red line is the average and blue region denotes the standard deviation of the values (20 microstructures) for a particular value of Weibull modulus.

Based on this study, 20 virtual microstructures were generated in further investigations to understand the relationship between the distributions of strength of the matrix material and the resulting composite.

3.5.2 Porosity Analysis

Pores are one of the major defects that are present in CMCs and adversely affect the performance of the component. However, their presence is unavoidable, and their size, shape and volume depends heavily on the processing route employed for the manufacturing of the CMC. For the so-called ‘weak matrix composites’, they are rather desired for the damage tolerance of the material and the porosity in such materials ranges from 5% (SiC/SiCN) to 40% (Ox/Ox) of the volume. SiC/SiCN, the material under

consideration, exhibits a volumetric porosity of 5% to 8% and can be controlled by the number of infiltration and pyrolysis cycles performed during manufacturing. SiC/SiCN does not belong to the 'weak interphase composite' like SiC fibre reinforced composites produced via Liquid Silicon Infiltration [84] (LSI) as it does not have a fibre coating to provide the weak interphase between the fibre and the matrix.

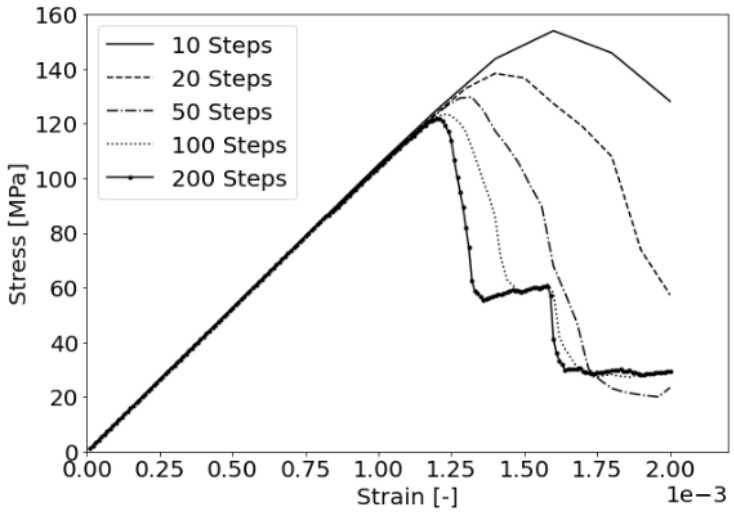

Figure 3.7: Stress-strain curves of UD-reinforced SiC/SiCN for different time steps for the parameter study of the matrix porosity.

A time-step study was performed to evaluate appropriate number of steps to be used for the parameter study of virtual microstructure with pores. Strain-driven simulation was performed where the microstructure was loaded by 0.02% strain and the number of time steps were varied. The stress-strain curves obtained from the virtual tensile tests are shown in Figure 3.7 and the time required by each simulation is summarized in Table 3.3. Since the difference between the strength values of 100 and 200 time-steps is negligible, it can be concluded that results are not going to converge anymore with increasing time-steps and 122 MPa can be considered as the strength of the matrix. If the time required by 20 steps and 200 steps is compared with each other, it can be noticed that for 10% deviation in the strength values, the time taken in the case of 200 steps is 12 times more than that by 20 steps. Even with 50 time-steps, time taken was 4 times more than that by 20 steps. Considering the number of simulations (900) to be run in the parameter study, a compromise was made, and 20 time-steps were used for the parameter study.

Table 3.3: Computational time required for different time steps for the parameter study of the matrix porosity.

Time-Steps	Time [s]	Strength [MPa]
10	13	154
20	33	138
50	120	130

100	207	123
200	397	122

The presence of the pores within the matrix directly affects the stiffness and the strength of the matrix. In order to obtain the effective properties of the matrix, the pores were physically modelled in the matrix and the effect of their size and volume was studied with the help of finite element models.

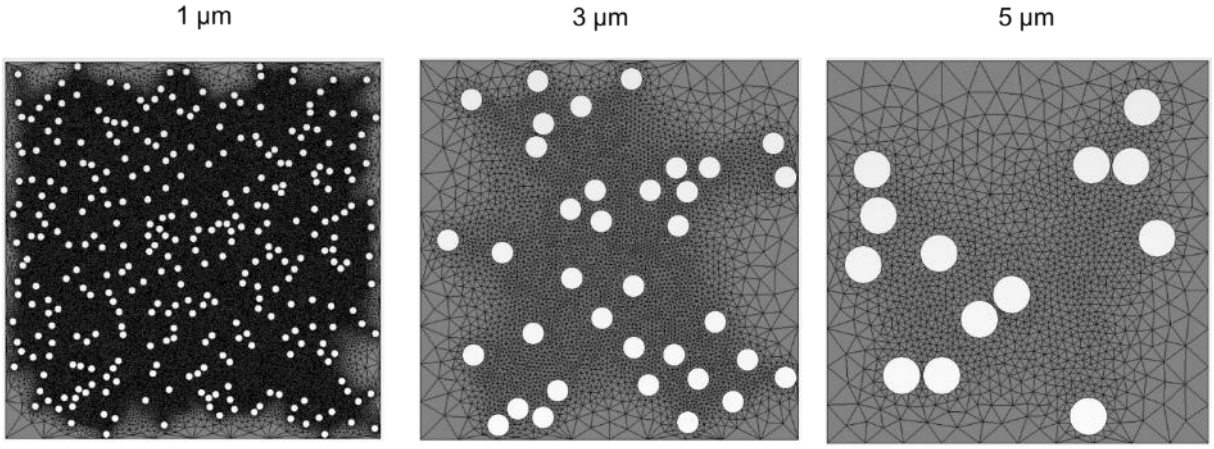

Figure 3.8: Virtual microstructures of matrix without fibres with different pore sizes with 5% porosity volume.

Virtual tensile tests were performed on the microstructures with pores ranging from 1 µm to 5 µm (Values: 1, 3 and 5) and the volume from 2.5% to 20% (Values: 2.5, 5, 7.5, 10, 12.5, 15, 17.5 and 20). Since the cohesive zone elements were considered in the finite element analysis, a 2D model was considered to be computationally efficient. The strength of the bulk matrix material was taken as 300 MPa and the stiffness as 118 GPa and the values were reverse calculated to match the experimental results reported by Ziegler et.al [85].

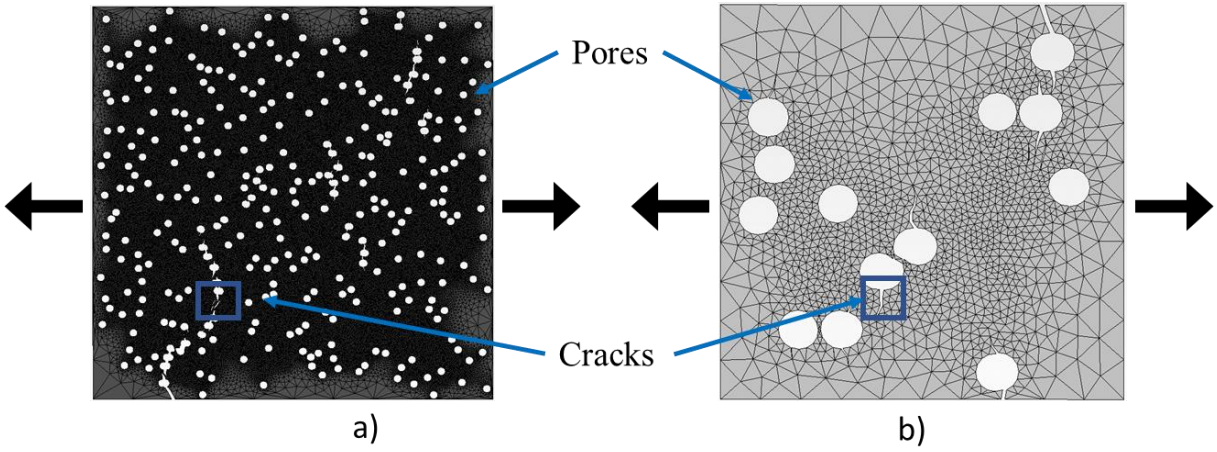

Figure 3.9: The crack growth in the virtual microstructures of matrix with different pore sizes a) 1 µm and b) 5 µm.

As observed in Figure 3.10 b), the stiffness decreases linearly with the increase in the porosity. On the other hand, the size of the pores does not affect the stiffness. It is expected as the effective load transfer between the nodes is not affected by the size of the pores. The volume of the matrix material present remains unchanged and therefore, the initial stiffness material is not affected by the pore size either. This is not the case with the strength of the material as the strength is higher in the case of larger pores. A plausible explanation for this phenomenon is that the presence of greater number of defects for the same volume makes it easier for the cracks to grow as the number of stress concentrations regions will be higher.

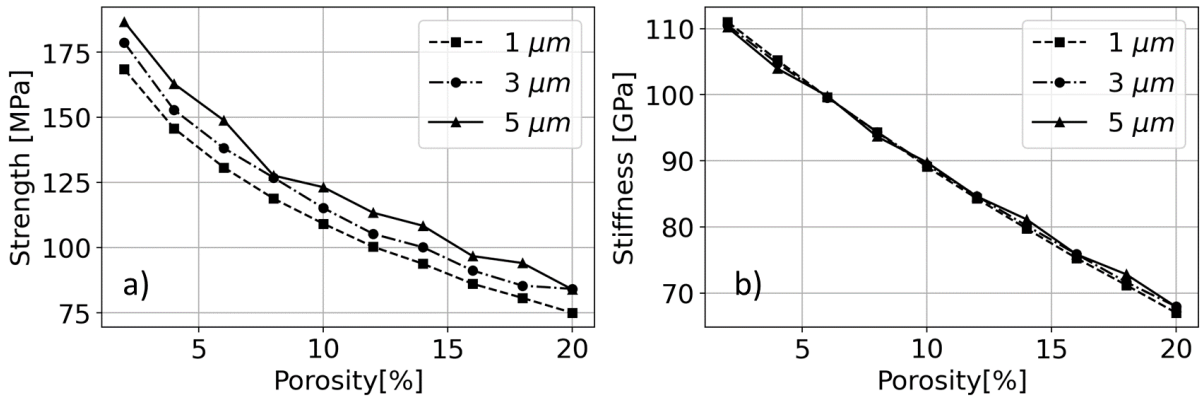

Figure 3.10: The effect of porosity on a) the strength and b) the stiffness of the matrix material for varying pore diameter.

It is important to note that the homogeneity of the pore distribution plays a major role in deciding the strength of the material. A conglomerate of pores degrades the properties in a more drastic way in comparison with homogenously pores or defects and influences the Weibull modulus of the material. However, this factor is not considered in this study as the distance between the individual pores could not be set as a parameter while generating the virtual microstructures. Nevertheless, Weibull modulus was evaluated for the microstructures with varying diameters, as shown in Figure 3.11.

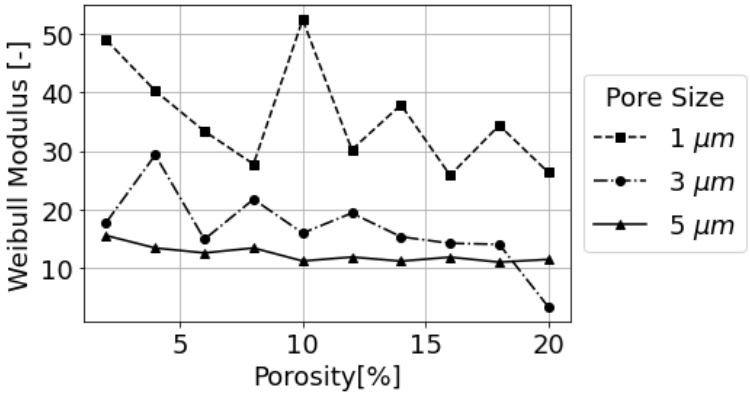

Figure 3.11: Relationship between the porosity and the resulting Weibull modulus of 20 samples with varying pore sizes of 1 µm, 3 µm and 5 µm.

The Weibull modulus of the microstructures with 1 µm diameter is very high when compared to 5 µm and remains so for all the porosity values. The higher number of defects present in the microstructure with smaller diameters possess lower strengths but the deviation among the values is not high as they are homogenously distributed in the microstructure. In the microstructure with 5 µm diameter, the pore close to the RVE edge (see Figure 3.9) might deviate from the strength value of an RVE with no pores on the edge as the lower number of pores will have higher chances of inhomogeneous distribution in the numerical case and their impact on the strength will be higher, resulting in lower values of Weibull modulus.

3.5.3 Virtual tensile test in transverse direction

2D finite element models with varying microstructural features and constituent properties were generated to evaluate the transverse properties of the composite. The virtual microstructures of size 50 µm x 50 µm were loaded with tensile stress in the transverse direction to the fibre (shown in Figure 3.12). Cohesive zone models were used to model the cracks between elements and the stress-strain curves for all the models were obtained. This simulation data served the basis for the ML algorithms. Python was used to extract the data from the models and evaluate the required properties from the stress-strain curves. The microstructural features and the constituent properties are the input variables and the acquired properties from the simulation are the target variables for the ML algorithms. Both the datasets are discussed in the subsequent section.

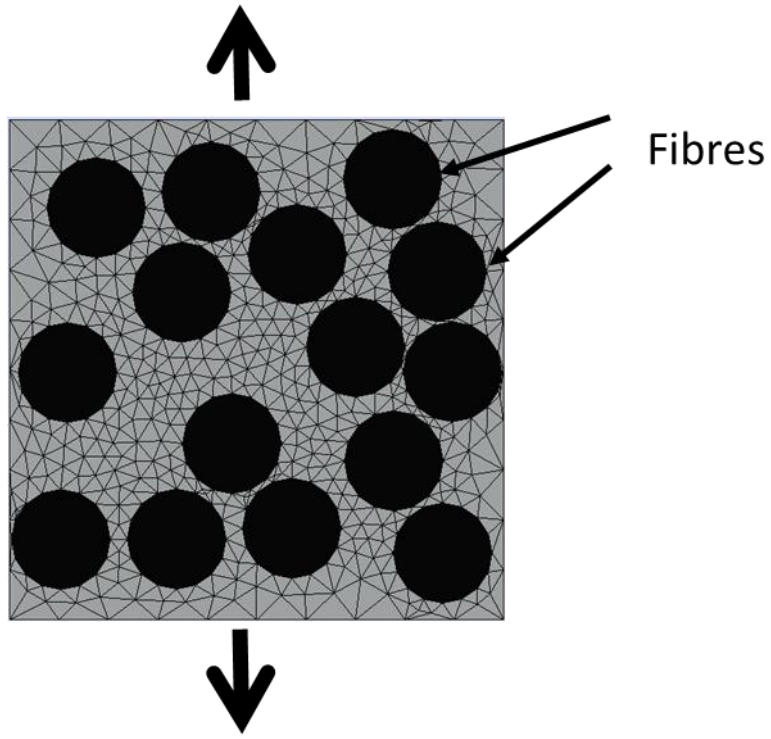

Figure 3.12: Virtual 2D microstructure under tensile stress in the transverse direction to the fibre.

Input Variables:

The input variables which were varied in the models are summarized in Table 3.4. Since the finite element simulation considering crack growth is computationally intensive, the choice of parameter variation to be varied was restricted to transverse properties and the longitudinal properties were kept constant. The range of the input variables is based on a literature study of CMCs representing different fibres such as carbon, silicon carbide and aluminium oxide. The Poisson's ratio and the shear modulus is assumed to be same in all the directions to reduce the number of variations. Moreover, these properties are not generally tested for the fibres and might not be available for material scientists while designing a composite or making a preliminary choice of the constituents. The range of matrix properties is based on the experience of different CMCs manufactured in the German Aerospace Centre at Stuttgart.

Table 3.4: Input variables used in the parameter study of virtual tensile testing in the transverse direction

Properties	**Symbol**	**Unit**	**Value**
Fibre			
Diameter	d	µm	10
Fibre Volume Fraction	V_f	%	35,45,55
Young's Modulus (longitudinal)	E_{f1}	GPa	400
Young's Modulus (transverse)	$E_{f2} = E_{f3}$	GPa	25,50,75
Poisson's Ratio	$\nu_{12} = \nu_{13} = \nu_{23}$	-	0.1

Shear Modulus	$G_{f12} = G_{f13} = G_{f23}$	GPa	25,50,75
Strength	σ_{f2-max}	MPa	25,50,75
Matrix			
Young's Modulus	E_m	GPa	100,200,300
Poisson's Ratio	ν	-	0.1
Strength	σ_{m-max}	MPa	25,50,75
Interface			
Strength	σ_{i-max}	MPa	25,50,75

Target Variables:

Following are the variables which are derived from the output obtained from the finite element simulations:

- E: Elastic modulus of UD-reinforced composite obtained from the stress-strain curve
- σ_{max}: Maximum stress value in a stress-strain curve of UD CMC
- ε_{max}: Value of strain at maximum stress in a stress-strain curve of UD CMC
- D_{max}: Damage variable which is given by $1 - \frac{E_{secant}}{E_0}$

  where E_{secant} is the secant modulus at maximum stress in the stress-strain curve and E_0 is the Young's modulus of UD CMC
- σ_{PL}: Proportional limit stress is the stress where the damage initiates i.e., the initiation of non-linear behaviour in a stress-strain curve of UD CMC
- ε_{PL}: Proportional limit strain is the value of strain at the proportional limit stress in a stress-strain curve of UD CMC

Correlation heatmap:

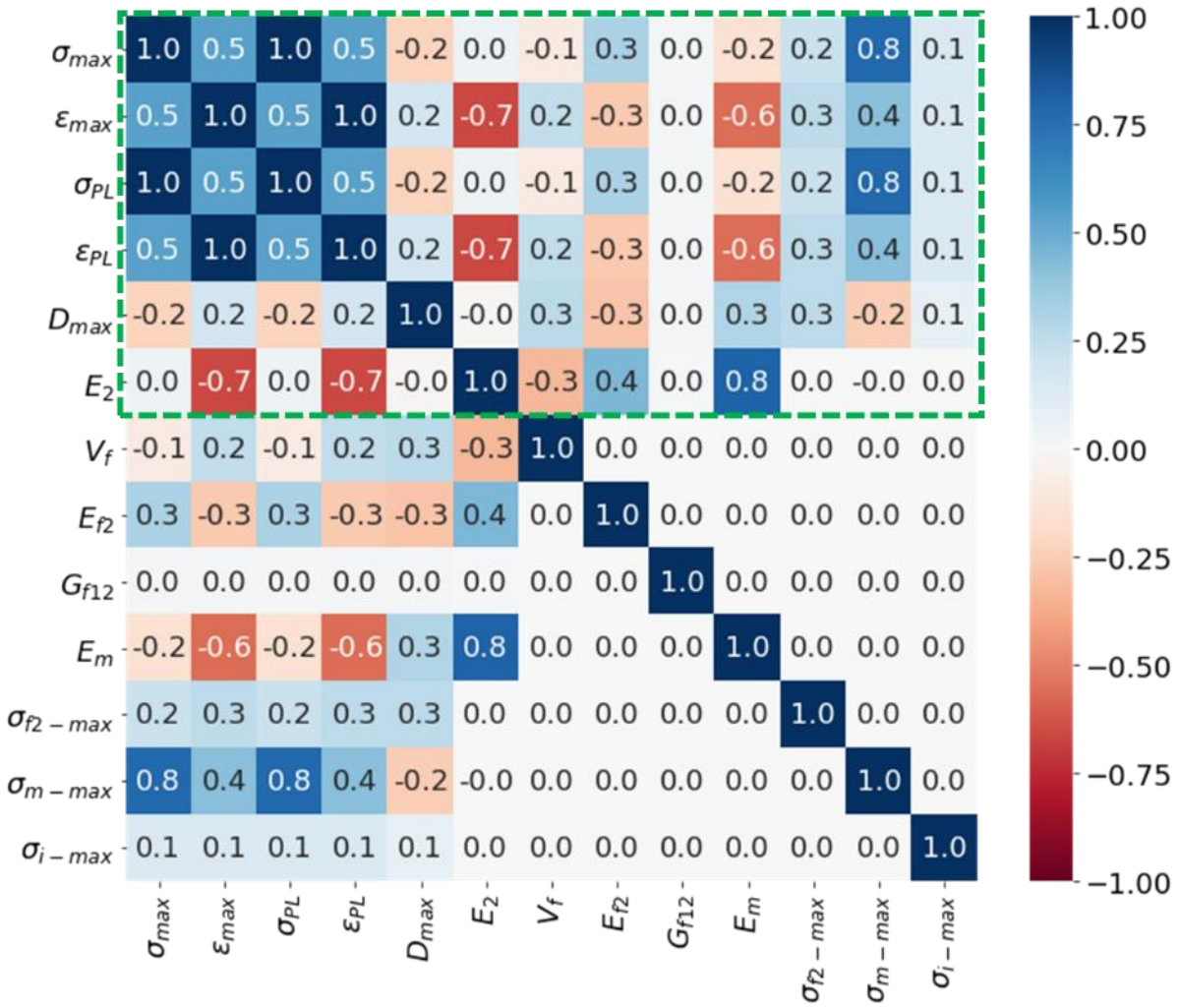

Figure 3.13: Pearson correlation heatmap for virtual tensile tests in the transverse direction in 2D unidirectional virtual composites with the target variables marked with green lines.

As mentioned earlier, Pearson correlation coefficient can be used for preliminary analysis of the data before using machine learning algorithms. The relationship between the different input variables and target variables can be analysed with the help of a correlation heatmap (shown in Figure 3.13). A value of '1' means a perfect positive correlation and '-1' means a perfect negative correlation between the input and target variables. Some observations which were made from the correlation map were:

- As expected in the matrix dominated transverse direction, Young's modulus is highly dependent on the stiffness of the matrix.
- Both σ_{max} and σ_{PL} are highly dependent on the matrix strength.

- ε_{PL} on the contrary, is inversely dependent on the matrix stiffness. With higher stiffness, the stress is higher for a particular strain value and material fails exhibiting relatively lower damage tolerance or non-linear behaviour. Due to the same reason, ε_{PL} and ε_{max} are also inversely dependent on the Young's modulus of the material.

Machine Learning Prediction

The machine learning algorithms introduced in Section 3.3 were used for the prediction of the target variables. The dataset obtained from 2187 simulations was divided into a training set that was used to train the models and a test set that was used for the validation of the algorithms. The performance of the different models in predicting the strength of the material is shown in Figure 3.14. The solid line in the figures show the 100% accuracy of the model and the region covered by the dotted lines represents the range of values with 90% accuracy. From all the models, decision tree and random forest show the highest accuracy in predicting the strength of the material, as most of the points lie within the 90% accuracy region.

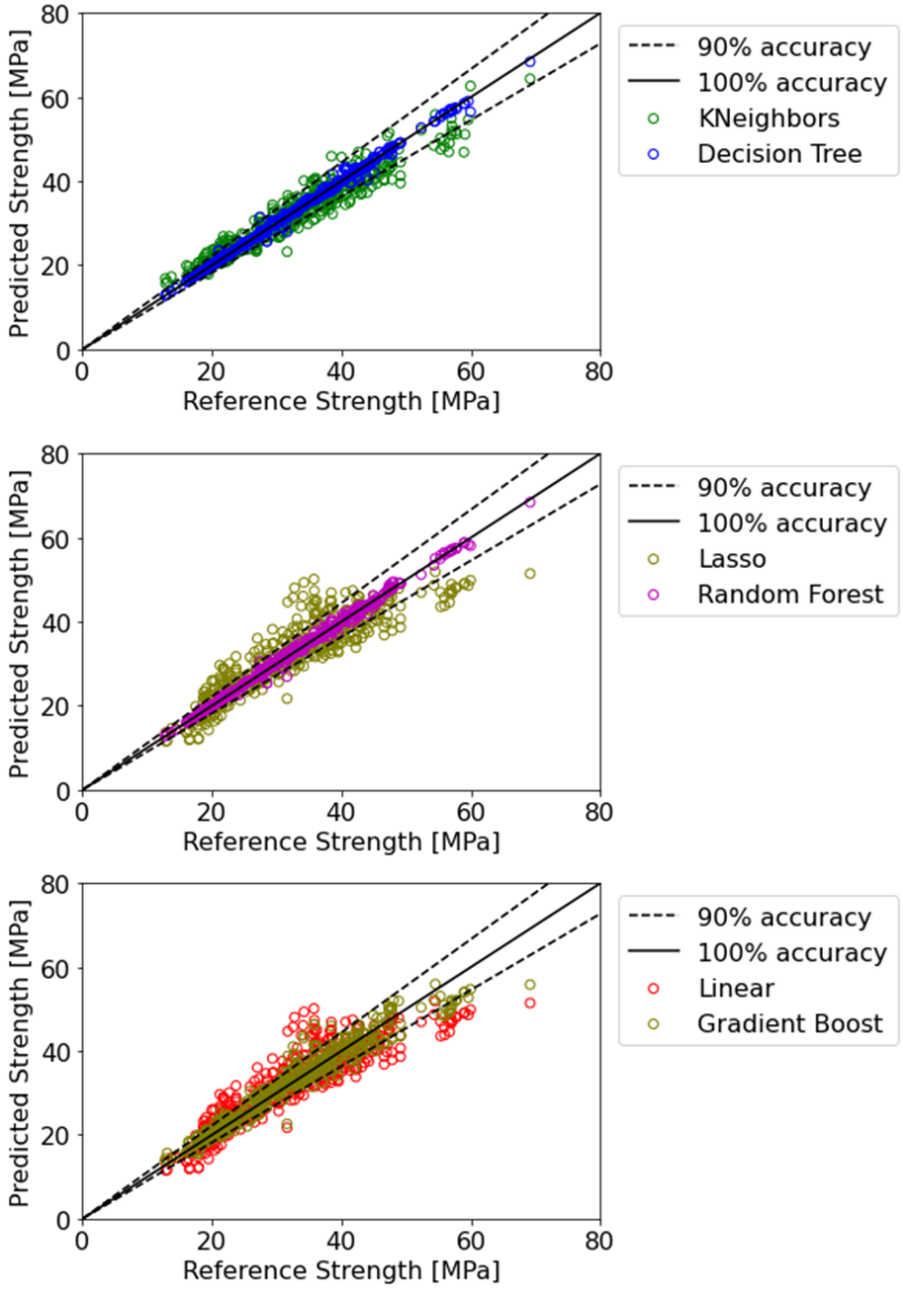

Figure 3.14: Comparison of the accuracies of the machine learning models in prediction of the transverse strength in 2D unidirectional virtual composites.

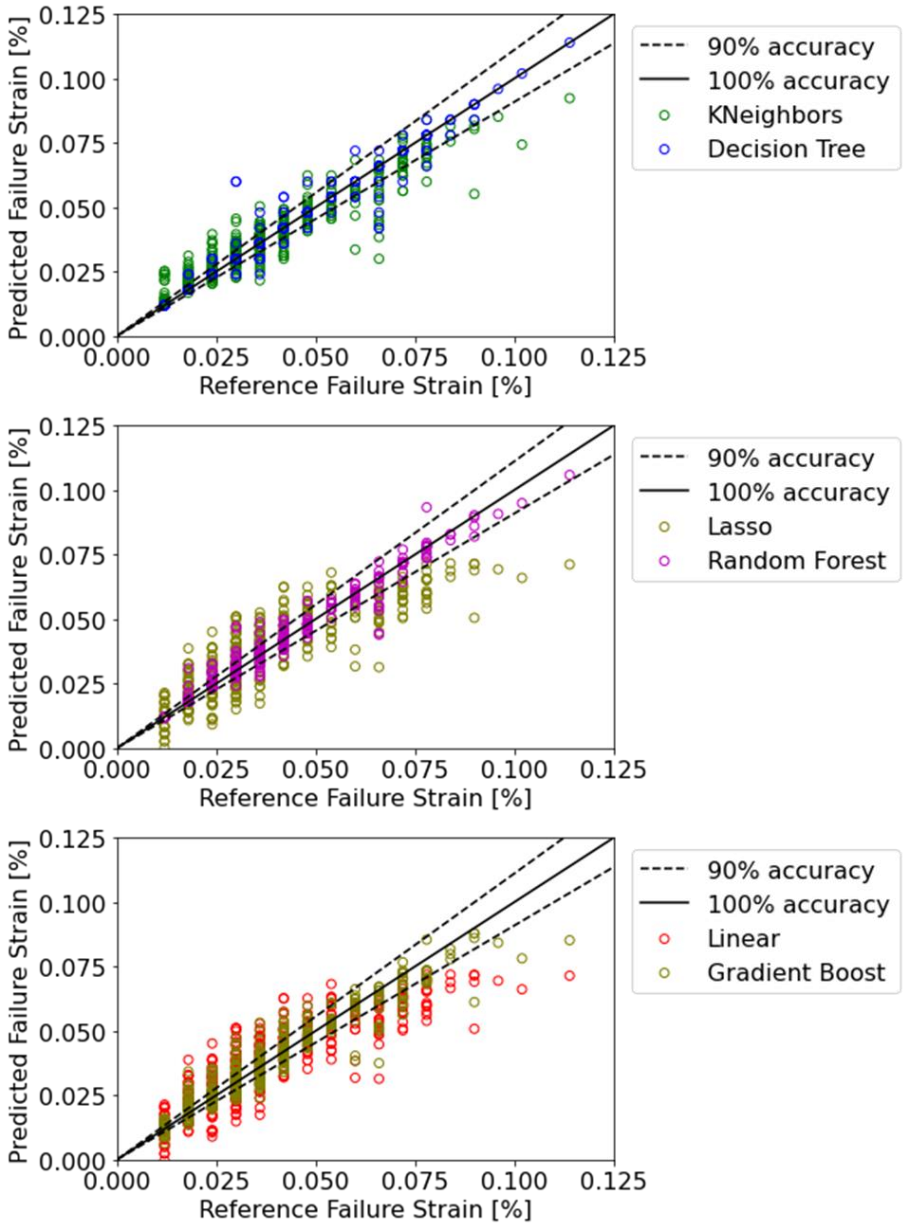

Figure 3.15: Comparison of the accuracies of the machine learning models in prediction of the transverse failure strain in 2D unidirectional virtual composites.

In a similar fashion, the ML algorithms were implemented to predict the failure strain as well and the results are shown in Figure 3.15. It can be noticed that the reference failure strain values occur in regular intervals. This is because the loading is strain-driven and is applied in pre-defined steps. Even in this case, decision trees and random forest show the highest accuracy in the prediction of the failure strain.

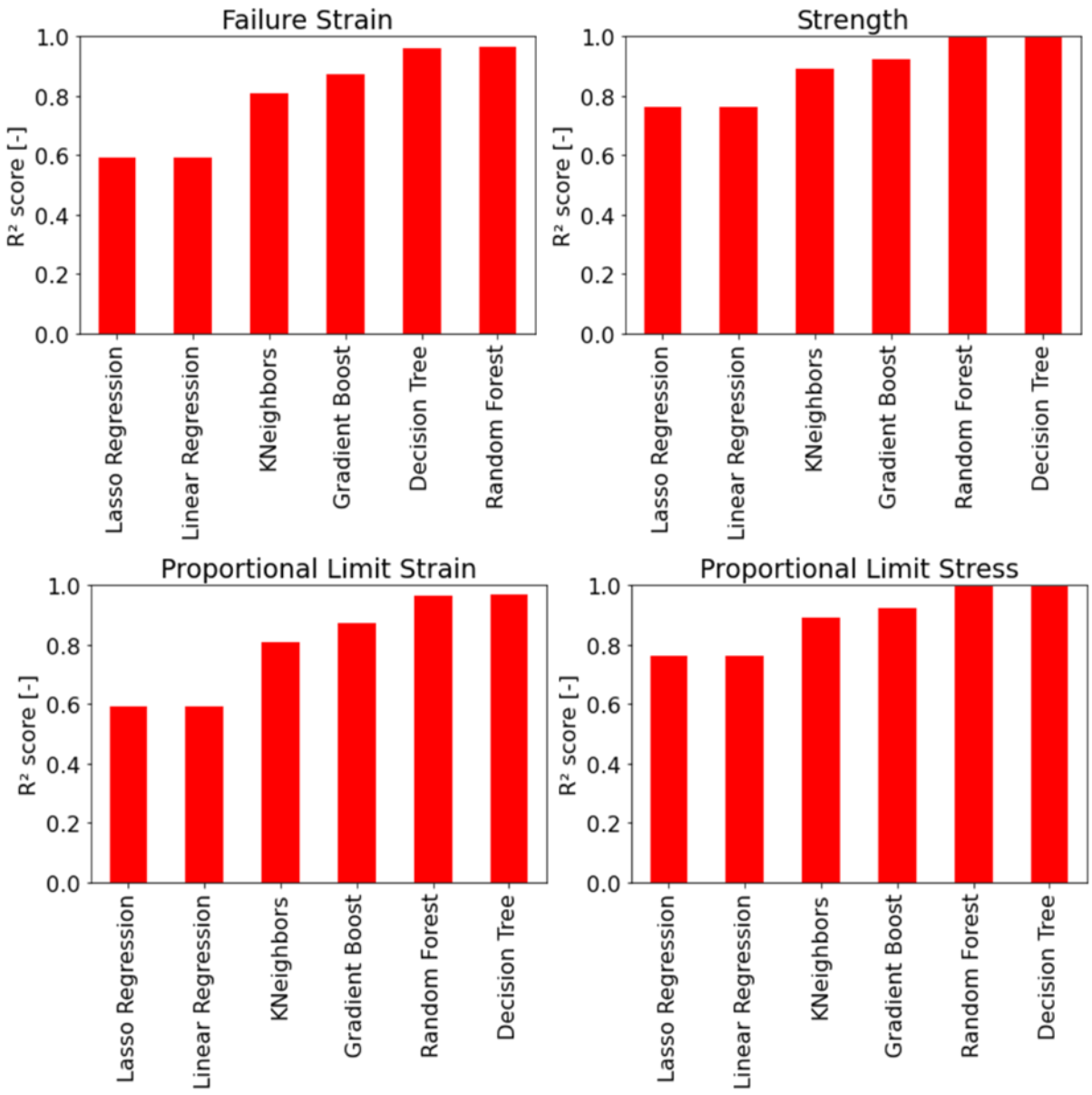

Figure 3.16: R^2 score of the machine learning models in the prediction of failure strain, failure strength, proportional limit stress and proportional limit strain in 2D unidirectional virtual composites.

The accuracy of the ML models can also be evaluated by R^2 score of an algorithm, which is given by the fraction of the mean squared error and the variance of the distribution [62]:

$$R^2 = 1 - \frac{\Sigma \left(y_{true} - y_{pred}\right)^2}{\Sigma \left(y_{true} - y_{true,mean}\right)^2} \tag{6}$$

The term 'true' stands for the original data and 'pred' stands for the predicted value for the same set of input variables. The accuracy of the models in the prediction of the other mechanical properties of the material are shown in Figure 3.16. The score factor '1' translates to 100% accuracy of any model. The

σ_{max} and σ_{PL} values of the material can be predicted with an accuracy of 99%. On the contrary, Linear Regression can predict the strength of the material only with an accuracy of 76%.

This implies that decision trees and random forest can predict all the four properties shown in Figure 3.16 with the same precision as the computationally intensive finite element simulations. In the current work, mean absolute error (MAE) between the predicted and the true values is used as another metric to compare the performance of ML algorithms. It is an arithmetic mean of the absolute errors $|y_i - x_i|$ where y_i is the predicted value and x_i is the true value for each set of the testing data. The MAE in the prediction of these properties is shown in Figure 3.17. It can be observed that the error is minimum in the case of decision tree and random forest algorithms since they exhibit the highest accuracy in the predictions.

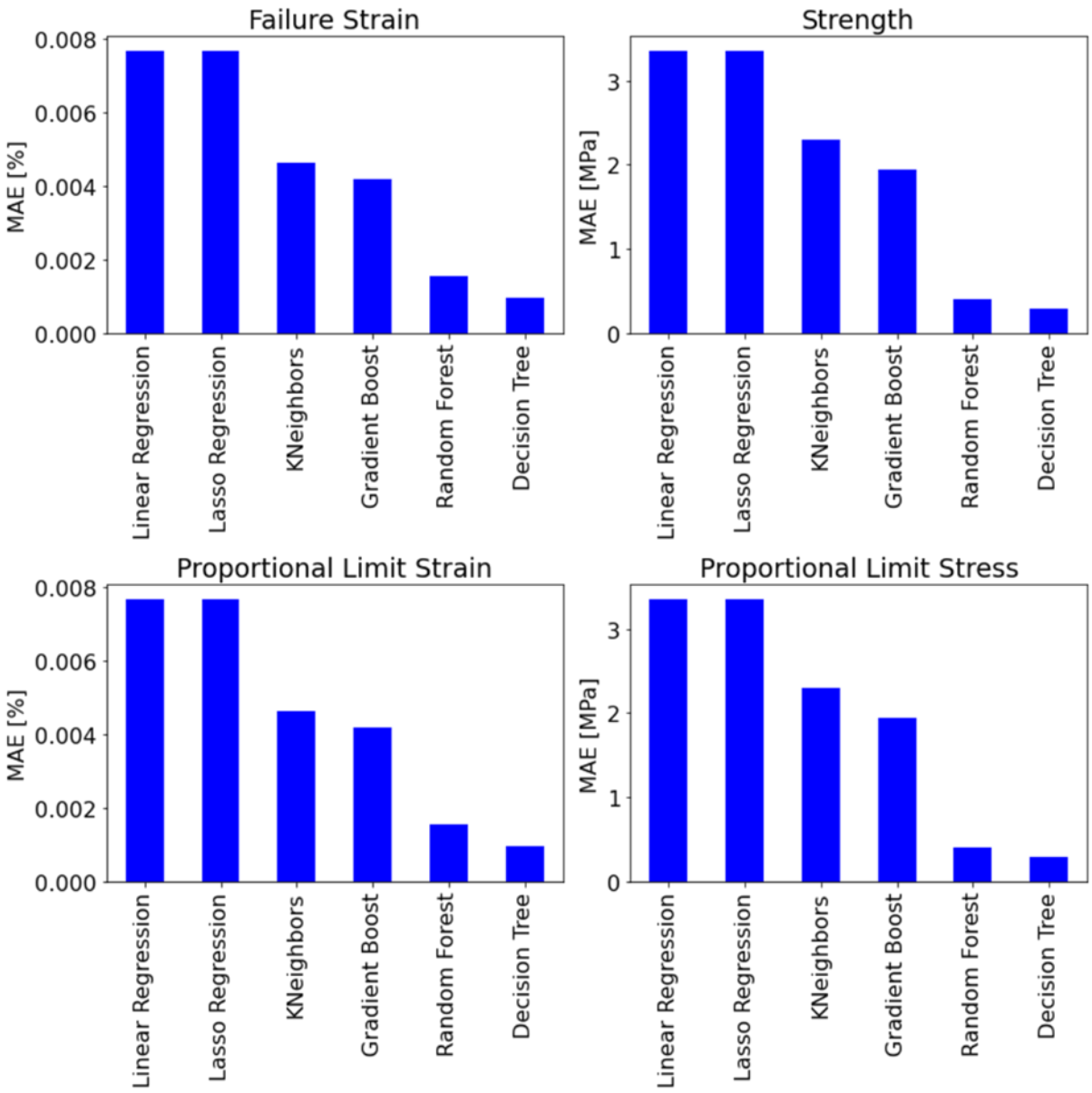

Figure 3.17: The mean average error (MAE) in prediction of the values of failure strain, failure strength, proportional limit stress and proportional limit strain by machine learning algorithms in the transverse direction in 2D unidirectional virtual composites.

It should be noted that the results for stiffness with the help of ML algorithms is not shown here as the relationship between the stiffness and the parameters like fibre volume content and Young's modulus of the constituents is rather straightforward and can be evaluated by analytical models. However, for the sake of completeness, the stiffness prediction by ML algorithms is shown in Figure 3.18. As observed the machine learning algorithms in Figure 3.18 b) can predict the stiffness with 100% accuracy. Furthermore, linear algorithms like Linear and Lasso Regression predicted the stiffness with 90% accuracy. Even though, there are analytical models with linear relationship between the transverse stiffness and Young's modulus of the constituents, presence of the other input variables creates noise in the data and affects the accuracy of the linear models.

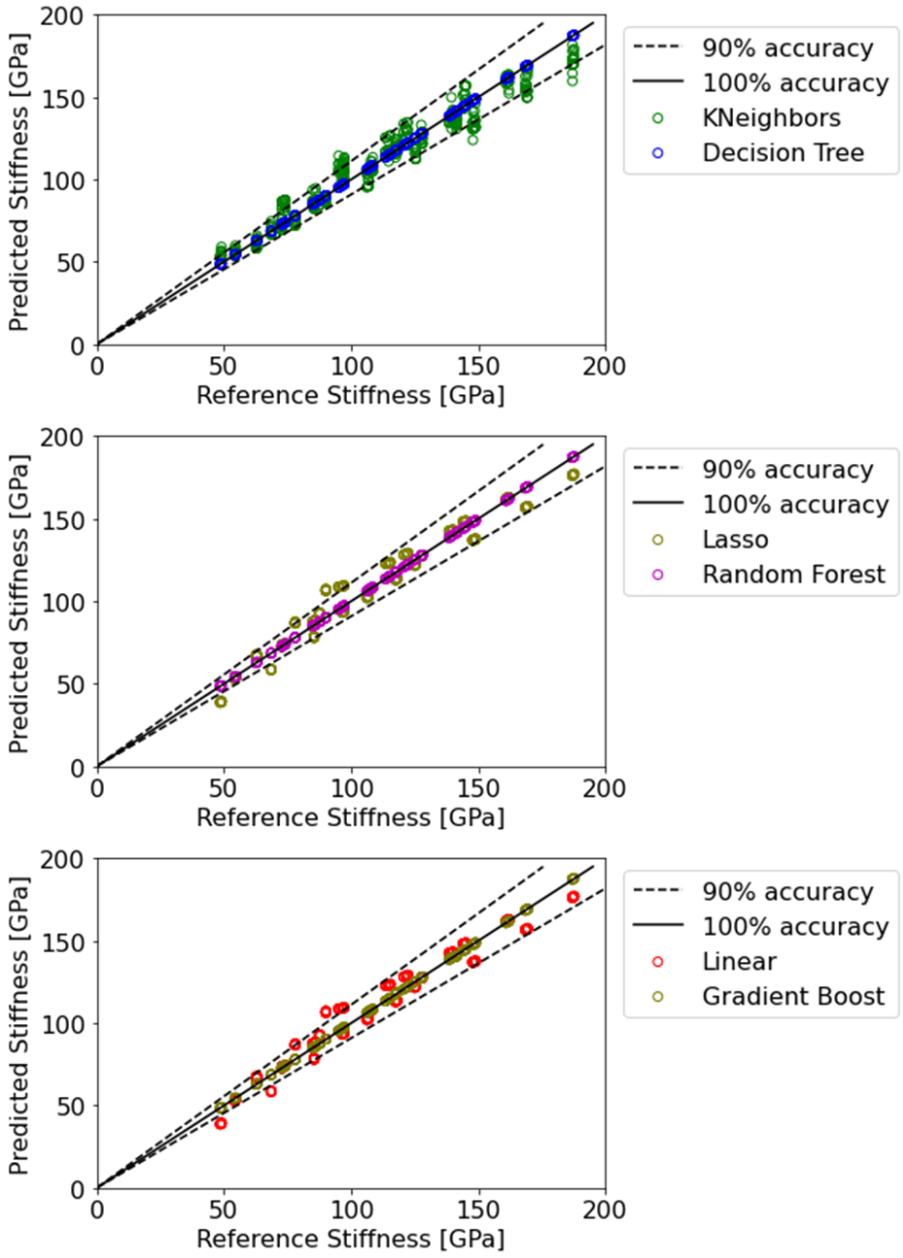

Figure 3.18: Comparison of the accuracies of the machine learning models in prediction of the transverse stiffness in 2D unidirectional virtual composites.

Feature Importance:

Techniques like feature selection are usually used to filter out the input parameters which are relevant for the prediction of the target variable. With the help of this method, important input parameters are filtered with the help of non-linear ML algorithms and the target variable is then evaluated with less computationally expensive linear algorithms. However, in the current study, the dataset under consideration was not large enough and therefore, the performance of the algorithms was neglected. The feature importance for stiffness as the target variable is shown in Figure 3.19. The sum of contribution from all the considered input variables is unity. It should be noticed in the figure that the Young's

modulus of the matrix and the fibre volume content are the most influential factors in the prediction of the transverse stiffness of the material. This inference does not imply that the transverse stiffness of the fibre does not contribute to the transverse stiffness of the composites, but the variation of the other parameters has a relatively higher influence on the target variable i.e., the transverse stiffness.

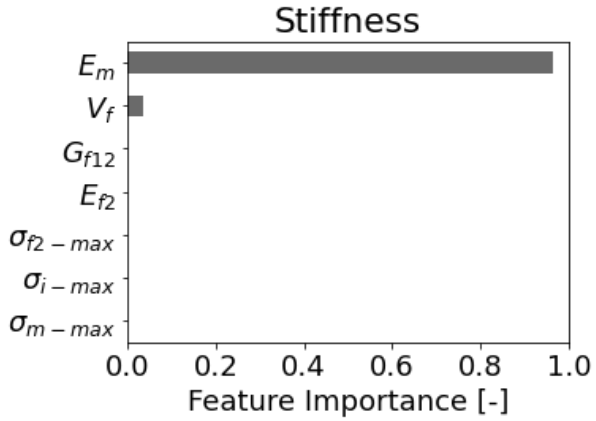

Figure 3.19: Feature importance evaluated with the help of random forest regression for transverse stiffness as the target variable in 2D unidirectional virtual composites.

In a similar way, feature importance can be evaluated for all other target variables as well, as shown in Figure 3.20. In the case of ε_{max}, Young's modulus of the matrix is the most influential factor followed by the strength of the matrix. The other input variables are also involved in the feature importance plot unlike stiffness prediction. In contrast, the contribution of matrix strength is very high compared to other input variables in the case of σ_{max}. For this reason, the prediction accuracy of the ML algorithms is better in the case of σ_{max}, as the number of variables contributing to the target variable are lesser when compared to ε_{max}. Similar trends were noticed in the feature importance plots of ε_{PL} and σ_{PL} as well.

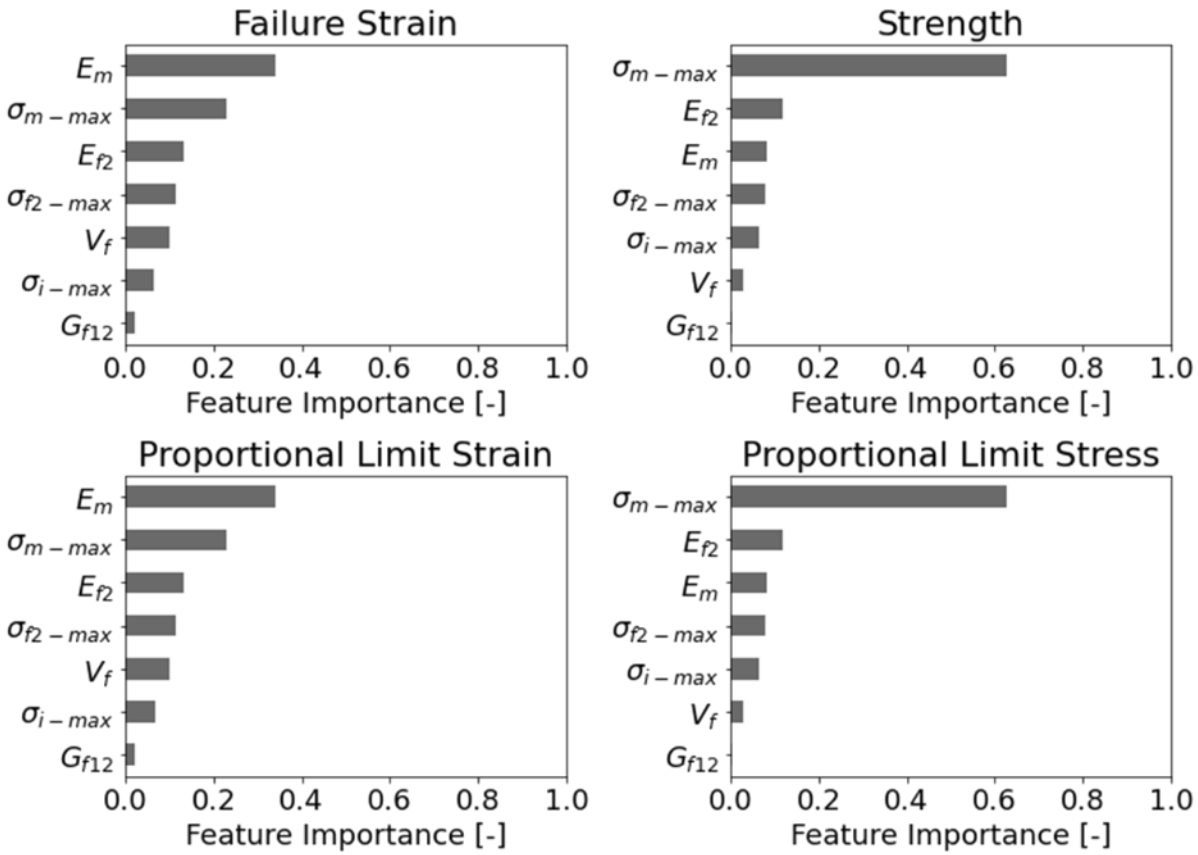

Figure 3.20: Feature importance evaluated with the help of random forest regression for failure strain, failure strength, proportional limit stress and proportional limit strain in the transverse direction in 2D unidirectional virtual composites.

Again, it should be mentioned that the other properties with lower importance values also influence the target variables. For example, interface strength of the material is an important property in deciding the damage tolerance behaviour of the material. In the case of samples with lower interface strength than the matrix strength, the cracks will be deflected onto the fibre/matrix interface, thus providing the desired damage tolerance to CMCs [86]. This was noticed in the simulations as well, as seen in Figure 3.21. The strength in the case of strong fibre/matrix interface is lower as the cracks appear everywhere in the matrix including in the fibre, thus decreasing the load carrying capacity of the composite. On the other hand, in the case of weak fibre/matrix interface, the cracks are deflected on the fibre/matrix interface because of the lower interface strength in the finite element model. As a result, the failure strength and the failure strain are higher in the weak fibre/matrix composite. The importance values are lower in the plot as the other variables are relatively more important as far as the relationship between the variance of the input and the output variables is concerned.

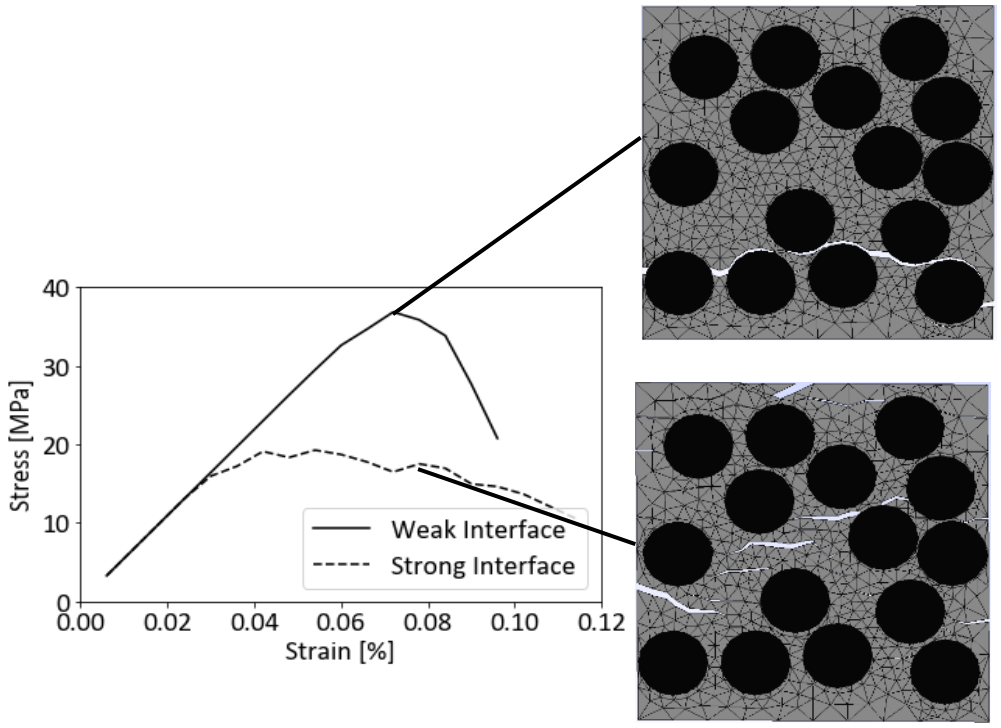

Figure 3.21: Comparison of stress-strain curves under transverse tensile loading in the variants with weak and strong fibre/matrix interface in 2D unidirectional virtual composites.

Decision Trees:

Till now, the regression capabilities of decision trees and random forest are discussed but as mentioned in the introduction section, these algorithms can be used for classification problems as well. Although, the problem at hand is a regression problem as the target variables are values rather than different classes or groups. However, in order to exploit the results of decision trees and improve the understanding of the results, the target variables were divided into groups. For example, in the case of stiffness as target variable, the results were divided into three groups, namely:

1. Low: values lower than 255 GPa
2. Medium: values between 255 GPa and 300 GPa
3. High: values higher than 300 GPa

Each group contains 729 samples and the criteria for decisions at the leaf nodes are shown in Figure 3.22. The level of nodes is called the depth of a particular decision tree. The depth of the decision trees depends on the number of variables, which contribute to the prediction of the target variable. A colour is assigned to each class: The information about the nodes is summarized in the boxes for the leaf nodes in the figure:

- First line: It shows the split criterion used at a particular node. In the first level, the decision criterion is the stiffness of the matrix, where the data is split at the value of 150 MPa.

- Second line: Gini score is mentioned in the second line, which is a metric that varies between 0 and 1. It represents the distribution of data into classes at a particular node. The value of 0.667 shows that 66.7% of the data is filtered out at this node based on the criterion in the first line. A gini score of 0 would mean that a node is pure, and all the samples belong to a particular class.
- Third line: The total number of samples left to be categorized are listed.
- Fourth line: The number of samples left to be categorized in a particular class is mentioned. The sequence is based on the classes defined during the data analysis. In the current case, the sequence is: [High, Low, Medium]
- Fifth line: The mentioned class in this line is the class that occurs the most within that node. In this example, it is irrelevant because the number of samples belonging to a class is always equally distributed.

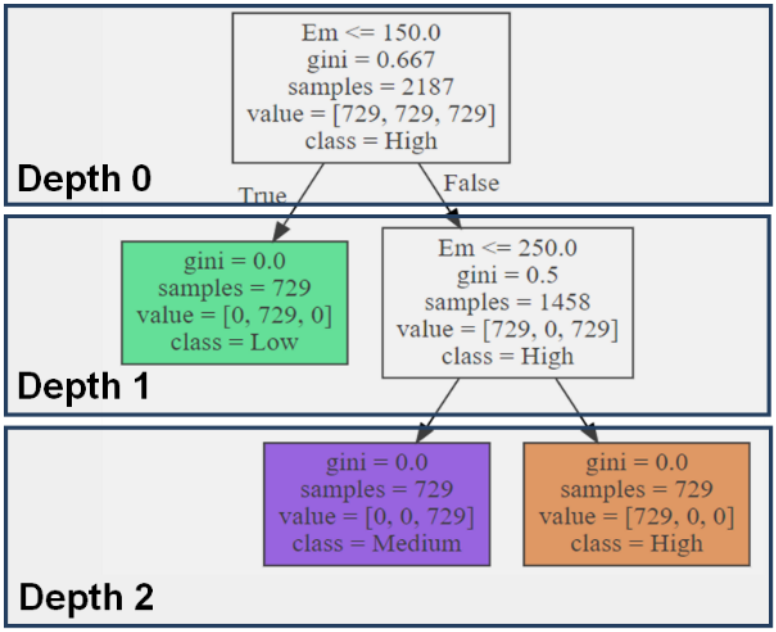

Figure 3.22: The conditions of split for each leaf node based on the importance of the feature to evaluate the respective groups of stiffness in 2D unidirectional virtual composites in the transverse direction.

The algorithm chooses a split based on the gini score and performs this for multiple thresholds till the best split is achieved. Once the root node at 'Depth 0' is determined by the feature, the tree grows to the next depth level and the same process is repeated for all the other nodes in the tree. As expected from the feature importance analysis in Figure 3.19, the split at the root node is based on the Young's modulus of the matrix and all the samples with matrix stiffness lower than 150 GPa will belong to 'Low' class where the transverse stiffness of the composite is below 225 GPa. Since, all the samples in this node belong to one class, there is no further depth required at this node. On the contrary, the other box splits again at the matrix stiffness value of 250 GPa where the values lower than it belong to the 'Medium' class and the rest to the 'High' class.

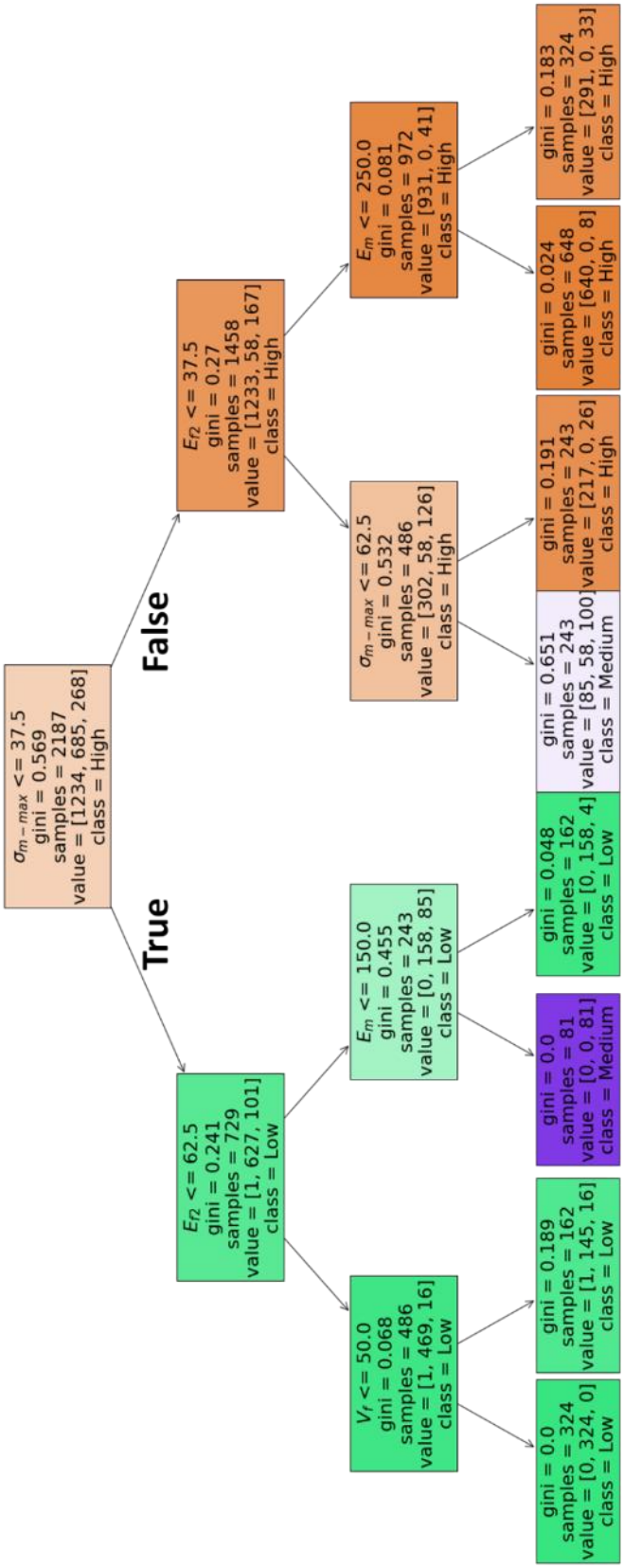

Figure 3.23: The conditions of split for each leaf node based on the importance of the feature to evaluate the respective groups of strengths in the transverse direction in 2D unidirectional virtual composites.

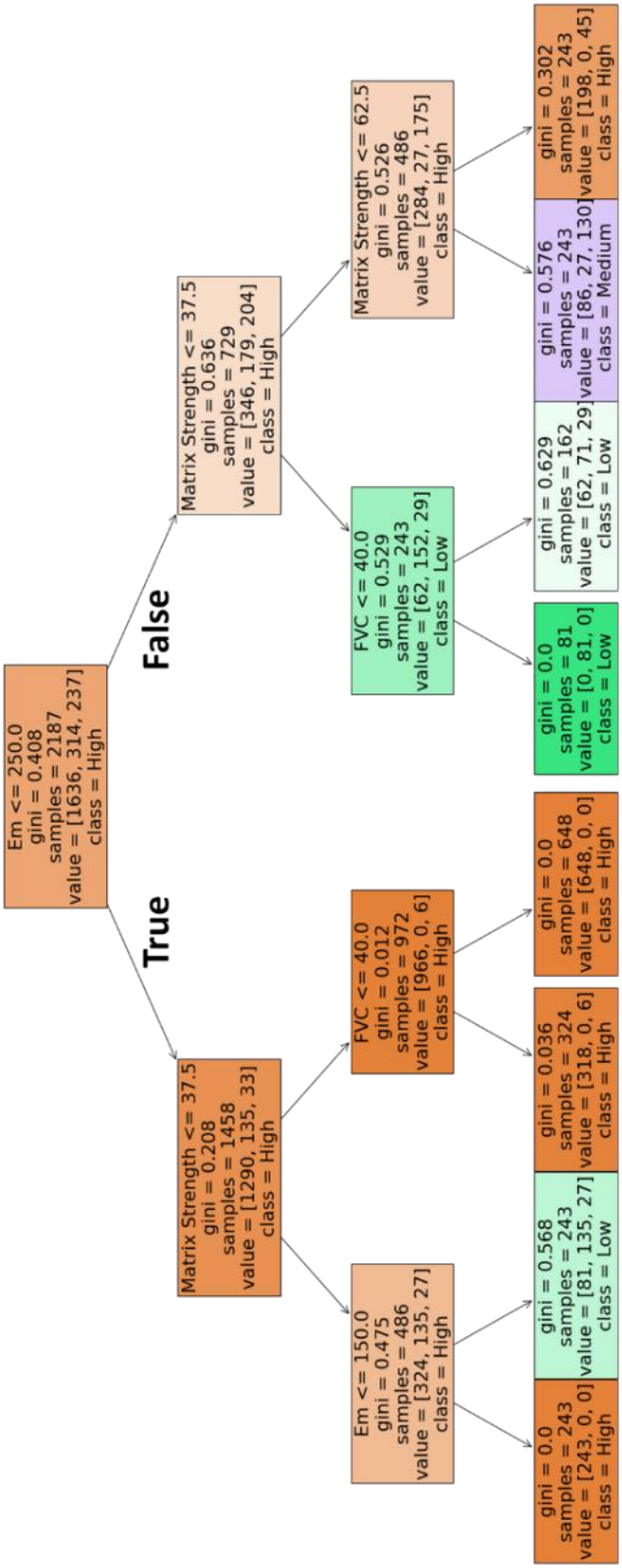

Figure 3.24: The conditions of split for each leaf node based on the importance of the feature to evaluate the respective groups of strains in the transverse direction in 2D unidirectional virtual composites.

Similar to the stiffness prediction, strength values can also be classified with the help of decision trees. Although, the relationship between the input variables and the target variable i.e., strength is not as direct as in the case of stiffness, the analysis gave some insight into the dependence of the input variables over the target variables. As observed in the feature importance in Figure 3.23, many input variables contribute to the prediction of transverse strength of the composite. For the sake of explanation, only three depth levels are shown in Figure 3.23 for strength prediction. The classes in the case of strength were defined as:

1. Low: values lower than 25 MPa
2. Medium: values between 25 MPa and 30 MPa
3. High: values higher than 30 MPa

The gini score is not zero in the third level which implies that more depth is required to classify all the samples into different groups. Based on the observations in Figure 3.23, to achieve a composite with the transverse strength higher than 35 MPa, the matrix strength should be higher than 37.5 MPa and the transverse stiffness of the fibre should be higher than 37.5 GPa. It is obvious that further splits are required and not all the samples will fall under 'High' category as there are samples left which belong to 'Medium' class as observed in the nodes on the bottom right side. It should be noted that the intensity of the colours assigned to classes becomes darker, as the gini score tends to zero for the respective classes.

This analysis was performed for the prediction of failure strains as well, as shown in Figure 3.24. In contrary to the strength prediction, the feature importance is shared with comparable contribution between all the input variables. Due to this reason, the prediction accuracy of the decision trees is lower than strength prediction and this can be observed in the figure too. For example, even in the third depth level, the gini score for 'Medium' class is very high and more splits were required to predict the chain of decisions required to fall into 'Medium' class.

Table 3.5: Range of the values of the target variables in transverse direction to create classification groups for decision trees in 2D unidirectional virtual composites

Properties	**Unit**	**Low**	**Medium**	**High**
Young's Modulus (E_2)	GPa	< 225	225 - 300	> 300
Failure Strength (σ_{max})	MPa	< 25	25 - 30	> 30
Proportional Limit Stress (σ_{PL})	MPa	< 25	25 - 30	> 30
Failure Strain (ε_{max})	%	< 0.02	0.02 - 0.03	> 0.03
Proportional Limit Strain (ε_{PL})	%	< 0.02	0.02 - 0.03	> 0.03

Decision trees were analysed for the values of proportional limit stress and strain as well. The decision trees of proportional limit stress and strain were found to be exactly the same as in the case of strength and failure strain respectively, as shown in Figure 3.25 and Figure 3.26. For this reason, the range of the classification groups of proportional limit stress and strain is same as that of the groups of strength and failure strain respectively (see Table 3.13). This was expected as the proportional limit values are identical to the strength values in the case of transverse strain as the fibres do not carry load in the transverse direction and the composite fails as soon as the matrix fails under the load. This direct correlation between the proportional limit values and the respective strength and strain values at failure was also noticed in the correlation map as shown in Figure 3.13.

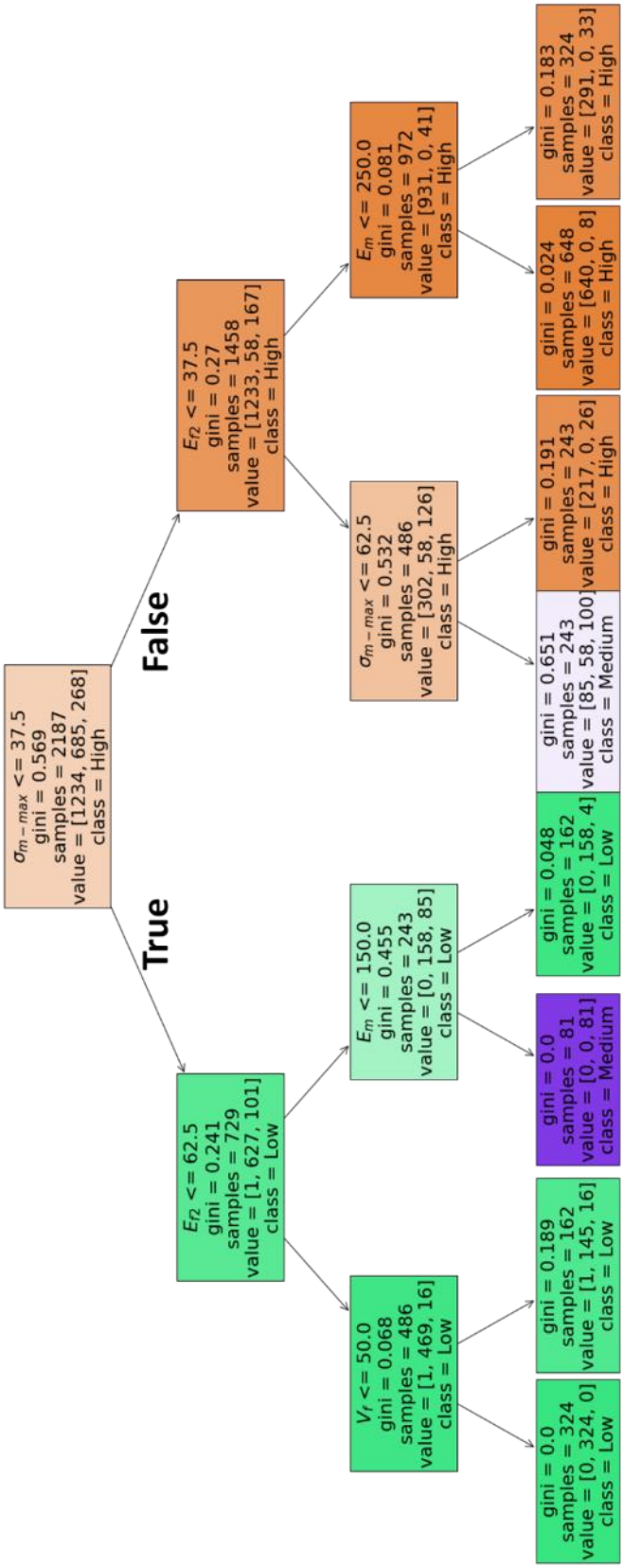

Figure 3.25: The conditions of split for each leaf node based on the importance of the feature to evaluate the respective groups of proportional limit stresses in the transverse direction in 2D unidirectional virtual composites.

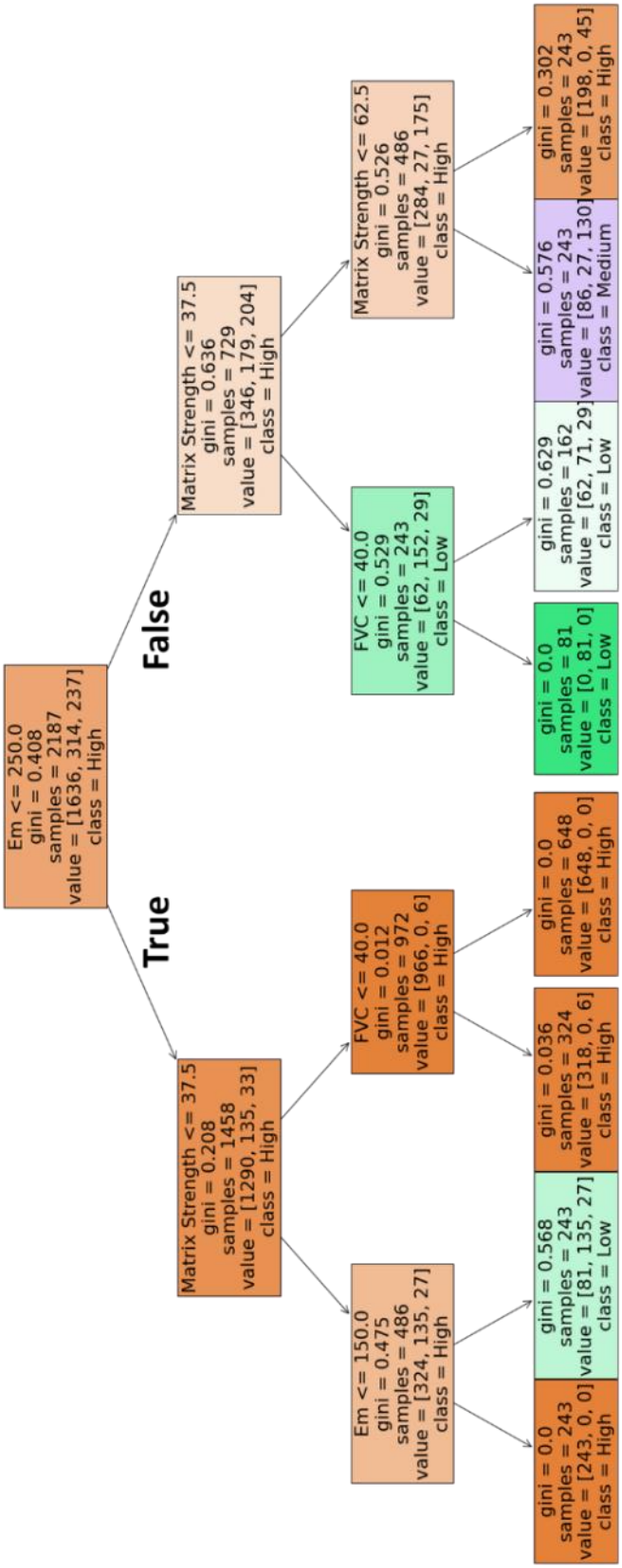

Figure 3.26: The conditions of split for each leaf node based on the importance of the feature to evaluate the respective groups of proportional limit strain in the transverse direction in 2D unidirectional virtual composites.

Weibull study:

The aim of this study was to understand the effect of Weibull distribution of the matrix strength over the transverse strength of the composite. For this study, all the other input variables apart from the matrix strength were kept constant, where 25 MPa, 50 MPa and 75 MPa were used as strength values. The shape parameter of the Weibull distribution (Weibull modulus) of the matrix strength was varied from 5 to 20 (Values: 5, 10, 15 and 20). For each set of matrix strength and corresponding Weibull modulus, 20 virtual microstructures with the same fibre volume content were generated. The distribution of the strength is shown in Figure 3.27. It can be observed that there are three peaks of composite strengths because of the three different values of matrix strengths.

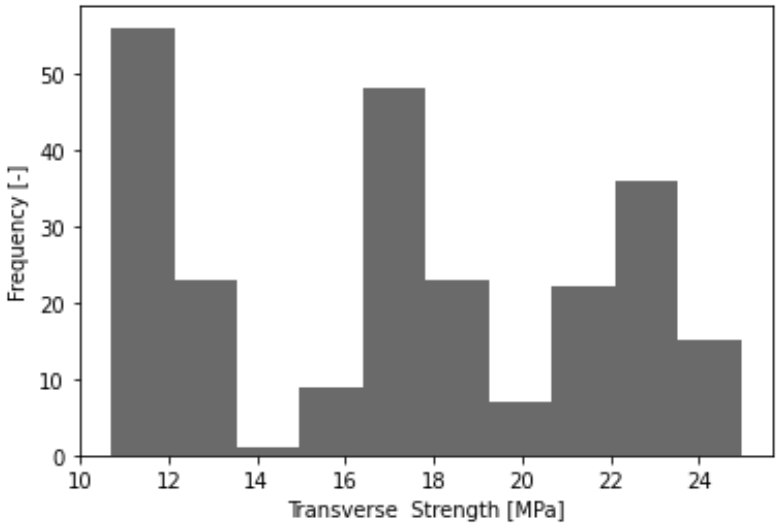

Figure 3.27: Distribution of the transverse strength in 2D unidirectional virtual composites with varying matrix strength and its Weibull distribution.

The variation of the Weibull modulus of the transverse strength distribution for different matrix strength values is plotted in Figure 3.28. An inference that can be drawn from the figure is that the presence of weak links such as porosity represented by Weibull modulus affects the deviation within the transverse strength of the composites when the values of Weibull modulus for matrix strength is low. For higher values of Weibull modulus, the Weibull modulus of the transverse strength distribution of 2D unidirectional virtual composites is high as well as the lower deviation between the matrix strength values represents more homogenous distribution of defects within the material and thus resulting in lower deviation in the strength.

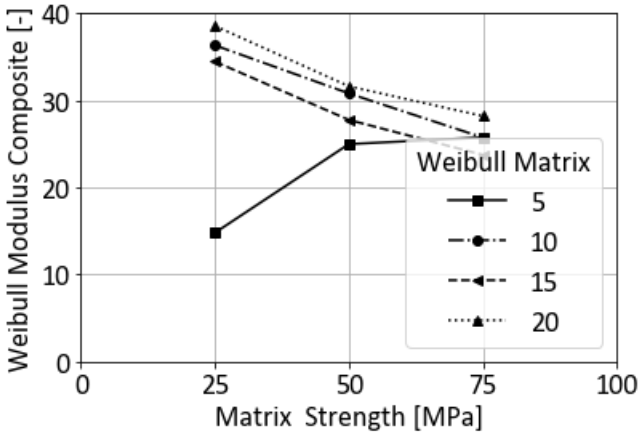

Figure 3.28: Variation of Weibull modulus of the transverse strength in 2D unidirectional virtual composites for different matrix strength values.

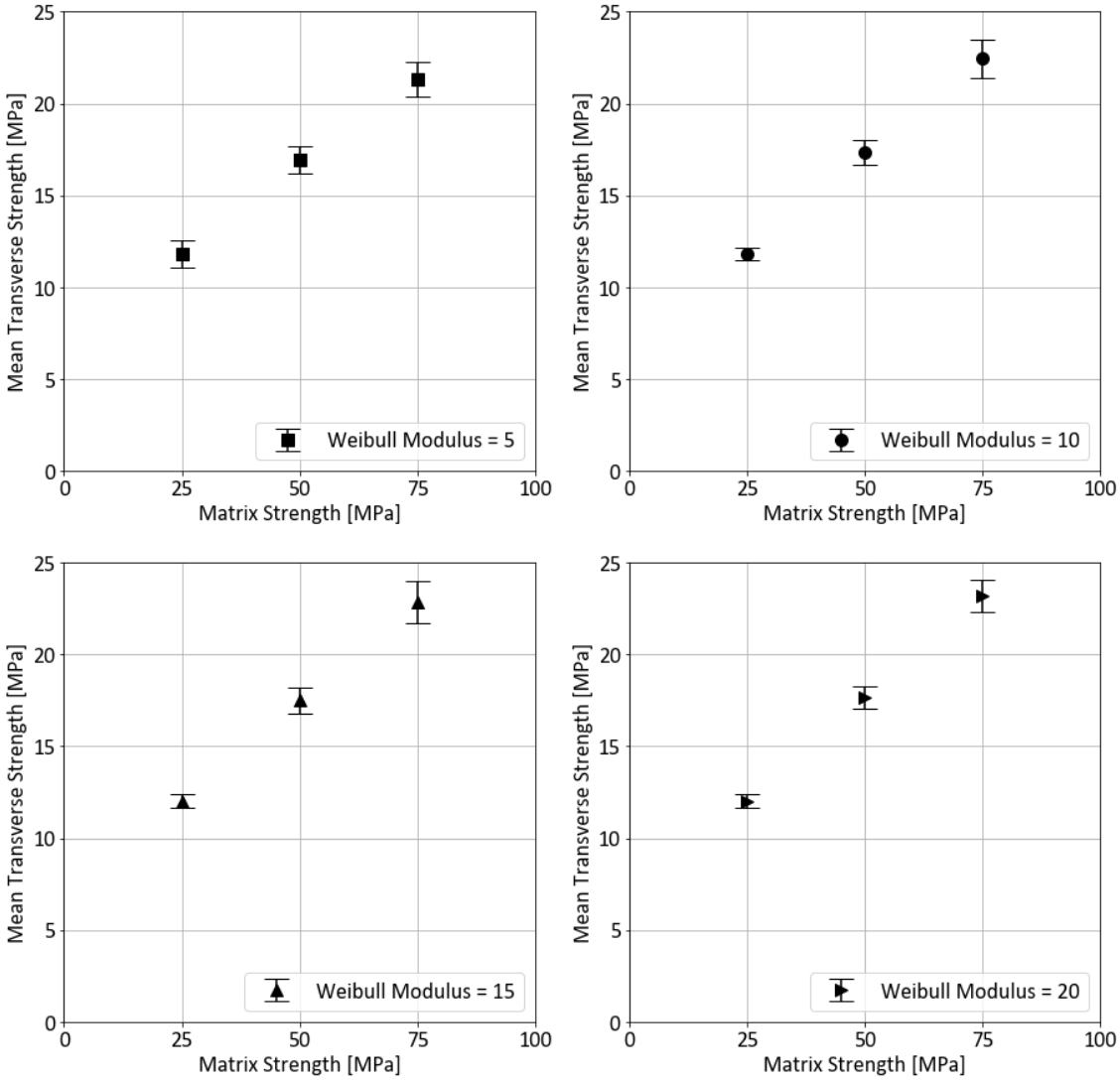

Figure 3.29: Mean transverse strength values for microstructures with varying matrix strength and Weibull shape parameter in 2D unidirectional virtual composites.

The mean strength values and deviation of the virtually generated microstructures for varying Weibull modulus and matrix strengths are shown in Figure 3.29. The mean transverse strength values for the different Weibull modulus values remain unchanged and it can be concluded from the results that Weibull modulus does not influence the transverse strength of a unidirectional composite. Although, the Weibull modulus for composite is relatively low for the value of 5 as Weibull modulus for matrix strength, the mean transverse strength is comparable with higher values of Weibull modulus.

3.5.4 Virtual tensile test in longitudinal direction

The case study discussed in the previous section was performed for the virtual microstructures with tensile loading in the fibre direction as well. Additionally, the tensile tests performed on four different CMCs, reported in a previous publication from DLR [69], were used to validate the finite element models. As mentioned in Section 3.4, four fibre types were embedded in SiCN matrix manufactured via PIP-route. The mechanical properties of the constituents used for the finite element simulation are listed in Table 3.6.

Table 3.6: Constituent properties of different material combinations used to perform the virtual tensile tests in the fibre direction

	Properties	**Unit**	**SA3**	**ZMI**	**T800**	**XN90**
	Fibre					
Diameter	d	µm	7.5	11	5	10
Fibre Volume Fraction	V_f	%	45	48	42	42
Young's Modulus (∥)	E_{f1}	GPa	380	195	294	860
Young's Modulus (⊥)	$E_{f2} = E_{f3}$	GPa	200 [25]	200 [25]	10 [87]	3 [87]
Poisson's Ratio (∥)	$\nu_{12} = \nu_{13}$	-	0.25 [25]	0.25 [25]	0.35 [88]	0.27 [89]
Poisson's Ratio (⊥)	ν_{23}	-	0.22 [25]	0.22 [25]	0.3 [88]	0.3 [88]
Shear Modulus	$G_{f12} = G_{f13} = G_{f23}$	GPa	80 [25]	80 [25]	28 [88]	28 [88]
Strength	σ_{f1-max}	MPa	2400	3400	5490	3430
Matrix						
Young's Modulus	E_m	GPa	108			
Poisson's Ratio	ν	-	0.2			
Strength	σ_{m-max}	MPa	75			
Interface						
Strength	σ_{i-max}	MPa	50	100	100	50

The constituent properties were obtained from literature and the datasheet provided by the manufacture in the case of fibres. As the fibre/matrix interface properties were not available in the literature, SEM images of the fractured surface of the samples (Figure 3.30) were used as the basis of the assumed interface strength values in Table 3.6. The matrix properties were taken from the previous section with consideration of the measured porosity of SiC/SiCN samples.

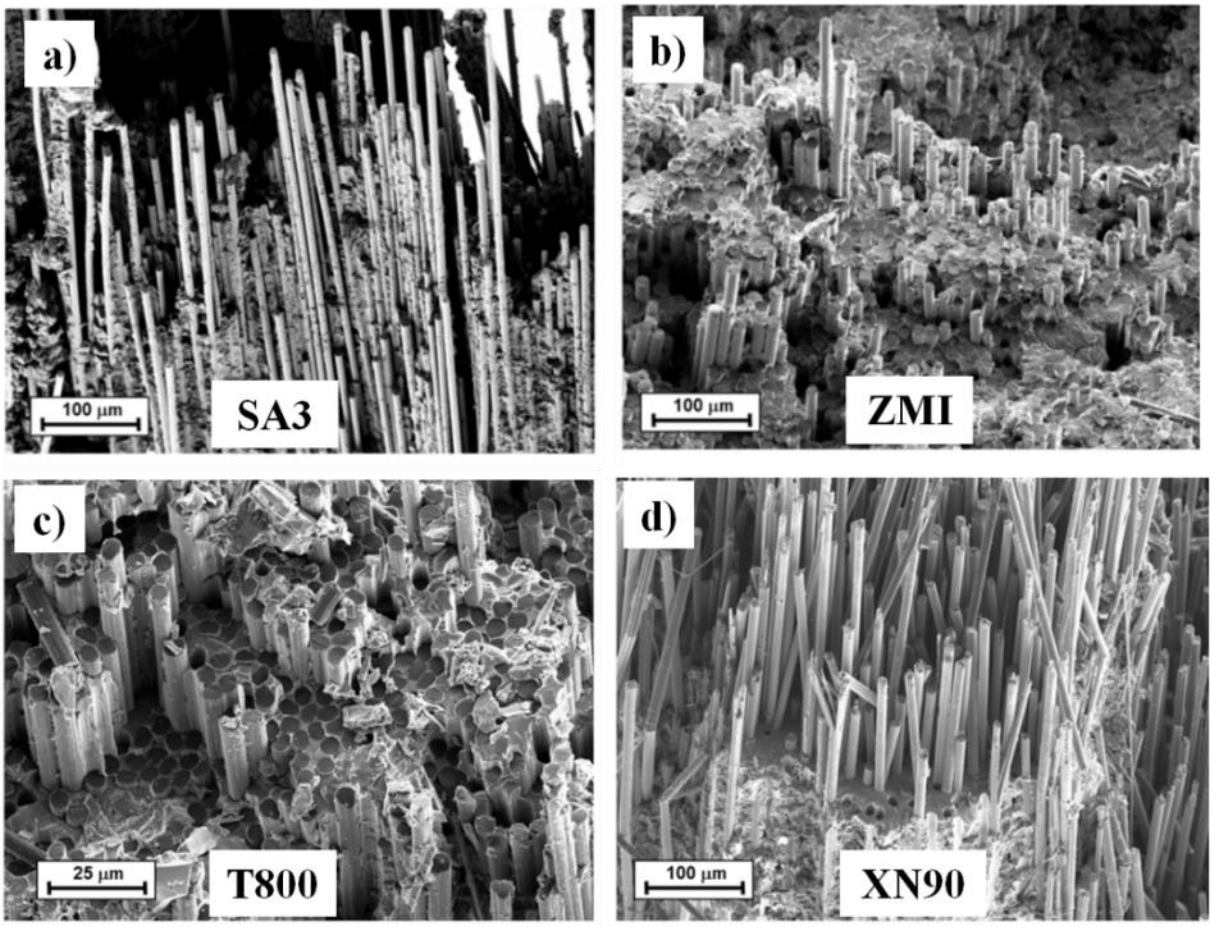

Figure 3.30: SEM images of the fractured surfaces of the SiC fibres (a and b) and carbon fibres (c and d) embedded in the SiCN matrix [79]

The finite element simulation was performed on the virtual microstructures of size 50 µm x 50 µm x 10 µm with 100 time-steps and the strain applied to the microstructure was 0.25%. Analogous to the previous section, cohesive zone elements with irreversible linear decay law were again used to capture the non-linear behaviour of the microstructures by modelling the crack initiation and growth between the elements.

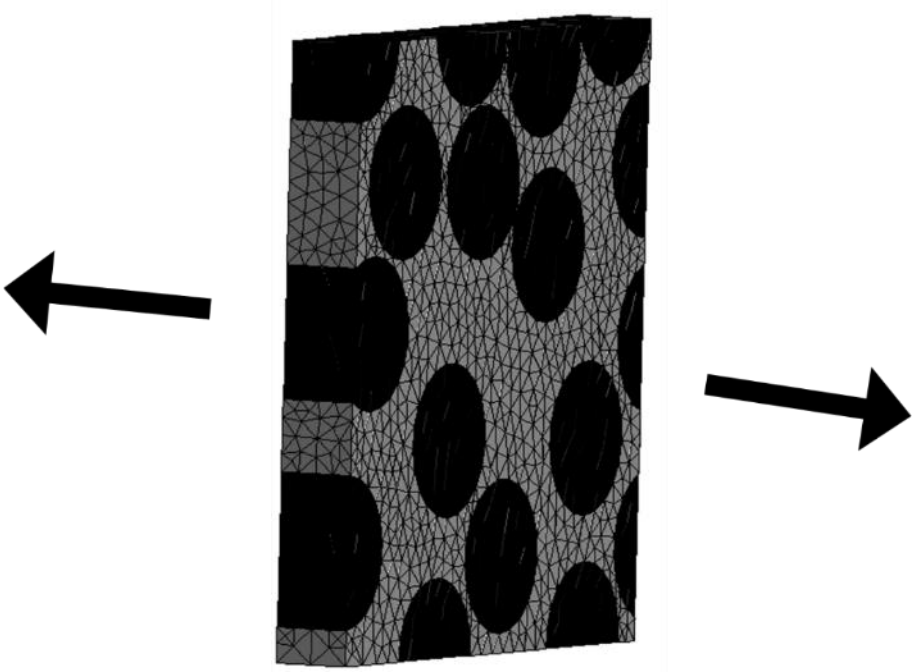

Figure 3.31: Virtual 3D microstructure under tensile stress in the parallel direction to the fibre

Since the experimental results were available for the tensile tests in the fibre direction, the simulation results could be compared with the experimental stress-strain curves and the comparison is shown in Figure 3.32. As far as the stiffness of different combinations is concerned, the simulation results are in good agreement with the experimental results except in the case of XN90 fibres. The average Young's modulus from the experiments is 275 GPa in comparison to the value of 430 GPa estimated by the simulation. It should be noted that the influence of the pores over the elastic modulus of the matrix is already taken into consideration which implies that some other phenomenon is responsible for this low stiffness of the composite. This reduced stiffness in the CMC with XN90 fibres might be attributed to the fact that the presence of residual stresses after cooling down during the heat treatment step of the manufacturing process is not considered in the model. Similar observation was made by Galizia et.al where the thermo-mechanical properties of a CMC with stiff pitch-derived carbon fibres (XN80) embedded in an ultra-high temperature ceramic matrix (ZrB_2-SiC) were investigated [90]. Due to the presence of residual stresses after manufacturing, the stiff fibres are under compression and the matrix is under tension. When an external tensile load is applied, the fibres follow the extension releasing the part of their bound energy and thus not contributing to the initial stiffness of the composite. Furthermore, the stiffer fibres are difficult to handle during processing and fibre damage might occur during the manufacturing of the composites.

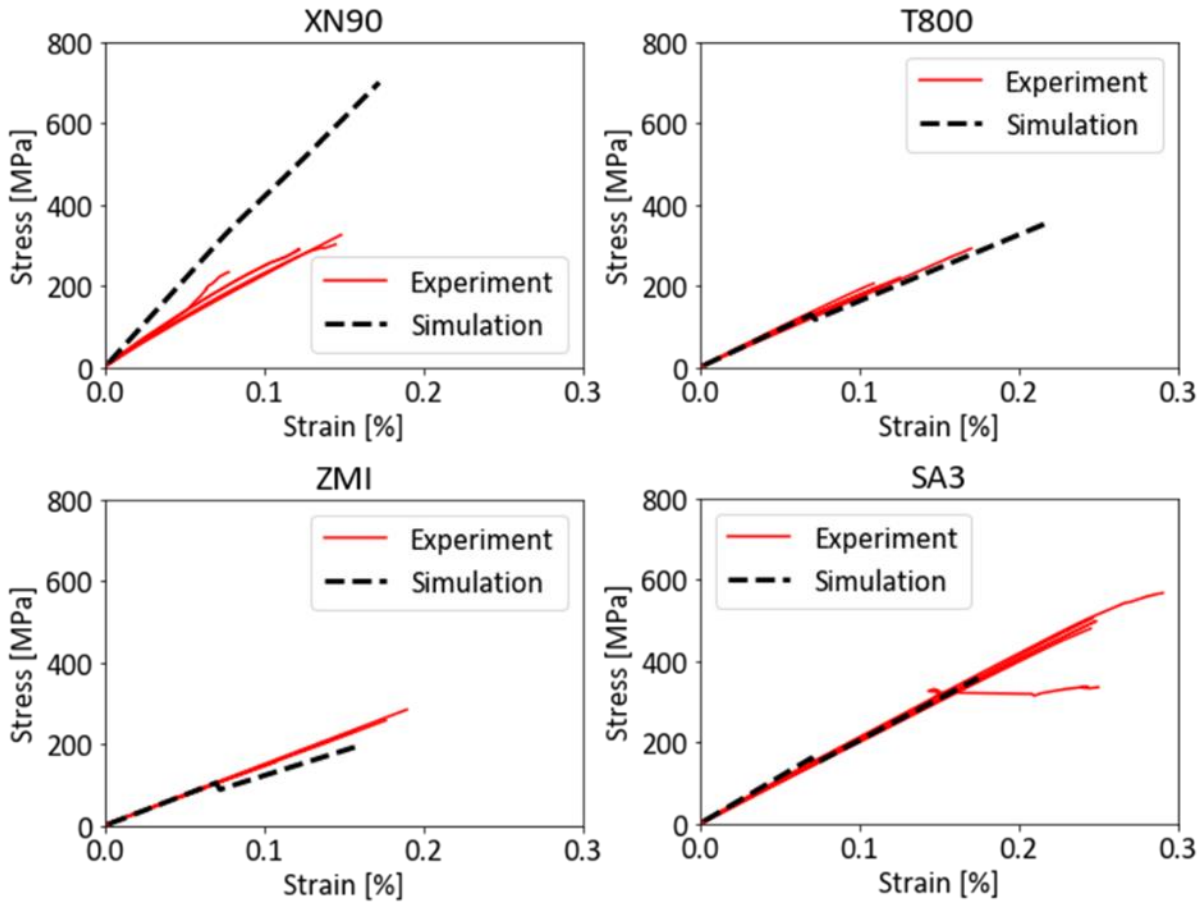

Figure 3.32: Comparison of the stress-strain curves obtained for different fibre types from the tensile tests and the finite element simulations performed in the longitudinal direction of unidirectional composites.

Table 3.7: Comparison between the properties obtained from the experiments (Exp.) and the simulation (Sim.) for the tensile tests performed on different CMC variants in the longitudinal direction.

Properties	**Unit**	**T800**		**XN90**		**SA3**		**ZMI**	
		Exp.	**Sim.**	**Exp.**	**Sim.**	**Exp.**	**Sim.**	**Exp.**	**Sim.**
Young's Modulus	GPa	182 ± 10	185	275 ± 23	430	206 ± 7	230	146 ± 3	150
Strength (σ_{max})	MPa	224 ± 40	357	288 ± 39	700	478 ± 85	357	205 ± 79	196
Proportional Limit Stress (σ_{PL})	MPa	162 ± 67	138	58 ± 11	333	342 ± 120	158	183 ± 77	107
Failure Strain (ε_{max})	%	0.13 ± 0.02	0.22	0.14 ± 0.05	0.17	0.25 ± 0.02	0.18	0.14 ± 0.05	0.16
Proportional Limit Strain (ε_{PL})	%	0.09 ± 0.04	0.08	0.02 ± 0.01	0.08	0.17 ± 0.06	0.08	0.12 ± 0.05	0.09
Damage at failure (D_{max})	-	0.03 ± 0.02	0.12	0.15 ± 0.1	0.08	0.09 ± 0.12	0.11	0.00 ± 0.01	0.18

Apart from the slope of the curves, there were some discrepancies found between the simulation and experimental results, as far as the failure stress and strain of different variants are concerned. In the case of XN90 fibres, the predicted value of the failure strain was in good agreement with the test results but due to overestimation of the stiffness, the predicted strength is also very high. In the variant with T800 fibres, the strength and failure strain both were overestimated. A plausible explanation is the strong bonding between the fibres and the matrix due to rough surface observed in T800 fibre, as shown in Figure 3.33. Due to this strong interface, the stress-strain curve obtained from the tests behaves almost linearly till the sample failed. The damage at failure (D_{max}) i.e., loss of stiffness during loading was found out to be 0.03 (shown in Table 3.7) in comparison to 0.12 predicted by the simulation, which implies that the slope of the curve didn't change much throughout the course of loading. For the same reason, the D_{max} in the case of ZMI fibres is close to zero in the experiments. The simulation is not able to model this effect, as the initiation of the matrix crack always show loss of stiffness at proportional limit stress/strain which leads to development of damage in the virtual models. It should be mentioned at this point that evaluation of damage is not always straightforward from experimental stress-strain curves because of strong non-linear behaviour of the samples just before the fracture. This is the reason behind the high values of standard deviation among the values. The evaluation of proportional limit strain and stress also pose a challenge and depends strongly on the elastic region defined for the determination of the elastic modulus. In the work of Mainzer [69], the source of experimental results , the region between 10 MPa and 30 MPa was taken as the elastic region.

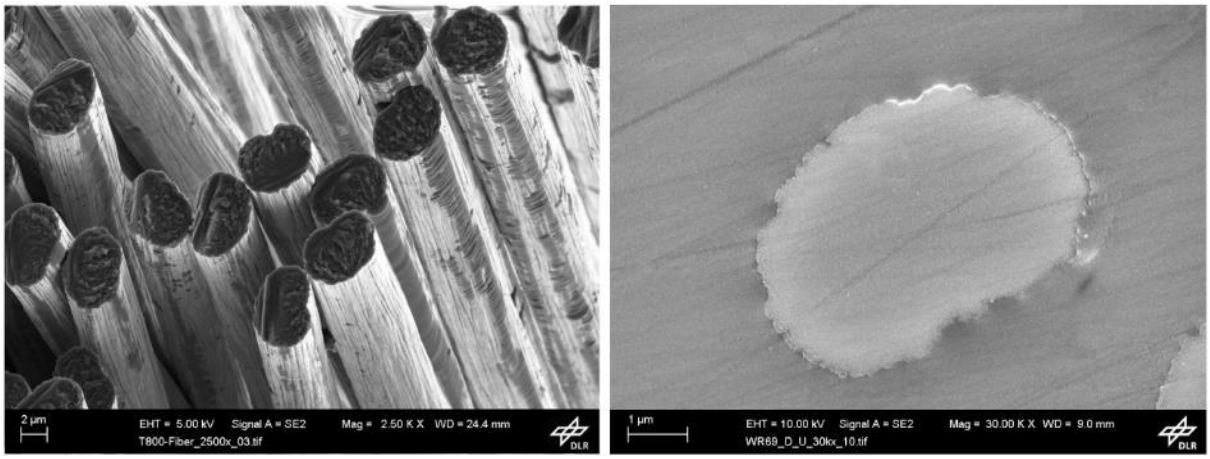

Figure 3.33: SEM images of oval shaped T800 fibres with gully structured rough surface [91].

A good agreement was found with the experimental results, considering the standard deviation among the experimental results and a purely mechanical model which did not include thermal and chemical effects occurring during the manufacturing. Analogous to the previous section, the finite element model was used to perform a parameter study in order the analyse the effects of the constituent properties over

the mechanical properties of the resulting composite. The input variables used to generate the simulation data for the parameter study are summarized in Table 3.8.

Table 3.8: Input variables used in the parameter study of virtual tensile testing in the longitudinal direction for unidirectional composites.

Properties	**Symbol**	**Unit**	**Value**
Fibre			
Diameter	d	µm	10
Fibre Volume Fraction	V_f	%	35,45,55
Young's Modulus (longitudinal)	E_{f1}	GPa	300,600,900
Young's Modulus (transverse)	$E_{f2} = E_{f3}$	GPa	20
Poisson's Ratio	$\nu_{12} = \nu_{13} = \nu_{23}$	-	0.1
Shear Modulus	$G_{f12} = G_{f13} = G_{f23}$	GPa	25,50,75
Strength	σ_{f1-max}	MPa	2000,3000,4000
Matrix			
Young's Modulus	E_m	GPa	100,200,300
Poisson's Ratio	ν	-	0.1
Strength	σ_{m-max}	MPa	25,50,75
Interface			
Strength	σ_{i-max}	MPa	25,50,75

Correlation heatmap:

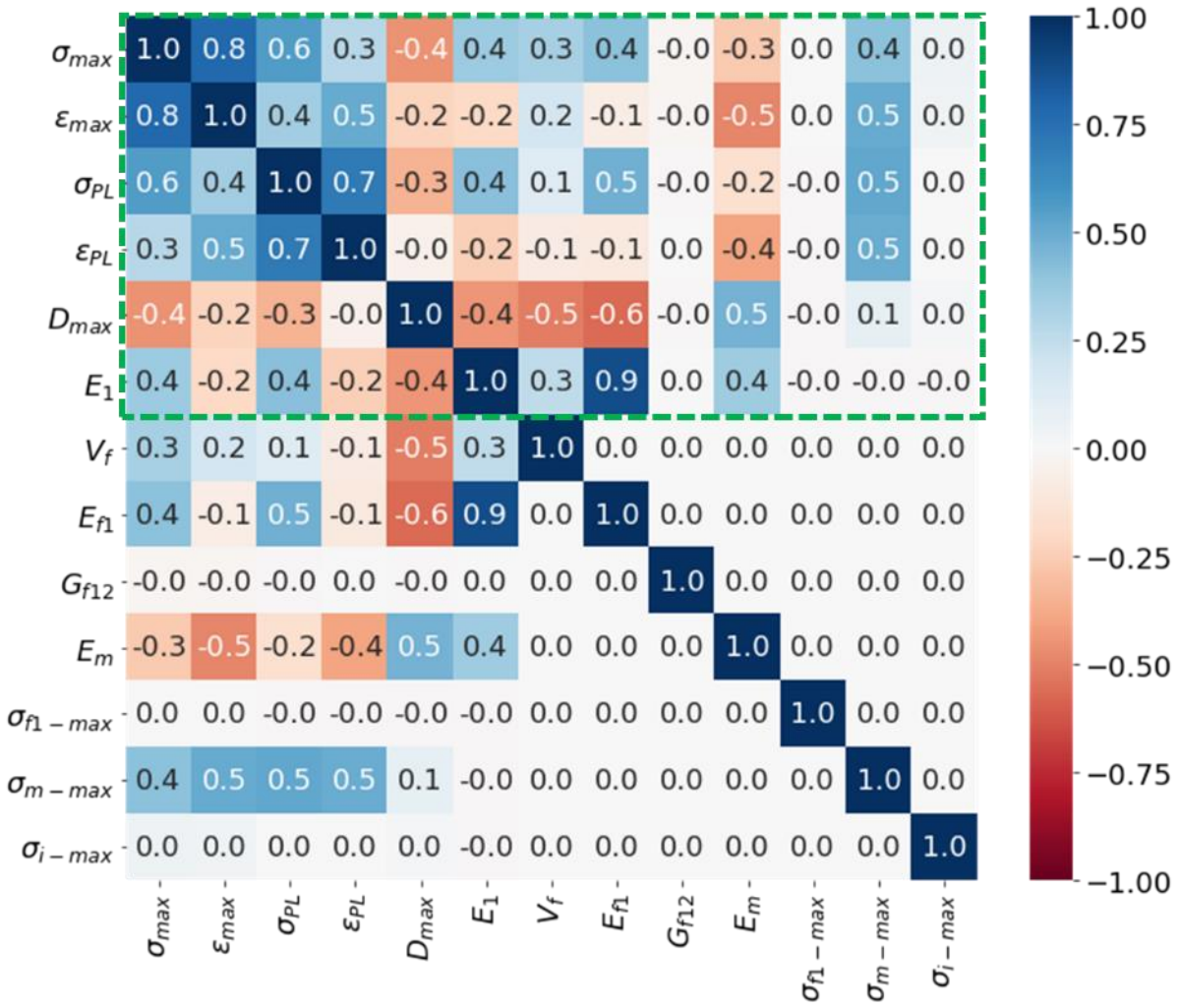

Figure 3.34: Pearson correlation heatmap for virtual tensile tests in the longitudinal direction of 3D unidirectional virtual composites with the target variables marked with green lines.

Pearson coefficient correlation analysis was performed for the case of virtual tensile test in the longitudinal direction as well. The input variables have changed in comparison to the previous section. The target variables are however the same: σ_{max}, ε_{max}, D_{max}, σ_{PL} and ε_{PL}. Some observations which could be made from the correlation map are:

- The stiffness of the composite shows high correlation with the Young's modulus of the fibre, as the tensile load is applied in the longitudinal or fibre-dominant direction
- σ_{max} and ε_{max} depend on the matrix strength rather than the fibre strength. A plausible explanation is that the composite fails after the cracks propagate all over the matrix. The fibres do not carry the load beyond this stress/strain (matrix failure) as the interface elements also fail

in the strong interface combinations and thus, do not contribute to the load carrying capacity after this point.

- The failure strain (ε_{max}) was expected to be dependent on the strength of the fibre/matrix interface but no correlation was observed in the heatmap. A reason might be that the fibre sliding which provides the damage tolerant behaviour to a fibre-reinforced composite is not considered in the current finite element model.
- D_{max} showed inverse dependence on the Young's modulus of the fibre and the fibre volume content. The reason is that both these properties are directly related to the elastic modulus of the composite and as the stiffness of the composite increases, the stresses are higher for the same value of strain (according to Hooke's law) and the sample fails with a lower damage value.
- ε_{max} is inversely proportional to the elastic modulus of the matrix for the same abovementioned reason. When the matrix is stiffer and if the matrix strength remains constant, the sample will fail at a lower strain value because the strain will be lower for the same value of stress at failure.

Machine Learning Prediction:

The ML algorithms discussed in the previous sections were used for the prediction of the target variables in the longitudinal direction as well. Similar to the transverse direction, the stiffness could be predicted with high accuracy by the ML algorithms (Figure 3.35). The decision tree and the random forest performed better than the linear and k nearest-neighbours algorithms. Even if there is a linear relationship between the properties like the fibre volume fraction and the elastic modulus of the constituents, other parameters create noise in the dataset and decrease the accuracy of the linear ML algorithms.

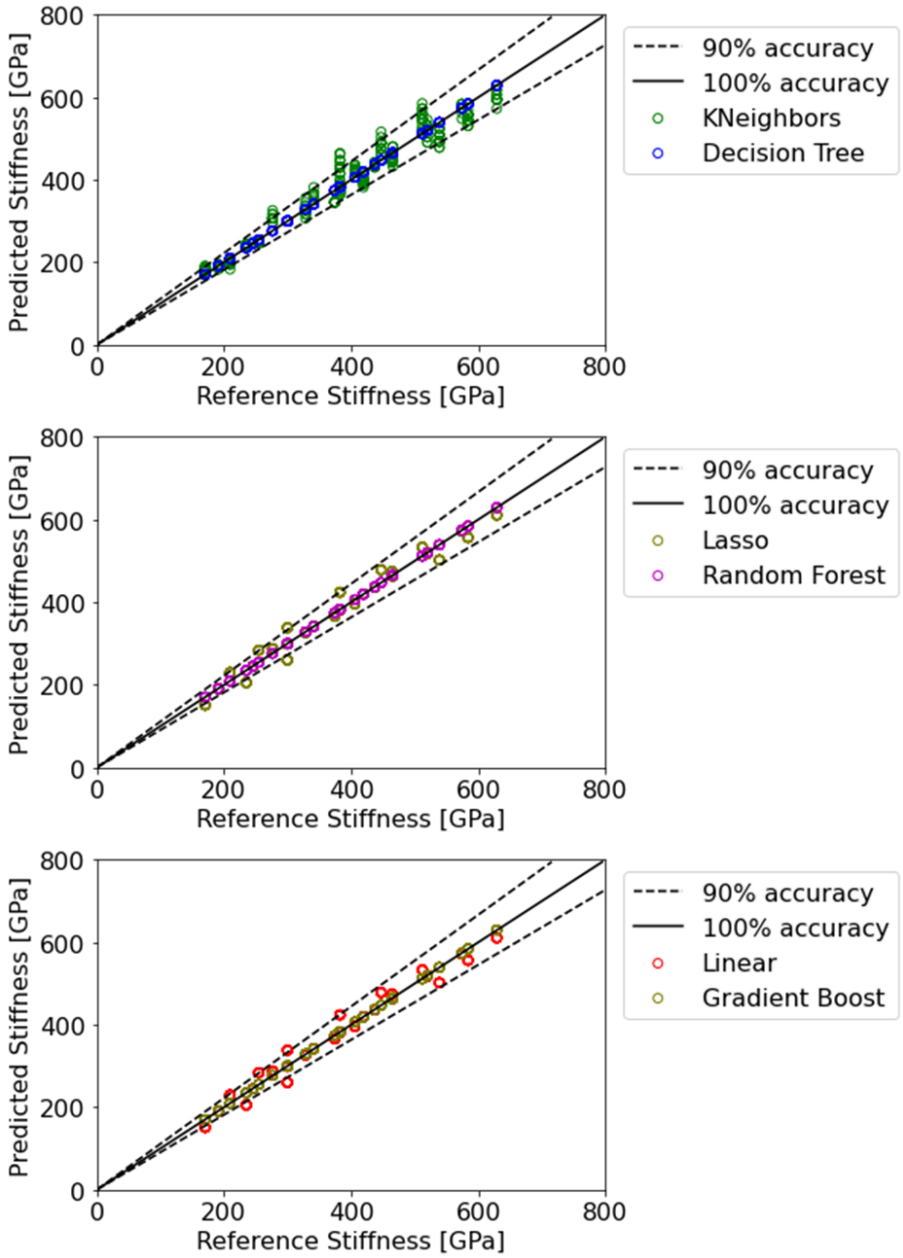

Figure 3.35: Comparison of the accuracies of the machine learning models in prediction of the longitudinal stiffness in 3D unidirectional virtual composites.

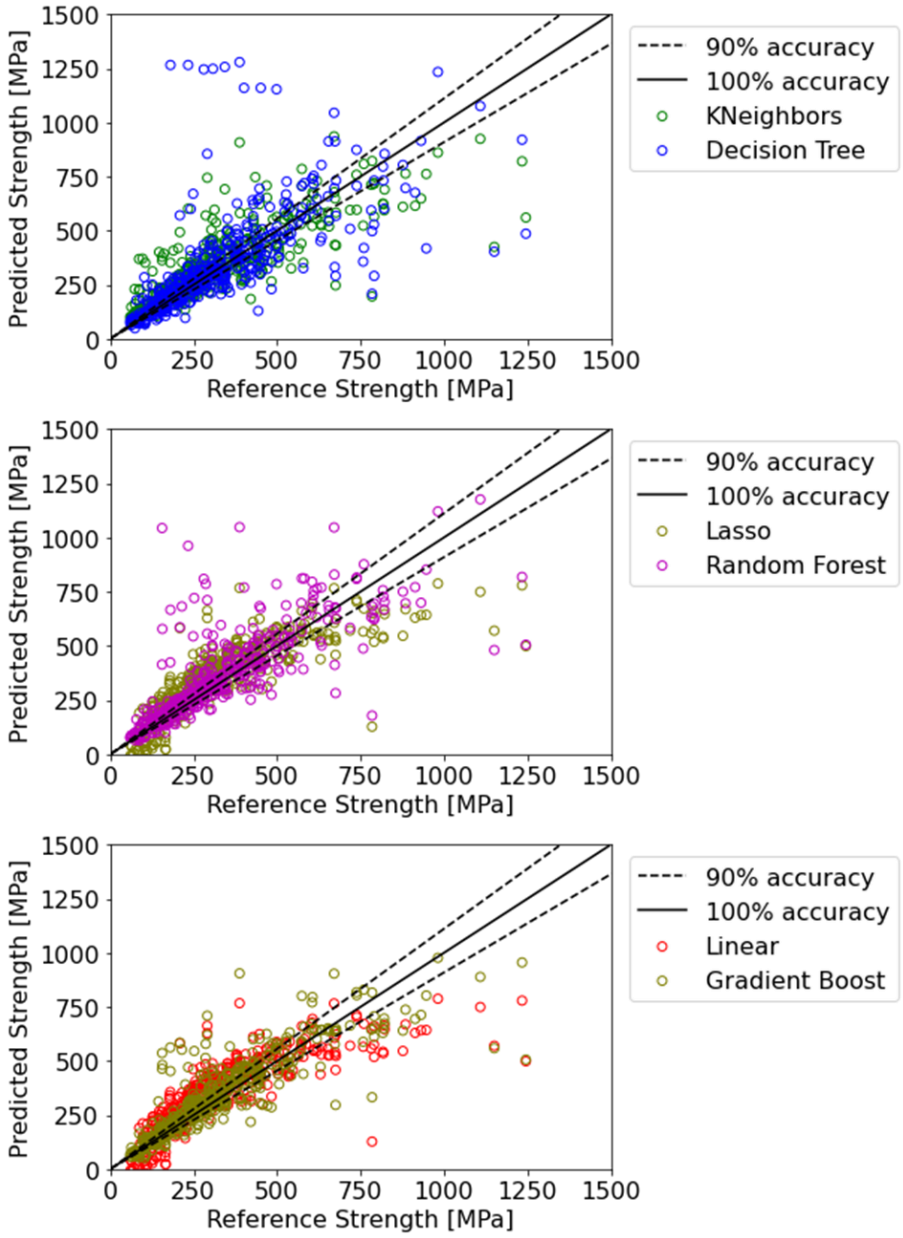

Figure 3.36: Comparison of the accuracies of the machine learning models in prediction of the longitudinal strength in 3D unidirectional virtual composites.

The longitudinal strength on the other hand, could not be predicted with higher accuracy by any ML algorithm. The reason behind this observation is that the failure strength is dependent on all the input variables with very close importance or weightage values (shown in Figure 3.43). This increases the interdependency of the features in the dataset and requires combination of ML algorithms or application of more advance ML algorithms like neural networks. In order to limit the scope of the work, these algorithms were not implemented to demonstrate the improvement in the accuracy of the prediction. Similar trend was noticed in the case of failure strain as well where the accuracy of the ML models was low.

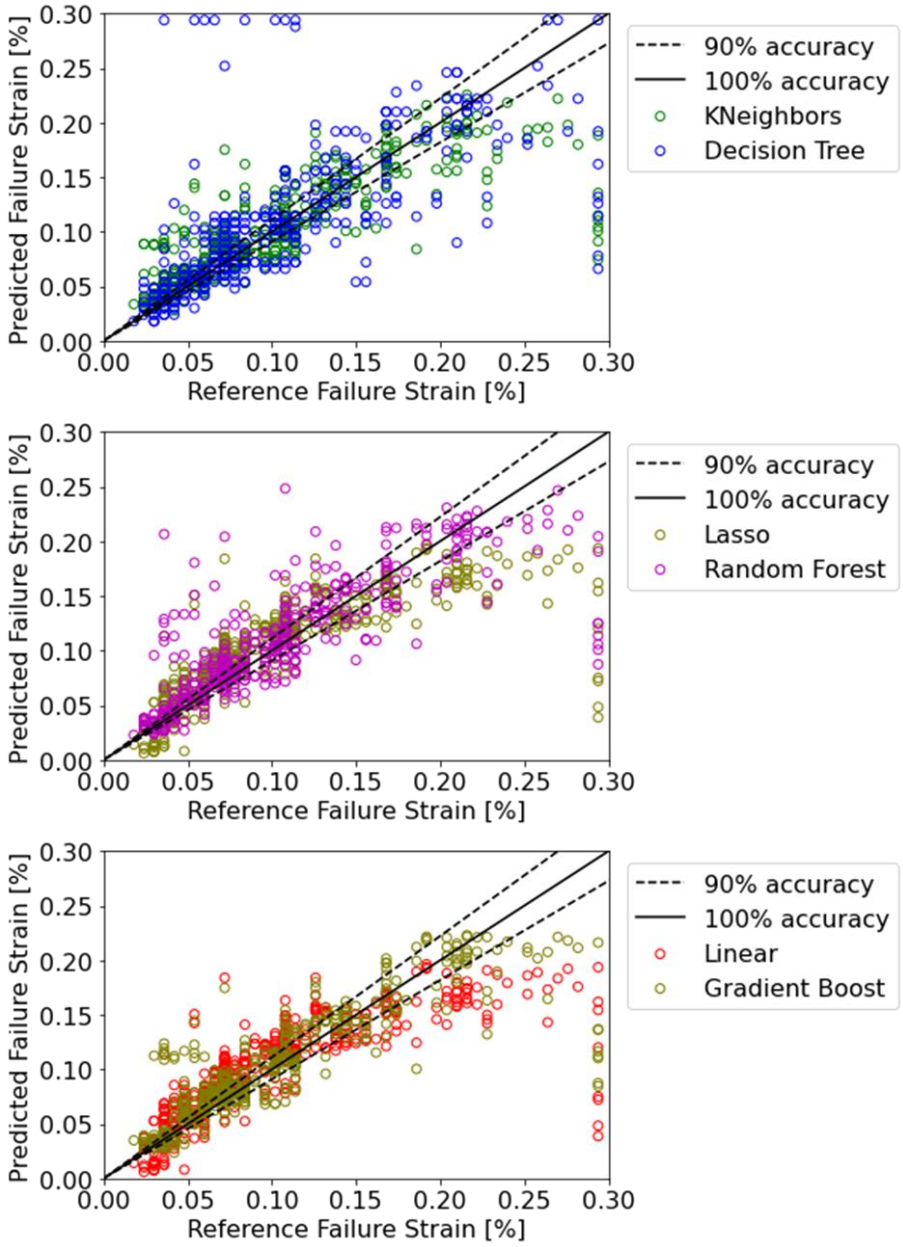

Figure 3.37: Comparison of the accuracies of the machine learning models in prediction of the longitudinal failure strain in 3D unidirectional virtual composites.

Contrarily, the proportional limit stress and strain could be predicted with higher accuracy with the non-linear ML algorithms as shown in Figure 3.38 and Figure 3.39. The higher accuracy can be explained by the help of feature importance shown in Figure 3.43. Both proportional limit stress and strain depend only on four input variables which makes it easier for the algorithms to establish the relationship between the input and target variables. This implies that the feature extraction or engineering is a useful method in understanding the predictions made by the ML algorithms.

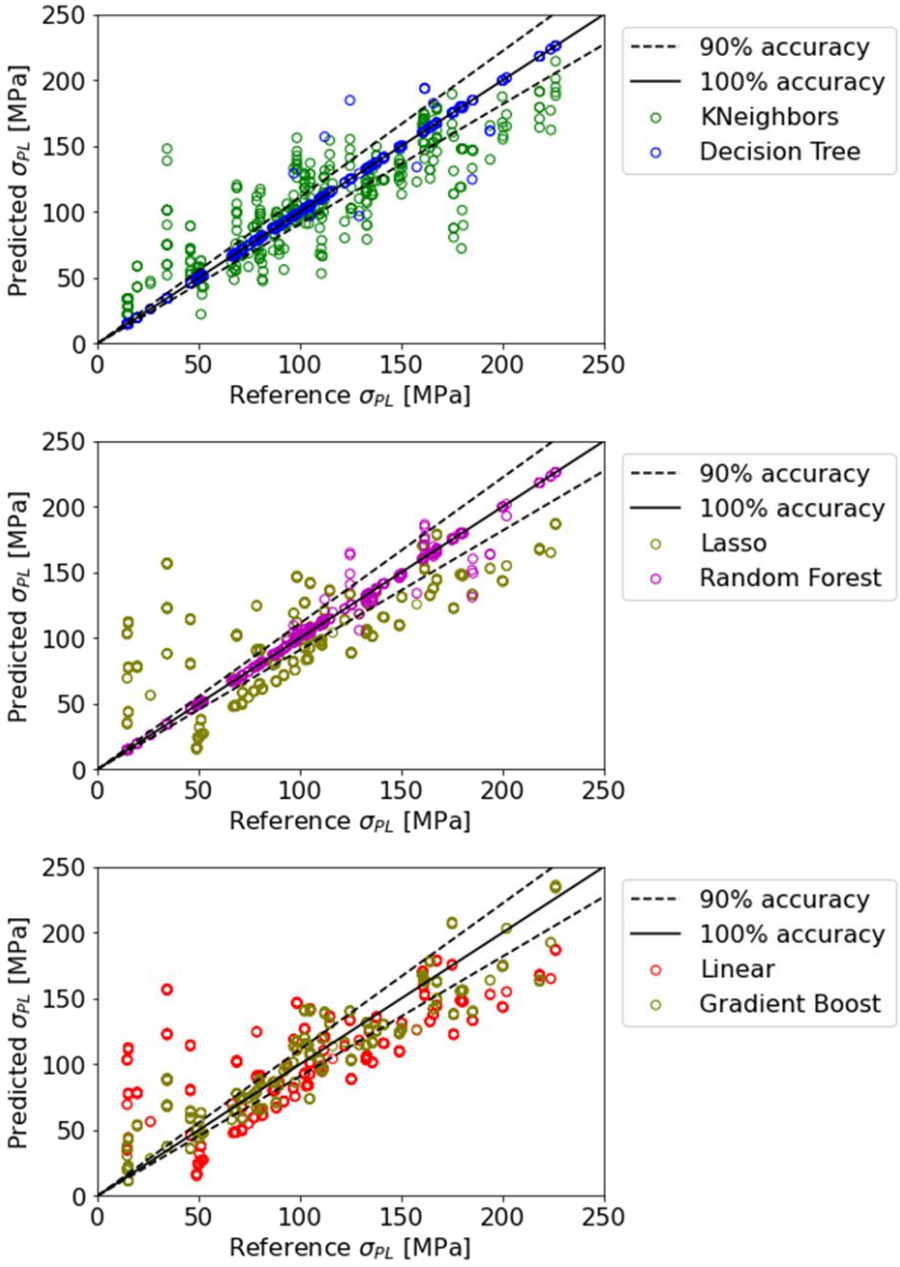

Figure 3.38: Comparison of the accuracies of the machine learning models in prediction of the longitudinal proportional limit stress in 3D unidirectional virtual composites.

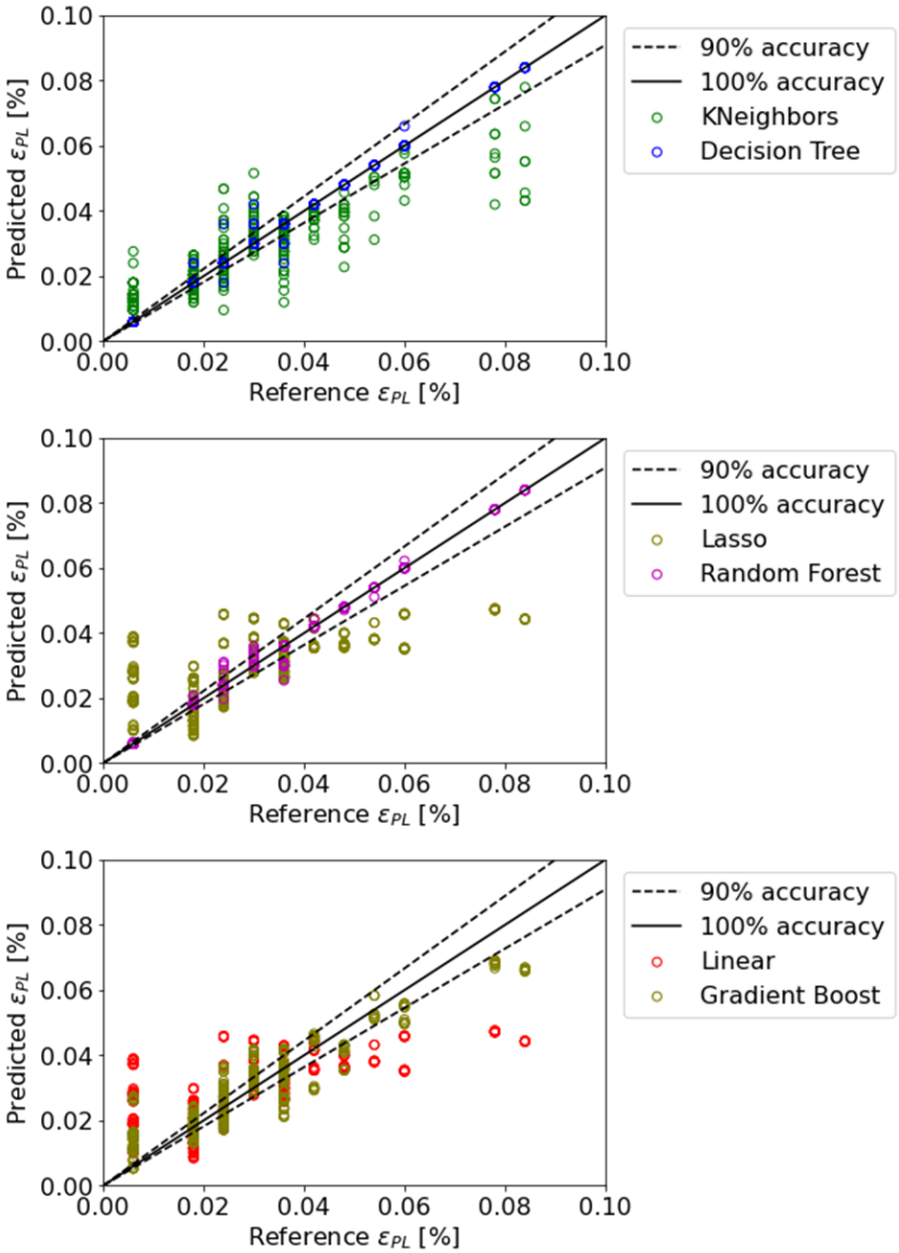

Figure 3.39: Comparison of the accuracies of the machine learning models in prediction of the longitudinal proportional limit strain in 3D unidirectional virtual composites.

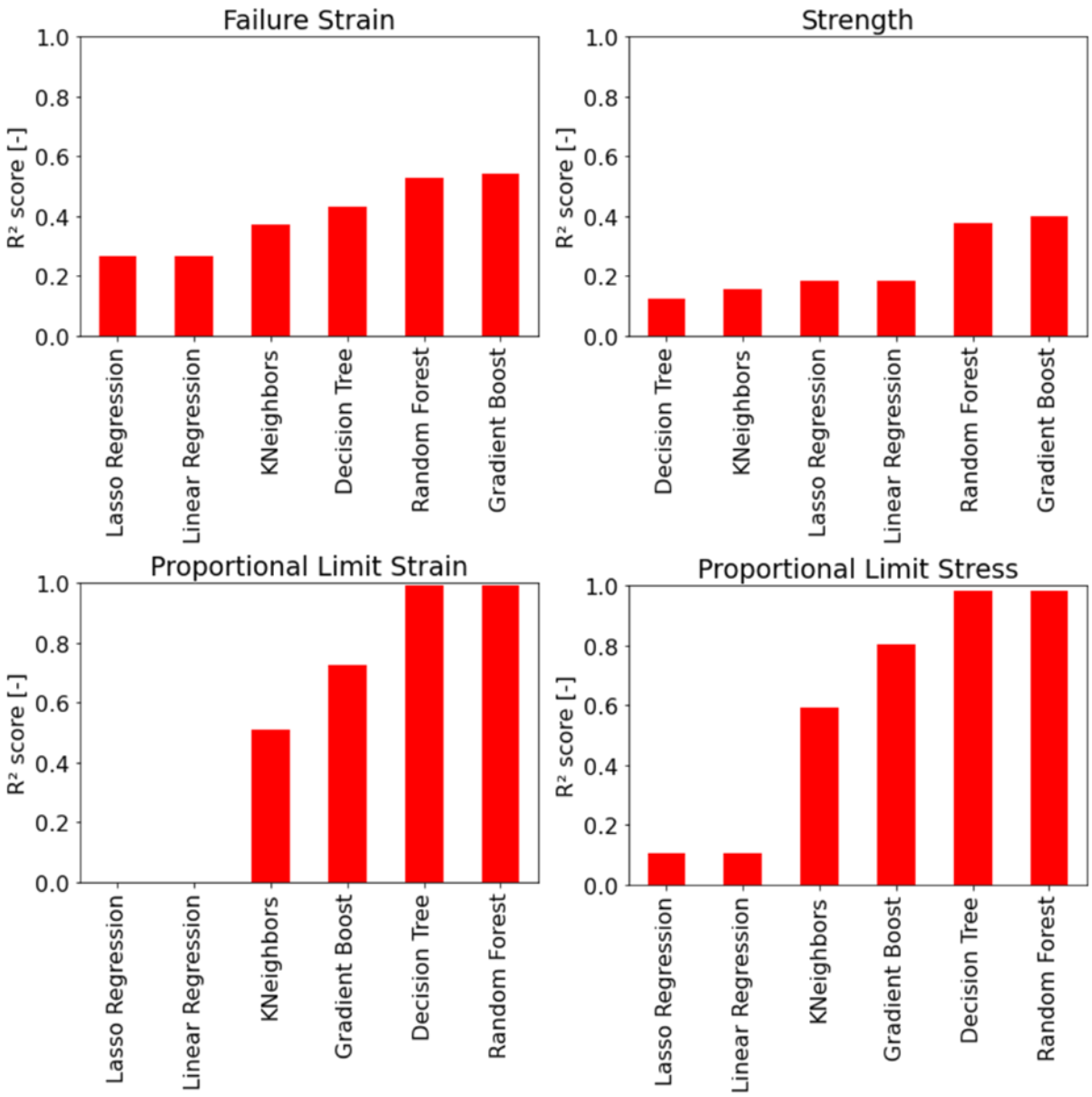

Figure 3.40: R^2 score of the machine learning models in the prediction of failure strain, failure strength, proportional limit stress and proportional limit strain in the longitudinal direction in 3D unidirectional virtual composites.

An overview of the accuracy of the ML models can also be given with the help of Figure 3.40 and Figure 3.41, where the R^2 score and the prediction error of the models are presented respectively. It can be noticed that the accuracy of the models is low in the prediction of strength and failure strain. However, the accuracy of the non-linear algorithms increases in the case of proportional limit stress and strain. It was observed that the prediction of the linear and the lasso regression was zero in the prediction of proportional limit strain. When the prediction is worse than the prediction made by a single horizontal line, the value of R^2 score becomes negative, which is mathematically impossible. This occurs when either the intercept or the slope in a linear regression is constrained in the algorithm. This means that a

particular model is a poor fit to the data and is not optimal for the prediction of that particular target variable. This conclusion could be validated with the fact that the error in the prediction of proportional limit strain is maximum in the case of linear and lasso regression, as shown in Figure 3.41.

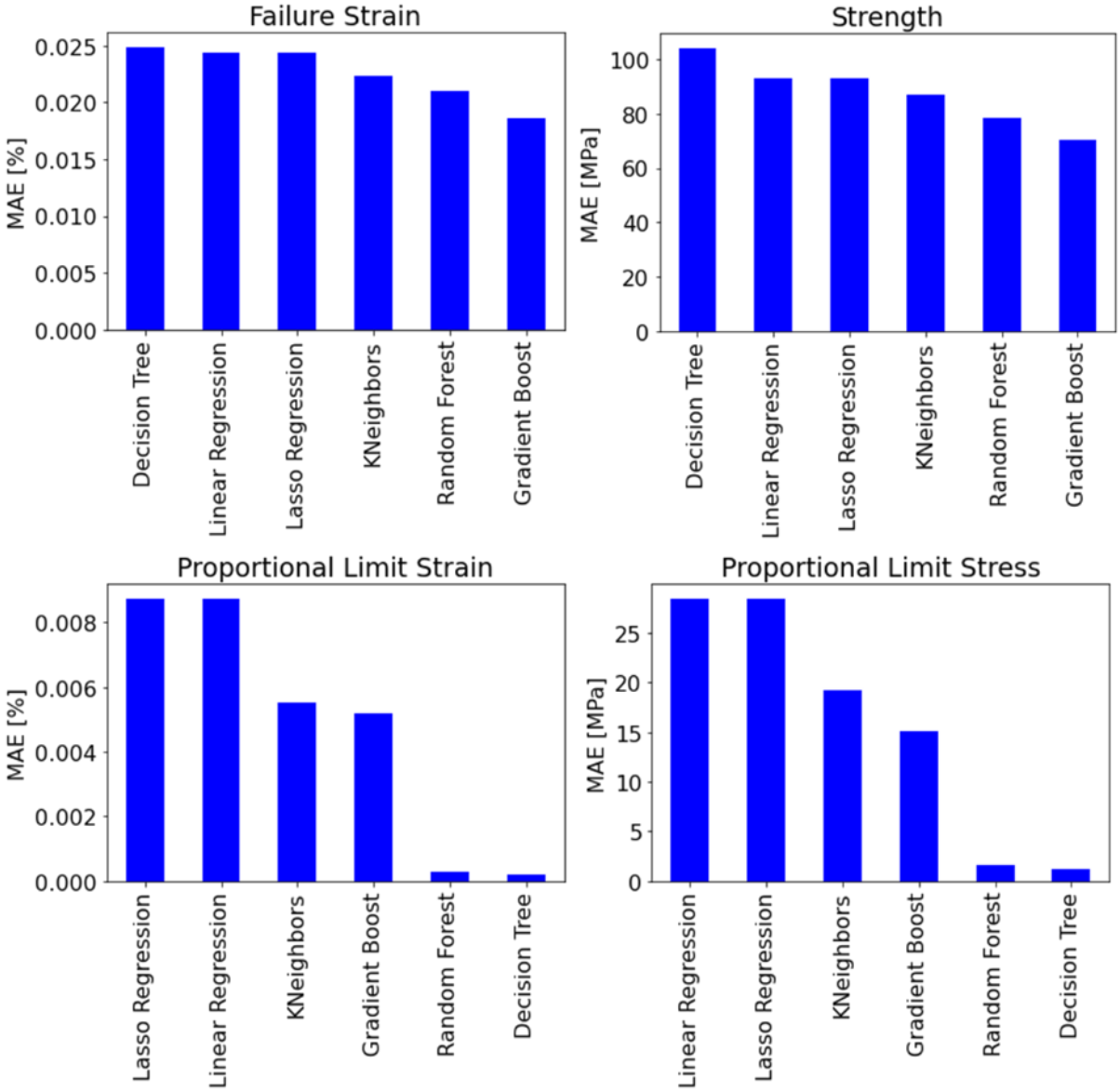

Figure 3.41: The mean absolute error (MAE) in prediction of the values of failure strain, failure strength, proportional limit stress and proportional limit strain by machine learning algorithms in the longitudinal direction in 3D unidirectional virtual composites.

The algorithms which were trained on the data obtained from the parameter study were used to predict the data for the four variants which were tested, and the results are discussed in the upcoming section. The abbreviations used for the algorithms in the tables between Table 3.9 and Table 3.12 are:

- LR: Linear Regression
- LaR: Lasso Regression
- KN: K Nearest Neighbours Regression

- DT: Decision Tree Regression
- RF: Random Forest Regression

It should be mentioned at this point that the input data in the case of tested variants sometimes lied outside the range of input parameters used in the parameter study. This means that in some cases, the ML algorithms had to extrapolate the results, and this gave the opportunity to test the algorithms in their extrapolation capabilities. Moreover, non-linear algorithms like decision tree, gradient boosted decision tress and random forest might perform poorly when the models are not trained with the exact same input variable values as the ones used for the prediction. For example, in the case of the prediction of the Young's modulus of the composite in the longitudinal direction, the non-linear algorithms performed well exhibiting the accuracy of approximately hundred percent. The reason is that the values of the test data were exactly the same as used in the input training variables (one value among 300 GPa, 600 GPa and 900 GPa in the case of fibre stiffness). There were no values in between, such as 380 GPa (SA3 fibre) or 860 GPa (XN90 fibre). The non-linear algorithms (DT,RF and GB) take the average value of all the observations made in a single decision box or leaf after satisfying a particular split criterion [92]. This can lead to an overestimation or underestimation based on the difference between the split criterion and the target variable to be predicted.

The values outside the training data range might also lead to poor performance of the algorithms due to the aforementioned issue of extrapolation. In the case of extrapolation, the non-linear algorithms will highly underestimate or overestimate the target variable depending on the difference between the input training variable and the input variable used for the prediction [92]. For example, the non-linear algorithms will treat fibre stiffness of 920 GPa and 1100 GPa as the same value as both are outside the range of the training dataset i.e., 900 GPa.

Table 3.9. Comparison between the values obtained from the experiments (tensile tests), simulation and machine learning algorithms for the composites with T800 fibres in longitudinal direction in 3D unidirectional virtual composites.

Properties	**Unit**	**Experiment**	**Simulation**	**Machine Learning**					
				LR	**LaR**	**KN**	**DT**	**RF**	**GB**
Young's Modulus	GPa	182 ± 10	185	179	178	187	191	191	191
Strength (σ_{max})	MPa	224 ± 40	357	414	415	355	507	476	450
Proportional Limit Stress (σ_{PL})	MPa	162 ± 67	138	110	110	99	46	46	66
Failure Strain (ε_{max})	%	0.13 ± 0.02	0.22	0.18	0.18	0.21	0.29	0.27	0.24
Proportional Limit Strain (ε_{PL})	%	0.09 ± 0.04	0.08	0.04	0.05	0.05	0.02	0.02	0.04
Damage at failure (D_{max})	-	0.03 ± 0.02	0.12	0.12	0.12	0.10	0.10	0.10	0.09

Table 3.10: Comparison between the values obtained from the experiments (tensile tests), simulation and machine learning algorithms for the composites with XN90 fibres in longitudinal direction in 3D unidirectional virtual composites.

Properties	Unit	Experiment	Simulation	Machine Learning					
				LR	LaR	KN	DT	RF	GB
Young's Modulus	GPa	275 ± 23	430	439	438	464	467	465	465
Strength (σ_{max})	MPa	288 ± 39	700	618	618	797	944	872	826
Proportional Limit Stress (σ_{PL})	MPa	58 ± 11	333	171	171	178	168	168	162
Failure Strain (ε_{max})	%	0.14 ± 0.05	0.17	0.17	0.16	0.17	0.21	0.19	0.18
Proportional Limit Strain (ε_{PL})	%	0.02 ± 0.01	0.08	0.04	0.04	0.04	0.04	0.04	0.04
Damage at failure (D_{max})	-	0.15 ± 0.1	0.08	0.05	0.05	0.03	0.03	0.03	0.03

Table 3.11: Comparison between the values obtained from the experiments (tensile tests), simulation and machine learning algorithms for the composites with SA3 fibres in longitudinal direction in 3D unidirectional virtual composites.

Properties	Unit	Experiment	Simulation	Machine Learning					
				LR	LaR	KN	DT	RF	GB
Young's Modulus	GPa	206 ± 7	230	231	231	183	191	191	191
Strength (σ_{max})	MPa	478 ± 85	357	439	439	317	365	377	421
Proportional Limit Stress (σ_{PL})	MPa	342 ± 120	158	122	122	73	46	46	64
Failure Strain (ε_{max})	%	0.25 ± 0.02	0.18	0.17	0.17	0.19	0.21	0.22	0.22
Proportional Limit Strain (ε_{PL})	%	0.17 ± 0.06	0.08	0.05	0.04	0.04	0.02	0.02	0.04
Damage at failure (D_{max})	-	0.09 ± 0.12	0.11	0.10	0.10	0.11	0.09	0.09	0.09

Table 3.12: Comparison between the values obtained from the experiments (tensile tests), simulation and machine learning algorithms for the composites with ZMI fibres in longitudinal direction in 3D unidirectional virtual composites.

Properties	Unit	Experiment	Simulation	Machine Learning					
				LR	LaR	KN	DT	RF	GB
Young's Modulus	GPa	146 ± 3	150	158	158	195	191	191	191
Strength (σ_{max})	MPa	205 ± 79	196	425	425	342	485	445	434
Proportional Limit Stress (σ_{PL})	MPa	183 ± 77	107	104	104	105	46	46	64
Failure Strain (ε_{max})	%	0.14 ± 0.05	0.16	0.19	0.19	0.19	0.28	0.26	0.22
Proportional Limit Strain (ε_{PL})	%	0.12 ± 0.05	0.09	0.06	0.05	0.05	0.02	0.02	0.04
Damage at failure (D_{max})	-	0.00 ± 0.01	0.18	0.11	0.11	0.08	0.10	0.10	0.09

Contrarily, the linear algorithms, despite their lower accuracy compared to non-linear algorithms, perform well in both interpolation and extrapolation. This argument could be validated based on the information presented in the tables between Table 3.9 and Table 3.12. For example, the accuracy of the prediction of the Young's modulus was high and in all the fibre variants, the results obtained were closest to the simulation results (training dataset) in comparison with other algorithms. Even in the case of target variables where the accuracy of the linear models was very low (lower than acceptable value 60%), the performance was better than the more accurate non-linear algorithms.

Based on this comparison, following recommendations can be considered as lessons learned from this investigation:

- The non-linear algorithms might be more accurate, but their use is constrained based on the range of the training dataset. In solving a regression problem, as in the current work, these algorithms behave poorly while interpolating or extrapolating the data. One solution is to generate a larger dataset, for example instead of using intervals of 300 GPa in fibre stiffness (range between 300 GPa and 900 GPa), smaller intervals of 10 or 50 GPa should be used. This will increase the number of simulations to be run in order to generate the dataset but will ensure the higher accuracy of the non-linear models.
- The linear algorithms should be preferred over non-linear algorithms despite their lower accuracy as they can deal efficiently with interpolation and extrapolation of the values. As observed in the current investigation, even with a smaller dataset their performance in predicting the values outside the training data range is better than non-linear algorithms.
- The linear algorithms can be combined with non-linear algorithms to make use of the capabilities of both. For example, in the work of Zhang et.al the lasso regression was combined with random forest regression to maintain the accuracy of random forest regression while performing extrapolation [93].
- Deep learning models can be used as the neural nets are capable of extrapolating the data [92].

Feature Importance:

As mentioned earlier, feature extraction is an important method in understanding the relationship between the input and the target variables. This analysis was performed for all the target variables involved in the parameter study. In Figure 3.42, the feature importance plot for elastic modulus in the longitudinal direction as the target variable is shown. As expected, elastic modulus of the fibre is the most influential factor followed by the matrix stiffness and the fibre volume content in the composite.

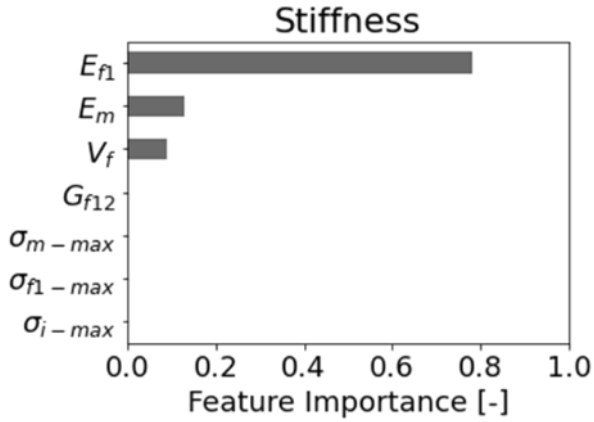

Figure 3.42: Feature importance evaluated with the help of random forest regression for stiffness in the longitudinal direction as the target variable in the case of 3D unidirectional virtual composites.

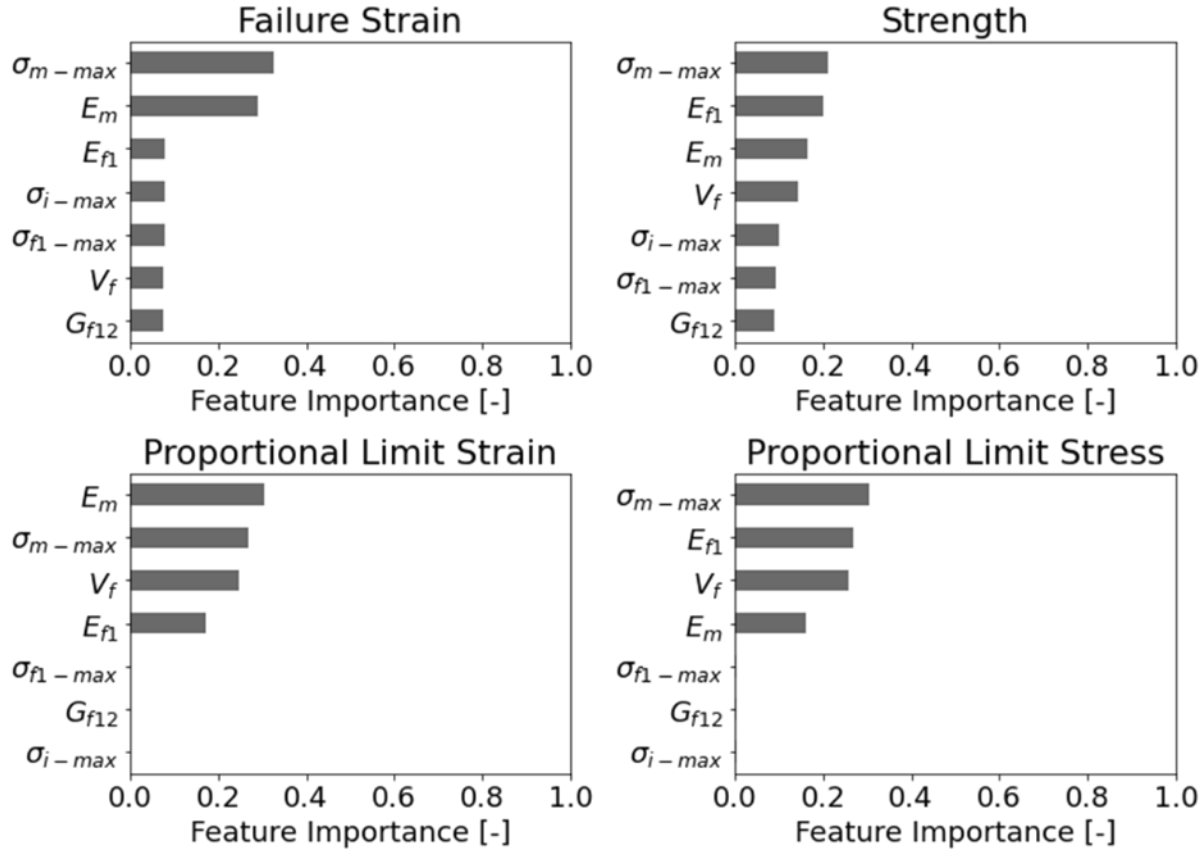

Figure 3.43: Feature importance evaluated with the help of random forest regression for failure strain, failure strength, proportional limit stress and proportional limit strain in the longitudinal direction in 3D unidirectional virtual composites.

The feature importance of the other target variables is shown in Figure 3.43. Starting with the failure strain, the strength and the elastic modulus of the matrix were found out to be the factors with highest feature importance. It was noticed in the correlation map as well where the strength showed a positive and the matrix stiffness exhibited negative correlation with the failure strain. The other input variables

had relatively lesser but an equal impact over the failure strain which adds to the total number of influential parameters involved in its prediction and thus, leading to lower accuracy in the prediction. Similar observation was made in the case of strength as well, where all the input variables had importance factors ranging between 0.1 and 0.2. For this same reason, decision tree and random forest regression algorithm performed badly in the prediction of the longitudinal strength of the material. When it comes to the prediction of proportional limit stress and strain, matrix strength and stiffness, fibre stiffness and fibre volume content were the most influential factors. Since, these target variables were dependent only on the four of the input variables, their prediction could be made with higher accuracy by the non-linear ML models.

Decision tree:

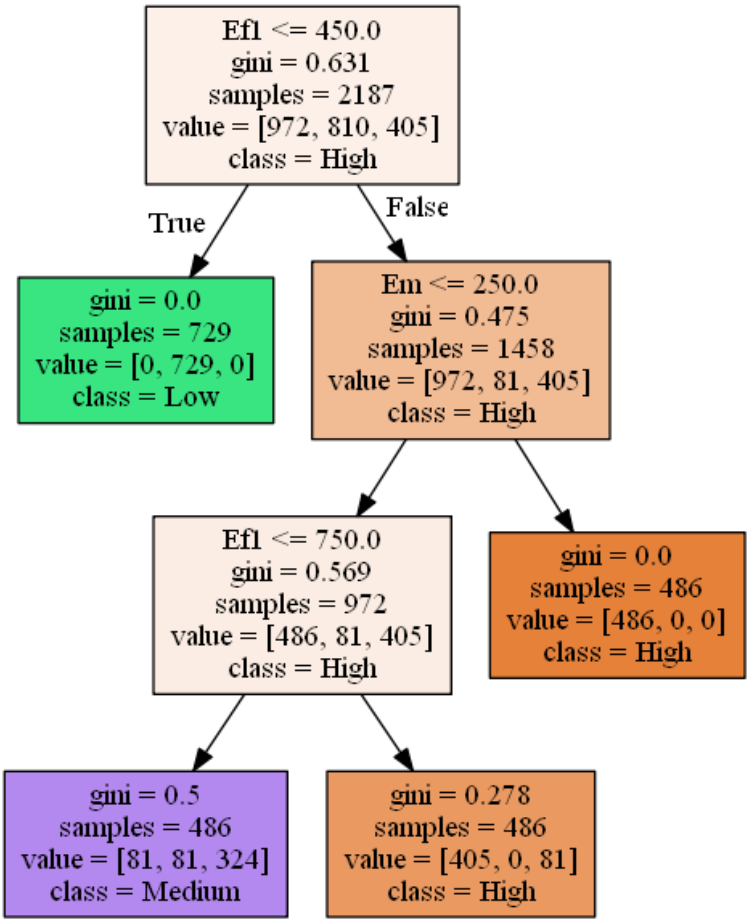

Figure 3.44: The conditions of split for each leaf node based on the importance of the feature to evaluate the respective groups of elastic moduli in the longitudinal direction in 3D unidirectional virtual composites.

As shown in Section 3.5.3, where the results of the virtual test in the transverse direction were discussed, decision trees were introduced as a method along with feature importance to better understand the decision tree regression model. In order to visualize the trees, the values are divided into groups to create a classification problem out of a regression problem. The decision splits for the stiffness prediction are shown in Figure 3.44 and the values were divided into three groups as follows:

1. Low: values lower than 300 GPa
2. Medium: values between 300 GPa and 400 GPa
3. High: values higher than 400 GPa

Again, there was no defined criterion behind the range of the values assigned to each group and the groups were created only for better understanding purposes. For a particular case, the groups can be assigned according to the requirement of an application. The meaning of technical terms and the colour coding is explained in Section 3.5.3 and can be referred if required. It was observed in the feature importance section, that the elastic modulus of the fibre is the most important feature. This observation is evident in the decision tree as well, as the first split criterion is based on the fibre stiffness. Some inferences can be made based on the information contained in the decision tree. For example, the combination of fibre with elastic modulus over 450 GPa and matrix with over 250 GPa will result in a high modulus composite, irrespective of the fibre volume content. Similarly, if the fibre stiffness is lower than 450 GPa, the composite stiffness will fall under low stiffness group.

The decision trees were generated for other target variables as well and the criteria for their group assignments are listed in Table 3.13.

Table 3.13: Range of the values of the target variables in longitudinal direction to create classification groups for decision trees in 3D unidirectional virtual composites

Properties	**Unit**	**Low**	**Medium**	**High**
Young's Modulus (E_1)	GPa	< 300	300 - 400	> 400
Failure Strength (σ_{max})	MPa	< 200	200 - 400	> 400
Proportional Limit Stress (σ_{PL})	MPa	< 80	80 - 150	> 150
Failure Strain (ε_{max})	%	< 0.08	0.08 - 0.11	> 0.11
Proportional Limit Strain (ε_{PL})	%	< 0.02	0.02 - 0.035	> 0.035

It was evident from the feature importance plot that the matrix strength was the most important feature for the prediction of strength and therefore, the first split criterion is the matrix strength (see Figure 3.45). As we go further down the tree, the colour of the decision boxes should get darker (lower gini values), as observed in the case of stiffness (Figure 3.44). The reason is that the strength classification contains more depth as compared to the stiffness classification but for the sake of visualisation only three levels are shown in Figure 3.45. From the three levels, it can be inferred that a variant with matrix strength higher than 37.5 MPa, fibre stiffness higher than 450 GPa and matrix stiffness lower than 150 GPa, will most likely end up in the group with high strength in the longitudinal direction. On the other hand, a variant with matrix strength lower than 37.5 MPa, fibre volume content lower than 50% and matrix stiffness higher than 150 GPa will end up in the group with lower strength.

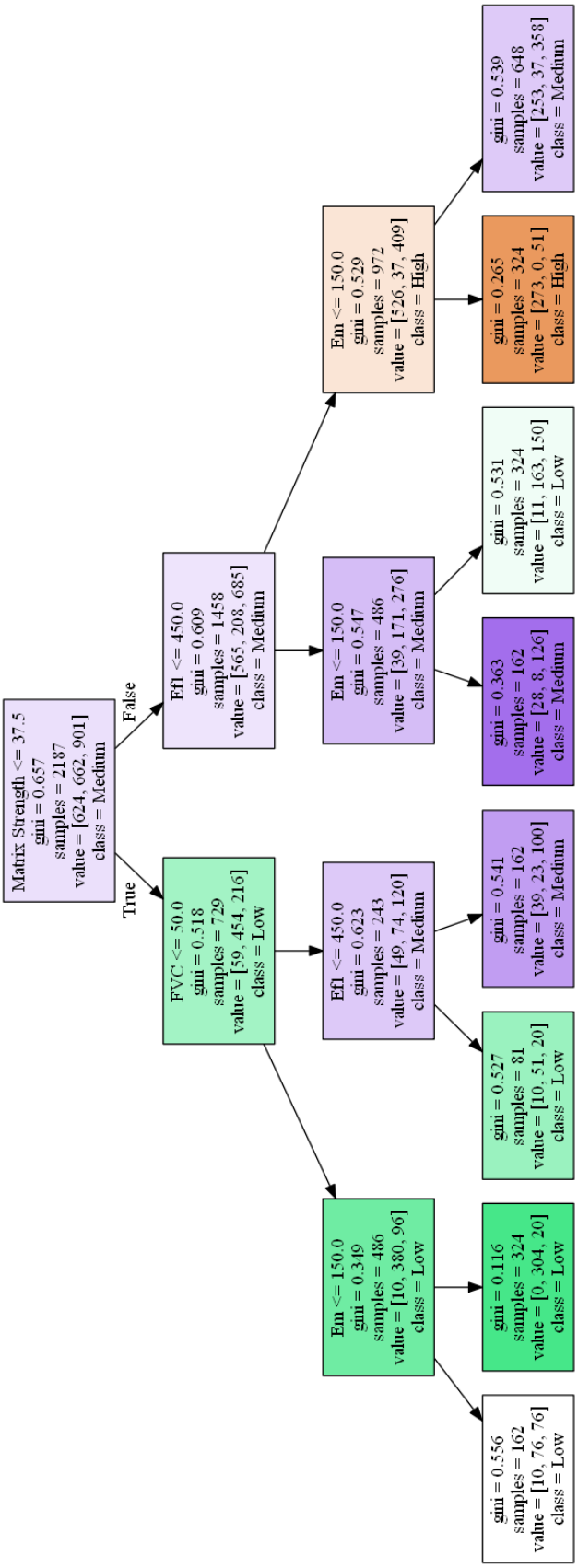

Figure 3.45: The conditions of split for each leaf node based on the importance of the feature to evaluate the respective groups of strengths in the longitudinal direction in 3D unidirectional virtual composites.

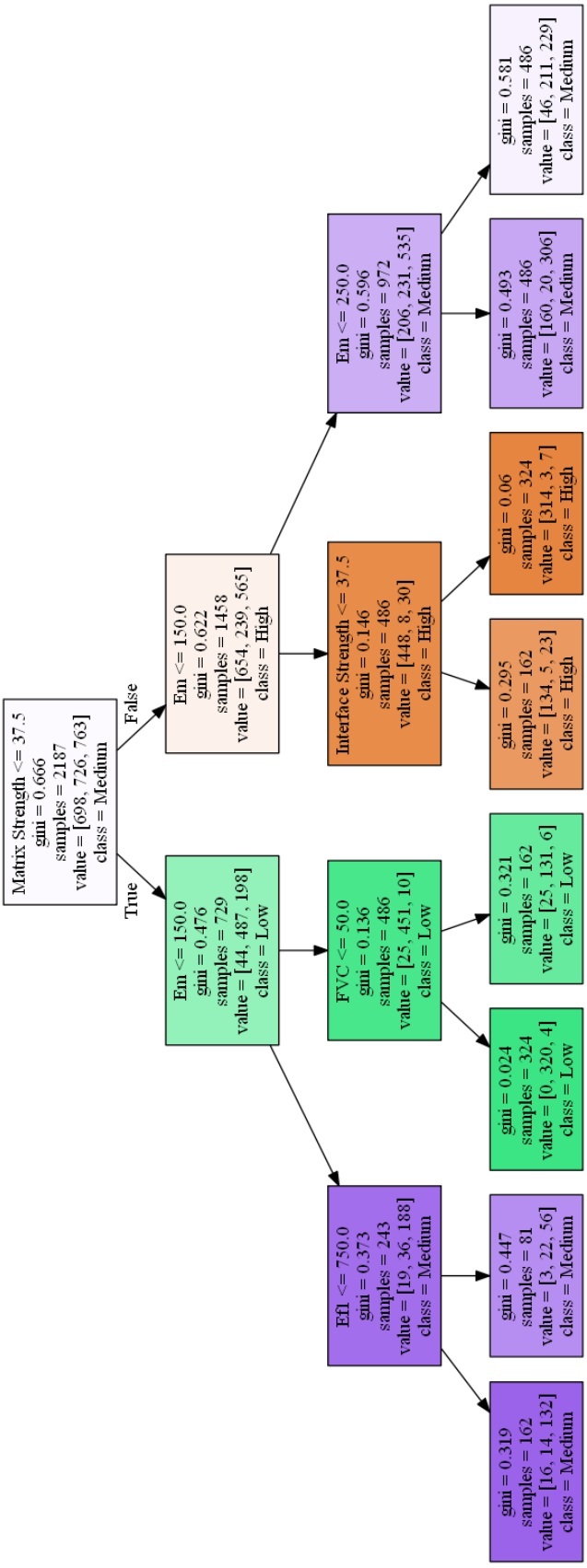

Figure 3.46: The conditions of split for each leaf node based on the importance of the feature to evaluate the respective groups of failure strain in the longitudinal direction in 3D unidirectional virtual composites.

In contrast to the decision tree for strength prediction, the colours of the decision boxes are darker (lower gini values) in the case of failure strain (Figure 3.46) which implies that a smaller number of levels are required to achieve the classification of the variants into different groups. For example, a variant with matrix strength higher than 37.5 MPa and matrix stiffness lower than 150 MPa will most likely fall in group with higher failure strain. On the other side, a variant with matrix strength lower than 37.5 MPa and matrix stiffness higher than 150 GPa will most likely belong the group with low failure strain values.

In the case of proportional limit stress, boxes with rather lower gini values and two with zero value were observed, as shown in Figure 3.47. This implies that the conditions followed to reach these two boxes will surely result in classification to one category. For example, a variant with matrix strength higher than 62.5 MPa, fibre volume content lower than 40% and matrix stiffness lower than 150 GPa will surely fall into high proportional limit stress category. Although, a variant with matrix strength lower than 37.5 MPa and matrix stiffness higher than 250 GPa will fall into the low value category.

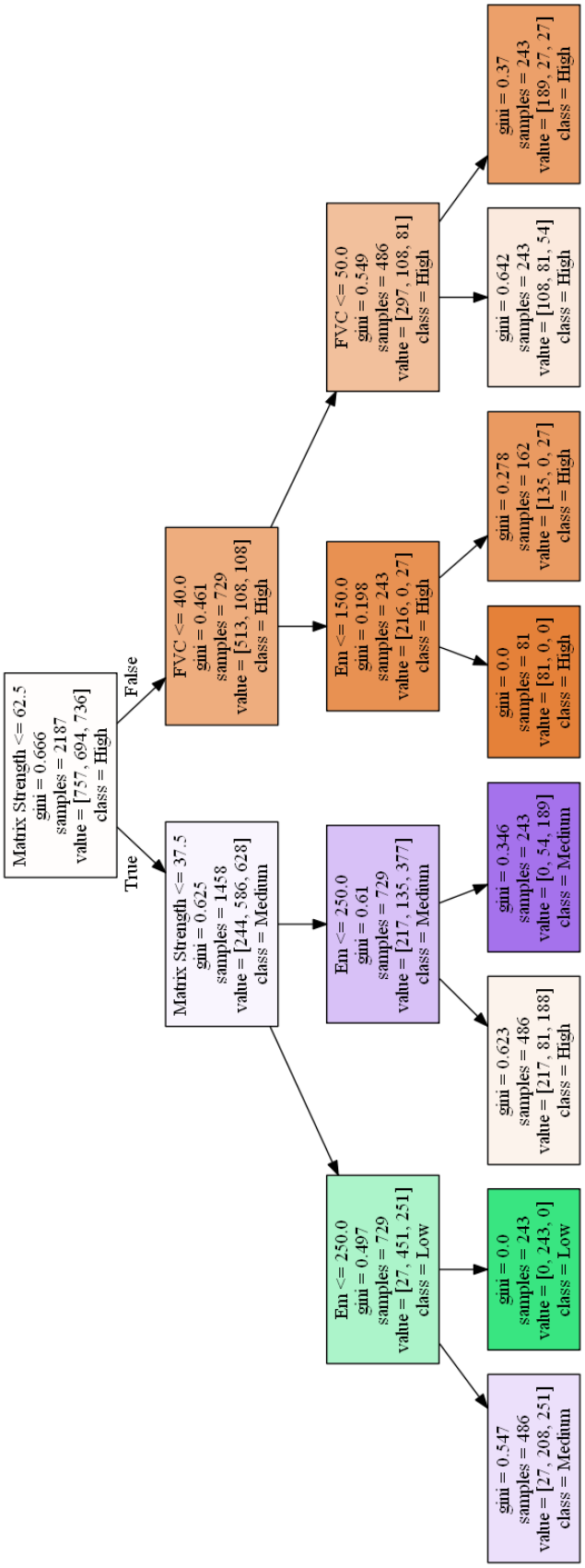

Figure 3.47: The conditions of split for each leaf node based on the importance of the feature to evaluate the respective groups of proportional limit stress in the longitudinal direction in 3D unidirectional virtual composites.

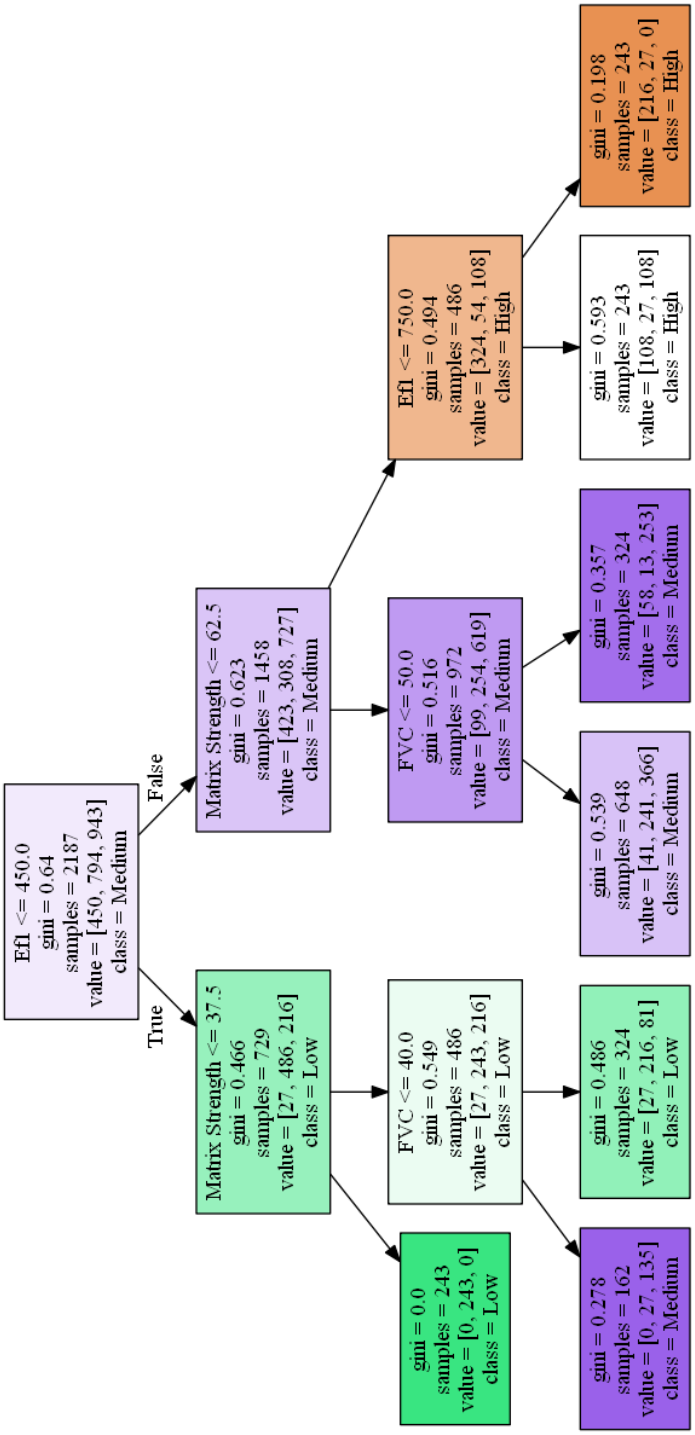

Figure 3.48: The conditions of split for each leaf node based on the importance of the feature to evaluate the respective groups of proportional limit strain in the longitudinal direction in 3D unidirectional virtual composites.

The decision tree for proportional limit strain, in contrast to stress, exhibits only one decision box with gini equal to zero. This was the one of the conditions for a variant, with fibre stiffness lower than 450 GPa and matrix stiffness lower than 37.5 MPa, to land in the low value group. The variant with fibre

stiffness higher than 750 GPa and matrix strength higher than 62.5 MPa will most likely end up in the group with high values of proportional limit strain.

Weibull Study:

The Weibull study like the one that was carried out for the virtual transverse tensile tests, where instead of a constant value of matrix strength, Weibull distribution of values was used and its impact over the composite strength was investigated. Three values of matrix strength were used for this study: 50 MPa, 100 MPa and 150 MPa. Similar to the study in the transverse direction, the Weibull modulus of the matrix was varied from 5 to 20 in the steps of 5. Contrary to the case in the transverse direction, there is no noticeable difference among the different values of Weibull modulus for matrix strength. Furthermore, the inclusion of the Weibull distribution of the matrix strength values itself exhibited a high impact on the Weibull distribution of the composite strength. A slight increase in the Weibull modulus of the composite strength with the increasing strength was noticed. This implies that the presence of defects or inhomogeneity in the matrix has a higher impact on a composite with weaker matrix.

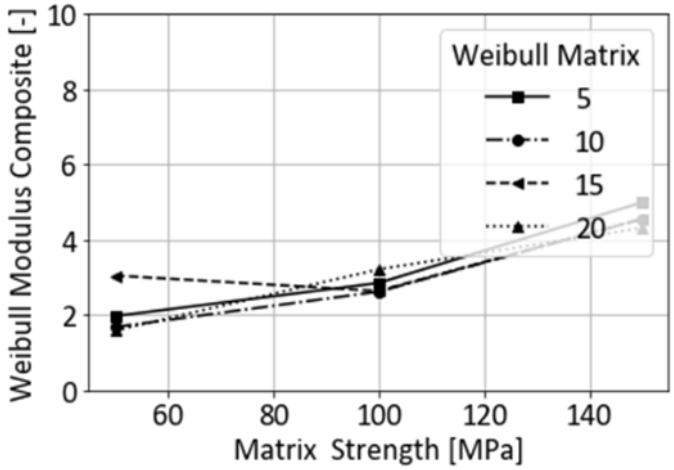

Figure 3.49: Variation of Weibull modulus of the longitudinal strength of the composite for different matrix strength values in 3D unidirectional virtual composites.

If the mean value of the strengths with standard deviation is considered for different microstructures with same parameters, they are comparable for all the values of Weibull modulus used in the parameter study. However, some discrepancies were noticed, such as in the case of Weibull modulus of 15 and matrix strength of 50 where the mean strength is approximately 300 MPa, a bit lower than the three other cases. Even in the case where the Weibull modulus was taken as 20 and the matrix strength as 150 MPa, the average strength was 700 MPa and lower compared to the other cases. These discrepancies though might be a result of the difference in randomly generated microstructure, as no pattern is noticed in the plots shown in Figure 3.50.

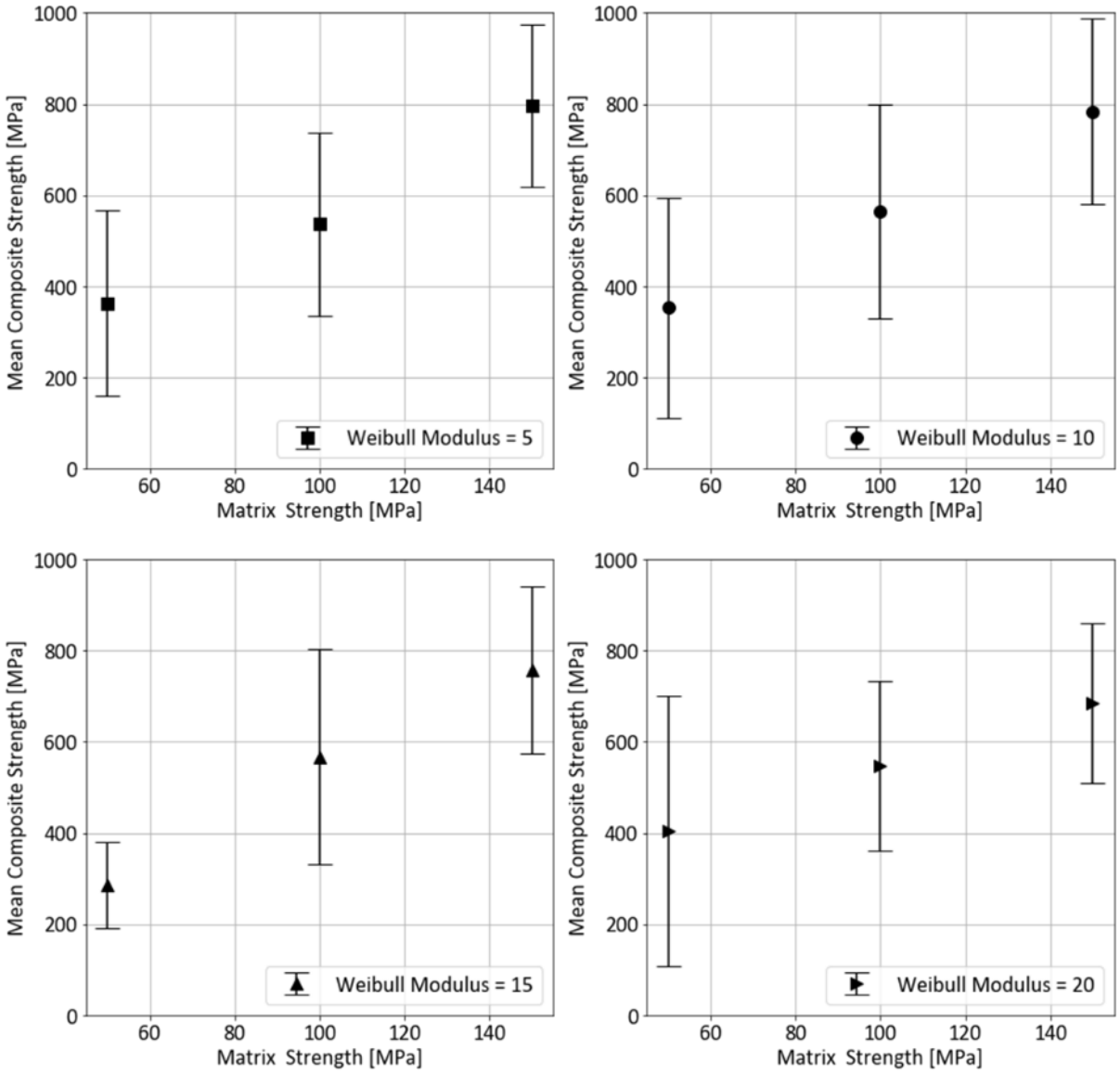

Figure 3.50: Mean longitudinal composite strength values for microstructures with varying matrix strength and Weibull shape parameter in the longitudinal direction in 3D unidirectional virtual composites.

3.6 Conclusion

This section dealt with the 'Structure-Property' part of the PSPP relationship. Finite element modelling was employed to analyse the virtual microstructures ranging from a pure matrix sample with defects to fibre-reinforced composites. Virtual tensile tests were performed to evaluate the mechanical properties like elastic modulus, strength, failure strain, damage, proportional limit stress and proportional limit strain. The tests can be extended to determine the same mechanical properties under other loading conditions like compression and shear as well. With the inclusion of the thermal models, the entire approach can also be used to evaluate the thermal properties or the temperature-dependent mechanical properties of the composites.

Weibull modulus was introduced as a property to integrate the effect of defects in the investigation of virtual microstructures. An attempt was made to establish the relationship between the pore properties (shape and volume) and the mechanical properties of the pure matrix material, so that these can be used as input properties for further modelling requirements. The Weibull distribution of only matrix material was considered but it can be extended to other constituents as well. For example, it was found in the literature study that the inhomogeneity in the ceramic fibres can also be represented by Weibull distribution.

In the current study fibre-reinforced microstructures, microstructural features like fibre volume content and the constituent properties were varied to understand their impact over the resulting composite properties. The data obtained from this parameter study was then used to train machine learning algorithms in order to create data-based surrogate models from physics-based finite element models. The performance of different linear and non-linear ML algorithms was compared in predicting the mechanical properties of the composite. Elastic modulus of the composite could be predicted with higher accuracy by all the algorithms but in the case of other properties, the non-linear algorithms outperformed the linear ones. However, for some properties even the non-linear algorithms did not perform well in the prediction. Further investigation of the data with the help of techniques like correlation heat map and feature importance plots revealed that similar dependency of the target variables on all the input variables lead to this low performance in some cases. Nevertheless, this study is first attempt in generating data-based models from physics-based models. Once the ML algorithms are trained on the time-consuming parameter studies, the predictions can be made in flash of seconds by the ML models. This is not trivial, as the complexity of the physics-based models increases based on the scale (mesoscale or multiscale) and boundary conditions (thermal or coupled). The time factor becomes more critical in these cases and ML algorithms can help the material scientists in designing the material based on the preliminary analysis instead of the conventional ‘trial and error’ methods.

4 Property-Performance Relationship

4.1 Introduction

In the previous chapter, the models at micro level were used to determine the properties of a fibre-reinforced composite. These models are computationally expensive though and usually cannot be employed in finite element analysis of CMC structures. Moreover, the complexity of the fibre preforms adds to the computational resources required and the use of homogenous material properties becomes inevitable for the modelling purposes at macro-level. The non-linear stress strain curves obtained from the micro models can be used as input for damage models to save time in the optimisation process of the part design based on finite element analysis and forms the basis of the 'Property-Performance' relationship.

Numerous damage models have been proposed in the literature to describe the inelastic behaviour of CMCs. The micromechanics-based approach proposed by Lamon [94] delivers accurate results in predicting damage but requires model parameters which can only be obtained from the individual constituents of a CMC, namely fibre, matrix and fibre-matrix interphase. However, in a complex matrix system like C–SiC, the material under consideration, it is challenging to evaluate the effective properties of a representative matrix material. Even the bulk material properties of a monolithic matrix material cannot be used because the matrix undergoes massive changes when employed for a fibre-reinforced material due, to effects such as hindered matrix shrinkage during the manufacturing process [95]. Baranger has summarized damage models and the rupture criterion at different microscopic scales in his work where stress and strain are used as limits to design a CMC component [96]. A thermodynamical formulation of the anisotropic damage model is discussed by Wulfinghoff et al. [97]. by linking crack channels and pores with degradation in properties. Models describing the damage of a homogenous CMC material at the macro-level have also been a topic of investigation for many researchers [98-102]. These models describe damage as the degradation of stiffness in principal material directions as the load increases. A model with a similar theoretical background of continuum damage mechanics is proposed by Barbero [103] and is implemented in the current work because of the lower number of tests required in parameter-identification for the model. Apart from that, testing standards for CMCs already exist for these required tests.

The above-mentioned continuum damage models successfully describe non-linearity in the material but do not explicitly predict the final failure of composite. A failure criterion is required in order to predict the failure stress or strain of a laminate. Several physics-based and empirical failure criteria for fibre-reinforced composites have been reported in the literature and are summarized in the World-Wide Failure Exercise (WWFE) [104]. Failure criteria based on micromechanics are not appropriate in the case of some CMCs because of the same above-mentioned reasons as for damage models. Apart from

that, phenomenological criteria such as Cuntze and Puck require material parameters based on tests conducted on unidirectional (UD) ply, which is not possible in the case of 2D reinforced materials under consideration. For these reasons, the Tsai-Wu failure criterion is found to be the most appropriate as the parameters required for its implementation can be obtained from standardized tests in case of CMCs. The availability of standardized tests for CMCs is not trivial. For example, there are no standardized combined shear–compression tests for CMCs to obtain the required friction parameter for the Cuntze criterion [105]. Based on the strength of tensile samples with different fibre orientations, failure stresses and strains for a virtual UD ply are evaluated. However, Tsai-Wu failure has its shortcomings as it is not able to differentiate between failure modes. The Tsai-Wu failure criterion is extended by Paepegem in order to determine the stress component responsible for the failure of a ply [106]. A quantitative comparison of direction-dependent failure modes is, though, not demonstrated in his work. Tushtev et al. implemented a damage model with a failure criterion based on thermodynamic forces for a 2D-woven C/C composite [107]. A similar damage-dependent quadratic failure criterion is proposed by Yang et al. as well, where strength predictions are made for a 2D-woven C/SiC material [108]. The proposed model is applicable not only on laminates with woven fibre architecture, but also on CMCs with wound fibre architecture.

In the current work, an attempt has been made to combine continuum damage mechanics with a damage-based quadratic failure criterion. Although only tensile and shear tests were considered for the materials under consideration, the proposed failure criterion allows the integration of damage under compression if the damage behaviour varies under tension and compression. A damage-based criterion has the advantage over the Tsai-Wu failure criterion in stress- or strain-space that it can give an insight into the fracture mechanics of the laminate because of its direction dependency. It can be used for designing CMC structures where damage, i.e., loss of stiffness in different directions, can be considered as a design limit instead of strength or strain. In this way, an empirical damage-based failure criterion based on macro-mechanics can deliver more information about phenomenon at the micro-level through damage variables which can be correlated to properties like crack density within a material. The proposed model exhibits an advantage over other empirical failure criteria as it can determine the responsible component in the damage-space, and thus can predict the failure mode in laminates with varying fibre orientations.

4.2 Finite Element Model

4.2.1 Continuum Damage Model

A progressive damage model based on the approach proposed by Barbero [109] is implemented for a 2D plane-stress case. The model incorporates the reduction of stiffness in an anisotropic material with increasing load to represent the loss of stiffness in a material due to the presence of cracks. In the current work, three independent scalar damage variables (d_1, d_2 and d_{12}) are used which are associated with

the Young's (E_1 and E_2) and shear moduli (G_{12}) of the material, respectively. The compliance tensor can be evaluated from a free energy density function, which is given by:

$$\chi = \frac{\sigma_1^2}{2(1-d_1)E_1} + \frac{\sigma_2^2}{2(1-d_2)E_2} + \frac{\sigma_{12}^2}{2(1-d_{12})G_{12}} + \frac{\nu_{12}\sigma_1\sigma_2}{E_1} \tag{7}$$

The partial derivative gives the compliance tensor S of the damaged material in Voigt notation:

$$S = \frac{\partial \chi}{\partial \sigma} = \begin{bmatrix} \frac{1}{(1-d_1)E_1} & \frac{\nu_{21}}{E_2} & 0 \\ \frac{\nu_{12}}{E_1} & \frac{1}{(1-d_2)E_2} & 0 \\ 0 & 0 & \frac{1}{(1-d_{12})G_{12}} \end{bmatrix} \tag{8}$$

A damage surface (g^d) in the thermodynamic force space is proposed by Barbero, where thermodynamic forces (Y) are given by:

$$Y = \frac{\partial \chi}{\partial d} \tag{9}$$

The damage surface (g^d) can be considered as analogous to the yield surface in the plasticity theory and is given by:

$$g^d = \sqrt{J_1 Y_1^2 + J_2 Y_2^2 + J_{12} Y_{12}^2} - (\gamma + \gamma_0) \tag{10}$$

where

J_i = internal material constants

Y_i = thermodynamic forces

γ = damage evolution variable

γ_0 = damage threshold

It has to be mentioned at this point that the H terms (internal material constants) proposed by Barbero [103] are not included in this work. H terms allow differentiation between the material behaviours under tension and compression, but this term is neglected in the current work. It is known to the author that CMCs generally behave differently under tension and compression, but due to a lack of the test data (stress–strain curve from a pure compression test) required for determination of the damage parameter, the behaviour is assumed to be linear elastic under compression. It was observed during the compression tests performed on WHIPOX™ [110] and C/C [86] that the samples either fail due to buckling or

delamination in the sample. Due to the presence of buckling during the compression test, it is difficult to separate material non-linearity from geometrical non-linearity in the compression test.

The evolution of the damage surface (g^d) can be explained with the help of Figure 4.1. There is no damage until the thermodynamic forces remain in the elastic domain with $g^d < 0$ and $\gamma = 0$, evaluated based on Equation (10) and (11) respectively. As the load on the material increases, the thermodynamic forces increase and leave the elastic domain of the material. At this point, $g^d = 0$ and based on the damage evolution law, accumulated damage is evaluated in a particular stress state. In the current work, an exponential law is used to determine the evolution of damage with increasing load, and is given by the following equation:

$$\gamma = c_1 \left(1 + \exp\left(\frac{\delta}{c_2}\right) \right) \tag{11}$$

where

δ is the kinematic variable and is always greater than zero to ensure the positive value of damage,

c_1 and c_2 are hardening parameters obtained after curve fitting from experimental data.

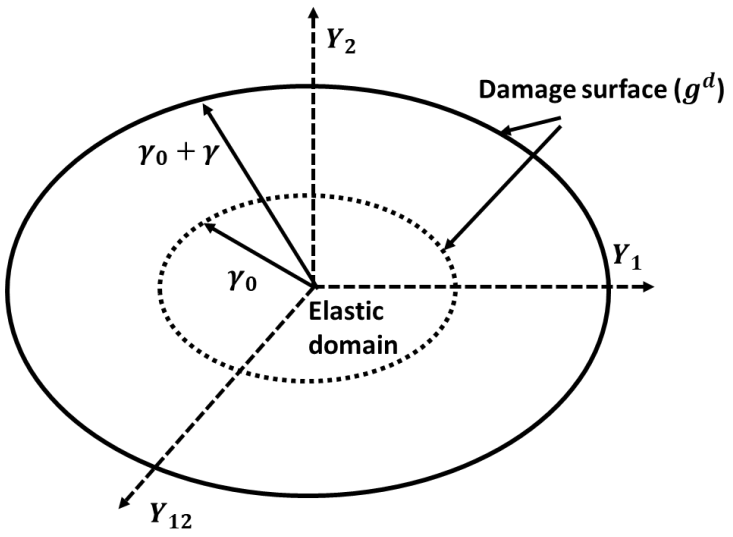

Figure 4.1: 2D representation of thermodynamic force space where no damage occurs in the elastic domain and the damage surface evolves based on the damage evolution law.

The damage hardening law used in the work is isotropic in nature, i.e., there is uniform expansion of the damage surface because there are insufficient test data to determine parameters for an anisotropic hardening law. It is also important to mention that the damage surface reduces to a Tsai-Wu surface in the stress-space. Analogous to the interaction of stress components in the Tsai-Wu failure criterion, the damage surface considers the interaction of damage components in the thermodynamic force space. The material parameters $J_1, J_2, J_{12}, \gamma_0, c_1$ and c_2 are obtained after performing curve fitting on experimental

data, as discussed in detail in [103, 111]. Other constitutive equations required for the evaluation of the elastic tangent stiffness matrix and the return mapping algorithm employed for its implementation in the commercial finite element software, ANSYS Workbench 2020R1, are based on the approach proposed by Barbero [109]. Two-dimensional 4-noded shell elements are used to perform finite element analysis and demonstrate the damage model in ANSYS. Boundary conditions are given in such a way that the sample represents pure tension and pure shear case to compare the results directly with the experimental results.

4.2.2 Tsai-Wu Failure Criterion

The continuum damage model discussed in the previous section determines the loss of stiffness in laminates but does not predict failure of the material. A failure criterion needs to be defined in order to predict the stress or strain at failure for a laminate. The Tsai-Wu failure equation is an empirical equation which can be used to predict stress or strain based on its implementation in stress- or strain-space, respectively. In this section, both these spaces with the extension of the Tsai-Wu criterion in the damage-space are discussed.

Stress- and Strain-Space:

The Tsai-Wu failure surface in the stress-space is given by [34]:

$$F_i\sigma_i + F_{ij}\sigma_i\sigma_j = 1 \tag{12}$$

where $i, j = 1,2, \dots ,6$, and F_i and F_{ij} are strength tensors of the second and fourth rank, respectively. Their values are obtained from the strength of a UD ply in different loading directions and $\sigma_{i,j}$ are corresponding stress components. A safety ratio (R) is integrated in Equation (6) and the equation can be reformulated based on [112] as:

$$\left(F_{ij}\sigma_i\sigma_j\right)R^2 + (F_i\sigma_i)R - 1 = 0 \tag{13}$$

The positive root of the quadratic equation gives a strength ratio which can be used as a linear scaling factor in order to design a certain component based on the Tsai-Wu failure criterion. In the current work, a plane stress case is considered, where Equation (6) reduces to:

$$F_1\sigma_1 + F_2\sigma_2 + F_{11}\sigma_1^2 + F_{22}\sigma_2^2 + F_{66}\sigma_{12}^2 + 2F_{12}\sigma_1\sigma_2 = 1 \tag{14}$$

Apart from F_{12}, all other parameters can be evaluated directly from the tensile, compressive and shear strengths of a unidirectional (UD) ply. The value of F_{12} must be determined from a bi-axial tensile test, where equal tensile loads are applied on two principal material axes of a UD layer, avoiding any shear load on the lamina. However, due to difficulty in performing such a test, certain empirical equations are

proposed for the evaluation of F_{12} in Ref. [113]. In the work of Narayanaswami et al. [114], the results show that the value of interaction parameter F_{12} can often be taken as zero for composite materials with low percentages of error when compared to experimentally determined F_{12}. Due to the lack of such bi-axial tests for both the materials under consideration, F_{12} was taken as zero for both the materials. Equation (8) then reduces to:

$$F_1\sigma_1 + F_2\sigma_2 + F_{11}\sigma_1^2 + F_{22}\sigma_2^2 + F_{66}\sigma_{12}^2 = 1 \tag{15}$$

The strength ratio can then be evaluated by solving the following quadratic equation for R:

$$(F_1\sigma_1 + F_2\sigma_2)R + (F_{11}\sigma_1^2 + F_{22}\sigma_2^2 + F_{66}\sigma_{12}^2)R^2 - 1 = 0 \tag{16}$$

The Tsai-Wu failure criterion can be implemented in strain-space with the help of the strain limit values of a UD ply. The quadratic failure equation, then, is given by [35]:

$$(G_1\varepsilon_1 + G_2\varepsilon_2)R + (G_{11}\varepsilon_1^2 + G_{22}\varepsilon_2^2 + G_{66}\varepsilon_{12}^2)R^2 - 1 = 0 \tag{17}$$

where G_i and G_{ij} are calculated in the exact same way as in the stress-space. The strain limit values from tests performed in different loading directions are used to determine these parameters. The criterion in the strain-space might be preferred in a laminate because global strains are uniform in all the plies or vary linearly over the thickness of a laminate.

Damage-Space:

The empirical nature of the quadratic equation proposed by Tsai-Wu has the advantage that it can be used in different spaces. As discussed in the previous section, the damage evolution is determined in the thermodynamic force space. This suggests that this quadratic equation can be used in the damage-space as well to define failure based on damage or loss of stiffness in different principal material directions in a particular ply. In a damage-based failure criterion, critical damage values in each direction are used to evaluate the parameters for the quadratic equation. Critical damage (d_{max}) in a ply is given by:

$$d_{max} = 1 - \frac{E_{failure}}{E} \tag{18}$$

where $E_{failure}$ is the secant modulus at failure or the ratio of failure stress to failure strain, and E is the Young's modulus or shear modulus, depending on the test. Analogous to strength parameters in the stress-space, parameters in the damage-space are evaluated as shown below:

$$H_1 = \frac{1}{d_{1max}^T} - \frac{1}{d_{1max}^C} \tag{19}$$

$$H_{11} = \frac{1}{d_{1max}^{T}\, d_{1max}^{C}} \tag{20}$$

$$H_{2} = \frac{1}{d_{2max}^{T}} - \frac{1}{d_{2max}^{C}} \tag{21}$$

$$H_{22} = \frac{1}{d_{2max}^{T}\, d_{2max}^{C}} \tag{22}$$

$$H_{66} = \frac{1}{(d_{12max})^{2}} \tag{23}$$

where superscripts 'T' and 'C' represent tension and compression, respectively. The quadratic failure criterion in the damage-space for a plane stress case is given as:

$$H_1 d_1 + H_2 d_2 + H_{11} d_1^2 + H_{22} d_2^2 + F_{66} d_{12}^2 = 1 \tag{24}$$

where d_1, d_2 and d_{12} are obtained from the damage model for any given load. It is important to mention that damage cannot take any negative values like in stress- or strain-space. However, the inelastic behaviour of material is known to be different under tension and compression [110]. For this reason, damage values under compression are taken as negative for the sake of the convexity of the quadratic equation, but physically, damage can only be positive according to the second law of thermodynamics. Since there were no data available under compression, the critical damage values under compression were assumed to be same as under tension. A strength ratio can be calculated in the damage-space as well:

$$(H_1 d_1 + H_2 d_2)R + (H_{11} d_1^2 + H_{22} d_2^2 + F_{66} d_{12}^2)R^2 - 1 = 0 \tag{25}$$

The R value obtained from the above equation is then directly multiplied with load to determine the failure stress and strain of the ply:

$$\sigma_{failure} = \sigma_{load} \,.R \tag{26}$$

where σ_{load} is applied stress on the material and $\sigma_{failure}$ is the failure stress of the material. Similarly, failure strain $\varepsilon_{failure}$ is evaluated as:

$$\varepsilon_{failure} = \varepsilon_{load} \,.R \tag{27}$$

where ε_{load} is the strain applied on the material. Failure stresses and strains obtained from the Tsai-Wu criterion in the stress-, strain- and damage-spaces are discussed in the next section.

4.3 Results and Discussion

4.3.1 Experimental Results

The behaviour of two different materials, namely C/C–SiC and WHIPOX™, is summarized in this section. Manufacturing and testing for both the materials were performed in the framework of two dissertations at DLR. Tensile and Iosipescu shear tests were carried out for different fibre orientations to characterize the material. All the tests were performed at room temperature. Detailed information about the manufacturing process and testing methods for C/C–SiC and WHIPOX™ can be found in the work of Breede [91] and Shi [110], respectively. It is evident from the stress–strain curves that the material starts behaving non-linearly when the fibre orientation increases from the fibre-dominated orientation of ±15° to the matrix-dominated orientation of ±75°. Although both the materials were manufactured via filament winding, the mechanisms resulting in non-linearity in the materials are different due to their microstructures. C/C–SiC is a material which falls between the categories of 'weak-interphase' and 'weak-matrix' CMCs. The quasi-brittle behaviour of C/C–SiC can be attributed to the pull-out of C/C blocks embedded in the SiC matrix. On the other hand, WHIPOX™ belongs to the 'weak-matrix' category where the energy is dissipated by matrix cracks present in the relatively porous material (open porosity up to 35%) [95]. The stress–strain curves under tensile and shear loadings are discussed in detail in Section 4.3.3.

The mechanical properties of both the materials for different fibre orientations are summarized in Table 4.1 and Table 4.2. Three to five samples were tested for each fibre orientation. It is evident from both tables that the strength of the material decreases when moving from fibre-dominated fibre orientation, e.g., ±15°, to the matrix-dominated fibre orientation, e.g., ±75°. The weak matrix in both the materials is the reason behind the low strength in the matrix-dominated fibre orientations. Young's modulus, on the other hand, first decreases till ±45°, and then increases again. This effect can be attributed to the lower intralaminar shear stiffness of the material, which is discussed in detail in the next section. In the case of WHIPOX™, the effect is more prominent because of the presence of manufacturing defects in the fibre orientations of ±30°, ±45° and ±60°. During the sintering process of the material, the shrinkage of the matrix is hindered by the stiff aluminium oxide fibres, which results in pre-existing cracks within the matrix before it is tested. This effect is dominant in the above-mentioned fibre orientations and results in a relatively weaker matrix with lower stiffness when compared with other fibre orientations. This phenomenon is discussed in detail in previous work [115].

Table 4.1: Mechanical properties of C/C–SiC obtained from tensile and shear tests for different fibre orientations.

Property	Unit	±15°	±30°	±45°	±60°	±75°
E_x	GPa	117 ± 20	77 ± 2	32 ± 3	34 ± 3	57 ± 4
G_{xy}	GPa	27 ± 2	-	41 ± 6	-	27 ± 1

$\sigma_{x\,max}$	MPa	149 ± 13	151 ± 26	95 ± 8	39 ± 5	35 ± 4
$\varepsilon_{x\,max}$	%	0.20 ± 0.02	0.34 ± 0.06	0.70 ± 0.25	0.42 ± 0.05	0.06 ± 0.01

Table 4.2: Mechanical properties of WHIPOX™ obtained from tensile and shear tests for different fibre orientations.

Property	**Unit**	**±15°**	**±22.5°**	**±30°**	**±45°**	**±60°**	**±67.5°**	**±75°**
E_x	GPa	202 ± 7	198 ± 15	131 ± 9	99 ± 2	68 ± 8	141 ± 14	114 ± 14
G_{xy}	GPa	51 ± 1	55 ± 12	50 ± 11	59 ± 2	50 ± 11	55 ± 12	51 ± 01
$\sigma_{x\,max}$	MPa	276 ± 5	233 ± 38	133 ± 19	96 ± 9	27 ± 3	37 ± 4	22 ± 4
$\varepsilon_{x\,max}$	%	0.14 ± 0.01	0.12 ± 0.01	0.12 ± 0.03	0.13 ± 0.02	0.07 ± 0.01	0.03 ± 0.01	0.02 ± 0.01

The shear modulus of the fibre orientations ±15° and ±75°, in the case of C/C–SiC, is almost the same as is expected from the classical laminate theory. The same conclusion can be drawn for the fibre orientations ±15° and ±75°, ±22.5° and ±67.5°, and ±30° and 60° in the case of WHIPOX™ [110].

4.3.2 Elastic Behaviour

In order to predict the elastic behaviour of composites, homogenisation methods such as rule of mixtures are typically employed. Based on the elastic properties of the individual constituents, namely fibre and matrix, the elastic properties of a composite with a definite fibre volume content can be determined. However, in the case of CMCs, the matrix properties as a constituent in the CMCs are different from the matrix as bulk material. For example, the properties of Al_2O_3 as bulk material cannot be used as representative of the matrix material in WHIPOX™ because the microstructure of Al_2O_3 in WHIPOX™ is completely different from the bulk material due to the presence of shrinkage cracks. Similarly, C/C–SiC exhibits a complex matrix system with carbon matrix embedded in the SiC regions, which makes it difficult to evaluate the properties of the representative matrix with the required accuracy. In the previous work of the authors, inverse laminate theory is successfully employed to evaluate the elastic properties of a virtual unidirectional (UD) layer. With the help of the elastic properties of these UD layers, the properties of laminates with different fibre orientations can be predicted with the help of classical laminate theory. The in-plane elastic properties of the virtual UD layers for both the materials are listed in Table 4.3.

Table 4.3: Elastic properties of the virtual unidirectional layer used for the evaluation of the elastic properties of laminates with varying fibre orientations.

Property	**Unit**	**C/C–SiC**	**WHIPOX™**
E_1	GPa	145.0	211.2
E_2	GPa	60.0	56.2
ν_{12}	-	0.2	0.2

G_{12}	GPa	9.0	40.0

The values of WHIPOX™ are taken from a previous publication [115]. In the case of C/C–SiC, the values of the UD values were evaluated from data fitting for other fibre orientations. A comparison between the values from classical laminate theory and the experimentally evaluated elastic properties is shown in Figure 4.2. A good agreement was found in the case of C/C–SiC. However, in the case of WHIPOX™, the Young's modulus of the sample with a ±75° winding angle is underestimated by the classical laminate theory. This discrepancy can be attributed to the elastic properties of the virtual UD layer. As discussed in the previous section, the material exhibits shrinkage in the case of winding angles ±30°, ±45° and ±60°. However, in the case of ±75°, there are no such shrinkage cracks, and the matrix is stiffer than the matrix for other winding angles (±30°, ±45° and ±60°). This effect is discussed in detail in [38], where two different sets of elastic properties are used for the determination of the elastic properties of the laminates based on the presence of shrinkage cracks. Since the focus of the paper is on the inelastic behaviour of the material, which is dominant in winding angles from ±30°to ±60°, the properties of virtual UD layers with shrinkage cracks were taken for all fibre orientations.

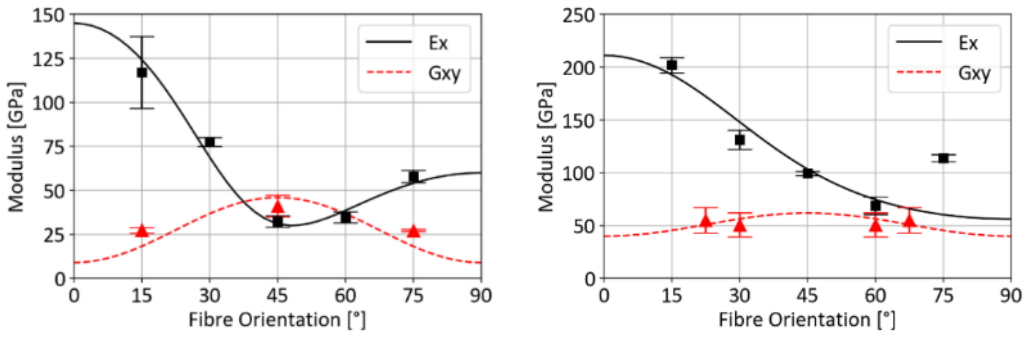

(a) (b)

Figure 4.2: Comparison between the values of Ex (black squares) and Gxy (red triangles) with standard deviation obtained from tensile and shear tests and values evaluated from implementation of classical laminate theory on virtual UD plies for different fibre orientations for (a) C/C–SiC and (b) WHIPOX™.

4.3.3 Inelastic Behaviour

The inelastic behaviour of the materials is modelled with the help of the continuum damage model discussed in Section 4.2.1. Parameter fitting is performed for both the materials, and they are listed in Table 4.4. The parameters J_{11}, J_{22} and J_{12} were fitted to the stress–strain curves of fibre orientations ±15°, ±75° and ±45°, respectively. The reason behind this is the dominant local stress component (σ_1, σ_2 and σ_{12}) in a particular fibre orientation, as shown in Figure 4.3. For example, if a global tensile load

is applied on a sample with a ±15° fibre orientation, the stress gets resolved into a higher value of σ_1 and lower values of σ_2 and σ_{12}. On the other hand, in a sample with ±75°, the stress gets resolved into higher values of σ_2 and lower values of σ_1 and σ_{12}. The sample with a ±45° fibre orientation exhibits equal values of σ_1, σ_2 and σ_{12}, and therefore, is the highest contribution of σ_{12} among all the other fibre orientations. Based on this local stress contribution of stresses, the limits in thermodynamic space, J_{11}, J_{22} and J_{12}, were obtained from stress–strain curves of different fibre orientations. The shape parameters (c_1 and c_2) of the curve were fitted with the help of a ±45° tensile sample, or in other words, the material behaviour under shear loading, where the material shows the maximum non-linearity.

Table 4.4: Damage parameters.

Property	C/C–SiC	WHIPOX™
J_{11}	15	0.1
J_{22}	45	50
J_{22}	28	10
γ_0	0.014	0.004
c_1	0.03	0.015
c_2	−0.025	−0.055

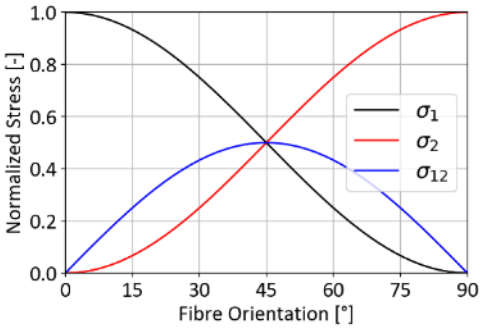

Figure 4.3: Normalized variation of local stress components after application of pure tensile load on a laminate with given fibre orientation.

Tensile Test:

Figure 4.4 shows the comparison between experimental results and simulation results for tensile and shear tests. Three to five samples were tested for each fibre orientation but only one curve is shown for better visualisation. The investigated continuum damage model can capture the inelastic behaviour of the material for different fibre orientations. It must be kept in mind that the continuum damage model describes the non-linearity or damage in the material but requires a failure criterion to predict the failure stress or strain of a particular laminate. In this section, only the inelastic deformation of the material is discussed, and the failure criterion is discussed in the next section. Displacement equivalent to the failure strain from the experiments was given as the input boundary condition in the finite element simulation.

Due to this reason, the damage model curves in Figure 4.4 end exactly where the experimental curves end.

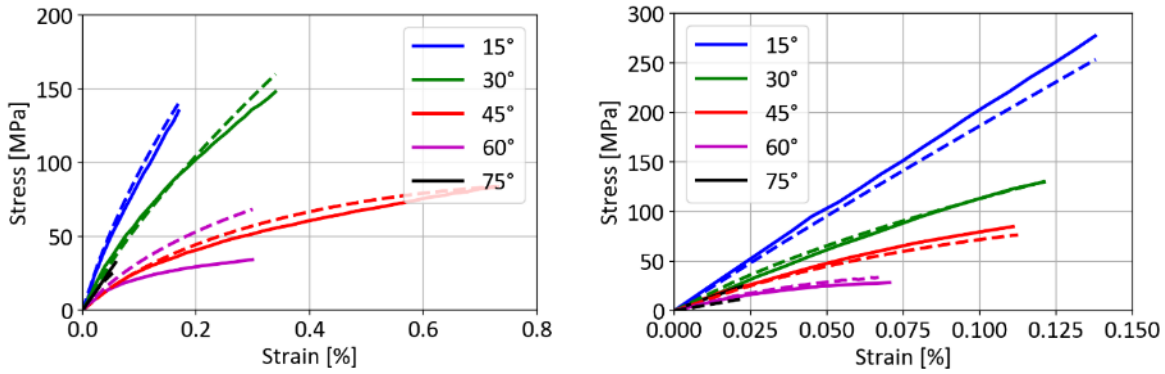

Figure 4.4: Comparison between stress–strain curves obtained from simulation (broken line) and tensile tests (solid line) with different fibre orientations: (a) C/C–SiC; (b) WHIPOX™.

In the case of C/C–SiC, the simulation results are in good agreement with the experimental results apart from the winding angle of ±60°. If the global load on a sample with a ±60° fibre orientation is resolved into local stress components, σ_2 and σ_{12} are present in the material with a small contribution of σ_1. This phenomenon can be explained with the help of Figure 4.5 and Figure 4.6. In Figure 4.5, the development of damage components (d_1, d_2 and d_{12}) with respect to the global loading strain is plotted. In the case of ±15°, the load is mostly carried by fibres and damage is noticed only in 1-direction (d_1). d_2 is zero and there is a small amount of d_{12} present in the sample. On the other hand, in the case of ±75°, the damage is only in the matrix-dominant 2-direction where only d_2 plays a role in the failure of the sample. For the sample with a ±45° fibre orientation, the major load is carried by the shear stiffness of the material, and there is a significant amount of d_{12} in the laminate. However, in the case of ±30°, there is the presence of d_1 and d_{12}, suggesting that there is damage in both the 1-direction and 12-direction. Similarly, for ±60°, the presence of d_2 and d_{12} suggests that there is damage in the 2-direction and the 12-direction. In other words, the combined effect of the damage indices is responsible for the failure in these laminates.

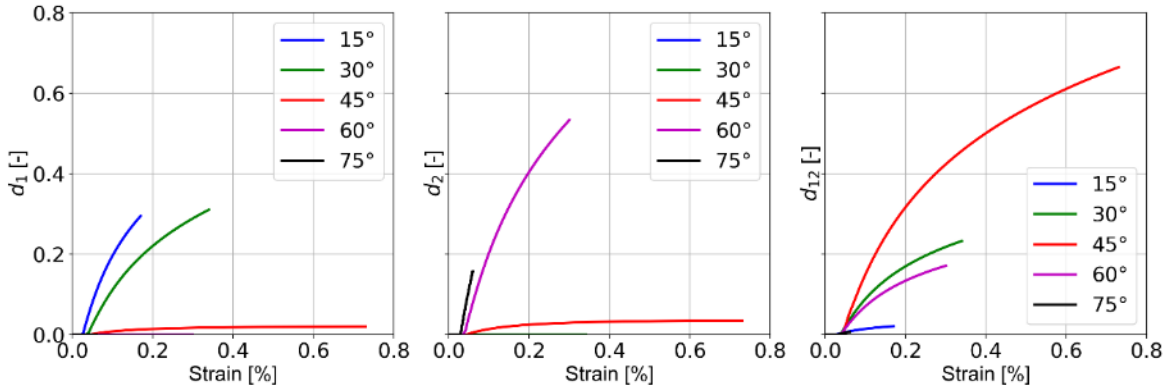

(a) (b) (c)

Figure 4.5: Comparison between damage values from the model with global strain values obtained from tensile tests for C/C–SiC with (a) d_1, (b) d_2 and (c) d_{12}.

Now let us consider Figure 4.6, where damage, i.e., loss in the global stiffness of the material under tension, is plotted against strain applied on the material. It can be observed that the global damage (broken line) determined by the damage model in the case of ±45° is in good agreement with that of the damage evaluated from the experiment (solid line). However, in the case of ±30° and ±60°, damage is underestimated by the damage model. It is known from the previous discussion that the sample with ±30° and ±60° fibre orientations exhibit multiple damage modes. A combined effect of the damage modes is, however, not considered in the model. In other words, the presence of multiple damage modes results in a higher or accelerated loss of global stiffness when compared to the presence of a single damage mode in a laminate. For example, in the case of ±60°, damage in both the 2-direction and the 12-direction leads to an excess loss of stiffness and results in a non-linear curve which is not considered in the current damage model. There might be cracks in the matrix (presence of d_2) but the load is still carried by the shear stiffness provided by the presence of fibres in the matrix. Similarly, in the case of ±30°, an excess loss of stiffness takes place due to the presence of both d_1 and d_{12} in the laminate. This explains the discrepancy between the stress–strain curve obtained from the tensile experiment and the damage model. This is a shortcoming of the proposed damage model and can be a topic for future work where an interaction parameter will be introduced to ensure accelerated damage evolution in the case of the presence of multiple damage modes, as shown in Figure 4.7. The damage surface in that case evolves faster under the presence of multiple stress components, when compared to the presence of a single dominating stress component. For example, in Figure 4.7, the damage evolution is enhanced when both Y_2 and Y_{12} are present in a particular load state when compared to a load state where only either Y_2 or Y_{12} is present.

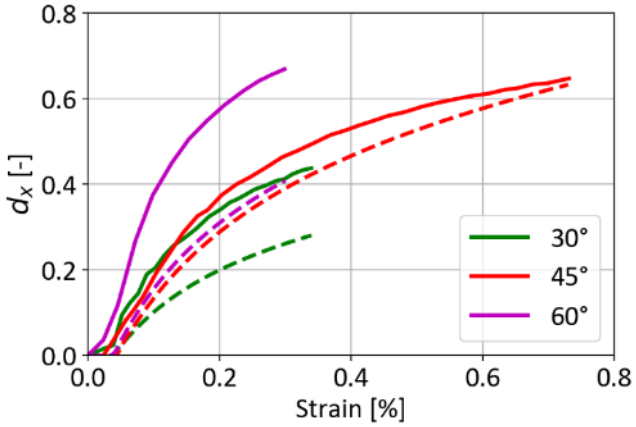

Figure 4.6: Comparison between damage curves obtained from experiments (solid line) and simulation (broken line) for C/C–SiC.

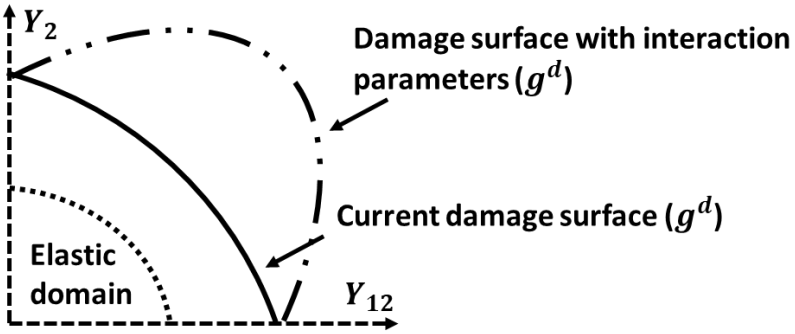

Figure 4.7: Damage surface with consideration of the interaction of damage parameters in the presence of multiple damage models in the thermodynamics space.

Iosipescu Shear Test:

In-plane Iosipescu shear tests were performed in the work of Breede [91] and Shi [110] for materials C/C–SiC and WHIPOX™, respectively. However, the stress–strain curves obtained were valid only in the elastic region. The test turned out to be invalid for the determination of the shear strength of the material, as the sample did not fail in the expected notched area. For this reason, it is important to note that the stress and strain values where the curves end should not be considered as the strength of the laminate under pure shear loading. Nevertheless, a comparison between the stress–strain curves is shown in Figure 4.8 and Figure 4.9 in order to demonstrate the non-linearity captured by the damage model.

As observed in Figure 4.8, the shear stiffness of laminates with ±15° and ±75° within the initial elastic region is comparable in the case of C/C–SiC. This is in accordance with the classical laminate theory, and for this particular reason, the curves from the damage model overlap each other. Similarly, in the case of WHIPOX™ laminates (as seen in Figure 4.9), the curves overlap each other in the elastic region in these fibre orientations: ±22.5° and 67.5°; ±30° and ±60°.

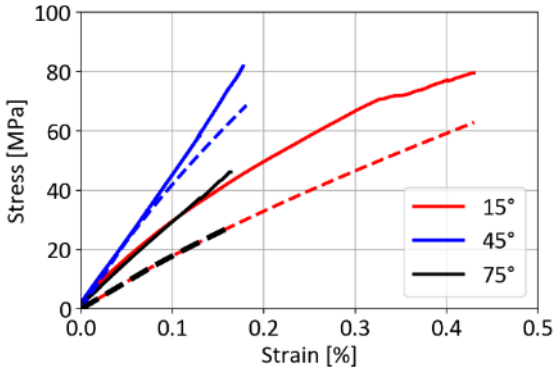

Figure 4.8: Comparison between the stress–strain curves obtained from the simulation (broken line) and Iosipescu shear tests (solid line) with different fibre orientations for C/C–SiC.

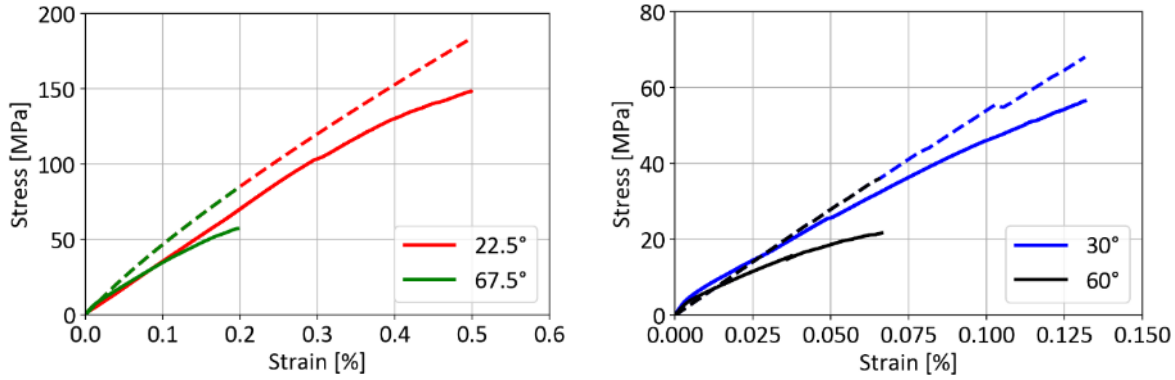

(a) (b)

Figure 4.9: Comparison between the stress–strain curves obtained from simulation (broken line) and Iosipescu shear tests (solid line) with different fibre orientations for WHIPOX™. (a) ±22.5° and 67.5°; (b) ±30° and ±60°.

If pure shear stress is resolved into local stress components (σ_1, σ_2 and σ_{12}), it is observed that the matrix is under compressive stress (as seen in Figure 4.10). The damage model in the current work does not consider any loss of stiffness under compression, i.e., $d = 0$ and the Young's modulus remains constant throughout the test. Another assumption which is considered in the model is that the Young's modulus is the same under compression and tension, which might not be the case with CMCs, as shown in the earlier publication with WHIPOX™ [115].

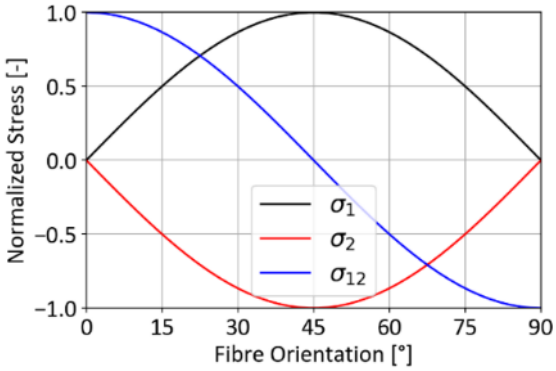

Figure 4.10: Normalized variation of local stress components after application of pure shear load on a laminate with given fibre orientation.

As discussed in the previous section, the Iosipescu shear test could not deliver the strength values for the laminates. However, the shear modulus could be accurately determined by the test, but the results were invalid for both the materials as soon as the material left the linear elastic region, i.e., as soon as crack evolution started in the laminate. This phenomenon raises the question of whether the Iosipescu test is an appropriate method to determine the shear strength of the material. The authors believe that due to the presence of notches in the sample, the strength of the material becomes a function of the shape and direction of the notch and the fibre orientation of the sample.

As shown in Figure 4.11, in case of ±15°, the crack might initiate from a region where the fibres are damaged while preparing the sample [116]. As the crack grows further, it gets deflected at the fibre boundary and moves along the fibres which are almost perpendicular to the direction of crack growth. In this manner, crack growth is hindered by the fibres and the crack follows a zig-zag path until it reaches the notch on the other side of the sample. This deflection of the crack leads to a higher amount of force required to fracture the sample, and consequently, the test gives a higher shear strength of the laminate. The C/C–SiC sample with ±15° fractured at a shear stress of 78 MPa. A similar phenomenon was observed in the case of the WHIPOX™ sample with a fibre orientation of ±22.5°, where the crack is deflected on the fibres, which act as a hindrance to its movement (see Figure 4.12). On the other hand, in the case of ±75°, the notches are aligned in the fibre direction. When a crack initiates, as in the former case, it grows along the boundary of the fibres. The only difference is that the growth is not hindered by the fibres as they are aligned in the direction of the notch. Ultimately, the force required to fracture the sample is relatively low. The shear stress at the fracture of the sample with ±75° was evaluated to be 46 MPa. Theoretically, the fibre orientations ±15° and ±75° should exhibit the same stiffness and strength under pure shear loading. Due to the different crack growth behaviour in the material in the Iosipesu test and the interdependence of the notch and fibre direction, it can be concluded that the Iosipescu shear test is not appropriate for the determination of the shear strength of CMCs.

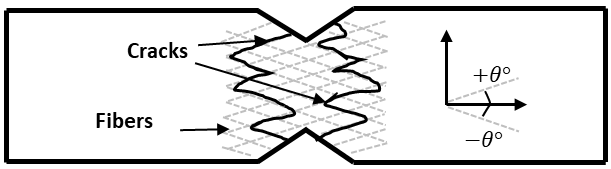

(a)

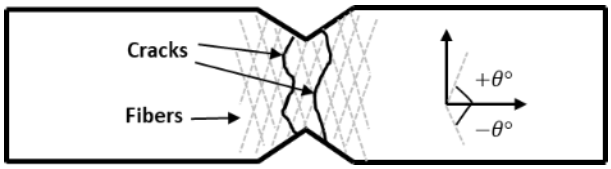

(b)

Figure 4.11: Crack growth in an Iosipescu test sample with fibre orientation (a) ±15° and (b) ±75°.

Figure 4.12: Crack growth in an Iosipescu test sample with fibre orientation of ±22.5° in the case of WHIPOX™ [110].

4.3.4 Tsai-Wu Failure Criterion

Similar to the determination of the representative elastic properties of a virtual UD layer in Section 4.3.2, the strength values are also fitted for a virtual UD layer. The maximum value for each component of the Tsai-Wu failure criterion in respective spaces (damage, strain or stress) is evaluated in such a way that the error percentage between the experimental values and the predicted values is minimum for all the fibre orientations. The results after the implementation of the Tsai-Wu failure criterion in different spaces are discussed in this section.

Damage-Space:

Analogous to the stress-based Tsai-Wu failure criterion, the maximum values of damage are used to define a failure envelope. The maximum values used for the implementation of the failure criterion are summarized in Table 4.5.

Table 4.5: Damage limits for stress-based Tsai-Wu failure criterion.

Property	Unit	C/C–SiC	WHIPOX™
d_{1max}	-	0.30	0.025
d_{2max}	-	0.17	0.45
d_{12max}	-	0.70	0.43

A two-dimensional representation of the failure envelope in 3D space is shown in Figure 4.13. It has to be mentioned at this point that there are no negative values of damage. The region with negative values in Figure 4.13 is shown only to visualize the points that lie on the zero axis. According to the definition of damage, it can only be positive in a material. Starting with ±15° fibre orientation, 'purple triangle' takes the maximum value of d_1, which suggests that the sample fails due to damage in the 1-direction, i.e., fibre-dominant direction. On the other hand, the sample with ±75° fibre orientation fails due to damage in the 2-direction, i.e., the matrix-dominant direction, as 'black triangle' lies on the boundary of d_2. As expected, the sample with a ±45° orientation fails due to loss in the shear stiffness of the material and the point 'green square' lies on the maximum values of the d_{12} axis. The sample with a fibre orientation of ±30° exhibits combined damage modes. It ('red circle') takes maximum values for d_1 and can be seen on the boundary of the envelope in the $d_{12} - d_1$ axis. As discussed in the previous section, the damage in the laminate with the ±60° fibre orientation is underestimated by the model, and for this reason, 'blue triangle' lies outside the envelope. Because of the presence of both the d_2 and d_{12} damage modes, the interaction parameter for the damage-failure criterion will also be considered in the future work and so will be the damage surface in the thermodynamic forces space.

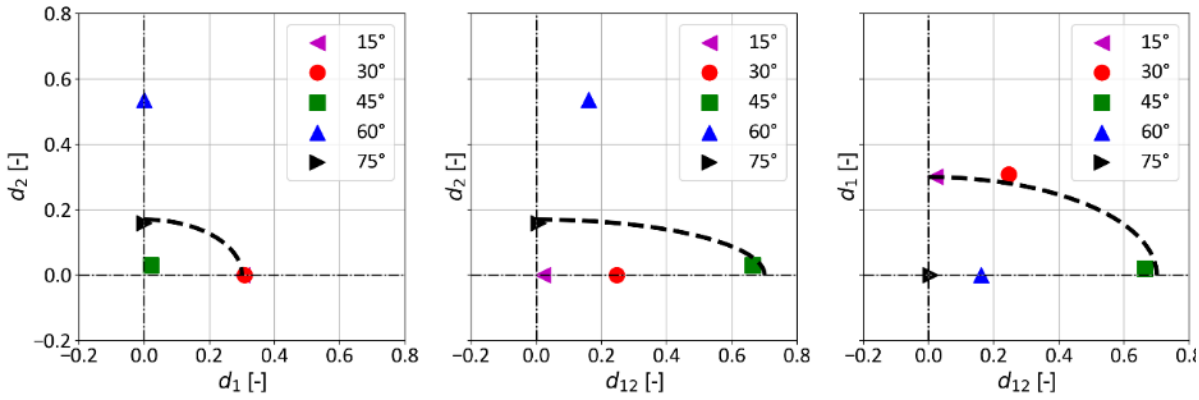

(a) (b) (c)

Figure 4.13: Two-dimensional representation of a 3D Tsai-Wu failure envelope for C/C–SiC with (a) d_1–d_2 axis, (b) d_{12}–d_2 axis and (c) d_{12}–d_1 axis with experimental results (markers) for different fibre orientations.

Stress-Space:

The Tsai-Wu failure criterion is implemented in the stress-space for both the materials. The strength values used for the virtual UD layers are listed in Table 4.6. Due to lack of data under compression for C/C–SiC, the strength values under compression are taken to be the same as those of tension. The strength values for WHIPOX™ are taken from a previous work [95].

Table 4.6: Stress limits for stress-based Tsai-Wu failure criterion where superscripts 'T' and 'C' denote tension and compression, respectively.

Property	Unit	C/C–SiC	WHIPOX™
σ_{1max}^{T}	MPa	190	279
σ_{2max}^{T}	MPa	35	22.5
σ_{1max}^{C}	MPa	190	243
σ_{2max}^{C}	MPa	35	45
σ_{12max}	MPa	70	65

Figure 4.14 shows a comparison between the values obtained from the test and the predicted failure stress values. The damage-based failure criterion performed better than the stress-based criterion for all the fibre orientations for C/C–SiC, except in the case of ±60°. The value of d_{2max} (0.17) is reached at a very low value of stress in the case of ±60°. The damage limits are set in such a way that the error between the experimental results and the predicted values is minimum. Since d_{2max} influences the strength of ±45° and ±75° as well, a compromise had to be made in the case of the ±60° laminate.

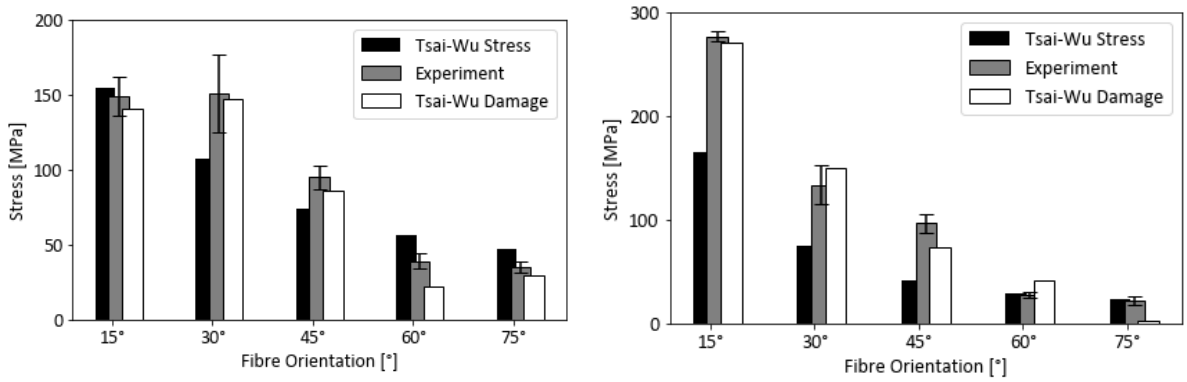

a) (b)

Figure 4.14: Comparison of the failure stress values between the tensile test and the predicted values from the damage-based and stress-based Tsai-Wu failure criterion for (a) C/C–SiC and (b) WHIPOX™.

In the case of WHIPOX™, a good agreement can be found between the experimental results and the predicted values of failure stresses according to damage-based failure criterion, with a low discrepancy in the case of ±45° and ±60° and a high discrepancy in the ±75° fibre orientation. As mentioned earlier,

the value of d_{2max} is set in such a manner that the error between the experimental results and the failure criterion is minimum. Now, when the ±75° fibre orientation is observed, the value of d_{2max} is high when compared to the experimental results where the stress–strain curve is almost linear. The damage limit in the experiment is reached at a very low stress value in the damage model, and the predicted strength is also consequently low. On the other hand, in the ±60° laminate, the predicted damage is lower when compared to the experimental results and the damage limit is reached at a higher stress value. A compromise had to be made while determining the value of d_{2max}. In a similar way, the value of d_{2max} influences the strength of the ±45° laminate as well because of the presence of the σ_2 component.

Strain-Space:

The Tsai-Wu failure criterion is implemented in the strain-space for both the materials. The strain limit values used for the virtual UD layers are listed in Table 4.7. The strain limit under compression is assumed to be same as under tension.

Table 4.7: Strain limits for strain-based Tsai-Wu failure criterion.

Property	Unit	C/C–SiC	WHIPOX™
ε_{1max}	%	0.20	0.15
ε_{2max}	%	0.10	0.023
ε_{12max}	%	0.70	0.60

Figure 4.15 shows a comparison between the values obtained from the test and the predicted failure strain values. The damage-based failure criterion performs even better in predicting failure strain than the strain-based Tsai Wu failure criterion. In the case of C/C–SiC, apart from ±60°, there is good agreement with the experimental results. As discussed in previous section, the laminate with the ±60° fibre orientation exhibits extremely high non-linear behaviour before fracture and has a very high failure strain. With the inclusion of an interaction parameter in the failure criterion, the model should be able to predict failure strain with higher accuracy.

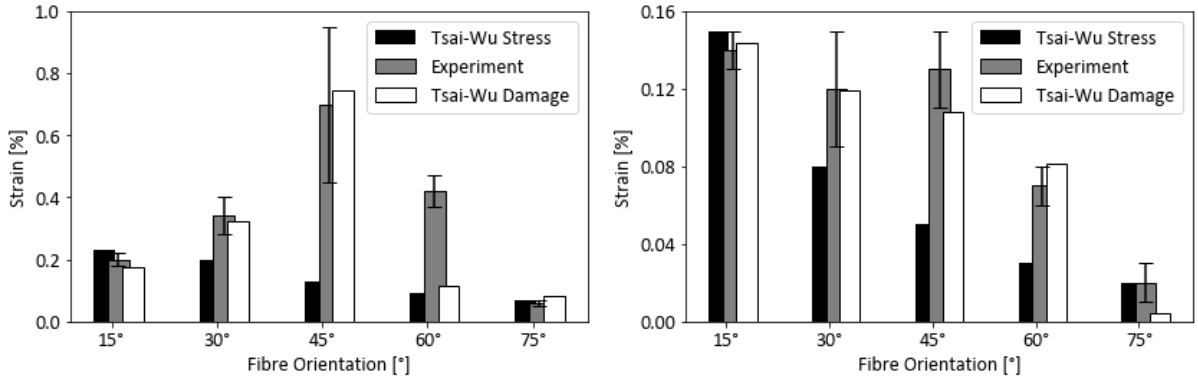

(a) (b)

Figure 4.15: Comparison of the failure strain values between the tensile test and the predicted values from the damage-based and strain-based Tsai-Wu failure criterion for (a) C/C–SiC and (b) WHIPOX™.

As far as WHIPOX™ is concerned, failure strain is predicted with a higher accuracy in comparison to Tsai-Wu in the strain-space as well. The discrepancy in the laminates with the ±45°, ±60° and ±75° fibre orientations is because of the same reason as discussed in the stress-space.

This comparison of the damage-based criterion with the Tsai-Wu failure criterion in stress- and strain-space demonstrates that it can predict the failure stress and strain with higher accuracy. It considers the losses in the Young's moduli and shear moduli, which are a result of changes in the microstructure of the material. In this manner, this criterion based on mechanical behaviour at the macro-level can be correlated to the physical properties of the microstructure, such as increases in crack density with increasing load. In Shi et al. [95], two sets of UD strength limits were required to predict the strength of laminates with different fibre orientations with consideration of microstructural effects. The damage-based criterion, on the other hand, can predict the strength with one set of damage limits, as the microstructural information (loss of stiffness, i.e., increase in cracks) is already considered in the evaluation of damage. In this manner, the damage limits can be used as design limits by engineers while designing a component with complex a fibre-layup via filament winding, such as a nozzle [91].

4.4 Conclusion

In this work, an anisotropic damage model based on continuum mechanics is integrated with a damage-based failure criterion to predict the inelastic behaviour of two ceramic matrix composites manufactured via filament winding technology. Damage in the material is defined as continuous stiffness reduction in the laminate with increasing load. As there were no test results available for unidirectional plies, the elastic properties of a virtual unidirectional ply were evaluated from the tensile tests carried out on laminates with different fibre orientations. The parameters required for damage models were derived from the stress–strain curves obtained from tensile tests. The damage model was implemented in a

commercial finite element software, ANSYS Workbench. It was observed that laminates with a fibre orientation where the fibre carries most of the load, e.g., ±15°, exhibit a relatively linear stress–strain curve compared to the matrix-dominant direction, e.g., ±60°. In this way, the inelastic behaviour of laminates with varying fibre orientations can be predicted with a single parameter set for damage description.

In order to predict the failure stress and strain of laminates, a damage-based failure criterion inspired by the Tsai-Wu failure criterion was proposed. The failure criterion considers the coupling of damage variables in different directions, which makes it appropriate to be used for anisotropic CMCs. The predictions made by the damage-based criterion were closer to the experimental results in comparison to the stress- or strain-based Tsai-Wu failure criterion. Moreover, a damage-based criterion can be directly related to the physical attributes of a material, such as crack density, and has potential to give an insight into the micromechanics of the material despite its macroscopic nature.

The application of the proposed model on Iosipescu shear tests showed discrepancy when compared with the experimental results. All three in-plane stress components (tension, compression and shear) are present in the sample based on its fibre orientation. This discrepancy is attributed to the assumption that the material behaves in a linear elastic manner under compression, i.e., no damage occurs under compression. The further investigation of the fracture surfaces of materials after failure led to the conclusion that the Iosipescu shear test can determine the shear modulus of the material but is not an appropriate test to evaluate the shear strength of the material because of the interdependence of notches and the fibre orientation of the laminate.

The proposed damage-based failure criterion considers loss of stiffness in principal material directions, which can be used as design limits for a CMC component under thermomechanical loading and can differentiate between damage mechanisms under tension and compression. Loss of stiffness can be measured via non-destructive testing (NDT) methods, such as acoustic emissions, and can be used as a quality assurance criterion to determine the life cycle of a CMC component after being in operation for a definite period of time. In a similar way, other properties like fatigue or creep can be modelled by employing models at micro level to obtain the material parameters for the homogenised material and then using those parameters for the conventional finite element analysis of the CMC structures.

5 Digital manufacturing process chain

5.1 Introduction

In the previous chapter, links between the individual relationships between process-structure, structure-property and property-performance with examples were illustrated. In order to implement such a relationship and optimize the manufacturing process, systematic connections between the involved steps are required. This ensures the seamless flow of the data over all the stages of the manufacturing process. Moreover, this process data is required as input parameters for the simulation models. For example, in the case of the simulation of the pyrolysis process in Chapter 2, the maximum temperature and the heating rate comes from the data obtained from the pyrolysis oven. In a similar fashion, the fibre orientation obtained from the filament winding process can be directly integrated into the simulation models and the thermo-mechanical performance can be predicted based on this process parameter [6].

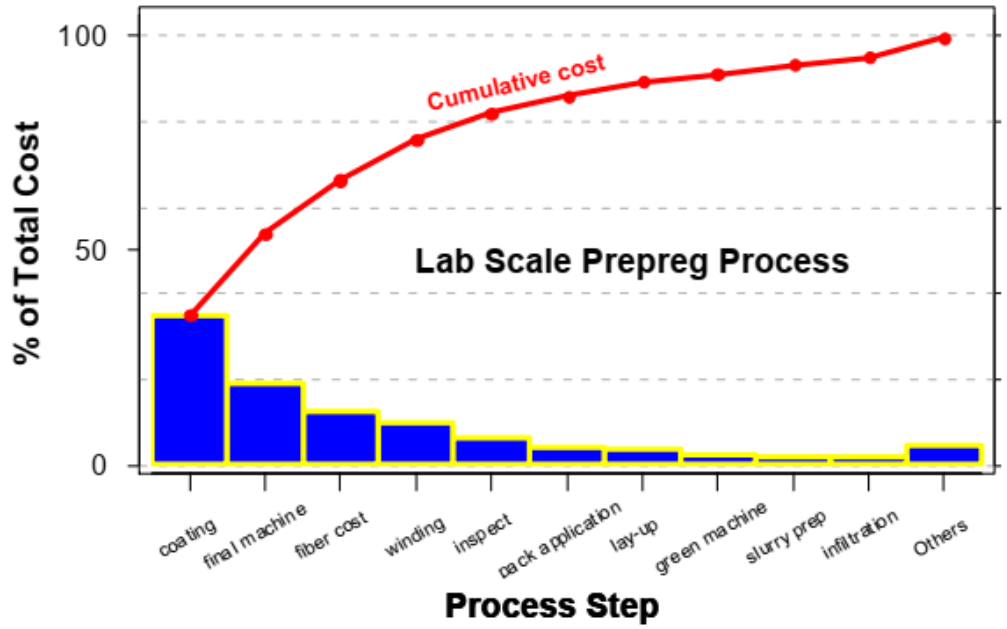

Figure 5.1: Distribution of costs involved in the manufacturing process of SiC/SiC [1].

Apart from the input for the multiscale simulations, systematic process data collection and analysis can help in reducing the production costs (as shown in Figure 5.1) of the material. With the help of a quality assurance method after each individual step, production of a component can be halted if any unexpected defects/features are observed in the component during the processing in an intermediate step. For example, if the fibre disorientation, detected via in-line optical methods or Computer Tomography during the filament winding process, is above the allowed tolerance, further processing of the component is not required as it will not deliver the required performance in the planned application.

Abovementioned issues are already addressed in the case of CFRPs in the automotive field. For e.g. in the work of Henning et.al, a case study from the perspective of automotive industry is presented [117]. CAE solutions for individual steps involved in carbon fibre reinforced plastics are reported but the challenge of combining them with the manufacturing equipment remains. Moreover, the computation time for such complex physical processes is very high and cannot be realistically used for the optimisation of the manufacturing chain. The application of data-based surrogate models obtained from physical models becomes inevitable in this case as well, as demonstrated in Chapter 3.

In this chapter, results from an extensive literature study of existing processes and their digital counterparts have been summarized. The inputs and outputs required from each individual step are defined. Based on these parameters, different processing routes can be used choosing the appropriate steps in order to achieve the CMC which is suited for a particular application. In addition to the digitalized manufacturing chain, connections to design and testing of a component must be established in order to include all the important aspects of a new CMC-component development and a concept is proposed to achieve the same.

5.2 Module-based digital manufacturing process chain

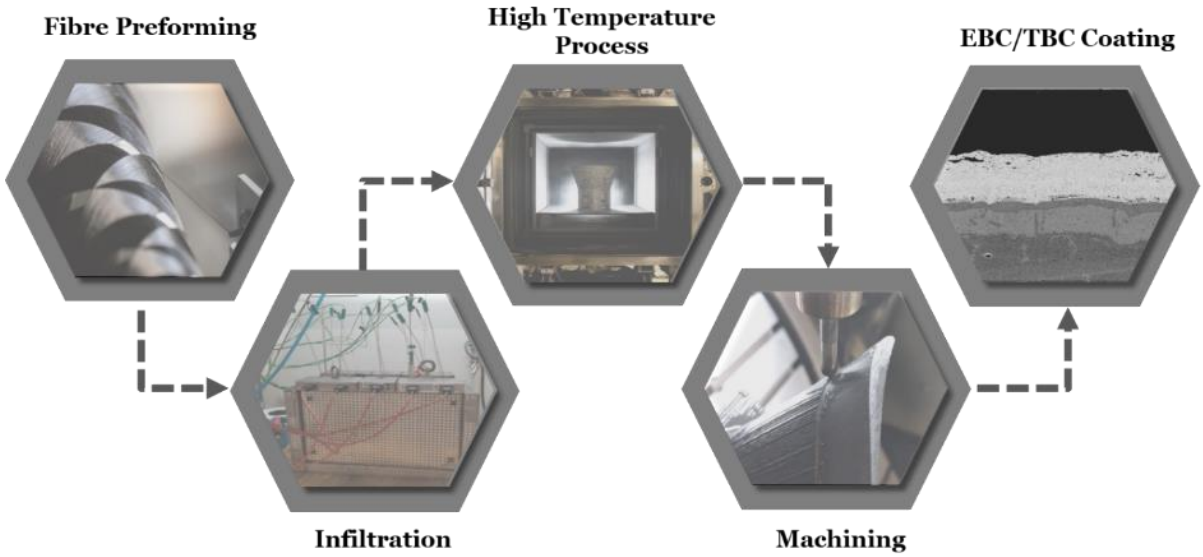

Figure 5.2: General manufacturing process chain of CMC for aerospace applications.

The manufacturing process of CMC can be broadly presented as shown in Figure 5.2. The actual processing route depends on the type of CMC required for any specified application. In the upcoming section, the digital counterparts of the steps involved and their interface with the manufacturing equipment is discussed. The aim is to give an overview of the available process modelling approaches for individual steps and the data that can be extracted from the manufacturing equipment with the help of inline controlling or post-step analysis.

5.2.1 Fibre Preforming

Fibres:

The choice of fibre highly depends on the operating conditions of the CMC-component to be manufactured. Carbon (C), silicon carbide (SiC), alumina (Al_2O_3), mullite and zirconia are majorly used as fibre reinforcement in the CMCs. Developments have also been reported for ceramic matrix reinforcement with metallic fibres such as molybdenum and tungsten [118]. Each fibre class comes with its own set of physical properties, and consequently a material designer must make this decision based on the required application. The cost also plays a major role, where it ranges from several hundred Euros/kg in the case of Al_2O_3 to several thousand Euros/kg in the case of SiC fibres.

The physical and thermo-mechanical properties of commercially available fibres is usually provided by the manufacturers. In order to ensure the quality of fibres, SEM images of the fibres can be taken and properties like fibre diameter and fibre circularity can be evaluated. However, a data sheet is provided with each batch of the fibres, which is usually sufficient to ensure the homogeneity of different batches obtained from the manufacturers.

Table 5.1: Possible quality assurance methods for fibres and their outputs

Test/Method	Output	Application
Scanning Electron Microscopy	Diameter, Circularity	Virtual microstructure: Fibre properties
Tensile Test	Strength, Weibull Modulus	Virtual microstructure: Fibre properties

Fibre Architecture:

Based on the required reinforcement direction and the employed shaping process, the fibre architecture of the composite is decided. Different kind of textile preforms which are available are [119]:

- 1D: Unidirectional tapes
- 2D: Weaves, Braids, Knitting, Winding
- 3D: Weaves, Braids, Stitching, Knitting

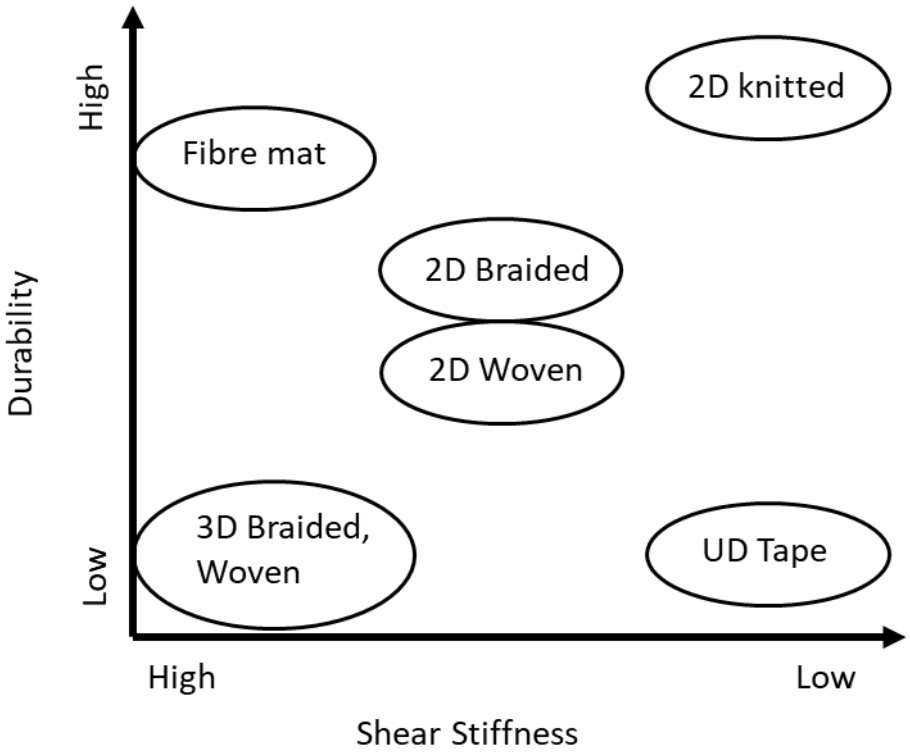

Figure 5.3: The characteristics of the textile fabrics based on their shear stiffness and drapability [119].

Some of the methods used in component shaping and their digital counterparts are discussed in detail:

Winding

Filament winding technique is usually used for the components which are axisymmetric in nature. Thanks to its cost effectiveness, even non-axisymmetric components like wind turbine blades and bus chassis are manufactured via filament winding. Based on the fibre type, the winding of the fibres is performed with (wet winding) or without resin (dry winding). Since it is an established way of shaping, many analytical methods and commercial software are available to simulate the process. Faria proposed a multi-physics model to include the parameters like winding pattern, fibre tension, winding speed, curing time after winding, etc. [120] and studied their effect over the wound component. A similar study was performed by Henninger et.al for glass fibres [121] and carbon fibres [122], in which parameters like roving pretension, process speed, impregnation temperature and fibre volume content were varied [121]. A detailed overview of dry filament winding is given by Sofi et.al [123] where the application of differential geometry to generate geodesic and non-geodesic trajectories on a mandrel is demonstrated. The commercial software available for filament winding were also listed in this work: Cadfil® (Crescent Consultants), CADWIND® (MATERIAL), Wound Composite Modeler (Abaqus, Dassault Systèmes) and ComposicaD™.

With the help of such software, the information about the local fibre orientation can be directly integrated into the finite element analysis of the manufactured component, as demonstrated in an earlier work of the author [6]. However, these values are the 'target values' and in an ideal case should be the same as the 'real values' obtained during the manufacturing. In order to detect the fibre misorientation or such other winding anomalies, several methods are reported in the literature. Toptas and Akkus proposed an electrical resistance methods to measure the damage detection of carbon fibre during the filament winding process [124]. Infrared thermography was used as inline controlling technique to detect the gaps between the tapes/roving in the work of Colas et.al [125]. A novel method based on infrared image acquisition was investigated by Hopmann et.al to detect and evaluate fibre-band during wet filament winding [126]. These techniques might be integrated into the process chain for data generation for simulation and quality control of the process itself.

Table 5.2 Inline control methods for filament winding and braiding

Test/Method	Output	Application
Electrical resistance (in-situ)	Damage in fibres	Virtual microstructure: Fibre strength
Infrared Thermography (in-situ)	Gaps between filaments	Input for infiltration simulation
Optical methods (in-situ)	Local fibre orientation	Input for infiltration simulation
Computer Tomography	Local morphology	Quality control

Braiding

Braiding is a textile manufacturing method with an interlace yarn to form a continuity between the layers and can deliver near-net shapes to the component. It provides improved through thickness properties in comparison with the filament winding. Several analytical and finite element models are presented in the literature. With consideration of phenomena like the slipping of yarns on the mandrel, the yarn trajectories were predicted by Kessels et.al [127] and was extended by Ravenhorst et.al [128] to predict the path and velocity of a complex mandrel shape through the guide ring. Dedicated commercial software like filament winding are not common for braiding process and often some extensions to the commercial software are required to model the braiding process. Hans et.al [129] combined Catia V5 (Dassault Systèmes), Matlab (Mathworks) and Abaqus (Dassault Systèmes) to obtain the mandrel's path and velocity. Czichos et. al used LS-Dyna (Livermore Software Technology Corporation) and established a relationship between yarn tension, process speed, contact friction energy and fibre damage during the process [130]. A detailed study of the braiding process and the influence of the process parameters over the performance of the component was analysed via finite element method for biaxially braided [131] and triaxially braided components [132, 133]. Swery et.al even evaluated the permeability

of the preform for the next step in the manufacturing process, i.e. polymer infiltration and studied the filling pattern based on different mandrels and braiding parameters [134].

The quality control methods of the braiding process are analogous to the filament winding. An extensive study of the available measurement techniques and the challenges associated with it, was presented in the work of Melenka et.al [135] and are summarized in Table 5.3.

Table 5.3: Quality measurement methods for braiding process [135]

Test/Method	Output	Application
Optical strain measurement (digital image correlation and high-speed imaging)	Local deformations	Virtual microstructure: Distance between rovings
Computer Tomography	Local morphology	Quality control
µ-CT	Braiding angles, pores and voids	Virtual microstructure generation

Draping:

The abovementioned techniques are employed for rather simple geometries like flat plates, cylindrical tubes (or other axisymmetric shapes), etc. However, for complex geometries like those of vanes, shrouds, exhaust cones, draping of weaves is one of the most common shaping techniques. The draping process can result in an inhomogeneous structure with varying local fibre orientation (due to shearing) and thickness based on the target geometry. To avoid wrinkles in the preform, the textile must be cut in a specific shape adjusted to the required geometry. For this reason among others like prediction of shearing in the weave, the simulation of draping process plays a crucial role in the component designing process and choosing the best draping strategy. Commercial software available for draping simulation are MSC laminate Modeler (MSC Software), PAM-Quikform (ESI Group), Composite Modeler (Dassault Sysèmes), Fibresim (Siemens) and Ansys Composite PrePost (ANSYS). An overview of modelling techniques for draping and their validation with the help of optical measurement systems is reported in by Hübner et.al and [136], Mallach et.al [137] and Döbrich et.al [138]. Local hot spots with high shear angles on the preform could be predicted in the geometry. The method of high-frequency eddy current testing was used and a comparison with finite element simulation was performed by Bardl et.al [139]. This technique has the advantage that the measurements are independent of the lighting conditions. The temperature effects during the following thermal treatment step coupled with draping simulation was studied by Tabiei und Murugesan [140]. The quality assurance methods mentioned in the ‘Winding’ and ‘Braiding’ sections are also applicable for the draping process.

Fibre Coating:

Based on the chosen manufacturing route, the fibre coating required for a certain application is performed before shaping [141] or after shaping [84]. Unlike previous processes, fibre coating is exclusively employed in the manufacturing process of CMCs to fulfil two purposes: a) protect the fibres during the heat treatment processes and b) provide the weak fibre-matrix interphase and increase the damage tolerance of the material. The coating can be applied on the fibres in liquid or gaseous form. The modelling of this step is not so prevalent when compared to other processing steps because of its complexity and its exclusivity to weak interface composites. An analytical process model was developed by Sandia National Laboratory for the deposition of BN and SiC interphases via Chemical Vapour Infiltration [142]. Optimized values of process parameters like time, temperature, reactant concentration, feed rate and stoichiometry were predicted by the model. Apart from this work, other gas infiltration models are more focussed on matrix generation via CVI and are discussed in Section 5.2.3.

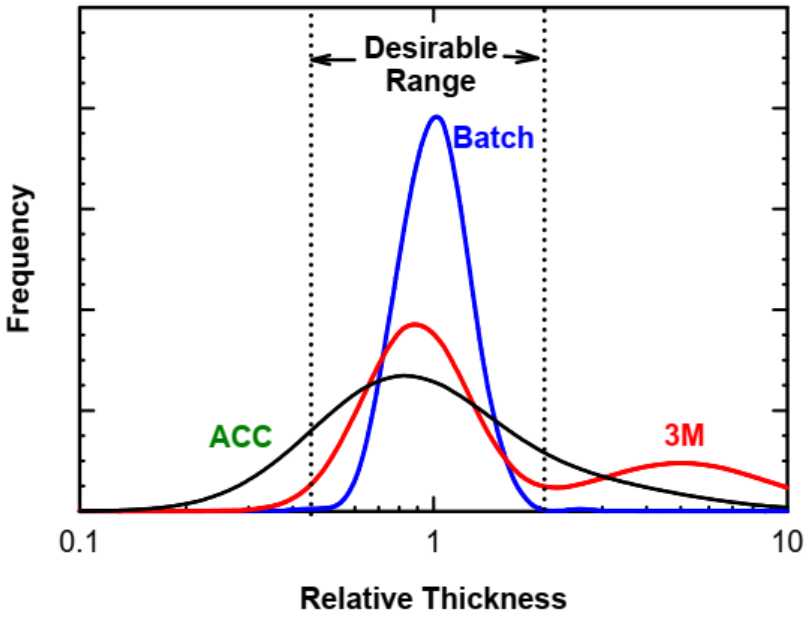

Figure 5.4: Frequency distribution of the achieved coating thickness obtained from coating processes from different companies [1] where ACC: Advanced Ceramics Corp. (now GE Advanced Ceramics); Batch: combined development of Synterials Inc. and GE Global Research; 3M: 3M Company

Although dedicated models for the prediction of the coating deposition behaviour are not mature enough, the fibre coating process and the involved parameters are intensively studied in the literature. Homogeneity and room temperature tensile strength were the criterion to choose the appropriate coating system for the SiC/SiC composite manufactured by GE Aviation [1]. For example, in Figure 5.4, a qualitative representation of the coating thickness distribution by different processing routes is shown. The acceptable thickness from the perspective of sufficient fibre debonding and protection from

chemical attack was denoted as ‘desirable range’ by the material scientists. Since, it was challenging to use the coating thickness as the quality criterion of the fibre coating due to extensive manual effort involved in the analysis of the SEM images, weight of the fibres before and after the fibre coating was used as the quality criterion. With the help of advanced image segmentation techniques, the analysis can be automated to a certain extent. However, preparing the samples for SEM characterisation and taking appropriate images is time consuming and is not practical to be used as an inline quality management method.

The techniques to monitor the process parameters like gas temperature, chemical composition near the substrate surface and the fluid flow during the process with their advantages and disadvantages are summarized in the work of Choy [143]. The relationship between the process parameters and the physical properties of the fibre coating was also discussed. This study showed that there is a strong relationship but the CVD process itself is very complex and expensive to perform detailed experimental parameter studies for different combinations of coatings and substrates.

Table 5.4: Post process quality measurement methods after chemical vapour deposition (CVD)

Test/Method	Output	Application
Scanning Electron Microscopy	Coating thickness	Virtual microstructure generation, quality control
Weighing machine	Change in the weight of the fibres	Quality control (not applicable in multi-coating system)
µ-CT	Homogeneity of the coating	Virtual microstructure generation, quality control

Few post-process methods are listed in Table 5.4 to control the quality of fibre coating after the chemical vapour deposition process.

5.2.2 Infiltration

In order to manufacture any composite with the perform from the previous step, matrix has to be generated with the help of precursors. The matrix can be generated either via CVD process or via precursor infiltration techniques. The infiltration can be classified into two types: [144]

- Particle infiltration: The target matrix is infiltrated in the form of a liquid-based slurry where the ceramic powder is mixed with a liquid and infiltrated into the fibre perform.
- Resin infiltration: A polymer precursor which later converts into ceramic after chemical reactions or a ceramic precursor which converts into ceramic after heat treatment is directly infiltrated into the fibre perform.

Since resin infiltration is a common technique involved in the manufacturing process of CFRPs, advanced simulation models are available to model this process. Modelling of particle infiltration, on the other hand, poses a challenge in modelling due to the presence of different phases in the slurry which adds to the complexity of the fluid flow problem that needs to be simulated. Furthermore, this technique is focussed on a certain class of CMCs (Ox/Ox and UHTCMC) such as WHIPOX™ where Al_2O_3 particles are infiltrated into the fibre perform with the help of a water-based slurry. Due to this reason, there is no dedicated commercial software to model the flow of particle slurry physically. However, with consideration of slurry properties like density, viscosity, surface tension and wetting angle, flow of the slurry as a homogenous liquid can be modelled. In the study of Baché et.al, with the help of flow simulations, the viscosity was found to be the most important property that influences the impregnation of the slurry in an oxide ceramic composite material [145]. Apart from this study, other research reported in the literature mostly focussed on resin infiltration techniques and are discussed in the following section.

Resin Transfer Moulding (RTM) is one of the most common techniques used to manufacture CFRP parts and is an intermediate step in the manufacturing process of CMCs via Reactive Melt Infiltration (RMI) and Polymer Infiltration and Pyrolysis (PIP). The resin is injected into a mould containing pre-placed fibres with inlet and outlet for the resin. Based on the resin and the viscosity required for the infiltration, the process might take place at temperatures higher than room temperature. A detailed review of the modelling techniques for RTM is given in the work of George [146], Yang et.al [147] and Michaud and Mortensen [148]. With the help of coupled numerical model for phenomena like permeability, compressibility, dynamic viscosity and capillary pressure, the resin infusion process was optimized by George. Yang et.al even modelled the formation of air bubbles during the filling process and suggested that the fibre bundle spacing and contact angle can reduce the formation of air bubbles and consequent voids in a composite part. The parameters which can be optimized in the process are the process temperature, pressure, permeability, the position of inlets and outlets for the resin and the choice of the resin itself i.e. influence of the physical properties of the resin such as viscosity, curing rate, etc. The commercial software which are available to model RTM are PAM-RTM from ESI-Group, Moldex3D from CoreTech System, Simcenter 3D from Siemens Industrial Software, ANSYS Fluent from ANSYS Inc. and RTM-Worx from Polyworx. An opensource software available for RTM simulation is OpenFOAM. The inputs required by the simulation are resin properties, fibre perform and the part geometry. Based on the information available, properties like permeability are either obtained from the experiments or performing infiltration simulation at micro level, i.e., infiltration of single fibre bundles. This local permeability is then used as input for modelling the infiltration of the fibre preforms. The output from RTM simulation is impregnation time and the presence of voids in the structure which in turn contributes to the performance of the component. Based on this information, the impregnation strategy for a specific part should be employed.

Vacuum Assisted Resin Transfer Moulding (VARTM) is preferred over the conventional RTM process to reduce costs, which unlike RTM requires just a vacuum bag to close the mould. The modelling techniques for RTM are valid for VARTM as well, although an overview about the process simulation models implemented for VARTM was given by Shah and Chaudhary [149].

In order to validate the simulation models and perform the quality control of the RTM process, in-situ and ex-situ characterisation techniques are required. Optical measurement of voids was reported by Lystrup et.al [150], where with the help of automated image analysis bubbles were detected and a minimum velocity threshold for the resin to minimize macro-void formation.

Table 5.5: Quality assurance methods available for in-situ and ex-situ observation of the infiltration process

Test/Method	Output	Application
Optical methods	In-situ void formation	Quality control, validation of the impregnation models
Ultrasound/ CT	Voids in the component	Quality control, validation of the impregnation models

5.2.3 High Temperature Process

The manufacturing process of CMCs always involves one or more high temperature processes based on the involved constituents and the target application. The process parameters during this step heavily influence the microstructure and the properties of the end material as the matrix formation takes place during this step. Even after the generation of the ceramic matrix after heating, effects like presence of thermal residual stresses after cooling down from the heating process can impact the structural integrity of the a CMC component under thermo-mechanical loading [151]. The major high temperature processes are discussed in this section.

Sintering:

Sintering is one of the oldest methods used to manufacture monolithic ceramics and is used for fibre-reinforced ceramics as well. The ‘green’ compact part with ceramic powder, usually infiltrated in the form of a slurry, is heated at high temperatures, ranging from 1300° C in the case of aluminium oxide matrix to 1800° C for ultra-high temperature ceramics (UHTC). Diffusion takes place at the grain boundaries resulting in the consolidation of the particles to form the ceramic matrix. The modelling of this phenomenon has been a topic of research for last few decades but was mostly restricted to monolithic ceramics. The presence of fibre as reinforcement poses an additional challenge in modelling a complex problem of sintering. An overview of existing models was given by Sarbandi [152]. The dimensional changes in ceramic parts during the sintering is a major issue and its prediction is always the desired outcome of the process simulation in order to optimize the process parameters or the part design to obtain a final component with predefined geometry for any application. A dedicated study for

the modelling of sintering process of fibre reinforced ceramic and its validation is not performed to the knowledge of the author. GeoDict from Math2Market GmbH, COMSOL Multiphysics® from the COMSOL Group and Star-CCM+ from Siemens Industrial Software are three commercially available software which consider the multi-physical nature of the sintering and can be used for its modelling.

Chemical Vapour Infiltration (CVI):

As discussed in the 'Fibre Coating' section, the Chemical Vapour Infiltration process can be used not only to fabricate fibre/matrix interphases but also to build the matrix in a CMC. CVI is the most complex process among the other high temperature processes as it includes simultaneous phenomena like transport and reaction of gases, infiltration of gases into fibre preforms and the structural evolution of the matrix. The number of process parameters that can be optimized is enormous and the lack of possibility of in-situ observation of the preform hinders the use of modelling and validation of results for this particular process [153]. Nevertheless, efforts have been made in the past decades to optimize certain aspects of the process analytically and introduction of concepts like thermal and pressure gradients are result of it. Most noteworthy work in the field of modelling of CVI process is done by Vignoles and the research work is summarized in [154, 155]. With the help of physico-chemical coupling and based on the complexity of the phenomenon, detailed multiscale modelling or semi-analytical approaches were proposed to investigate the infiltration of gases into the preform. Micro Computer Tomography (µCT) was used to validate the gas infiltration and matrix deposition results obtained for a representative volume element at meso-scale. In a more recent work of Sankaran et.al [156], CVI process was modelled via Computational Fluid Dynamics (CFD) for a 3-D woven preform in order to optimize the manufacturing of SiC/SiC. Realistic modelling of forced flow CVI technique and SiC deposition kinetics were identified as major challenges in optimizing and reducing the processing time of CVI. CFD simulations were also used by Li et.al to optimize the deposition rates of pyrolytic carbon [157]. Phenomena like mass transport, chemical vapour deposition and surface growth, gas-phase and surface chemical reactions were coupled together with the help of finite element approach in order to gain the optimum values for concentration of inlet gases. A multiphase field model coupling abovementioned phenomena was proposed by Zhu and Schnack for the deposition of SiC during CVI [158]. The effectiveness of the thermal gradient in achieving full densification of the preform was also found out in this study. In a further work of the authors [159], the evolution of the microstructure was predicted and the approach was validated with the results obtained from three different deposition strategies at varying temperatures.

Pyrolysis:

It is a process where the organic substances present in the resin infiltrated fibre preform decompose under elevated temperatures usually above 900° C for long periods (up to some days) and result into a ceramic matrix. The heat treatment is usually conducted in the presence of an inert atmosphere and in absence of oxygen. The effect of pyrolysis parameters on CMCs is reported in many research works. The effect of carbonisation temperature over the mechanical properties of C/C-SiC was shown by Reichert et.al. An increase in the stiffness of the derived C/C-SiC samples after the temperature was increased from 1600° C to 2000° C during the pyrolysis and generation of intermediate C/C composites [160]. The nature of the pores in C/C state and its subsequent impact on the capillary forces during siliconisation is also affected by the temperature as reported in the work of Wu et.al [161]. An increase in the temperature range of the pyrolysis from 900°-1300° C to 1400°-1600° C results in a decrease in the capillary infiltration rate C/C composite during liquid silicon infiltration.

Pyrolysis process, like other high temperature manufacturing processes, consists of coupling of mechanical, thermal and chemical problems. This increases the complexity of the model which is generally reduced to a simplified thermo-mechanical problem, as shown in Chapter 2 and reported in the work of Schulte-Fischedick [33]. In the work of Qin, a multiscale approach was used to model the pyrolysis process of a CFRP [162]. Temperature evolution, mass loss and mass loss rate were predicted with the help of a transient analysis of pyrolysis. Modelling of PIP process including multiple cycles of resin impregnation and pyrolysis was published by Jiang et.al by coupling thermo-chemical, resin flow and mechanical aspects of the process [163]. The delamination of the plates due to the residual stresses and their locations were predicted and a relationship between the residual stresses, the plate geometry and pressure was established. It was also observed that the defects usually occur in the early cycles rather than later cycles, suggesting focus on early PIP stages for defect detection in the components.

Reactive Melt Infiltration (RMI):

Near-net shaped manufacturing of CMCs parts can be achieved by RMI process with shorter processing time and cost effectiveness when compared to CVI. The reactive melt infiltrates into the porous preform obtained after pyrolysis with the help of capillary forces where the melt reacts with the matrix to form the ceramic matrix. Most of the work reported in the literature deals with the infiltration of liquid silicon into a porous carbon matrix preform where the molten silicon reacts with carbon to form silicon carbide matrix in the case of CMCs such as C/SiC, SiC/SiC, etc. However, in the recent years, RMI has also been used to manufacture Ultra High Temperature Ceramic Matrix Composites (UHTCMC). In the works of Kütemeyer et.al and Vinci et.al, carbon fibre-reinforced ZrB_2 matrix was processed with the help of reaction between boron based preform and Zr alloy melts such as Zr_2Cu. Apart from the fibre

reinforced CMCs, RMI is also being used in the additive manufacturing of ceramics. After the 3D printed preform is pyrolyzed, molten silicon is used to form Si-SiC composite with carbon preform or molten Zr_2Cu reacts with WC preform to form W-ZrC composite.

The parameters of the RMI process were first studied by Behrendt and Singh [164] where the relationship between the pore size and the infiltration mechanism in the manufacturing of monolithic ceramic was investigated. The range of pore size was later extended by Nelson and Colella and it was shown that the chemical reaction of the melt with the matrix retards the process of melt infiltration [165]. This suggests that the infiltration rate is also a function of the reaction rate of the melt and the matrix. In his study and modelling of the siliconisation process, Einset found out that the siliconisation is most sensitive to these two parameters: the pore-neck diameter and the SiC reaction barrier thickness which forms when silicon reacts with carbon [166]. In the work of Naikade, the effect of the pores, infiltration temperature and Si-Zr alloy melt instead of conventional molten silicon on the siliconisation process of C/C and SiC/C preforms was studied [167]. Additionally, an analytical model based on the parameter study was developed. Dutka proposed a modelling approach that uses permeability properties of the porous preforms and investigated the relationship between infiltration distance in the preform and the infiltration time, which was found to be more important than the shape and size of the infiltration zone [168]. All the physical and chemical phenomenon taking place during the siliconisation and their relationship with each other was investigated by Mica et.al [169] and is shown in Figure 5.5. They proposed a fully integrated multi-physics model of the RMI process and demonstrated the application of the coupled modelling approach in the processing of a gas-turbine engine shroud. The deformation in the engine shroud due to the siliconisation process is the output of this computational methodology. Based on this information, the CMC components can be design accordingly keeping the geometrical effects of process into consideration.

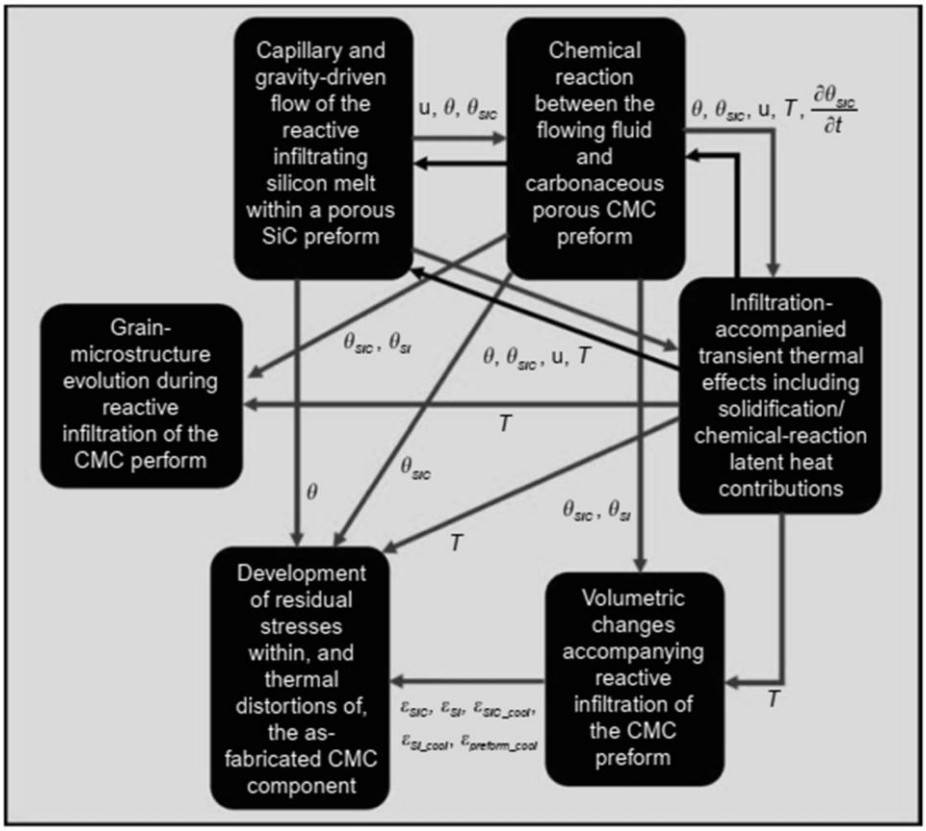

Figure 5.5: Pictorial representation of the modelling approach proposed by Mica et.al to simulate the liquid siliconisation approach [169].

The validation of the modelling results with the experimental values always poses a challenge in a high temperature process. Optical microscopy with quantitative digital image analysis and weight measurements are the techniques which can be used to ensure the quality of the process. In the study of Hofbauer, six reaction stages were identified based on the examination of the phase distribution and structural changes during the reaction. These results can also be used to validate the simulation results [170, 171].

Table 5.6: In-situ and ex-situ methods to monitor the quality of high temperature processes

Test/Method	Output	Application
Thermo-optical measurements	Process temperature	Quality control, temperature field validation
Weight measurements	Mass before and after process	Quality control, validation of mass conservation models
Ultrasound/ CT/ µCT/ SEM	Microstructure information	Quality control, validation of the post-process virtual microstructures

5.2.4 Machining

CMCs exhibit excellence properties which are advantageous for many high temperature applications but properties like anisotropy, brittleness and hardness pose a challenge when it comes to machining of the CMC components. The issue of brittleness is resolved to a certain extent with the fibre reinforcement. However, machining of the CMC components is indispensable as more and more components find their use in different applications and need to deliver certain tolerance or have to be integrated into an existing system with other materials around it. If optimum tools and machining parameters are not used, it can adversely affect the performance and structural integrity of a CMC component as it is a kind of subtractive process. Since it also affects the microstructure of the material, machining of a novel material also needs to be considered in material development and component design process. A detailed overview of the machining techniques for fibre reinforced SiC with their advantages and disadvantages is presented in the work of An et.al [172]. Defects like fibre damage, matrix cracks, interfacial debonding, delamination and bifurcation of yarns were observed in the CMC components during machining. Machining parameters, tool parameters and material parameters such as fibre orientation, machining direction and density should be optimized to avoid the occurrence of abovementioned defects. Surface defects were studied specifically in the work of Diaz et.al where the effects of different machining techniques over the surfaces of the material was investigated [173]. Suggestions regarding the appropriate machining technique based on the required feature or operation were made with the help of surface quality control via electron microscopy and Computer Tomography.

Table 5.7: Methods to monitor the effects of machining over the material

Test/Method	Output	Application
Electron microscopy	Microstructural information	Input for modelling to consider the surface defects after machining
CT measurements	Geometrical changes	Monitor structural integrity

5.2.5 TBC/EBC Coating

Thermal or Environmental Barrier Coating (TBC/EBC) are usually employed in CMCs based on the target application. In order to ensure longer lifetime of hot section components of a gas-turbine engine, the application of TBCs/EBCs become inevitable under harsh environmental conditions. However, application of such coating and their interaction with the substrate material (CMC) increases the complexity of an existing multi-process manufacturing chain. The behaviour and the properties of the substrate material, the bond coat and the final coating must be compatible with each other or else, the coating system will not survive the aggressive turbine conditions resulting in reduced life of the component. A detailed overview of coating systems was given by Abdul-Aziz with processing, testing

and modelling of different TBC and EBC systems [174]. The characteristic differences between both the coating systems were also discussed. The author concluded that the life of the coating plays a more important role in the life of a CMC component under operation than the substrate material itself. However, the amount of research in the field of testing and understanding of the failure modes and their causes is very limited. In an another work of the author, different NDT techniques like optical microscopy, computer tomography and Digital Image Correlation (DIC) were used and their capabilities to capture the crack initiation on the coating was assessed [175]. DIC was found out to be the most appropriate method to analyse the crack initiation, however it is limited to room temperature analysis. Furthermore, a progressive failure analysis using finite-element method was performed in order to predict damage initiation and propagation in a SiC/SiC sample with an EBC. The model was extended with a fracture mechanics based approach and crack deflection/penetration criteria were established for a single layer coating system based on parameters like coating thickness, crack length and strain energy release rate [176]. A detailed review of numerical methods which can be employed for the modelling of the behaviour of the EBCs in service conditions was given by Lv et,al which can be extended to other coating systems as well [177].

5.2.6 NDT Techniques

Non-Destructive Testing (NDT) is an integral part of any manufacturing chain to ensure the stability of the process and the quality of the manufactured components. Few methods were summarized for the different manufacturing steps involved in the processing of CMCs. The NDT methods which are used and reported in the literature for quality assurance of the CMC-components in the intermediate stages of manufacturing or before putting them into operation:

- Vibrational analysis
- Acoustic Emission Testing
- Eddy current testing
- Thermography
- High Frequency Radiowave Technique
- Ultrasound Testing
- Optical Analysis
- Radiography
- Computed Tomography

Apart from these methods, NDT via image analysis has gained popularity in the recent years, thanks to the developments in automatic image analysis assisted by machine learning and artificial intelligence. For example, Pierce and Liu used different lighting conditions and the reflections from the fibres to

obtain the fibre orientation at the surfaces in a component [178]. The technique was even demonstrated for short fibre reinforced composites and can be implemented to detect other surface anomalies as well.

5.3 CMC Part Development Concept

Different manufacturing steps, respective quality control methods and modelling techniques were discussed in the previous section. However, in order to optimize the process, these quality control methods and modelling techniques need to be combined with each other to realize a digital manufacturing process chain. Certain inline process control concepts are already reported in the literature for CFRPs. For example, an inline process control concept (Figure 5.6) was proposed by Gubernatis et.al for CFRPs produced via Liquid Composite Moulding (LCM) [179]. It can be observed that there are in-situ process parameters for each individual steps which is assisted by a quality control method for the intermediate product after each step. Since, production of fibre (C or SiC fibres) reinforced polymer is an intermediate step itself in the LSI-processing, the concept can be extended to CMCs as well. The integration of the results gained from the process models can optimize an individual ongoing process based on the characteristics obtained after quality control of an intermediate product. For example, if the fibre orientation at the surface deviates from the desired value, the direction parameters for machining can be varied according to the deviated values of the fibre orientation.

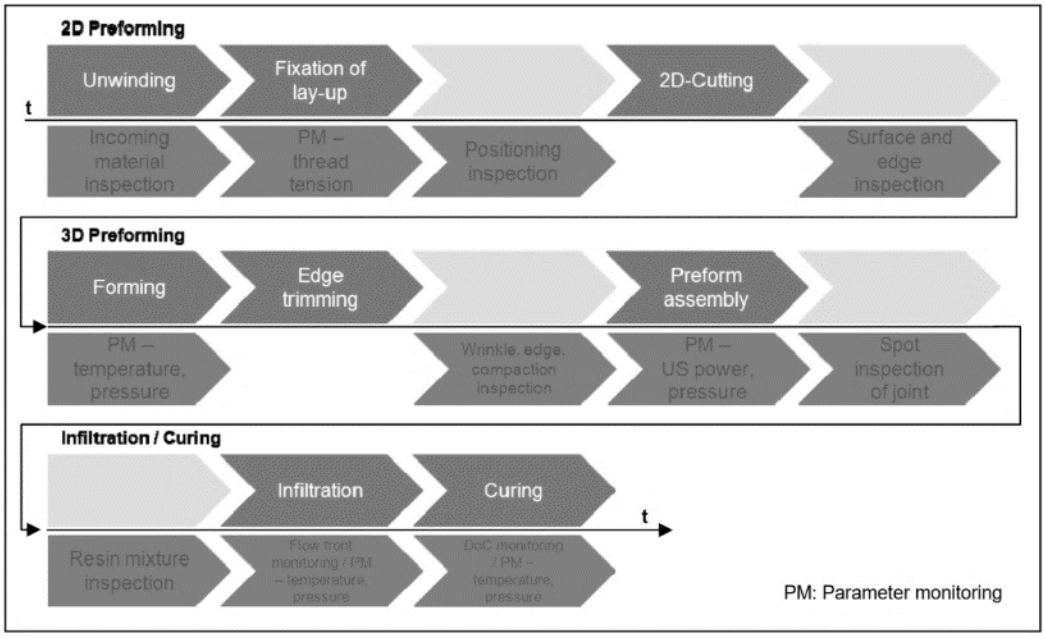

Figure 5.6: Process chain for CFRPs produced via Liquid Composite Moulding with individual steps [179].

In the current section, a digital manufacturing process chain for the design of a SiC/SiC vane is proposed based on the literature study in the previous sections and the experience at DLR in manufacturing CMCs. The manufacturing process preferred to manufacture a SiC/SiC gas turbine vane is Reactive Melt

Infiltration, or precisely Liquid Silicon Infiltration in this case. This process exhibits advantages like denser matrix providing high conductivity, strength at higher temperatures or cost-effectiveness over other processes like PIP or CVI. The temperatures during operation in an aeroengine can rise up to 1500°C and the service hours in the case of combustors is minimum 24,000 hours and 48,000 in the case of shrouds [1]. Although, the surface temperature of the components is expected to be around 1200°C, the LSI SiC/SiC exhibits superior properties than the PIP SiC/SiC [69]. The lower porosity value compared to Polymer Infiltration and Pyrolysis (PIP) ensures the desired oxidation and corrosion resistance during the operation under harsh environments.

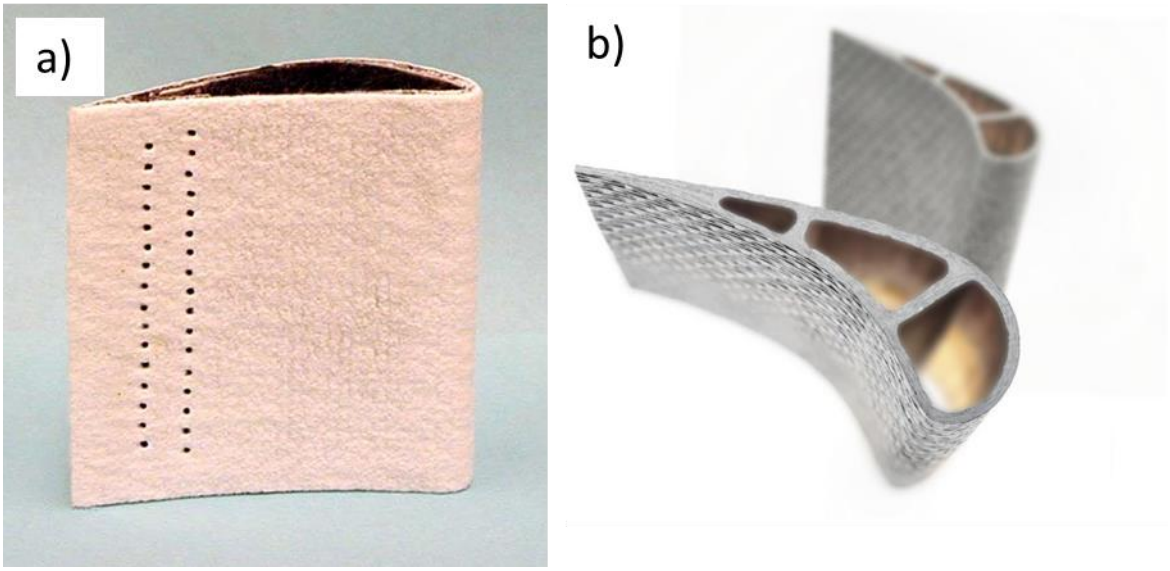

Figure 5.7: Turbine vanes from SiC/SiC a) coated with an EBC (NASA) [180] and b) without EBC (Rolls Royce) [181].

Few examples of SiC/SiC vane manufactured by NASA and Rolls Royce are shown in Figure 5.7. It can be observed that despite the use of CMCs as vane, the vanes possess air channels to allow internal cooling of the blades. The holes on the trailing edge ensure the passage of cold air towards from the internal channel towards the hot region of the turbine. It should be mentioned at this point that the aim of using CMCs in gas turbines is to completely avoid the use of cooling to achieve higher combustion efficiency. However, these prototypes were developed for testing and for comparison of the cooling efficiency of CMC vanes with their metallic counterparts. This implies that the design of the components highly depends upon the type of application which leads to the first stage of any manufacturing process chain, as shown in Figure 5.8.

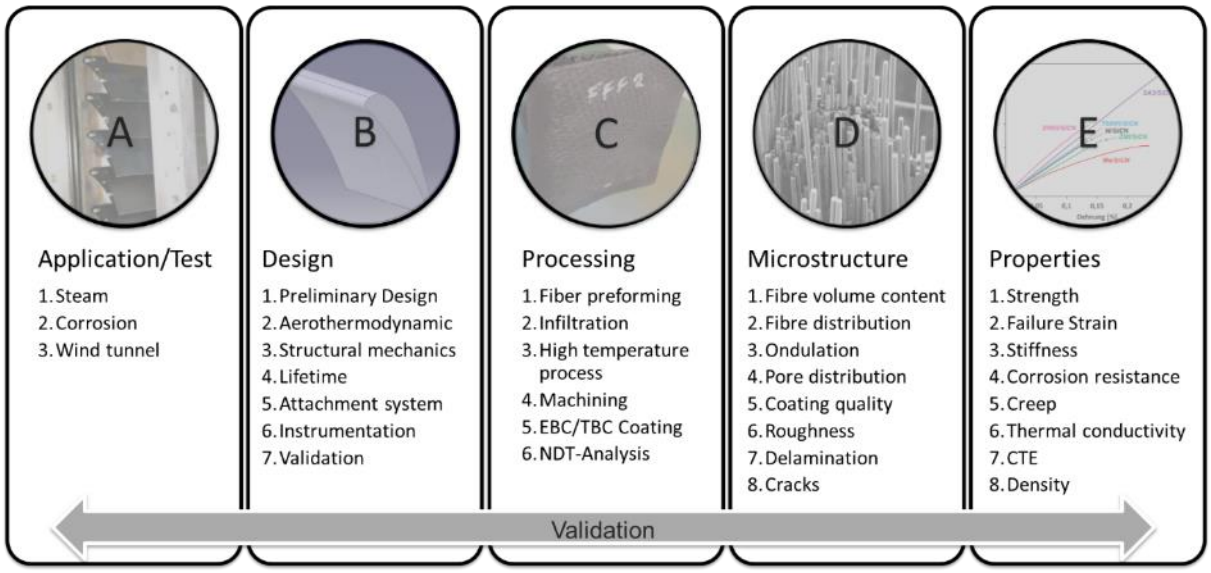

Figure 5.8: Steps involved in the CMC product development for a specific application or a test campaign.

5.3.1 Application/Test

As mentioned earlier, the first step in the development of a CMC component is the definition of the application or the test of the component. Based on this information, the geometry and component features like cooling holes are planned in this step. For a relative new material class like CMCs, most of the research is oriented towards constituent screening, prototype development and testing. This implies that the first step usually involves testing and the expected outcome of the testing is pre-decided. The instrumentation possibilities in order to measure the experimental values also needs to be considered in this step because they usually differ from the tests designed for metallic parts to be replaced, which might be the case with CMCs. In this scenario, the tests and the instrumentation techniques have to be adapted to receive reliable values from a test for a CMC sample or prototype. A few examples of tests to qualify a CMC sample or prototype for a vane application are shown in Figure 5.8. These tests also provide the boundary conditions for the simulation of material behaviour under the test or operation conditions. The test setup is usually fixed and it is the design of the CMC-component which needs to be adapted in order to integrate it into the existing system.

5.3.2 Design

In this section, the inputs and outputs from all other sections are collected and analysed to provide the optimum part design based on the requirements of the test or application. The design process starts with a preliminary design suggested by the team based on the experience from the earlier tests. In case of CMCs, it is mostly a metallic part geometry which is not necessarily adapted to the design limitations of CMCs. For example, geometrical features of a metallic vane like curvatures with small radius, trailing edges, cooling holes, air channels, small cross-section area, etc. should be adapted to CMCs and requires an extensive discussion between the design and materials team. Moreover, the design of attachment

systems to integrate the CMC component into an existing set-up poses an additional challenge that needs to be addressed because of the substantial differences in the coefficient of thermal expansion between metals and CMCs.

Based on the complexity of a problem, the modelling techniques are chosen. For example, in the case of a wind tunnel test, CFD (Computational Fluid Dynamics) modelling is required while in the case of test under steam, a coupled thermo-chemical model is required. With the help of the instrumentation techniques which are apt for the test set-up and the material class, it is ensured that the test provides some quantified values which can be directly compared with the results from the simulation and validate the models. In order to optimize the material based on the test results, high fidelity models, i.e., interconnected multi-scale models are required. Finally, the data from the models and equipment is collected and the machine learning models are trained on it. In this way, optimum material and manufacturing parameters can be decided based on the output from the data analysis.

5.3.3 Processing

The processing includes all the factors which are discussed in Section 5.2. The information exchange between the processing and the design group combines the knowledge of material limitations/challenges with the design requirements of the component to end up with the optimum constituent and manufacturing-parameter selection. The limitations should be quantified to integrate them into the design optimisation constraints required by the design team. For example, there is a minimum wall thickness which should be maintained in the case of a SiC/SiC vane otherwise there will not be enough fibre reinforcement to successfully carry the mechanical loads. This combined with the tolerance during machining provides the thickness constraints to the part design. Similarly, the bending radius in a vane depends on the wall thickness as found out in the SiC/SiC development of GE Aviation and NASA [1]. The conclusion from this bending radius study was that the tightest radius should not be smaller than twice the wall thickness of the vane, otherwise distortion of the layers can occur.

5.3.4 Microstructure

This section includes the information about the resulting microstructure of the manufactured material. In order to use this information, the microstructural features should be extracted, quantified and integrated into the database of the material. Image segmentation technique is the most promising method to realise the quantification of the microstructural information. Based on the feature, automated image segmentation with the help of machine learning and artificial intelligence can be applied. As shown in the examples in Chapter 2 and 3, the manufacturing parameters influence the microstructure of the material, which in turn decides its physical properties.

5.3.5 Properties

The tests defined in the first section ‘Application/Test’ can be as simple as a pure tensile test on rectangular geometry to a complicated vane geometry in a wind tunnel test. The thermo-mechanical properties like failure strength, failure strain, Young’s Modulus, thermal conductivity, etc. are derived from tests on rather simple geometries. It should be noted that the strength of the material is a constant property which highly depends on the geometry and the volume of the material. For example, a sample with curved geometry might exhibit degraded properties compared to a flat sample. The reason is that the fabrication of a sample with curve geometry might destroy fibres or distortion of fibres might take place resulting in a weak spot in the component. For this reason, it is important to establish a relationship between the microstructure and the properties as the changes in the geometry will be reflected in the microstructure of the material. In this way, the features like distorted or pre-stressed fibres can be predicted and included in the prediction of the performance of a component with complicated geometry.

5.3.6 Working Example

In the previous sections, various aspects of a CMC part design have been discussed. It can be noticed that each section is assigned an alphabet and each subset carries a number with it. This is part of a component development plan where different teams or individuals with expertise in the respective fields collaborate together. The idea is to clearly define the input and output of each subsection to ensure the flow of data and information whenever required. This plan would also help in laying out the requirements of a CMC component development project.

The first step in this process is to define the sub steps or modules in each section as shown in Figure 5.8. These modules may vary depending on the test or application in a particular project and the material to be developed based on their requirements. Based on the complexity of the sub steps, they can be further divided into sub steps.

Table 5.8: Each sub step or module is assigned to the person or group according to their expertise

Module Number	**Module Name**	**Lead**
A3	Wind Tunnel	Person/Group 1
B1	Preliminary Design	Person/Group 2
C1	Fibre Preforming	Person/Group 3
….	….	….

After assigning the modules to different groups or individuals, the assignee makes a list of all the information, material or component required to fulfil the tasks of that particular module. Each element

of the list should carry the number of the module, from where it is going to get that particular input. If the input required by a module is not found in any section, then a sub-section is created that can deliver the input to the module.

Table 5.9: The inputs (exemplary) required by the module 'Wind Tunnel' from the other modules

Input Required	**Delivered by module number**	**Module Name**
CAD-geometry of the component	B1	Preliminary Design
Recommendations for test parameters	B2	Aerothermodynamics
Attachment systems for integration of the component in the existing system	B5	Attachment systems
Measurement methods to capture the experimental values	B6	Instrumentation
Comparison of the simulation results	B7	Validation
Machines vane to be tested	C4	Machining
Quality of the vane after machining via NDT analysis	C6	NDT-analysis
….	….	….

In this way, the interdisciplinary teams can work together by ensuring that the requirements of each expert individual or group is satisfied to deliver the best part design with the best possible CMC for the target application.

5.4 Conclusion

The manufacturing process of CMC is a multi-step process which includes highly complex intermediate steps. In order to ensure the quality of the final product, methods and techniques are required to maintain the quality of intermediate processes and products. Many modelling approaches for the individual processes involved in the production of CMC are reported in the literature. The most challenging task is although, to adapt or extend the existing numerical methods and combine them to establish an end-to-end digital manufacturing chain of a CMC. This requires exact definition of the involved process,

process route to be employed and the input-output of the either physics-based or data-based modelling tools. At the same time, validation of these models requires automatized process data extraction and analysis via in-situ or ex-situ non-destructive techniques. The aim of the author is to give a detailed overview of the modelling techniques investigated by other researchers and lay the foundation of a digital manufacturing process chain by connecting the different aspects of the complex manufacturing chain for CMCs.

The implementation of this approach requires expertise in the following fields:

- Numerical methods
- Material science (development and testing)
- Data Management and Analysis
- Application knowledge

With the combined effort of these experts, all the aspects of real and virtual CMC part development can be taken into consideration. With the approach proposed in this chapter, the exchange of the information required to materialise model (both physics- and data-based-models) based material development can take place in a structured manner. The author proposes the establishment of the module- and link-based interfaces between the sub-sections of the above-mentioned expertise and then dive into the detail in the case of every field. This early-stage collaboration between the research streams can help in prioritising the focus on individual process simulations. For example, input from a material scientist regarding the accuracy of the measurements of a thermoelement within a pyrolysis oven can help the simulation team to design the parameter study to find the optimum pyrolysis temperature. It would be inefficient to invest the resources in parameter study for each 1°C temperature change where the measurements of the oven temperature and consequent setting of temperature is in range of ±25°C of the desired temperature. In another example, the thickness of a sample or a component is not just crucial from the point of view of load carrying capacity but also for the quality of the fibre coating during the CVD process. This information will again set the constraints for the material and component design team. This exchange of information is not trivial and might lead to inappropriate allocation of resources during a material development program. For this reason, the module-based approach ensures an active interaction of all the stakeholders during every stage of material and component development.

6 Conclusion and outlook

The current work investigated the digital aspects of the ceramic matrix composites as materials and the steps included in their manufacturing process. From the material point of view, the 'Process-Structure-Property-Performance' relationship was studied und with the help of a numerical example, each part of this relationship was analysed.

The pyrolysis process of C/C-SiC was modelled as a working example for the process-structure relationship. With the help of finite element modelling and cohesive zones, the crack initiation and growth during the cooling down of the microstructure with weak and strong fibre/matrix interface was analysed. For validation purposes, image segmentation techniques using Python were employed to quantify the crack size in both the microscopic images and the images obtained from the simulation. Microstructural features like fibre volume content and the Weibull distribution of the matrix strength were then varied to study their effect on the crack development in the microstructure.

In order to represent the structure-property relationship, virtual tensile tests were carried on pure matrix material and fibre-reinforced composite in the transverse and the longitudinal direction. The results from the tensile tests performed on carbon and silicon carbide fibre reinforced SiCN were used for the validation of the results obtained from the finite element modelling. Additionally, parameter studies were performed to understand the effect of the microstructural features and constituent properties over the composite properties. This data also served as the basis for machine learning algorithms to generate data-based surrogate models which are computationally inexpensive once trained. The performance of the algorithms was compared with each other and the experimental results. The use of machine learning is not just restricted to this part of the relationship but can be extended to the data obtained from all the aspects of the PSPP relationship. Such surrogate models are efficient when it comes to preliminary selection of the CMC constituents and the manufacturing material parameters. The physics-based modelling can still be used for validation purposes and detailed analysis of the filtered choices.

The aspect property-performance relationship was then analysed, where a damage-based failure criterion was introduced to predict failure stress and strain in the CMC components. Two different fibre architectures for different CMCs were investigated: wound (C/C-SiC) and woven (WHIPOX™). The damage-based criterion performed better than the stress or strain-based quadratic failure criteria in the prediction of strength or failure strain.

After the numerical examples for material modelling at different scales, a detailed review of process modelling for different steps involved in the manufacturing process was given. The results from the numerical methods combined with the information obtained from in-situ and ex-situ process monitoring techniques serve as the basis of a digital manufacturing process chain. The data analysis methods used in PSPP relationship like image segmentation and machine learning algorithms

also serve as an integral part of this chain to exploit the data generated by numerical methods and process monitoring.

The use cases investigated in Chapter 2, 3 and 4 covered a part of the modules introduced in Chapter 5 as module-based material development approach, as shown in Figure 6.1. Manufacturing parameters of a high temperature process combined with the fibre volume content and fibre distribution influence the crack development in the matrix, which was the focus of Chapter 2. In Chapter 3, the relationship between the factors like fibre volume content combined with the information from processing such as fibre and matrix types and the composite properties were studied. The homogenisation non-linear behaviour of the composites was modelled in the Chapter 4 which supports the computational efficient analysis of the component designs from structural mechanics point of view. The aim of any material development program should be to complete the list of involved modules in the manufacturing process and then establish the connection between them. Such an approach will lead to an end-to-end manufacturing digital chain leading to accelerated material development and will pave the way for cost-efficient production of CMCs.

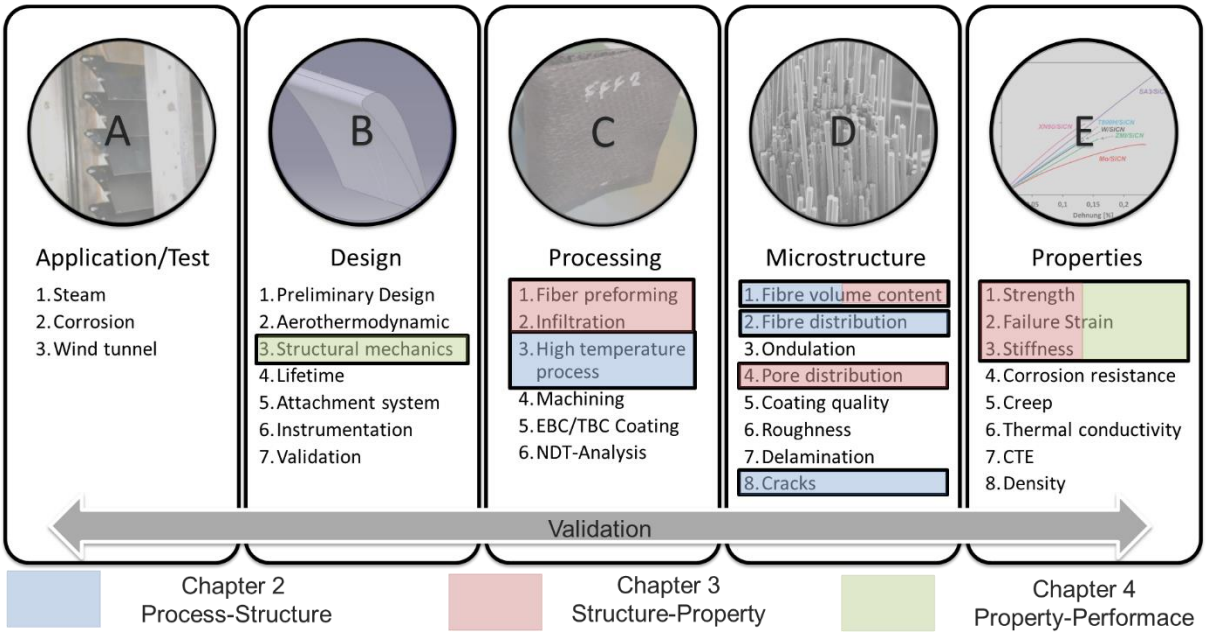

Figure 6.1: The contribution of the use cases investigated in Chapter 2, 3 and 4 to different modules in the module-based material development approach introduced in Chapter 5.

The development and use of such a digital chain are crucial from the point of view of two types of industries:

1. Component Manufacturers: To understand the effect of the process parameters over the material properties and optimize them accordingly
2. Original Equipment Manufacturers (OEM): With such detailed information about each product, 'Predictive Performance' of the components can be performed based on individual quality

The cost of the manufacturing process of CMCs is the largest limiting factor for their use in the high temperature applications and is restricted to niche areas like aerospace and nuclear energy. With employment of such a digital chain, the process parameters can be optimized to achieve the best CMC part design and cost effectiveness at the same time. Moreover, the waste and use of other energy resources can be reduced as well and thus, contributing to the sustainable and green manufacturing of CMCs in the future.

Literature

[1] G. Corman and K. Luthra, "Melt Infiltrated Ceramic Composites (Hipercomp) for Gas Turbine Engine Applications,"; Tiax Llc2005.

[2] G. Gardiner. (2015). *Aeroengine Composites, Part 1: The CMC invasion*. Available: https://www.compositesworld.com/articles/aeroengine-composites-part-1-the-cmc-invasion

[3] "Technology Roadmap Update for Generation IV Nuclear Energy Systems," ed, 2014.

[4] J. D. Buckley and D. D. Edie, *Carbon-carbon materials and composites*: William Andrew, 1993.

[5] D. Sciti, L. Zoli, L. Silvestroni, A. Cecere, G. D. Di Martino, and R. Savino, "Design, fabrication and high velocity oxy-fuel torch tests of a Cf-ZrB2- fiber nozzle to evaluate its potential in rocket motors," *Materials & Design,* vol. 109, pp. 709-717, 2016/11/05/ 2016.

[6] F. Breede, S. Hofmann, N. Jain, and R. Jemmali, "Design, Manufacture, and Characterization of a Carbon Fiber-Reinforced Silicon Carbide Nozzle Extension," *International Journal of Applied Ceramic Technology,* vol. 13, pp. 3-16, 2016.

[7] W. Krenkel and R. Renz, "CMCs for Friction Applications," in *Ceramic Matrix Composites*, ed, 2008, pp. 385-407.

[8] G. Corman, K. Luthra, J. Jonkowski, J. Mavec, P. Bakke, D. Haught*, et al.*, "Melt infiltrated ceramic matrix composites for shrouds and combustor liners of advanced industrial gas turbines," General Electric Company, Boston, MA (United States)2011.

[9] S. Nohut, "Influence of sample size on strength distribution of advanced ceramics," *Ceramics International,* vol. 40, pp. 4285-4295, 2014/04/01/ 2014.

[10] J. Llorca and M. Elices, "Influence of specimen geometry and size on fracture of fiber-reinforced ceramic-matrix composites," *Engineering Fracture Mechanics,* vol. 44, pp. 341-358, 1993/02/01/ 1993.

[11] S. M. Arnold, D. Cebon, and M. Ashby, "Materials selection for aerospace systems," NASA/TM2012.

[12] S. M. Arnold, F. A. Holland, B. A. Bednarcyk, and E. J. Pineda, "Combining material and model pedigree is foundational to making ICME a reality," *Integrating Materials and Manufacturing Innovation,* vol. 4, pp. 37-62, 2015/12/01 2015.

[13] G. Ziegler, J. Heinrich, and G. Wötting, "Relationships between processing, microstructure and properties of dense and reaction-bonded silicon nitride," *Journal of Materials Science,* vol. 22, pp. 3041-3086, 1987/09/01 1987.

[14] S. C. Zunjarrao, "Polymer derived ceramics: Processing-structure-property relationships," PhD Thesis, Oklahoma State University, 2008.

[15] C. Clausell and A. Barba, "Processing–microstructure–properties relationship in a CuNiZn ferrite," *Boletín de la Sociedad Española de Cerámica y Vidrio,* vol. 57, pp. 29-39, 2018/01/01/ 2018.

[16] H. Ma, Y. Tian, and G. Li, "Effects of Sintering Temperature on Microstructure, Properties and Crushing Behavior of Ceramic Proppants," *International Journal of Applied Ceramic Technology,* vol. 16, 02/11 2019.

[17] Y. L. He Li, Yansong Liu, Kehui Hu, Zhigang Lu, Jingjing Liang, "Influence of Sintering Temperature on Microstructure and Mechanical Properties of Al2O3 Ceramic via 3D Stereolithography," *Acta Metallurgica Sinica (English Letters),* vol. 33, pp. 204-214, 2020-02-10 2020.

[18] D. D. L. Chung, "Processing-structure-property relationships of continuous carbon fiber polymer-matrix composites," *Materials Science and Engineering: R: Reports,* vol. 113, pp. 1-29, 2017/03/01/ 2017.

[19] B. Zheng, M. Li, T. Deng, H. Zhou, Z. Huang, H. Zhou*, et al.*, "Process–structure–property relationships of thermoformed woven carbon-fiber-reinforced polyether-ether-ketone composites," *Polymer Composites,* vol. 40, pp. 3823-3834, 2019.

[20] J. Xie, S. Wang, Z. Cui, and J. Wu, "Process Optimization for Compression Molding of Carbon Fiber–Reinforced Thermosetting Polymer," *Materials,* vol. 12, p. 2430, 2019.

[21] R. J. D'Mello, M. Maiarù, and A. M. Waas, "Virtual manufacturing of composite aerostructures," *The Aeronautical Journal,* vol. 120, pp. 61-81, 2016.

[22] A. M. Waas, R. J. D'Mello, M. Maiaru, and R. Koon, "Integrated Computational Modeling for Efficient Material and Process Design for Composite Aerospace Structures," in *AIAA Scitech 2020 Forum*, ed, 2020.

[23] H. Xu, "Process Integration and Optimization of ICME Carbon Fiber Composites for Vehicle Lightweighting: A Preliminary Development," *SAE International Journal of Materials and Manufacturing,* vol. 10, 03/28 2017.

[24] J. Shi, T. Cook, and J. Matlik, "Integrated Computational Materials Engineering for Ceramic Matrix Composite Development," in *53rd AIAA/ASME/ASCE/AHS/ASC Structures, Structural Dynamics and Materials Conference*, ed, 2012.

[25] M. Grujicic, J. Snipes, R. Galgalikar, R. Yavari, V. Avuthu, and S. Ramaswami, "Multi-length-scale derivation of the room-temperature material constitutive model for SiC/SiC ceramic-matrix composites," *Proceedings of the Institution of Mechanical Engineers, Part L: Journal of Materials: Design and Applications,* vol. 231, pp. 443-462, 2017.

[26] M. Grujicic, J. Snipes, R. Yavari, S. Ramaswami, and R. Galgalikar, "Computational investigation of foreign object damage sustained by environmental barrier coatings (EBCs) and SiC/SiC ceramic-matrix composites (CMCs)," *Multidiscipline Modeling in Materials and Structures,* vol. 11, pp. 238-272, 2015.

[27] M. Grujicic, S. Ramaswami, and J. S. Snipes, "Use of the Materials Genome Initiative (MGI) approach in the design of improved-performance fiber-reinforced SiC/SiC ceramic-matrix composites (CMCs)," *AIMS Materials Science,* vol. 3, pp. 989-1021, 2016.

[28] B. Mainzer, R. Jemmali, P. Watermeyer, K. Kelm, M. Frieß, and D. Koch, "Development of Damage-Tolerant Ceramic Matrix Composites (SiC/SiC) using Si-BN/SiC/pyC Fiber Coatings and LSI Processing," *Journal of Ceramic Science and Technology,* vol. 08, pp. 113-120, 2017.

[29] W. Krenkel, "Entwicklung eines kostengunstigen Verfahrens zur Herstellung von Bauteilen aus keramischen Verbundwerkstoffen," PhD Thesis, Universität Stuttgart, 2000.

[30] M. Frieß, R. Renz, and W. Krenkel, "Graded ceramic matrix composites by LSI-processing," in *Proceedings of the 10 th International Congress and 3 rd Forum on New Materials*, Florence, Italy, 2002, pp. 14-18.

[31] W. Krenkel, J. Hausherr, T. Reimer, and M. Frieß, "Design, manufacture and quality assurance of C/CSiC composites for space transportation systems," in *28th International Conference on Advanced Ceramics and Composites: B, Ceramic Engineering and Science Proceedings*, 2004, p. 4958.

[32] D. B. Adolf, J. E. Martin, R. S. Chambers, S. N. Burchett, and T. R. Guess, "Stresses during thermoset cure," *Journal of Materials Research,* vol. 13, pp. 530-550, 1998.

[33] J. Schulte-Fischedick, "Die entstehung des rissmusters wahrend der pyrolyse von CFK zur herstellung von C/C-werkstoffen," PhD Thesis, Universität Stuttgart, 2006.

[34] K. A. Trick and T. E. Saliba, "Mechanisms of the pyrolysis of phenolic resin in a carbon/phenolic composite," *Carbon,* vol. 33, pp. 1509-1515, 1995/01/01/ 1995.

[35] J. B. Gilbert, J. J. Kipling, B. McEnaney, and J. N. Sherwood, "Carbonization of polymers I—Thermogravimetric analysis," *Polymer,* vol. 3, pp. 1-10, 1962/01/01/ 1962.

[36] Y. N. Sazanov, N. G. Stepanov, L. A. Shibaev, T. A. Antonova, A. V. Gribanov, I. Bertoti*, et al.*, "Some aspects of the carbonization of polyimides," *Acta Polymerica,* vol. 39, pp. 431-434, 1988.

[37] S. Hofmann, "Effect of interlaminar defects on the mechanical behaviour of carbon fibre reinforced silicon carbide," PhD Thesis, Faculty of Aerospace Engineering and Geodesy, Universität Stuttgart, German Aerospace Centre, 2013.

[38] J. Schulte-Fischedick, S. Seiz, N. Lützenburger, A. Wanner, and H. Voggenreiter, "The crack development on the micro- and mesoscopic scale during the pyrolysis of carbon fibre reinforced plastics to carbon/carbon composites," *Composites Part A: Applied Science and Manufacturing,* vol. 38, pp. 2171-2181, 2007/10/01/ 2007.

[39] F. K. Wittel, J. Schulte-Fischedick, F. Kun, B.-H. Kröplin, and M. Frieß, "Discrete element simulation of transverse cracking during the pyrolysis of carbon fibre reinforced plastics to carbon/carbon composites," *Computational Materials Science,* vol. 28, pp. 1-15, 2003/07/01/ 2003.

[40] D. S. Dugdale, "Yielding of steel sheets containing slits," *Journal of the Mechanics and Physics of Solids,* vol. 8, pp. 100-104, 1960/05/01/ 1960.

[41] G. I. Barenblatt, "The Mathematical Theory of Equilibrium Cracks in Brittle Fracture," in *Advances in Applied Mechanics*. vol. 7, H. L. Dryden, T. von Kármán, G. Kuerti, F. H. van den Dungen, and L. Howarth, Eds., ed: Elsevier, 1962, pp. 55-129.

[42] G. T. Camacho and M. Ortiz, "Computational modelling of impact damage in brittle materials," *International Journal of Solids and Structures,* vol. 33, pp. 2899-2938, 1996/08/01/ 1996.

[43] F. Zhou and J. F. Molinari, "Dynamic crack propagation with cohesive elements: a methodology to address mesh dependency," *International Journal for Numerical Methods in Engineering,* vol. 59, pp. 1-24, 2004.

[44] W. M. Mueller, J. Moosburger-Will, M. G. R. Sause, and S. Horn, "Microscopic analysis of single-fiber push-out tests on ceramic matrix composites performed with Berkovich and flat-end indenter and evaluation of interfacial fracture toughness," *Journal of the European Ceramic Society,* vol. 33, pp. 441-451, 2013/02/01/ 2013.

[45] J. Gelb. (2017). *Investigating Structure-property Relationships in a Carbon-fiber Composite*. Available: https://www.zeiss.com/content/dam/Microscopy/us/download/pdf/application-notes/x-ray-microscopy/en_44_013_042_correlative-composite.pdf

[46] S. Bricker, J. P. Simmons, C. Przybyla, and R. Hardie, "Structure Quantification and Gestalt of Continuous Fiber Reinforced Composite Microstructures for ICME," *MRS Proceedings,* vol. 1709, pp. mrss14-1709-ww09-07, 2014.

[47] S. Bricker, J. Simmons, C. Przybyla, and R. Hardie, *Anomaly detection of microstructural defects in continuous fiber reinforced composites* vol. 9401: SPIE, 2015.

[48] H. Xu, R. Liu, A. Choudhary, and W. Chen, "A machine learning-based design representation method for designing heterogeneous microstructures," *Journal of Mechanical Design,* vol. 137, p. 051403, 2015.

[49] W. C. Oliver and G. M. Pharr, "An improved technique for determining hardness and elastic modulus using load and displacement sensing indentation experiments," *Journal of Materials Research,* vol. 7, pp. 1564-1583, 1992.

[50] G. M. Jenkins and K. Kawamura, *Polymeric carbons: carbon fibre, glass and char*: Cambridge University Press, 1976.

[51] R. Kulkarni and O. Ochoa, "Transverse and Longitudinal CTE Measurements of Carbon Fibers and their Impact on Interfacial Residual Stresses in Composites," *Journal of Composite Materials,* vol. 40, pp. 733-754, 2006.

[52] P. Rakesh, "Mechanical properties evaluation of T800 carbon fiber reinforced hybrid composite embedded with silicon carbide microparticles: A micromechanical approach," *Multidiscipline Modeling in Materials and Structures,* vol. 14, pp. 589-608, 2018.

[53] "Subvolume A: Polymer Solids and Polymer Melts - Part 3: Mechanical and Thermomechanical Properties of Polymers.," in *Advanced Materials and Technologies*, K.-F. Arndt and M. D. Lechner, Eds., ed: Springer-Verlag Berlin Heidelberg, 2014, pp. 106-151.

[54] C. Li and A. Strachan, "Molecular dynamics predictions of thermal and mechanical properties of thermoset polymer EPON862/DETDA," *Polymer,* vol. 52, pp. 2920-2928, 2011/06/08/ 2011.

[55] H. Riedel, "Fracture Mechanisms," in *Plastic deformation and fracture of materials*. vol. 6, H. Mugharabi, Ed., ed: Weinheim ; New York : VCH 1993, pp. 565-633.

[56] N. Song, M. Jackson, C. Montgomery, S. Wu, N. Jain, R. Sweat*, et al.*, "Using Multiscale Modeling to Advance Industrial and Research Applications of Advanced Materials," *International Journal for Multiscale Computational Engineering,* 2021.

[57] W. Weibull, "A statistical distribution function of wide applicability," *Journal of applied mechanics,* vol. 18, pp. 293-297, 1951.

[58] Y. Shi, Y. L. Xiu, and D. Koch, "Investigation of Statistical Distribution of C/C-SiC Composite's Mechanical Properties," *Key Engineering Materials,* vol. 809, pp. 131-139, 2019.

[59] T. Mueller, A. G. Kusne, and R. Ramprasad, "Machine learning in materials science: Recent progress and emerging applications," *Reviews in Computational Chemistry,* vol. 29, pp. 186-273, 2016.

[60] C.-T. Chen and G. X. Gu, "Machine learning for composite materials," *MRS Communications,* vol. 9, pp. 556-566, 2019.

[61] S. Dabetwar, S. Ekwaro-Osire, and J. P. Dias, "Damage Classification of Composites Using Machine Learning," in *ASME 2019 International Mechanical Engineering Congress and Exposition*, 2019.

[62] D. Reimann, K. Nidadavolu, H. ul Hassan, N. Vajragupta, T. Glasmachers, P. Junker*, et al.*, "Modeling Macroscopic Material Behavior With Machine Learning Algorithms Trained by Micromechanical Simulations," *Frontiers in Materials,* vol. 6, 2019-August-13 2019.

[63] I. B. C. M. Rocha, P. Kerfriden, and F. P. van der Meer, "Micromechanics-based surrogate models for the response of composites: A critical comparison between a classical mesoscale constitutive model, hyper-reduction and neural networks," *European Journal of Mechanics - A/Solids,* vol. 82, p. 103995, 2020/07/01/ 2020.

[64] S. Yan, X. Zou, M. Ilkhani, and A. Jones, "An efficient multiscale surrogate modelling framework for composite materials considering progressive damage based on artificial neural networks," *Composites Part B: Engineering,* vol. 194, p. 108014, 2020/08/01/ 2020.

[65] S. Ye, B. Li, Q. Li, H.-P. Zhao, and X.-Q. Feng, "Deep neural network method for predicting the mechanical properties of composites," *Applied Physics Letters,* vol. 115, p. 161901, 2019.

[66] C. Yang, Y. Kim, S. Ryu, and G. X. Gu, "Prediction of composite microstructure stress-strain curves using convolutional neural networks," *Materials & Design,* vol. 189, p. 108509, 2020/04/01/ 2020.

[67] L. Xin, *Multiscale modeling of textile composite structures using mechanics of structure genome and machine learning*, 2020.

[68] A. Vinci, L. Zoli, D. Sciti, C. Melandri, and S. Guicciardi, "Understanding the mechanical properties of novel UHTCMCs through random forest and regression tree analysis," *Materials & Design,* vol. 145, pp. 97-107, 5/5/ 2018.

[69] B. Mainzer, "Entwicklung von keramischen SiC/SiC-Verbundwerkstoffen mit Tyranno SA3 Fasern auf Basis des PIP- und LSI-Verfahrens," Ph.D. Thesis, Karlsruher Institut für Technologie (KIT), 2020.

[70] "Siemens MultiMech (19.0) Documentation," 2021.

[71] P. Pattnaik, A. Sharma, M. Choudhary, V. Singh, P. Agarwal, and V. Kukshal, "Role of machine learning in the field of Fiber reinforced polymer composites: A preliminary discussion," *Materials Today: Proceedings,* 2020/12/19/ 2020.

[72] W. Article. Available: https://en.wikipedia.org/wiki/Pearson_correlation_coefficient

[73] J. Brownlee. (2016). *Linear Regression for Machine Learning*. Available: https://machinelearningmastery.com/linear-regression-for-machine-learning/

[74] B. Tuychiev. (2020). *Intro to Scikit-learn's k-Nearest-Neighbors Classifier And Regressor*. Available: https://towardsdatascience.com/intro-to-scikit-learns-k-nearest-neighbors-classifier-and-regressor-4228d8d1cba6

[75] D. Kumar. (2020). *A Complete understanding of LASSO Regression*. Available: https://www.mygreatlearning.com/blog/understanding-of-lasso-regression/

[76] R. Gandhi. (2018). *Support Vector Machine — Introduction to Machine Learning Algorithms*. Available: https://towardsdatascience.com/support-vector-machine-introduction-to-machine-learning-algorithms-934a444fca47

[77] P. Gupta. (2017, 25/09/2021). *Decision Trees in Machine Learning*. Available: https://towardsdatascience.com/decision-trees-in-machine-learning-641b9c4e8052

[78] T. Yiu. (2019). *Understanding Random Forest: How the Algorithm Works and Why it Is So Effective*. Available: https://towardsdatascience.com/understanding-random-forest-58381e0602d2

[79] C. Lin, "Manufacturing of C_f/SiCN and SiC_f/SiCN Ceramic Matrix Composites via PIP Process," M.Sc. Thesis, Technische Universität Darmstadt, German Aerospace Centre Stuttgart, 2017.

[80] I. Toray Composite Materials America. Available: https://www.toraycma.com/file_viewer.php?id=5121

[81] Nippon Graphite Fiber Corporation. *Granoc Yarn XN Series*. Available: http://www.ngfworld.com/dcms_media/other/GRANOCXNCNfiber2016.pdf

[82] "Ube Industries Ltd., Tyranno Fiber (Datasheet), Corporate Research and Development, Ube, Japan," ed.

[83] S. Salem and A. Salem, "Reliability and fracture statistics of highly vitrified ceramics: Effect of technical factors on strength distribution," *Construction and Building Materials,* vol. 101, pp. 1097-1104, 2015/12/30/ 2015.

[84] B. Mainzer, K. Kelm, P. Watermeyer, M. Frieß, and D. Koch, "How to Tame the Aggressiveness of Liquid Silicon in the LSI Process," *Key Engineering Materials,* vol. 742, pp. 238-245, 2017.

[85] G. Ziegler, H. J. Kleebe, G. Motz, H. Müller, S. Traßl, and W. Weibelzahl, "Synthesis, microstructure and properties of SiCN ceramics prepared from tailored polymers," *Materials Chemistry and Physics,* vol. 61, pp. 55-63, 1999/09/30/ 1999.

[86] D. Koch, K. Tushtev, and G. Grathwohl, "Ceramic fiber composites: Experimental analysis and modeling of mechanical properties," *Composites Science and Technology,* vol. 68, pp. 1165-1172, 2008.

[87] S. Kawabata, "Measurement of the Transverse Mechanical Properties of High-performance Fibres," *The Journal of The Textile Institute,* vol. 81, pp. 432-447, 1990/01/01 1990.

[88] B. Drach, I. Tsukrov, A. Trofimov, T. Gross, and A. Drach, "Comparison of stress-based failure criteria for prediction of curing induced damage in 3D woven composites," *Composite Structures,* vol. 189, pp. 366-377, 2018/04/01/ 2018.

[89] I. Krucinska and T. Stypka, "Direct measurement of the axial poisson's ratio of single carbon fibres," *Composites Science and Technology,* vol. 41, pp. 1-12, 1991/01/01/ 1991.

[90] P. Galizia, L. Zoli, and D. Sciti, "Impact of residual stress on thermal damage accumulation, and Young's modulus of fiber-reinforced ultra-high temperature ceramics," *Materials & Design,* 2018/10/13/ 2018.

[91] F. Breede, "Entwicklung neuartiger faserkeramischer C/C-SiC Verbundwerkstoffe auf Basis der Wickeltechnik für Raketendüsen," PhD Thesis, Fakultät für Luft- und Raumfahrttechnik und Geodäsie, Universität Stuttgart, German Aerospace Centre, 2017.

[92] D. Mwiti. (2021, 24/09/2021). *Random Forest Regression: When Does It Fail and Why?* Available: https://neptune.ai/blog/random-forest-regression-when-does-it-fail-and-why

[93] H. Zhang, D. Nettleton, and Z. Zhu, "Regression-enhanced random forests," *In JSM Proceedings (2017), Section on Statistical Learning and Data Science, Alexandria, VA: American Statistical Association. 636 -- 647,* 2019.

[94] J. Lamon, "A micromechanics-based approach to the mechanical behavior of brittle-matrix composites," *Composites science and technology,* vol. 61, pp. 2259-2272, 2001.

[95] Y. Shi, N. Jain, and D. Koch, "Investigation and modeling of tensile failure properties of wound ceramic matrix composites," *Composites Part A: Applied Science and Manufacturing,* vol. 114, pp. 316-326, 2018/11/01/ 2018.

[96] E. Baranger, "5.8 Modeling Mechanical Behavior of Ceramic Matrix Composites," in *Comprehensive Composite Materials II*, P. W. R. Beaumont and C. H. Zweben, Eds., ed Oxford: Elsevier, 2018, pp. 237-268.
[97] S. Wulfinghoff, M. Fassin, and S. Reese, "A damage growth criterion for anisotropic damage models motivated from micromechanics," *International Journal of Solids and Structures,* vol. 121, pp. 21-32, 2017/08/15/ 2017.
[98] P. Ladeveze and E. LeDantec, "Damage modelling of the elementary ply for laminated composites," *Composites science and technology,* vol. 43, pp. 257-267, 1992.
[99] L. Marcin, J.-F. Maire, N. Carrère, and E. Martin, "Development of a Macroscopic Damage Model for Woven Ceramic Matrix Composites," *International Journal of Damage Mechanics,* vol. 20, pp. 939-957, August 1 2011.
[100] G. Camus, "Modelling of the mechanical behavior and damage processes of fibrous ceramic matrix composites: application to a 2-D SiC/SiC," *International Journal of solids and Structures,* vol. 37, pp. 919-942, 2000.
[101] R. Talreja, "A continuum mechanics characterization of damage in composite materials," *Proceedings of the Royal Society of London. A. Mathematical and Physical Sciences,* vol. 399, pp. 195-216, 1985.
[102] R. S. Kumar, "Analysis of coupled ply damage and delamination failure processes in ceramic matrix composites," *Acta Materialia,* vol. 61, pp. 3535-3548, 2013/06/01/ 2013.
[103] E. J. Barbero and L. D. Vivo, "A Constitutive Model for Elastic Damage in Fiber-Reinforced PMC Laminae," *International Journal of Damage Mechanics,* vol. 10, pp. 73-93, 2001.
[104] M. Hinton, P. Soden, and A.-S. Kaddour, *Failure criteria in fibre reinforced polymer composites: the world-wide failure exercise*: Elsevier, 2004.
[105] E. Petersen, R. G. Cuntze, and C. Hühne, "Experimental determination of material parameters in Cuntze's Failure-Mode-Concept-based UD strength failure conditions," *Composites Science and Technology,* vol. 134, pp. 12-25, 2016/10/06/ 2016.
[106] W. Van Paepegem, "Development and finite element implementation of a damage model for fatigue of fibre-reinforced polymers," PhD Thesis, Ghent University, 2002.
[107] K. Tushtev, J. Horvath, D. Koch, and G. Grathwohl, "Deformation and Failure Modeling of Fiber Reinforced Ceramics with Porous Matrix," *Advanced Engineering Materials,* vol. 6, pp. 664-669, 2004.
[108] C. P. Yang, G. Q. Jiao, B. Wang, T. Huang, and H. B. Guo, "Damage-based failure theory and its application to 2D-C/SiC composites," *Composites Part A: Applied Science and Manufacturing,* vol. 77, pp. 181-187, 2015.
[109] E. J. Barbero, *Finite element analysis of composite materials using ANSYS®*: CRC press, 2013.
[110] Y. Shi, "Characterization and modeling of the mechanical properties of wound oxide ceramic composites," PhD Thesis, Fakultät für Maschinenbau, Karlsruhe Institut für Technologie (KIT), 2017.
[111] K. K. Sikkil, "Finite element damage modeling of plain weave fabrics," Master of Science (M.Sc.) Thesis, Department of Mechanical and Aerospace Engineering, West Virginia University, College of Engineering and Mineral Resources, 2003.
[112] K.-S. Liu and S. W. Tsai, "A progressive quadratic failure criterion for a laminate," *Composites Science and Technology,* vol. 58, pp. 1023-1032, 1998/07/01/ 1998.
[113] R. M. Jones, *Mechanics Of Composite Materials*: Taylor & Francis, 1998.
[114] R. Narayanaswami and H. M. Adelman, "Evaluation of the Tensor Polynomial and Hoffman Strength Theories for Composite Materials," *Journal of Composite Materials,* vol. 11, pp. 366-377, 1977.
[115] Y. Shi, N. Jain, R. Jemmali, S. Hofmann, D. Koch, and S. Hackemann, "Prediction of Elastic Properties for a Wound Oxide Ceramic Matrix Composite Material," *International Journal of Applied Ceramic Technology,* vol. 12, 2015.

[116] B. S. Spigel, "An Experimental and Analytical Investigation of the Iosipescu Shear Test for Composite Materials," Master of Science (MS) Thesis, Mechanical & Aerospace Engineering, Old Dominion University, 1994.
[117] F. Henning, L. Kärger, D. Dörr, F. J. Schirmaier, J. Seuffert, and A. Bernath, "Fast processing and continuous simulation of automotive structural composite components," *Composites Science and Technology,* vol. 171, pp. 261-279, 2019/02/08/ 2019.
[118] B. Mainzer, C. Lin, M. Frieß, R. Riedel, J. Riesch, A. Feichtmayer*, et al.*, "Novel ceramic matrix composites with tungsten and molybdenum fiber reinforcement," *Journal of the European Ceramic Society,* vol. 41, pp. 3030-3036, 2021/05/01/ 2021.
[119] A. Saboktakin, "3D textile preforms and composites for aircraft strcutures: A review," *International Journal of Aviation, Aeronautics, and Aerospace,* vol. 6, p. 2, 2019.
[120] H. Q. de Faria, "Analytical and Numerical Modelling of the Filament Winding Process," Mechanical Engineering, University of Porto, 2013.
[121] F. Henninger, J. Hoffmann, and K. Friedrich, "Thermoplastic filament winding with online-impregnation. Part B. Experimental study of processing parameters," *Composites Part A: Applied Science and Manufacturing,* vol. 33, pp. 1684-1695, 2002/12/01/ 2002.
[122] D. Cohen, "Influence of filament winding parameters on composite vessel quality and strength," *Composites Part A: Applied Science and Manufacturing,* vol. 28, pp. 1035-1047, 1997/01/01/ 1997.
[123] T. Sofi, S. Neunkirchen, and R. Schledjewski, "Path calculation, technology and opportunities in dry fiber winding: a review," *Advanced Manufacturing: Polymer & Composites Science,* vol. 4, pp. 57-72, 2018/07/03 2018.
[124] E. Toptaş and N. Akkuş, "Damage detection of carbon fibers in filament winding machines using an electrical resistance method," *The International Journal of Advanced Manufacturing Technology,* vol. 93, pp. 671-679, 2017/10/01 2017.
[125] O. Colas, B. Courtemanche, and A. Le Reun, "Online infrared thermography: Application to filament winding process defects detection," in *Proc. 2018 Int. Conf. Quant. InfraRed Thermogr., QIRT Council, Berlin, Germany*, 2018.
[126] C. Hopmann, N. Magura, N. Rozo Lopez, D. Schneider, and K. Fischer, "Detection and evaluation of the fibers' deposition parameters during wet filament winding," *Polymer Engineering & Science,* vol. 61, pp. 1353-1367, 2021.
[127] J. F. A. Kessels and R. Akkerman, "Prediction of the yarn trajectories on complex braided preforms," *Composites Part A: Applied Science and Manufacturing,* vol. 33, pp. 1073-1081, 2002/08/01/ 2002.
[128] J. H. van Ravenhorst and R. Akkerman, "Circular braiding take-up speed generation using inverse kinematics," *Composites Part A: Applied Science and Manufacturing,* vol. 64, pp. 147-158, 2014/09/01/ 2014.
[129] T. Hans, J. Cichosz, M. Brand, and R. Hinterhölzl, "Finite element simulation of the braiding process for arbitrary mandrel shapes," *Composites Part A: Applied Science and Manufacturing,* vol. 77, pp. 124-132, 2015/10/01/ 2015.
[130] R. Czichos, O. Bareiro, A. K. Pickett, P. Middendorf, and T. Gries, "Experimental and numerical studies of process variabilities in biaxial carbon fiber braids," *International Journal of Material Forming,* vol. 14, pp. 39-54, 2021/01/01 2021.
[131] J. Cichosz, "Experimental characterization and numerical modeling of the mechanical response for biaxial braided composites," PhD Thesis, Technische Universität München, 2016.
[132] A. K. Pickett, J. Sirtautas, and A. Erber, "Braiding Simulation and Prediction of Mechanical Properties," *Applied Composite Materials,* vol. 16, p. 345, 2009/09/16 2009.
[133] Y. Kyosev, M. Hübner, and C. Cherif, "Virtual development and numerical simulation of 3D braids for composites," *IOP Conference Series: Materials Science and Engineering,* vol. 406, p. 012025, 2018/09/21 2018.

[134] E. E. Swery, T. Hans, M. Bultez, W. Wijaya, P. Kelly, R. Hinterhölzl*, et al.*, "Complete simulation process chain for the manufacturing of braided composite parts," *Composites Part A: Applied Science and Manufacturing,* vol. 102, pp. 378-390, 2017/11/01/ 2017.
[135] G. W. Melenka and C. Ayranci, "Advanced measurement techniques for braided composite structures: A review of current and upcoming trends," *Journal of Composite Materials,* vol. 54, pp. 3895-3917, 2020.
[136] M. Hübner, O. Diestel, C. Sennewald, T. Gereke, and C. Cherif, "Simulation of the Drapability of Textile Semi-Finished Products with Gradient-Drapability Characteristics by Varying the Fabric Weave," *Fibres & Textiles in Eastern Europe,* vol. Nr 5 (94), pp. 88-93, 2012.
[137] A. Mallach, F. Härtel, F. Heieck, J.-P. Fuhr, P. Middendorf, and M. Gude, "Experimental comparison of a macroscopic draping simulation for dry non-crimp fabric preforming on a complex geometry by means of optical measurement," *Journal of Composite Materials,* vol. 51, pp. 2363-2375, 2017.
[138] O. Döbrich, A. Anderegg, N. Gort, and C. Brauner, "Machine Vision for As-Built Modeling of Complex Draped Composite Structures," *Materials (Basel, Switzerland),* vol. 14, p. 682, 2021.
[139] G. Bardl, A. Nocke, M. Hübner, T. Gereke, M. Pooch, M. Schulze*, et al.*, "Analysis of the 3D draping behavior of carbon fiber non-crimp fabrics with eddy current technique," *Composites Part B: Engineering,* vol. 132, pp. 49-60, 2018/01/01/ 2018.
[140] A. Tabiei and R. Murugesan, "Thermal Structural Forming Simulation of Carbon and Glass Fiber Reinforced Plastics Composites," *International Journal of Composite Materials,* vol. 5, pp. 182-194, 2015.
[141] G. Corman and K. Luthra, "Silicon melt infiltrated ceramic composites (HiPerComp™)," in *Handbook of ceramic composites*, ed: Springer, 2005, pp. 99-115.
[142] P. Craig, "Continuous Fiber Ceramic Composites CFCC Program for DMO Materials.," The Unites States Department of Energy2002.
[143] K. L. Choy, "Chemical vapour deposition of coatings," *Progress in Materials Science,* vol. 48, pp. 57-170, 2003/01/01/ 2003.
[144] J. A. García-Manrique, B. Marí, A. Ribes-Greus, L. Monreal, R. Teruel, L. Gascón*, et al.*, "Study of the Degree of Cure through Thermal Analysis and Raman Spectroscopy in Composite-Forming Processes," *Materials,* vol. 12, p. 3991, 2019.
[145] E. Baché, C. Dupleix-Couderc, E. Arquis, and I. Berdoyes, "Impregnation of Composite Materials: a Numerical Study," *Applied Composite Materials,* vol. 25, pp. 1287-1305, 2018/12/01 2018.
[146] A. George, "Optimization of resin infusion processing for composite materials: simulation and characterization strategies," PhD Thesis Faculty of Aerospace Engineering and Geodesy, University of Stuttgart, 2011.
[147] W.-K. Yang, S.-C. Chang, and W.-B. Young, "Simulation of the Resin Infiltration in Fiber Bundles Using the Lattice Boltzmann Method," *Journal of Aeronautics, Astronautics and Aviation,* vol. 51, pp. 321-333, 2019.
[148] V. Michaud and A. Mortensen, "Infiltration processing of fibre reinforced composites: governing phenomena," *Composites Part A: Applied Science and Manufacturing,* vol. 32, pp. 981-996, 2001/08/01/ 2001.
[149] M. Shah and V. Chaudhary, "Flow modeling and simulation study of vacuum assisted resin transfer molding (VARTM) process: A review," *IOP Conference Series: Materials Science and Engineering,* vol. 872, p. 012087, 2020/06/27 2020.
[150] C. Lystrup, A. George, B. Zobell, K. Boster, C. Childs, H. Girod*, et al.*, "Optical measurement of voids in situ during infusion of carbon reinforcements," *Journal of Composite Materials,* vol. 55, pp. 775-786, 2021.
[151] W. Chen and D. Zhang, "A micromechanics-based processing model for predicting residual stress in fiber-reinforced polymer matrix composites," *Composite Structures,* vol. 204, pp. 153-166, 2018/11/15/ 2018.

[152] S. Nosewicz, J. Rojek, M. Chmielewski, and K. Pietrzak, "Discrete Element Modeling of Intermetallic Matrix Composite Manufacturing by Powder Metallurgy," *Materials,* vol. 12, p. 281, 2019.
[153] G. L. Vignoles, W. Ros, I. Szelengowicz, C. Mulat, C. Germain, and M. Donias, "Modelling Infiltration of Fibre Preforms From X-Ray Tomography Data," *Advances in Science and Technology,* vol. 71, pp. 108-117, 2011.
[154] G. Vignoles, "Modelling of the CVI Processes," *Advances in Science and Technology,* vol. 50, pp. 97 - 106, 2006-10 2006.
[155] G. L. Vignoles, "17 - Modeling of chemical vapor infiltration processes," in *Advances in Composites Manufacturing and Process Design*, P. Boisse, Ed., ed: Woodhead Publishing, 2015, pp. 415-458.
[156] R. Sankaran, V. A. Ramanuj, C. M. Cha, and D. Liliedahl, "Level-set Modeling Simulations of Chemical Vapor Infiltration for Ceramic Matrix Composites Manufacturing,"; Oak Ridge National Lab. (ORNL), Oak Ridge, TN (United States) ORNL/TM-2019/1206; CRADA/NFE-16-06412; Other: CRADA/NFE-16-06412 United States 10.2172/1615819 Other: CRADA/NFE-16-06412 ORNL English, 2019.
[157] A. Li, K. Norinaga, W. Zhang, and O. Deutschmann, "Modeling and simulation of materials synthesis: Chemical vapor deposition and infiltration of pyrolytic carbon," *Composites Science and Technology,* vol. 68, pp. 1097-1104, 2008/04/01/ 2008.
[158] Y. Zhu and E. Schnack, "Numerical Modeling Chemical Vapor Infiltration of SiC Composites," *Journal of Chemistry,* vol. 2013, p. 836187, 2012/12/23 2013.
[159] E. Schnack, A. Li, A. Rahman, and Y. Zhu, "A coupled numerical modelling and experimental approach in chemical vapour infiltration (CVI) process of SiC/SiC composites," *International Journal of Computational Methods and Experimental Measurements,* vol. 3, pp. 230-249, 2015.
[160] F. Reichert, A. M. Pérez-Mas, D. Barreda, C. Blanco, R. Santamaria, C. Kuttner*, et al.*, "Influence of the carbonization temperature on the mechanical properties of thermoplastic polymer derived C/C-SiC composites," *Journal of the European Ceramic Society,* vol. 37, pp. 523-529, 2017/02/01/ 2017.
[161] X. Wu, N. Langhof, W. Krenkel, R. Habath, and F. Lenz, "Effect of pyrolysis temperature on the microstructure and capillary infiltration behavior of carbon/carbon composites," *Ceramics International,* vol. 44, pp. 16325-16332, 2018/10/01/ 2018.
[162] X. Qin, "Modeling Study of Pyrolysis of Composite Materials: Application to Wood and Carbon/Epoxy Composite," PhD Thesis, Chasseneuil-du-Poitou, Ecole nationale supérieure de mécanique et d …, 2021.
[163] T. Jiang, Z. Guan, Z. Li, X. Liu, and K. Geng, "Process modelling of precursor impregnation and pyrolysis used in manufacturing ceramic-matrix composites," *Ceramics International,* vol. 47, pp. 7195-7206, 2021/03/01/ 2021.
[164] D. Behrendt and M. Singh, "Effect of carbon preform pore volume and infiltrants on the composition of reaction-formed silicon carbide materials," *J. Mater. Synth. Process.(USA),* vol. 2, pp. 117-123, 1994.
[165] E. S. Nelson and P. Colella, "Parametric study of reactive melt infiltration," International Mechanical Engineering Congress and Exposition, American Society of Mechanical Engineers2000.
[166] E. O. Einset, "Analysis of reactive melt infiltration in the processing of ceramics and ceramic composites," *Chemical Engineering Science,* vol. 53, pp. 1027-1039, 1998/02/06/ 1998.
[167] M. K. Naikade, "Study and characterization of silicon metal alloys systems for the reactive infiltration process of ceramic matrix composites," PhD Thesis, EPFL, 2021.
[168] V. A. Dutka, "Numerical modeling of liquid-phase infiltration in the process of sintering ceramic composites," *Journal of Superhard Materials,* vol. 36, pp. 105-116, 2014/03/01 2014.
[169] G. Mica, G. Rohan, R. S., S. Jennifer, Y. Ramin, and B. R. K., "Multi-physics modeling and simulations of reactive melt infiltration process used in fabrication of ceramic-matrix

composites (CMCs)," *Multidiscipline Modeling in Materials and Structures,* vol. 11, pp. 43-74, 2015.
[170] P. J. Hofbauer, F. Raether, and E. Rädlein, "Finite element modeling of reactive liquid silicon infiltration," *Journal of the European Ceramic Society,* vol. 40, pp. 251-258, 2020/02/01/ 2020.
[171] P. J. Hofbauer, "In-situ-Messung und Simulation der Flüssigphasensilicierung," 21 PhD Thesis, Universitätsverlag Ilmenau, Ilmenau, 2020.
[172] Q. An, J. Chen, W. Ming, and M. Chen, "Machining of SiC ceramic matrix composites: A review," *Chinese Journal of Aeronautics,* vol. 34, pp. 540-567, 2021/04/01/ 2021.
[173] O. Gavalda Diaz, G. Garcia Luna, Z. Liao, and D. Axinte, "The new challenges of machining Ceramic Matrix Composites (CMCs): Review of surface integrity," *International Journal of Machine Tools and Manufacture,* vol. 139, pp. 24-36, 2019/04/01/ 2019.
[174] A. Abdul-Aziz, "Durability Modeling Review of Thermal- and Environmental-Barrier-Coated Fiber-Reinforced Ceramic Matrix Composites Part I," *Materials,* vol. 11, p. 1251, 2018.
[175] A. Abdul-Aziz and A. C. Wroblewski, "Durability Analysis and Experimental Validation of Environmental Barrier Coating (EBC) Performance Using Combined Digital Image Correlation and NDE," *Coatings,* vol. 6, p. 70, 2016.
[176] A. Abdul-Aziz, R. T. Bhatt, and J. E. Grady, "Criteria for Crack Deflection-Penetration in EBC Coated Ceramics: A Parametric Study," *Mechanics of Advanced Materials and Structures,* vol. 22, pp. 1039-1047, 2015/12/02 2015.
[177] B. Lv, X. Jin, J. Cao, B. Xu, Y. Wang, and D. Fang, "Advances in numerical modeling of environmental barrier coating systems for gas turbines," *Journal of the European Ceramic Society,* vol. 40, pp. 3363-3379, 2020/08/01/ 2020.
[178] R. S. Pierce and X. Liu, "Exploiting the optical reflectance behaviour of carbon fibre composites for low-cost inspection and orientations analysis," *Journal of Reinforced Plastics and Composites,* vol. 39, pp. 869-879, 2020.
[179] S. Gubernatis, J.-M. Balvers, and C. Weimer, "Concept Development for Inline Process Control of the Preform-LCM ProductionChain," in *4th International Symposium on NDT in Aerospace*, 2012.
[180] M. Verrilli, A. Calomino, R. C. Robinson, and D. J. Thomas, "Ceramic Matrix Composite Vane Subelement Testing in a Gas Turbine Environment," in *ASME Turbo Expo 2004: Power for Land, Sea, and Air*, 2004, pp. 393-399.
[181] "3-D printed parts and new materials help Rolls-Royce to engine test success," ed: Rolls Royce, 2018.